Semiconductors, Vol. 37, No. 9, 2003, pp. 1031–1032. Translated from Fizika i Tekhnika Poluprovodnikov, Vol. 37, No. 9, 2003, pp. 1056–1057.
Original Russian Text Copyright © 2003 by Nazyrov.

ATOMIC STRUCTURE AND NONELECTRONIC PROPERTIES OF SEMICONDUCTORS

Diffusion of Ytterbium in Silicon

D. É. Nazyrov

Ulugbek National University of Uzbekistan, Tashkent, 700174 Uzbekistan
Submitted December 9, 2002; accepted for publication December 17, 2002

Abstract—Diffusion of ytterbium in silicon is studied by the direct method of radioactive isotopes in the temperature range of 1100–1250°C. Diffusion coefficients of ytterbium impurity in silicon are determined. © *2003 MAIK "Nauka/Interperiodica".*

In recent years, interest has increased in the study of the properties of silicon doped with rare-earth elements (REEs) because of the high thermal and radiation resistance of REE-doped silicon and the possibility of the application of Si:REE-structures in optoelectronics as light sources [1–3]. This is why the study of diffusion of REE in Si deserve attention and are of particular interest.

We studied the diffusion of REE ytterbium in silicon by the direct method of radioactive isotopes. The results of this study are presented in this publication. Previously, the diffusion of Yb in Si was studied mainly by indirect methods [4–8] and by neutron-activation analysis [9].

The samples were prepared by depositing either a metallic layer of radioactive isotope ^{175}Yb on the surface of n-Si (ρ = 15 Ω cm, surface area ~1.5 cm^2, thickness ~350 μm) or a layer of ytterbium chloride solution containing radioactive isotope ^{175}Yb. Activation of Yb atoms was performed at the Konstantinov Institute of Nuclear Physics, Russian Academy of Sciences (St. Petersburg).

The cells containing the samples were placed into an SDO-1 diffusion furnace with a REPID programmable temperature control which ensured temperature control within ±1 K. Diffusion annealing was performed in air, in evacuated cells (residual pressure ~10^{-4} Torr), and in evacuated cells in an argon atmosphere in the temperature range of 1100–1250°C. The annealing duration varied from 5 to 48 hours, depending on the diffusion temperature.

After the diffusion annealing, the samples were repeatedly rinsed in hydrofluoric acid, aqua regia, and also in an H_2O_2 : HCl boiling mixture. Such rinsing usually ensures almost complete removal of the remains of the diffusion source from the surface of a sample. After this procedure, the edges of a sample were scraped to a depth of ~100 μm, which was much larger than the diffusion depth (~10 μm). The concentration profile of Yb impurity in Si was analyzed by etching off thin layers in a 1 HF : 50 HNO_3 solution with subsequent rinsing in a H_2O_2 : HCl mixture and the measurement of the residual radioactivity of the sample. The residual activity was measured using a UMF-1500M low-background setup with an SBT-11 beta counter. Identification of ^{175}Yb was also performed using an AI-1024 pulse analyzer (Ioffe Physicotechnical Institute, Russian Academy of Sciences, St. Petersburg). The thickness of etched-off layers (0.05–0.5 μm) was determined by the weighing of the sample. Autoradiograms obtained prior and after annealing, as well as in the course of etching off layers, point to the uniformity of the distribution of Yb impurities across the sample section and to the absence of inclusions.

The diffusion coefficient D of Yb in Si in our experiments was determined on the assumption that the Fick law was obeyed and that the surface concentration of impurity was independent of time (diffusion from an inexhaustable constant source).

The experimental curve of the residual amount of impurity was approximated, as in [10], by the theoretical curve for the diffusion from an inexhaustable source; i.e.,

$$Q(x) = 2C_0\sqrt{Dt}\,\mathrm{ierfc}(x/2\sqrt{Dt}),$$

where C_0 is the surface concentration, x is the total thickness of the etched-off layers, and t is the diffusion time.

As follows from the data obtained (see figure), the diffusion coefficient for Yb in Si increases from 3×10^{-13} to 4×10^{-12} cm^2 s^{-1} with increasing temperature. The temperature dependence obeys the Arrhenius law and can be described by the relation

$$D_{\mathrm{Yb}} = 3 \times 10^{-2} \exp(-3.0\ \mathrm{eV}/kT)\,\mathrm{cm}^2\,\mathrm{s}^{-1} (1100\text{–}1250°\mathrm{C}).$$

The surface concentration of Yb is 10^{18}–10^{19} cm^{-3}. The depth of Yb penetration into Si, which was estimated using the value of $2\sqrt{Dt}$, was about several micrometers in the entire range of temperatures under consideration.

The analysis of data obtained shows that the diffusion coefficients for various temperatures and activation energies cover the range of values typical of the

1063-7826/03/3709-1031$24.00 © 2003 MAIK "Nauka/Interperiodica"

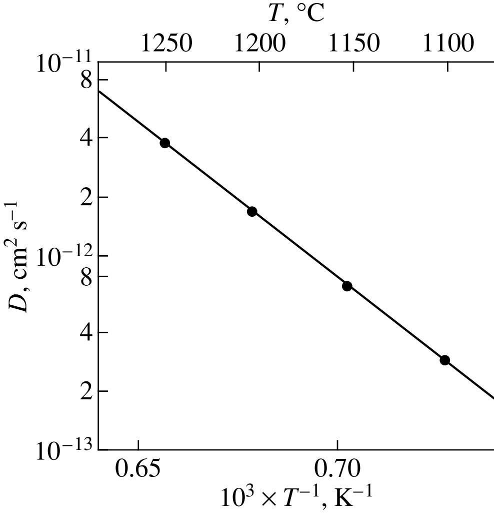

Temperature dependence of diffusion coefficient for ytterbium in silicon.

diffusion of other elements of the III *B* Group, such as B, Al, In, Ga, and Tl, which are the substitutional impurities that diffuse over the crystal-lattice sites. It is known that the elements of the Groups III and V at thermal equilibrium occupy Si and Ge lattice sites. On theoretical grounds it is commonly assumed that the equilibrium concentration of the interstitial atoms of these elements is several orders of magnitude (3 or greater) less than their concentration at the lattice sites [11]. However, even if the elements of group III (Ho, Er, Yb [12–14] and others) are introduced into Si by ion implantation (i.e., when the concentration of nonequilibrium interstitial atoms is quite high), no appreciable diffusion of REEs is observed with the diffusion parameters different from classical ones. Thus, we may assume that Yb, a Group III element, is also a substitutional impurity and diffuses over the lattice sites of Si (vacancy-diffusion mechanism).

The comparison of our data on the diffusion of Yb in Si with previous data on the diffusion of other REEs in Si [10, 14–16] obtained by radioactive and other methods shows that the procedure of deposition of the diffusant and the diffusion medium do not significantly affect the diffusion parameters of REE in Si.

REFERENCES

1. V. M. Glazov, A. Ya. Potemkin, G. G. Timoshina, and M. S. Mikhaĭlova, Fiz. Tekh. Poluprovodn. (St. Petersburg) **31**, 1025 (1997) [Semiconductors **31**, 875 (1997)].
2. N. G. Bagraev, L. S. Vlasenko, V. M. Volle, *et al.*, Zh. Tekh. Fiz. **54**, 917 (1984) [Sov. Phys. Tech. Phys. **29**, 547 (1984)].
3. N. A. Sobolev, Fiz. Tekh. Poluprovodn. (St. Petersburg) **29**, 1153 (1995) [Semiconductors **29**, 595 (1995)].
4. A. I. Borisenko, Yu. M. Volokobinskiĭ, V. N. Kokovina, *et al.*, Dokl. Akad. Nauk SSSR, Ser. Khim. **262**, 1409 (1982).
5. M. K. Bakhadyrkhanov, F. M. Talipov, U. S. Dzhurabekov, *et al.*, Élektron. Tekh., Ser. 6: Mater., No. 5 (190), 79 (1984).
6. V. N. Abrosimova, E. P. Troshina, and L. F. Chepik, *Properties of Doped Semiconductor Materials* (Nauka, Moscow, 1990).
7. V. V. Ageev, V. N. Kokovina, N. E. Prikhod'ko, and E. P. Troshina, Izv. Leningr. Élektrotekhnich. Inst. **186**, 51 (1976).
8. A. G. Kozlov, Izv. Leningr. Élektrotekhnich. Inst. **338**, 79 (1984).
9. M. K. Bakhadyrkhanov, F. M. Talipov, N. V. Sultanova, *et al.*, Izv. Akad. Nauk SSSR, Neorg. Mater. **26** (3), 458 (1990).
10. D. É. Nazyrov, V. P. Usacheva, G. S. Kulikov, and R. Sh. Malkovich, Pis'ma Zh. Tekh. Fiz. **14**, 1102 (1988) [Sov. Tech. Phys. Lett. **14**, 483 (1988)].
11. *Atomic Diffusion in Semiconductors*, Ed. by D. Shaw (Plenum, London, 1973; Mir, Moscow, 1975).
12. V. V. Emtsev, V. V. Emtsev, Jr., D. S. Poloskin, *et al.*, Fiz. Tekh. Poluprovodn. (St. Petersburg) **33**, 649 (1999) [Semiconductors **33**, 603 (1999)].
13. O. V. Aleksandrov, A. O. Zakhar'in, and N. A. Sobolev, Fiz. Tekh. Poluprovodn. (St. Petersburg) **36**, 134 (2002) [Semiconductors **36**, 126 (2002)].
14. D. É. Nazyrov, S. A. Goncharov, and A. V. Suvorov, Pis'ma Zh. Tekh. Fiz. **26** (8), 24 (2000) [Tech. Phys. Lett. **26**, 326 (2000)].
15. D. É. Nazyrov, G. S. Kulikov, and R. Sh. Malkovich, Fiz. Tekh. Poluprovodn. (Leningrad) **25**, 1653 (1991) [Sov. Phys. Semicond. **25**, 997 (1991)].
16. G. K. Azimov, S. Zaĭnabidinov, and D. É. Nazyrov, Fiz. Tekh. Poluprovodn. (Leningrad) **23**, 556 (1989) [Sov. Phys. Semicond. **23**, 347 (1989)].

Translated by A. Zalesskiĭ

Semiconductors, Vol. 37, No. 9, 2003, pp. 1033–1036. Translated from Fizika i Tekhnika Poluprovodnikov, Vol. 37, No. 9, 2003, pp. 1058–1061.
Original Russian Text Copyright © 2003 by Pagava, Basheleĭshvili.

Migration Energy of Vacancies in *p*-Type Silicon Crystals

T. A. Pagava and Z. V. Basheleĭshvili

Georgian Technical University, ul. M. Kostaza 77, Tbilisi, 380075 Georgia

Submitted June 25, 2002; accepted for publication December 19, 2002

Abstract—*p*-Si:B samples were irradiated with 8-MeV electrons. The values of the activation energy of annealing for K centers and for $(V + \mathrm{B})$ complexes obtained from the curves of isochronous annealing of these centers are found to be equal to 0.915 and 1.6 eV, respectively. The volumetric measurements of photovoltage over the irradiated region make it possible to estimate the values of the migration energy of vacancies. The migration energy is found to be $E^M_{V^{++}} \approx 0.6$ eV for positively charged vacancies and $E^M_{V^0} \approx 0.345$ eV for neutral vacancies. © *2003 MAIK "Nauka/Interperiodica".*

In [1–3], the charge state of metastable Frenkel pairs in *n*- and *p*-Si was studied by the method of local irradiation with the subsequent measurement of the volume photovoltage over the irradiated region. It was found that the damaged region of a crystal expanded with variation in the irradiation doze Φ. It was suggested [1, 3] that the expansion of the damaged area was caused by the diffusion of primary radiation defects from the irradiated region of the crystal into unirradiated regions under a high ionization level.

It can be inferred that the expansion of the damaged area of a sample can be observed not only during irradiation but also in the course of isochronous annealing due to the diffusion of primary radiation defects the products of the dissociation of the secondary radiation defects that form highly thermostable defects in unirradiated regions from the irradiated region of a crystal into an unirradiated region.

This study is devoted to the mechanism of the expansion of the damaged regions of a crystal and to the effect of potential barriers at the boundaries between the damaged and intact regions of a sample which are formed during irradiation and isochronous annealing.

We studied *p*-Si crystals, with a hole concentration $p = 6 \times 10^{13}$ cm^{-3}, grown by the Czochralski method. The concentration of oxygen was about 5×10^{17} cm^{-3}; the density of grown-in dislocations was no higher than 10^3–10^4 cm^{-2}. Crystals $1 \times 3 \times 20$ mm in size were irradiated with 8-MeV electrons through a mask with a slit of 1 mm. The intensity of irradiation was 5×10^{12} cm^{-2} s^{-1}; the dose $\Phi = 1.35 \times 10^{16}$ cm^{-2}. Isochronous annealing of irradiated samples was performed in the temperature range of 20–600°C. The samples were kept at a constant temperature for 10 min. Secondary radiation defects that are formed during isochronous annealing outside the irradiated stripe of the sample can create primary radiation defects and, thus, affect the true dimension L of the damaged region. To avoid this effect, new, identical crystals that had not been previously heat treated were annealed at various temperatures. In order to minimize error in the measurements of the duration t of isochronous annealing and the width L of a damaged stripe, the crystals were quenched in liquid nitrogen after each isochronous annealing. After quenching, the volumetric distribution of photovoltage U_{ph} over the sample was measured at 300 K. $U_{ph} \propto \partial\rho/\partial x \propto N_{RD}$, where $\partial\rho/\partial x$ is the gradient of resistivity, and N_{RD} is the concentration of radiation defects with energy levels $\Delta E > E_v + 0.3$ eV. The relative error in measuring the photovoltage was 20%.

In samples irradiated over their entire volume, after each heat treatment the hole concentration p was determined at 77–300 K from the Hall effect measurements. The energy levels of defects ΔE were determined from the formula $p_0 = N_v F_{1/2}$, where p_0 is the concentration of free holes, N_v is the effective density of states in the valence band, and $F_{1/2}$ is the Fermi–Dirac integral with an index of 1/2. When the Fermi level $F = \Delta E$, p_0 can be calculated from the $p = f(10^3/T)$ curves with due regard for the depletion of a certain level and the degree of degeneracy of the valence band of Si. In heavily compensated samples, ΔE was determined from the slope of the $p = f(10^3/T)$ curves. The concentrations of different radiation defects after each isochronous annealing were calculated from the dependences $p = f(10^3/T)$ and $p = f(T_{ann})$ in the ranges of 77–300 K and 20–500°C, respectively. The error in measuring these values did not exceed 10%.

The distribution of U_{ph} over the irradiated region of the sample is shown in Fig. 1. It can be seen that L increases from 1 to 2.9 mm with Φ increasing to 1.35×10^{16} cm^{-2}, while annealing at 220°C results in an increase of L to 10 mm (curves *2* and *3*, respectively). When $T_{ann} = 600$°C, the peaks in the curves $U_{ph}(L)$ disappear (curve *4*).

The analysis of temperature dependences $\ln p = f(10^3/T)$ shows that in *p*-Si, in the course of irradiation, defects with levels $E_v + 0.45$. $E_v + 0.3$, and $E_v + 0.35$ eV

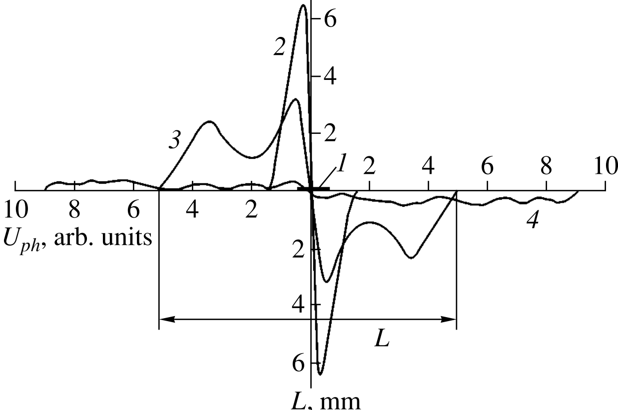

Fig. 1. Distribution of volumetric photovoltage U_{ph} over locally irradiated sample of *n*-Si: (*1*) the slit width in the mask; (*2*) distribution of U_{ph} after irradiation with 8-MeV electrons (a dose $\Phi = 1.35 \times 10^{16}$ cm^{-2}); (*3*), (*4*) distribution of U_{ph} after annealing at 200 and 600°C, respectively.

are formed along with other defects (Fig. 2a). As can be seen from curve *1* in Fig. 2b, these defects are annealed in the temperature ranges of 180–220, 250–300, and 330–440°C, respectively (curve *1* corresponds to the variation of *p* at 260 K). Judging by their thermostability, these levels can be attributed to (V + B) complexes, divacancies, and *K* centers [4, 5]. It is known [6–8] that the dominant defects in Si crystals with a high concentration of oxygen (10^{17}–10^{18} cm^{-3}) are *K* centers. In fact, the concentration of the *K* centers in the sample under consideration is higher than the concentration of divacancies by a factor of 2.5 (Fig. 2b, curve *1*). The activation energy of annealing E_a was determined from the curves of isochronous annealing of these defects [9] (Fig. 2b, curves *2*–*4*). The calculations yielded $E_a = 1.6$, 1.54, and 0.9 eV, respectively.

The dependence of $l = L/2$ on the temperature of isochronous annealing is shown in Fig. 3. It can be seen that *l* sharply increases in the temperature ranges of 180–220 and 300–340°C, which coincide with the annealing temperatures of the (V + B) complexes and *K* centers, respectively [4, 5]. The slope of the $l(T_{ann}^{-1})$ dependence during the decomposition of the (V + B) complexes in the temperature range of 180–220°C is larger than that for the dissociation of the *K* centers in the range of 300–340°C. The effect observed is likely associated with the change in the charge state of vacancies and the products of dissociation of radiation defects in the process of transition from impurity conductivity to intrinsic conductivity.

As can be seen from Fig. 3, the increase of *l* corresponding to the decomposition of divacancies is absent in the temperature range of 250–300°C. In all likelihood, the charge state of the components of the secondary radiation defects in this temperature range is unfa-

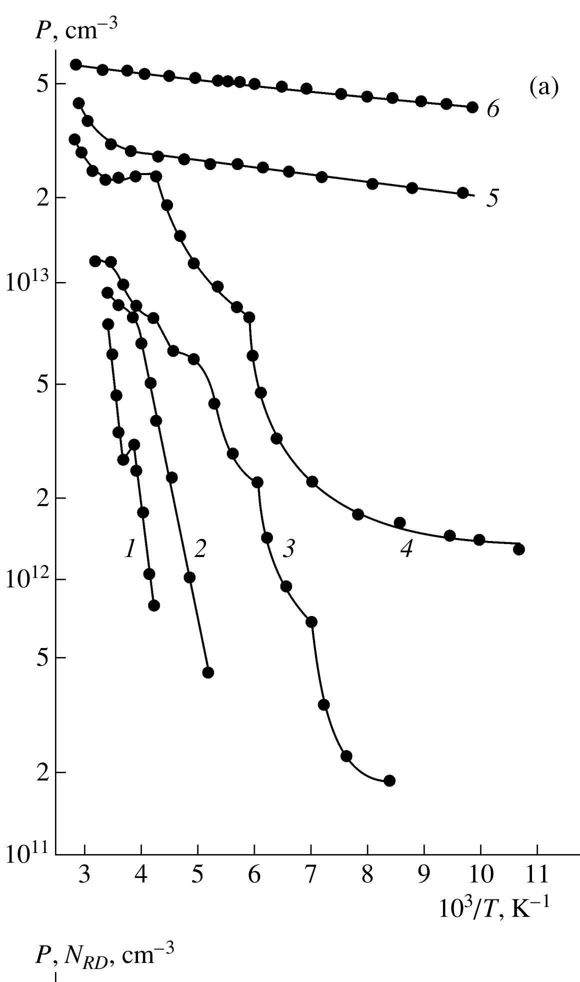

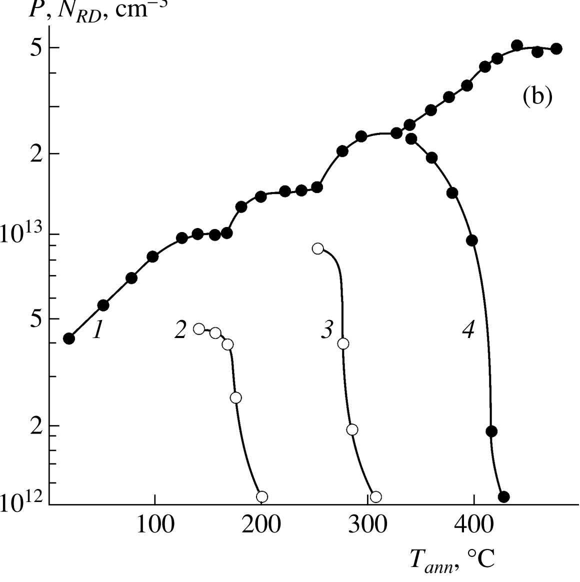

Fig. 2. (a) Hole concentration *p* as a function of temperature in electron-irradiated *p*-Si crystals ($\Phi = 1.35 \times 10^{16}$ cm^{-2}): (*1*) prior to annealing and after annealing at T_{ann} = (*2*) 100, (*3*) 170, (*4*) 270, (*5*) 500, and (*6*) 600°C; (b) hole concentration *p* and the concentration of some radiation defects (N_{RD}) as a function of the temperature of isochronous annealing. (*1*) *p*, (*2*) (V + B), (*3*) V_2, (*4*) *K*-centers; the change in *p* was observed at 260 K.

vorable for their formation outside the irradiated region in the course of isochronous annealing.

In order to obtain the heights of the potential barrier at the boundaries between irradiated and intact regions of the sample, we used the formula $E_b = kT\ln(p_1/p_2)$, where k is the Boltzmann constant; T is the absolute temperature; and p_1 and p_2 are the hole concentrations in the unirradiated and irradiated regions, respectively. At room temperature, $E_b = 0.065$ eV. With increasing temperature of isochronous annealing, the simultaneous processes of trapping electrons from the valence band by radiation defects and the dissociation of radiation defects themselves occur, which results in an increase of p inside the irradiated stripe of the crystal. At $T_{ann} \approx 130°C$, $p_1 = p_2$ and $E_b = 0$; therefore, the internal electrical fields acting at the boundaries between the damaged and intact regions of the crystal in the course of isochronous annealing can affect the migration energy of vacancies E_V^M only at the initial stages of annealing ($T_{ann} \leq 130°C$).

It is known that $l = \sqrt{Dt}$, where l is the distance from the center of the irradiated stripe to the edge of the damaged crystal region which expands in the process of isochronous annealing (Fig. 1), t is the time of annealing at a fixed temperature (10 min), and D is the diffusion coefficient. From this formula it follows that $l^2/t = D$ and $l^2/t = D_0\exp(-E_S/kT)$, where $D_0 = Za^2\nu$, Z is the coordination number, a is the lattice constant, ν is the lattice vibration frequency, and E_S is the energy of self-diffusion. Since t = const, $\ln l = 1/2\ln D_0 t - E_S/2kT$. From the experimental dependence $\ln l = f(10^3/T)$, one can determine the activation energy of self-diffusion of vacancies E_S (Fig. 3).

It is known [4] that, if self-diffusion proceeds according to the monovacancy mechanism, $E_S = E_V^F + E_V^M$, where E_V^F is the energy of vacancy formation and E_V^M is the vacancy-migration energy.

When determining E_V^M, we disregarded the energy of the complex formation E_C because the vacancy trapping affects only the pre-exponential factor in the diffusion coefficient D_0 and does not affect E_S determined from the temperature dependence of D [10].

Our estimations yield $E_S \approx 2.2$ eV for the temperature range of 180–220°C and $E_S \approx 1.26$ eV for 300–340°C.

At 180–220°C, the source of nonequilibrium vacancies in the bulk of a crystal is the (V + B) complex. The energy E_a of this complex, i.e., the energy of formation of the vacancies, $E_V^F \approx 1.6$ eV. Therefore, in this temperature range, $E_{V_1}^M = E_{S_1} - E_V^F \approx 0.6$ eV.

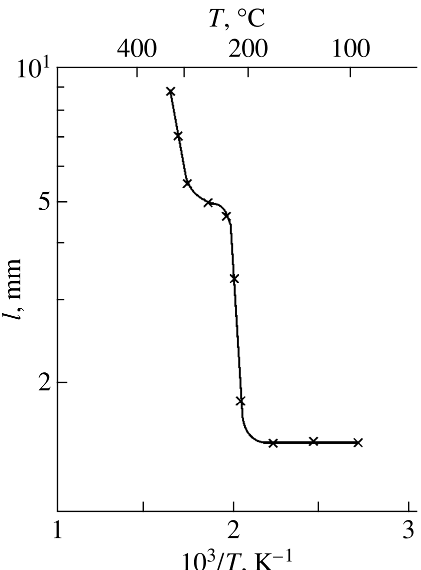

Fig. 3. Dependence of the half-width l of the damaged region of a sample on the temperature of isochronous annealing in locally irradiated p-Si crystals.

According to [7], positive vacancies are dominant in p-Si at $T < 300°C$, while at $T > 300°C$, in the range of intrinsic conductivity, neutral vacancies are dominant. The stable charge states of vacancies in p-Si are V^{++} and V^0 [4]; therefore, we may assume that $E_{V_1}^M = E_{V^{++}}^M \approx$ 0.6 eV at $T < 300°C$.

As shown in [11], depending on the charge state, E_V^M can vary within the range of 0.18–0.48 eV. It should be noted that the dependence $E_V^M(Z)$ of the migration energy of vacancies on the parameter Z (Z characterizes the charge state of a vacancy), with the variation of Z from –2 to zero, follows a linear law (Fig. 4, curve *1*). Assuming that the dependence $E_V^M(Z)$ for Z varying within the interval 0–2 also obeys a linear law, $E_{V^{++}}^M = 0.625$ eV, which coincides within the experimental accuracy with our calculations (Fig. 4, curve *2*).

In the range of intrinsic conductivity ($T > 300°C$), vacancies V^0 with a migration energy $E_{V^0}^M = 0.33$ eV [11] and other states are presumably the products of decomposition of K centers. Our calculations yield $E_{S_2} \approx 1.26$ eV. These data allow for the determination of E_a of the K center: $E_a = E_V^F = E_{S_2} - E_{V^0}^M \approx 0.93$ eV. E_a of the K center determined from the curve of isochronous annealing of this defect (Fig. 2b, curve *4*) is approximately equal to ≈0.9 eV. The mean values of E_a and E_V^F are $E_a = E_V^F = 0.915$ eV. Correspondingly,

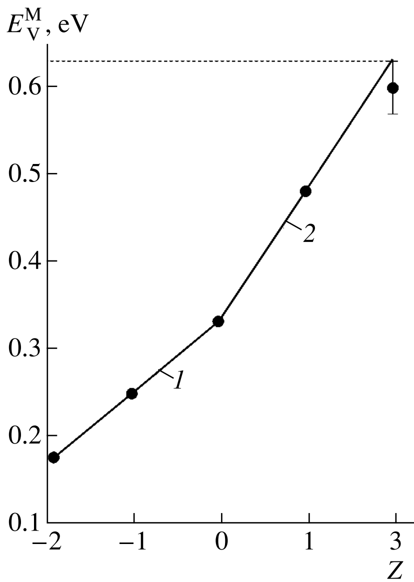

Fig. 4. Dependence of migration energy of (*1*) negative and (*2*) positive vacancies on the parameter *Z* in Si crystals.

$E^M_{V^0} \approx 0.345$ eV, which, within experimental accuracy, is in a good agreement with the published data.

The results obtained show that, in locally irradiated *p*-Si crystals in the process of isochronous annealing at temperatures of 180–220 and 300–340°C, migration of the products of dissociation of the (V + B) complexes and the *K* centers (V^{++} and V^0) occur, respectively. In unirradiated regions, these products of dissociation form complexes with a high thermostability.

If the nature of defects formed in unirradiated regions is judged from their thermostability, they are probably multicomponent defects like $V_3 + O_2$ or $V_3 + O_3$, which are annealed at 600°C [4, 12].

Thus, the values of E_a for the *K* centers obtained by two methods virtually coincide. The mean value of E_a is 0.915 eV. E_a for the (V + B) complexes obtained from the curve of isochronous annealing of this defect is approximately equal to ≈1.6 eV. Correspondngly, $E^M_{V^{++}} \approx$ 0.6 eV and $E^M_{V^0} \approx 0.345$ eV.

ACKNOWLEDGMENTS

We are grateful to O.G. Kharashvili for discussing the results and helpful comments.

REFERENCES

1. L. S. Milevskiĭ and V. S. Garnyk, Fiz. Tekh. Poluprovodn. (Leningrad) **13**, 1369 (1979) [Sov. Phys. Semicond. **13**, 801 (1979)].
2. Z. V. Basheleĭshvili, T. L. Bzhalava, T. A. Pagava, and V. V. Sanadze, Soobshch. Akad. Nauk Gruz. SSR **116** (2), 297 (1984).
3. G. Tsintsadze, T. Pagava, V. Garnic, and Z. Basheleishvili, Bull. Georgian Acad. Sci. **160** (3), 444 (1999).
4. V. V. Emtsev and T. V. Mashovets, *Impurities and Point Defects in Semiconductors* (Radio i Svyaz’, Moscow, 1981).
5. I. D. Konozenko, A. K. Semenyuk, and V. I. Khivrich, *Radiation Effects in Silicon* (Naukova Dumka, Kiev, 1974).
6. A. H. Kalma and J. C. Corelli, Phys. Rev. **173**, 734 (1968).
7. Y. H. Lee, J. W. Corbett, and K. L. Brower, Phys. Status Solidi A **41**, 637 (1977).
8. P. F. Lugakov and V. V. Luk’yanitsa, Fiz. Tekh. Poluprovodn. (Leningrad) **20**, 742 (1986) [Sov. Phys. Semicond. **20**, 469 (1986)].
9. A. C. Damask and G. J. Dienes, *Point Defects in Metals* (Gordon and Breach, New York, 1963; Mir, Moscow, 1966).
10. V. A. Panteleev, S. N. Ershov, V. V. Chernyakhovskiĭ, and S. N. Nagornykh, Pis’ma Zh. Éksp. Teor. Fiz. **23**, 688 (1976) [JETP Lett. **23**, 633 (1976)].
11. S. N. Ershov, V. A. Panteleev, S. N. Nagornykh, and V. V. Chernyakhovskiĭ, Fiz. Tverd. Tela (Leningrad) **19**, 322 (1977) [Sov. Phys. Solid State **19**, 187 (1977)].
12. J. Bourgoin and M. Lannoo, *Point Defects in Semiconductors*, Vol. 2: *Experimental Aspects* (Springer, New York, 1983; Mir, Moscow, 1985).

Translated by A. Zalesskiĭ

Semiconductors, Vol. 37, No. 9, 2003, pp. 1037–1041. Translated from Fizika i Tekhnika Poluprovodnikov, Vol. 37, No. 9, 2003, pp. 1062–1066.
Original Russian Text Copyright © 2003 by Gall', Rut'kov, Tontegode.

Thermal Stability and Transformation of C_{60} Molecules Deposited on Silicon-Coated (111) Iridium

N. R. Gall', E. V. Rut'kov, and A. Ya. Tontegode

Ioffe Physicotechnical Institute, Russian Academy of Sciences, Politekhnicheskaya ul. 26, St. Petersburg, 194021 Russia

e-mail: gall@ms.ioffe.ru

Submitted January 13, 2003; accepted for publication January 13, 2003

Abstract—Thermal stability and transformation of C_{60} molecules deposited onto a silicon film on (111) iridium have been studied in ultrahigh vacuum within the temperature range of 300–1900 K. The temperature range covered is shown to break up into four consecutive regions, each dominated by its own specific process; namely, thermal stability of C_{60} films ($T < 600$ K), desorption of fullerene molecules from the second and subsequent molecular layers (800–900 K), decomposition of these molecules in the first layer which contacts the substrate (650–850 K), graphitization of the carbon layer into a thermally stable two-dimensional graphite film (900–1700 K), and thermal desorption of carbon from the surface ($T > 1900$ K). These processes retain their qualitative character as one passes from Si submonolayer films to (4–5)-monolayer-thick films. © *2003 MAIK "Nauka/Interperiodica".*

1. INTRODUCTION

Investigation of the interaction of fullerene molecules with matter, in particular, with the surfaces of solids, is of importance from both fundamental and applied perspectives. A wealth of scientific information is presently available on the adsorption of fullerenes on, and their stability in contact with, clean surfaces (silicon [1–5], noble [6–8] or refractory metals [9–15]). In contrast, film systems intended as substrates for fullerenes remain almost unexplored. At the same time, such systems have considerable application potential, primarily due to the diversity of their physicochemical and adsorption properties. Of particular interest is the investigation of such an interaction over a broad temperature range, where the adsorbed layer can undergo rearrangement and solid-state reactions can occur in the surface region of the substrate.

Adsorbed C_{60} molecules were found to retain their fullerene nature on the surface of Si, Ir, Re, and Mo up to a temperature specific for a given substrate (~800 K for Re [12], ~1000 K for Ir [10]). At higher temperatures, the molecules break up, and the carbon released in the adlayer dissolves in the bulk of the substrate (on Re and Mo) or undergoes graphitization (on Ir). This communication reports on the study of the thermal transformation of the fullerenes adsorbed on a complex film structure, more specifically, on a silicon film deposited on (111) iridium, and identification of the sequence of the processes involved therein.

2. EXPERIMENTAL

The experiments were conducted in ultrahigh vacuum ($P \approx 10^{-10}$ Torr) using a high-resolution Auger spectrometer, which is described in [6]. The Auger peaks of silicon ($E = 92$ eV), iridium (a triplet with energies 150–170 eV), and carbon ($E = 269$–272 eV) were measured. It was possible to record Auger peaks directly from heated samples in the range of 300–2100 K. The samples were directly heated iridium ribbons with a predominantly (111)-oriented surface, $0.02 \times 1 \times 40$ mm^3 in size, which were cleaned by successive annealing in oxygen ($P_{O_2} \approx 10^{-6}$ Torr, $T = 1500$ K, $t \approx 30$ min) and high-temperature heating (~2100 K) for several hours. After this cleaning, only peaks of iridium were detected in the Auger spectra from the surface.

Silicon was deposited by sublimation from silicon ribbons by the technique described in [17]. The absolute value of the silicon flux could be determined. The fullerenes were deposited onto the entire ribbon surface from a Knudsen cell (see [14]). After corresponding heat treatment, the cell produced a stable and easily controllable flow of fullerene molecules with a density $\nu_C = 10^{10}$–10^{13} mol/(s cm^2). The absolute number of the adsorbed fullerenes was established by the method described in [14]. To discriminate the fullerenes adsorbed on the surface from other possible carbon states, as well as to identify the chemical state of the adsorbed C_{60} molecules, we used the specific shape of the C_{KVV} Auger peak as suggested in [10].

3. SEPARATE INTERACTION OF IRIDIUM (111) SURFACE WITH SILICON, CARBON, AND FULLERENES

3.1. Interaction of Silicon with the Iridium (111) Surface

The interaction of silicon with the iridium (111) surface was described by us in detail in [18]. Multilayer

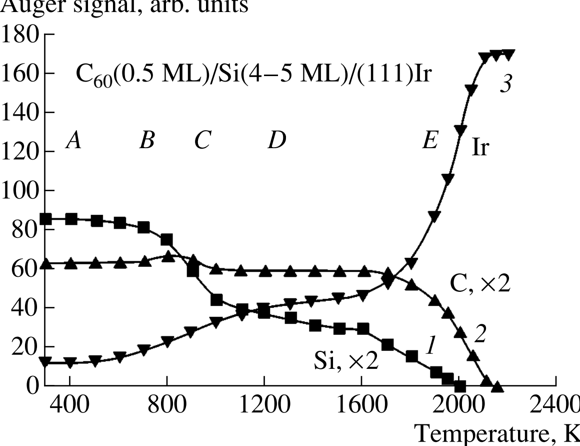

Fig. 1. Intensities of Auger signals from (*1*) silicon, (*2*) carbon, and (*3*) iridium obtained upon annealing of a submonolayer (~0.5 monolayer) fullerite film deposited at $T = 300$ K on a multilayer ($n \approx 4$–5 monolayers) silicon film on (111) iridium. The heating time at each temperature is 30 s. *A* is the region of thermal stability of the C_{60} adlayer, *B* is the silicide-formation region, *C* is the region of transformation of C_{60} molecules to clusters with a nonfullerene structure, *D* is the region of carbon graphitization and formation of an ordered submonolayer graphite film with intercalated silicide, and *E* is the region of thermal desorption of silicon from the silicide and of carbon from the graphite film.

silicon films remain thermally stable on an iridium surface up to 700–800 K, when intense reactive diffusion starts with the formation, first, of surface silicide Ir_5Si with $N_{Si} = 0.3 \times 10^{15}$ cm^{-2}, and, after that, of bulk silicide Ir_3Si. The bulk silicide is stable up to 1500–1700 K; both silicides are destroyed at higher temperatures by thermal desorption. The surface can be completely cleaned of silicon only at 2200 K, the temperature above which iridium samples loose their mechanical strength and disintegrate.

3.2. Interaction of (111) Iridium Surface with Carbon and C_{60} Molecules

Iridium is the only one of the refractory metals in which carbon does not dissolve in the bulk up to 2000 K. Multilayer carbon films, fullerenes from the first adlayer, and cores of hydrocarbon molecules are thermally stable on the iridium surface up to 600 K. Within the 700–1000-K interval, they gradually break up, releasing mobile carbon atoms, which coalesce to form graphite islands [10, 11, 19]. At higher temperatures, the surface carbon exists in two phases—a 2D chemisorbed carbon gas and a graphite film—which are at equilibrium. The surface concentration of the chemisorbed carbon gas at $T < 1600$ K is extremely low, but reaches an observable level (~10^{15} cm^{-2}) at 1800–1900 K [19]. Carbon can be removed from the iridium surface by thermal desorption at $T > 1900$ K.

4. RESULTS AND DISCUSSION

When C_{60} molecules are evaporated on the surface of a silicon single crystal, crystallites are observed to grow on the first molecular layer of the fullerenes [20]. The kinetics of variation of the carbon and silicon Auger signals during the fullerene deposition on a silicon-coated metal provide supportive evidence that a similar growth mechanism operates here as well.

Figure 1 shows the variation in the Auger signals from silicon, carbon, and substrate during annealing of a submonolayer (~0.5 monolayer) C_{60} film deposited on a multilayer silicon film on iridium. The silicon-film thickness was estimated to be ~4–5 monolayers [(6–7) × 10^{15} cm^{-2}]. In the temperature region *A* (300–600 K), all three signals are seen to remain constant, which suggests that the state of the adlayer does not change. This is shown schematically in Fig. 2a. In this region, the carbon Auger line has a typical fullerene-type shape, thus indicating the constancy of the chemical state of C atoms [10].

In region *B* (Fig. 1), reactive silicon diffusion into the metal substrate begins and bulk silicide forms. The Auger signal of silicon begins to decrease, and that of iridium, to grow, both variations having the same character as in the absence of fullerenes. The silicon Auger line also acquires a shape typical of the bulk silicide [18], whereas the carbon Auger line remains unchanged, which shows that the C_{60} molecules are not involved in this solid-phase reaction.

At higher temperatures (region *C* in Fig. 1), the silicon Auger signal continues to fall off, and the Auger signal of iridium, to increase. In this region, the rearrangement of the silicide film apparently continues, with a possible change in the film composition. Although the intensity of the carbon Auger signal is almost constant, its shape suffers noticeable changes; indeed, it is no longer fullerene-like and becomes rather characteristic of that of single carbon clusters chemisorbed on a metal [19]. The C_{60} molecules apparently break up in this region, as they do on a clean iridium surface. A schematic of the processes involved is shown in Fig. 2c.

At even higher temperatures (region *D* in Fig. 1), carbon graphitizes and its signal remains unchanged up to the onset of thermal desorption. The Auger line of carbon has a shape typical graphite. The silicon atoms of the bulk silicide become intercalated between the graphite film and the metal (Fig. 2d).

Finally, for $T > 1900$ K (region *E* in Fig. 1), the Auger signal of silicon disappears and the Auger signal of carbon starts to decrease sharply, in marked contrast to that of iridium, which grows to the level characteristic of pure iridium. In this region, silicon and carbon atoms are desorbed from the metal surface, leaving the latter clean.

Let us now consider the sequence of thermal processes occurring in the case of a multilayer fullerite film deposited on a silicon monolayer. The relevant experimental data are shown in Fig. 3, and the schematic rep-

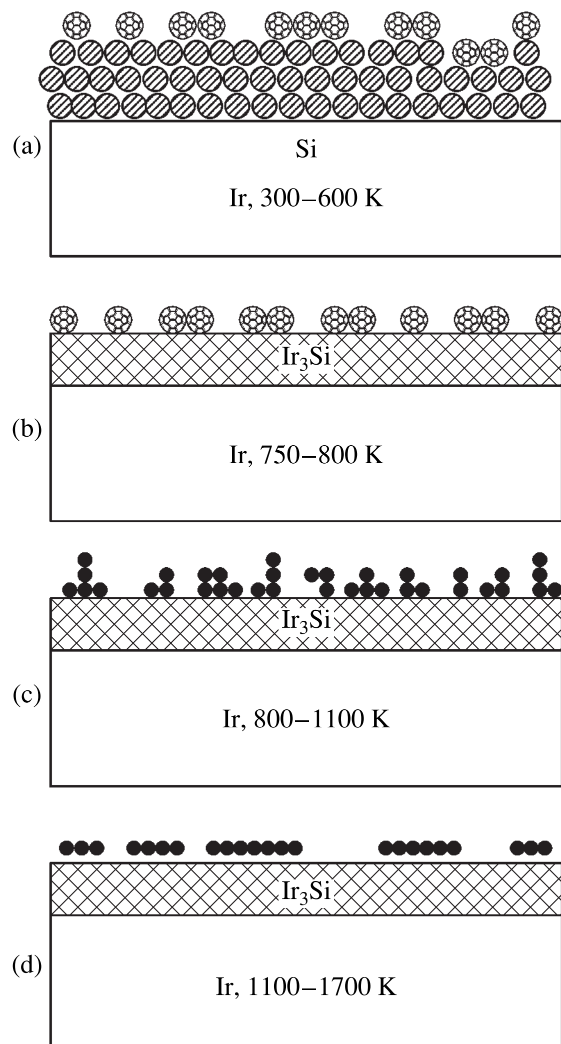

Fig. 2. Schematic diagram of the processes occurring upon heating of a submonolayer fullerite film deposited above a multilayer (4–5 monolayers) silicon film on (111) iridium. Panels (a–d) correspond to temperature regions *A*, *B*, *C*, and *D*, respectively, in Fig. 1.

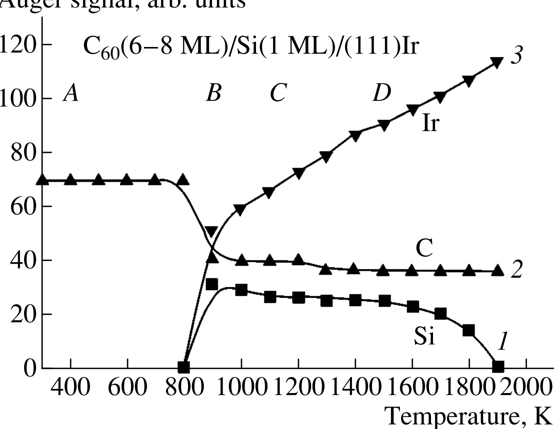

Fig. 3. Intensities of Auger signals from (*1*) silicon, (*2*) carbon, and (*3*) iridium obtained upon annealing of a ~(6–8)-monolayer-thick fullerite film deposited at $T = 300$ K on a monolayer silicon film on (111) iridium. Heating time at each temperature is 30 s. The following temperature regions are indicated: (*A*) the region of thermal stability of the C_{60} adlayer; (*B*) the region of desorption of C_{60} molecules from the second and higher lying layers and silicide formation; (*C*) the region of transformation of C_{60} molecules into clusters with a nonfullerene structure on top of the silicide; and (*D*) the region of formation of a 2D graphite film.

resentation of the processes involved is shown in Fig. 4. We readily see that, up to 800 K, (region *A* in Fig. 3) the Auger signal of carbon does not change, and the energy of the relevant Auger peak (269 eV) indicates that it is the C_{60} molecules that are present on the surface. The Auger signals of iridium and silicon are not seen, because the substrate and the Si film are screened heavily by the C_{60} molecules.

Within the narrow temperature range from 800 to 900 K (region *B* in Fig. 3), the Auger signal of carbon drops by 40%, with the signals of silicon and iridium appearing simultaneously. At these temperatures, thermal desorption of fullerene molecules from the second and subsequent layers was observed to occur both on the clean Si surface and on the surfaces of metals. This also suggests thermal desorption, with C_{60} molecules from the first monolayer remaining on the surface rather than desorbing. The processes occurring in this temperature range are shown schematically in Fig. 4b.

At higher temperatures, $T > 1000$ K, the Auger signal of carbon remains practically constant, which implies that the surface concentration of C does not change. Apparently, the C_{60} molecules that formed the first monolayer break up to transform gradually in this case into carbon clusters whose structure has little in common with that of the fullerenes (Fig. 4c). The shape of the C_{KVV} Auger line of carbon, even at 1100–1200 K, also differs radically from the shape of the corresponding line observed for fullerene. Indeed, there is a clearly pronounced “horn” at 251 eV, and the main peak is now located at 270 eV. This shape, however, is not typical of carbide, but indicates the presence of distinct C–C bonds [19]. Similar processes occur at these temperatures on the surface of silicon single crystals as well (Fig. 4c).

After the temperature rises even higher, the released carbon starts to graphitize, so that, beginning from $T =$ 1500 K, the shape of the Auger line of carbon becomes identical to that of pure graphite. The Auger signal of silicon decreases weakly in the range of 1100–1600 K, dropping to zero at higher temperatures. Its intensity, like that of the Auger signal of iridium, is substantially lower than it should be in the case of clean silicide. It may be supposed that the silicide thus formed resides in the intercalated state under the graphite film, as shown in Fig. 4d.

Let us discuss the results obtained. The character of the processes occurring in the system is seen to depend

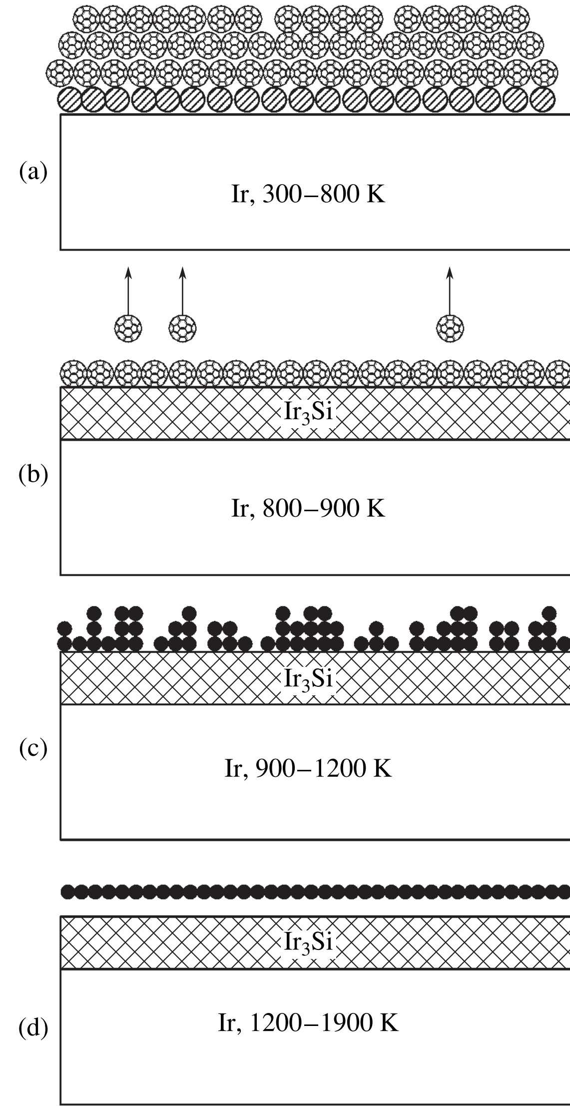

Fig. 4. Schematic of the processes occurring upon annealing of a ~(6–8)-monolayer-thick fullerite film deposited at $T = 300$ K on top of a monolayer silicon film on (111) iridium. Panels (a–d) correspond to temperature regions *A*, *B*, *C*, and *D*, respectively, in Fig. 3.

only weakly on the amount of deposited silicon and fullerenes. In both cases, four temperature regions differing in the dominant process can be discriminated; indeed, C_{60} films are thermally stable at low temperatures ($T < 600$ K), fullerene molecules are desorbed from the second and higher lying molecular layers at 800–900 K, decomposition of these molecules occurs at 650–850 K in the first layer contacting the substrate, the carbon layer graphitizes and the 2D graphite film is thermally stable in the range from 900 to 1700 K, and it is observed that the thermal desorption of carbon from the surface begins at $T > 1900$ K. The exact boundaries of the above temperature regions depend on the actual amounts of silicon and fullerenes present in the system; in particular, the region of thermal stability of a film of C_{60} molecules narrows as the Si dose increases. On the whole, the system considered reminds one of the C_{60}–Si–Re system [21], the main difference between them being the high-temperature behavior of the C–Re and C–Ir binary systems.

5. CONCLUSION

Thus, we have studied the transformation, in the range of 300–1300 K, of the fullerene adlayer deposited on top of a multilayer silicon film on (111) iridium. The system demonstrates clearly the stages of thermal stability of a fullerite film, thermal desorption of fullerenes from the second and higher-lying layers, transformation of the remaining molecules to carbon clusters of a nonfullerene nature, and, finally, total decomposition of clusters with graphitization of the released carbon. It is shown that these processes do not affect the main features of the silicide formation occurring in the system upon heating. It is concluded that this independence of the processes involved may also be characteristic of other metal–silicon systems with adsorbed fullerenes.

ACKNOWLEDGMENTS

This study was supported by the Presidium of the Russian Academy of Science though the program “Low-Dimensional Quantum Structures” (project no. 4G19) and, in part, by the Ministry of Industry, Science, and Technology of the Russian Federation through the program “Controlled Synthesis of Fullerenes” (project no. 8C78).

REFERENCES

1. Hang Xu, D. M. Chen, and W. N. Creager, Phys. Rev. Lett. **70**, 1948 (1993).
2. Y. Z. Li, M. Chander, J. C. Partin, and J. H. Weaver, Phys. Rev. B **45**, 13837 (1992).
3. T. Sato, T. Sueyoshi, and M. Iwatsuku, Surf. Sci. Lett. **321**, L137 (1994).
4. D. Chen and D. Sarid, Surf. Sci. **319**, 74 (1994).
5. P. H. Beton, A. W. Dunn, and P. Moriarty, Surf. Sci. **361–362**, 878 (1996).
6. T. Hashizume, K. Motai, X. D. Wang, *et al.*, J. Vac. Sci. Technol. A **12**, 2097 (1994).
7. T. Chen, S. Howelles, M. Gellager, *et al.*, J. Vac. Sci. Technol. B **9**, 2461 (1991).
8. D. K. Kin, Y. D. Suh, K. H. Park, *et al.*, J. Vac. Sci. Technol. A **11**, 1675 (1993).
9. G. K. Wertheim, Solid State Commun. **88**, 97 (1993).
10. E. V. Rut'kov, A. Ya. Tontegode, and Yu. S. Grushko, Pis'ma Zh. Éksp. Teor. Fiz. **57**, 712 (1993) [JETP Lett. **57**, 724 (1993)].
11. E. V. Rut'kov, A. Ya. Tontegode, and M. M. Usufov, Phys. Rev. Lett. **74**, 758 (1995).
12. N. R. Gall, E. V. Rut'kov, A. Ya. Tontegode, and M. M. Usufov, Mol. Mater. **7**, 187 (1996).

13. N. R. Gall', E. V. Rut'kov, A. Ya. Tontegode, and M. M. Usufov, Pis'ma Zh. Tekh. Fiz. **23** (23), 56 (1997) [Tech. Phys. Lett. **23**, 911 (1997)].
14. N. R. Gall', E. V. Rut'kov, A. Ya. Tontegode, and M. M. Usufov, Zh. Tekh. Fiz. **69** (11), 117 (1999) [Tech. Phys. **44**, 1371 (1999)].
15. N. R. Gall, E. V. Rut'kov, and A. Ya. Tontegode, Fullerene Sci. Technol. **9** (2), 111 (2001).
16. N. R. Gall, S. N. Mikhailov, E. V. Rut'kov, and A. Ya. Tontegode, Surf. Sci. **191**, 185 (1987).
17. N. R. Gall', E. V. Rut'kov, and A. Ya. Tontegode, Zh. Tekh. Fiz. **60** (4), 125 (1990) [Sov. Phys. Tech. Phys. **35**, 475 (1990)].
18. N. R. Gall', E. V. Rut'kov, and A. Ya. Tontegode, Poverkhnost, No. 10, 47 (1989).
19. N. R. Gall', M. S. Kobrin, S. N. Mikhaĭlov, *et al.*, Poverkhnost, No. 9, 21 (1984).
20. N. R. Gall', E. V. Rut'kov, and A. Ya. Tontegode, Fiz. Tekh. Poluprovodn. (St. Petersburg) **36**, 1084 (2002) [Semiconductors **36**, 1008 (2002)].
21. N. R. Gall', E. V. Rut'kov, and A. Ya. Tontegode, Pis'ma Zh. Tekh. Fiz. **29** (2), 55 (2003) [Tech. Phys. Lett. **29**, 66 (2003)].

Translated by G. Skrebtsov

Semiconductors, Vol. 37, No. 9, 2003, pp. 1042–1046. Translated from Fizika i Tekhnika Poluprovodnikov, Vol. 37, No. 9, 2003, pp. 1067–1071.
Original Russian Text Copyright © 2003 by Ushakov, Klevkov.

ELECTRONIC AND OPTICAL PROPERTIES OF SEMICONDUCTORS

Microphotoluminescence Spectra of Cadmium Telluride Grown under Nonequilibrium Conditions

V. V. Ushakov* and Yu. V. Klevkov

Lebedev Physical Institute, Russian Academy of Sciences, Leninskiĭ pr. 53, Moscow, 119991 Russia

**e-mail: ushakov@mail1.lebedev.ru*

Submitted November 10, 2002; accepted for publication December 4, 2002

Abstract—Microphotoluminescence spectroscopy and imaging were used to study impurities and defects in CdTe crystals grown by nonequilibrium techniques. The growth procedure includes low-temperature synthesis and purification of the material via congruent sublimation, with subsequent deposition under the conditions of gas-dynamic vapor flow and high-rate low-temperature condensation. Although the growth conditions are highly nonequilibrium, the obtained polycrystalline material with a grain size of 1–2 mm exhibits strong low-temperature exciton luminescence, whose intensity is nearly uniform over the bulk of the ingots. At the same time, it is found that residual impurities and defects have a tendency to accumulate to form clusters within certain areas which are a hundred micrometers in size; the density of some impurities in these clusters is sufficiently high. © *2003 MAIK "Nauka/Interperiodica".*

1. INTRODUCTION

Over the years, cadmium telluride has been an interesting object for physical studies and a promising material for technology. Its application potential has been growing steadily and now includes optoelectronics, X-ray and γ-ray spectrometry, and solar-cell manufacturing [1]. However, despite progress in materials science, it is not always possible with up-to-date technology to ensure proper control over the processes responsible for the content of impurities and defects and the structure of the crystal forming during growth. It was shown [2] that CdTe with superior optical and electrical parameters can be produced by low-temperature synthesis and sublimation purification of the compound, with its composition being brought to the lowest-pressure point. However, it turned out that the material obtained still incorporates a number of background impurities, whose content in some cases exceeds their content in the source materials of 99.9999% purity. To enhance the purification efficiency, in the present study we used nonequilibrium processes occurring under the conditions of congruent sublimation and gas-dynamic vapor flow in a reactor [3]. Combined with deep purification of source materials, this technique enabled us, at the output, to obtain polycrystalline ingots of CdTe with the lowest possible deviation from stoichiometry and a concentration of major background impurities not exceeding 10^{15} cm^{-3}. The rate of vapor deposition at temperatures around 600°C amounted to ~500 μm/h, which is an order of magnitude larger than the close-to-equilibrium values typical of conventional techniques. The properties of the material obtained were studied by low-temperature microphotoluminescence spectroscopy and imaging; these methods combine high sensitivity to the presence of impurities and defects in the crystal with the possibility of carrying out local analysis.

2. EXPERIMENTAL

The samples under study were [111] textured polycrystals with a single-crystal grain size of 1–2 mm. They were cut parallel to the {111} planes; the surface was treated by grinding, polishing, and etching in a bromomethanol solution. Subsequently, the grain boundaries and the structure defects within grains were revealed by treatment with the selective etchant E-Ag-1. The main structural defects revealed by chemical etching were grain boundaries, twin boundaries, and isolated dislocations with a density of less than 10^3 cm^{-2} within the grain. According to the Hall data, at room temperature, the samples have p-type conductivity and a resistivity of 10^3–10^4 Ω cm.

After carrying out measurements of as-grown samples, they were subjected to 70-h annealing in an atmosphere of saturated Cd vapor at 700°C.

The measurements were carried out using an automated microphotoluminescence scanner, which makes it possible to record luminescence spectra from a given spot on the sample surface and luminescent images of the surface at a given wavelength. The samples were mounted on a cold finger in a cryostat; their temperature could be varied from 100 to 300 K and was monitored by a copper–constantan thermocouple. The luminescence was excited by the radiation of a He–Ne laser (632.8 nm) using a focusing optical system. The typical power of excitation radiation on the sample surface was 2.5–3.0 mW, with the spot diameter being 8–10 μm; optical filters were used to reduce the excitation level. The sample emission in the wavelength range up to

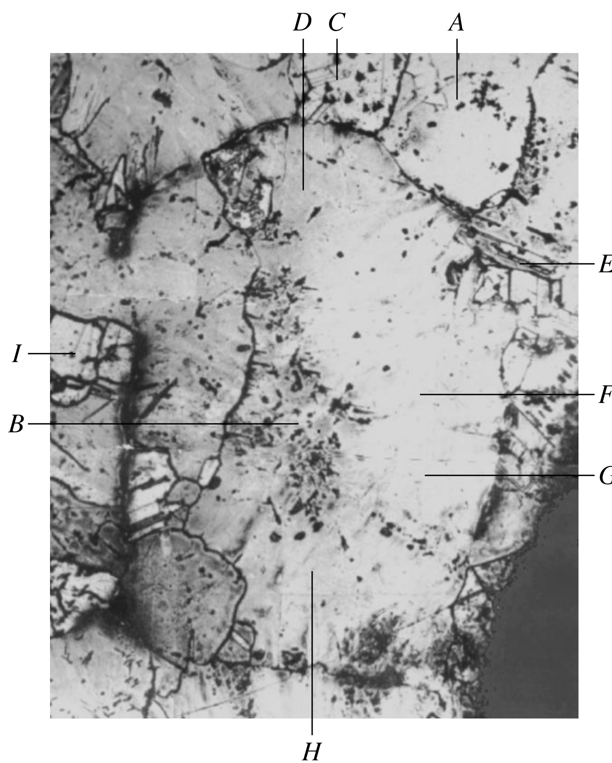

Fig. 1. The structure of the 1.8 × 1.2-mm single-crystal grain under study; the points to which the luminescence spectra shown below correspond are indicated.

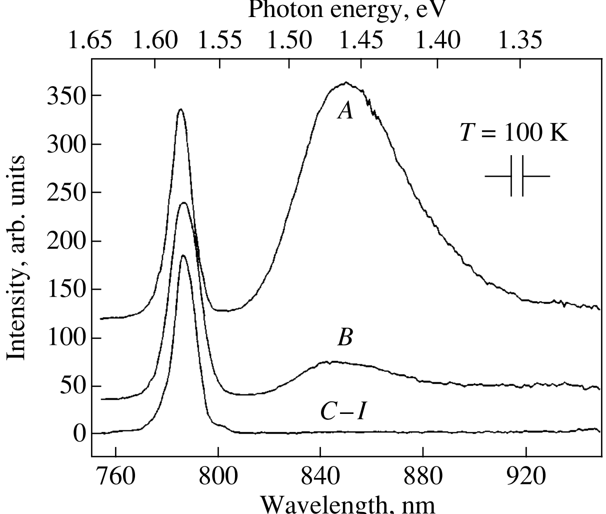

Fig. 2. A representative set of microphotoluminescence spectra recorded at points *A–I* of the single-crystal grain under study (see Fig. 1) at 100 K.

1 μm was spectrally analyzed by an MDR-12 fast grating monochromator (1200 grooves/mm) with reciprocal linear dispersion of 2.4 nm/mm and detected by a cooled FÉU-83 photomultiplier; the output signal was lock-in detected and processed by a computer. The position of the excitation spot on the sample surface was monitored visually using a microscope-based guidance system. The cryostat was mounted on a special table whose motion was controlled by computer commands. Scanning was performed by translating the table along two mutually perpendicular axes normal to the laser-beam direction, which was kept constant. The step size was varied according to the requirements of the experiment; usually, it amounted to 25 μm. In the course of a spatial scan at a given wavelength, the data were output on the display using color representation of the luminescence intensity; at any spot of interest, the scan could be paused to record the emission spectrum. Below, the luminescence spectra obtained in this study are given with the corrections made to account for the spectral sensitivity of the setup.

3. RESULTS AND DISCUSSION

Excitonic lines were dominant in the low-temperature spatially integrated luminescence spectra of the samples, while the intensity of the long-wavelength impurity and defect bands was low; this is evidence of the high quality of the material. The measurements reported here were carried out for the region of the grain of 1.8 × 1.2 mm in size, whose photograph is shown in Fig. 1; we indicate in Fig. 1 the spots from which the luminescence spectra shown below were recorded. The crystal surface was "aged" and covered with a stable oxide layer; thus, there was no luminescence "degradation," i.e., no decrease in the emission intensity with time as a result of the action of a focused laser beam [4]. All the data reported below correspond to a sample temperature of 100–110 K; in this case, radiative transitions involving relatively deep-level impurity and defect centers become most important.

When comparing the spatially resolved and integrated luminescence spectra, one should take into account that the difference in the excitation level for these two cases may be several orders of magnitude. If the excitation-level dependences of the intensities of different bands are not the same [5], the shapes of the spectra recorded by the two methods noted may differ from each other considerably. In particular, a higher intensity of exciton lines in comparison with the impurity and defect lines differentiates between cathodoluminescence and microphotoluminescence spectra; this can be easily verified by defocusing the excitation beam. Taking into account the power of the laser beam incident on the sample, the absorption coefficient for the laser radiation, the spot size, and the literature data on the lifetime and diffusion length of nonequilibrium charge carriers, we estimate the maximum carrier density in the excitation region to be as high as 10^{18} cm^{-3}. This value is 1.5–2 orders of magnitude higher than the excitation level typical of conventional, spatially integrated measurements.

Figure 2 shows a representative set of microphotoluminescence spectra recorded at different points of the

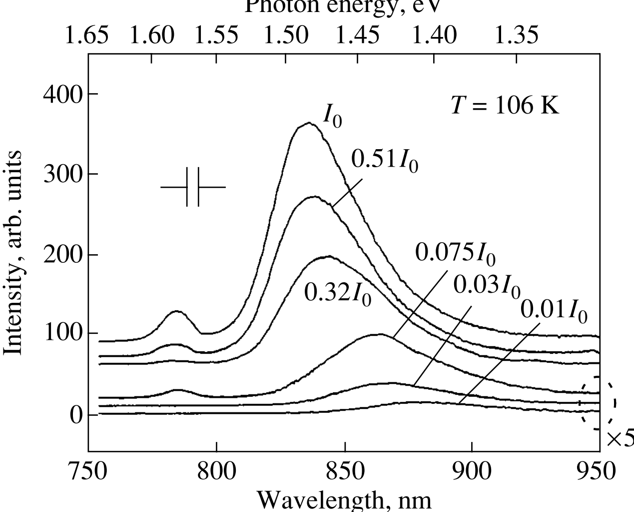

Fig. 3. Variation in the microphotoluminescence spectra with the excitation level; the spectra correspond to the region of intense impurity–defect emission around point *A* in Fig. 1.

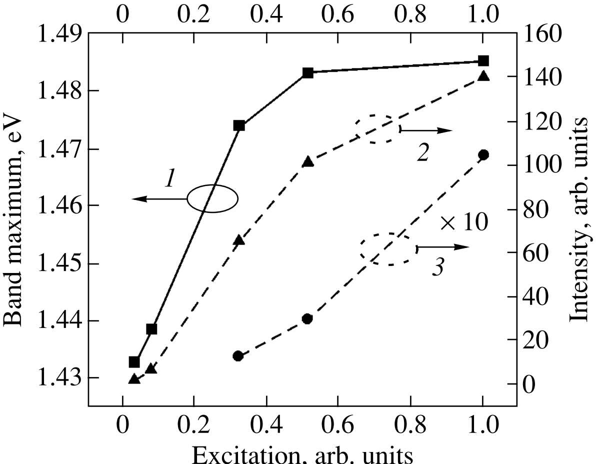

Fig. 4. Excitation-level dependences of (*1*) the peak spectral position and (*2*) the intensity of the impurity–defect band at 1.4 eV; curve *3* shows the relevant dependence of the intensity for the edge emission band at 1.58 eV. The plot is compiled from the data in Fig. 3.

crystal under study. A line of edge (exciton) emission at 1.578 eV is present in all the recorded spectra, the distribution of its intensity over the sample surface being relatively uniform (variation by no more than a factor of 2–3). In contrast, the impurity- and defect-related emission band at 1.4 eV has a high intensity only in some local areas of ~100 μm in size (see below). In the spectra recorded from these areas at the highest excitation level, this band is peaked at 1.48 eV. The band width at half-maximum is 80 meV, and its shape corresponds to the envelope of the Poisson distribution of intensity in a typical "self-activation" band with a Huang–Rhys factor of about 2 [1, 6–10]. When, using optical filters, the excitation intensity was reduced (without varying the laser-spot diameter) to 1% of its initial level (i.e., to the level characteristic of spatially integrated measurements), the position of the exciton band remained unchanged and the peak of the defect–impurity band shifted steadily from 1.485 to 1.433 eV (Fig. 3). It is noteworthy that this shift was not accompanied by a change in the band shape and the results of microluminescence mapping of the grain were identical for the highest and the lowest excitation levels. Thus, the shift observed does not result from the fact that several overlapping bands with different dependences of intensity on the excitation level were measured. Specifically, this shift represents an intrinsic property of the radiative transitions involved. Taking into account all the spectral characteristics of the band under consideration, it is reasonable to attribute it to the emission of donor–acceptor pairs involving shallow donors and *A*-center acceptors (V_{Cd}–D) [11, 12]. In this context, the position of the band peak at 1.433 eV in the case of the lowest excitation level (which corresponds to the common case of spatially-integrated luminescence) is quite typical. The unusually large shift of the band position with increasing excitation level (50 meV in comparison with 5–10 meV usually observed [6, 13]) is due to the very high excitation level attained and to the local nature of the luminescence measurements carried out in the regions of the crystal with a high density of recombination centers. We can see from Fig. 4 that, with an increase in the excitation level, there appears a clear trend toward flattening-out in the dependences of the shift and the intensity of the 1.4-eV band on the excitation level. Most likely, such behavior is related both to the saturation of the donor–acceptor recombination channel itself and to the rapidly increasing competition from the efficient exciton radiative channel (where the excitation-level dependence of the recombination rate is nearly quadratic).

On the basis of the literature data on the position of the zero-phonon lines (ZPLs) in the "self-activation" band for various elements [1, 7, 14, 15], we may try to identify the local centers responsible for microphotoluminescence emission. We should use the results obtained for the lowest excitation level, make allowance for the temperature shift, and take into account the typical position of ZPLs with respect to the peaks of self-activation bands in CdTe. The value for the low-temperature position of the ZPL thus obtained is ~1.47 eV. This value corresponds to *A*-centers formed with the participation of group-VII elements, chlorine being the most probable impurity among them.

Luminescence mapping at the 840-nm wavelength of a 2.5 × 2.5 mm region including a single-crystal grain shown in Fig. 1 indicates that the intensity of the defect- and impurity-related band under consideration is high only over certain limited areas of 100–150 μm size, mainly located relatively close to the grain boundaries (see Fig. 5). We do not yet understand in detail

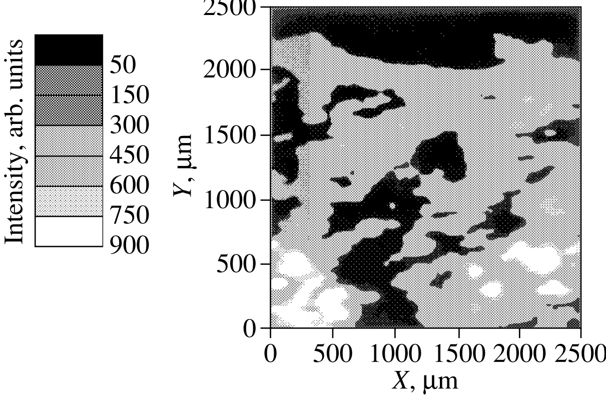

Fig. 5. Microphotoluminescence map of the 2.5 × 2.5-mm area of the sample including the single-crystal grain shown in Fig. 1; the scan is recorded at a wavelength of 840 nm.

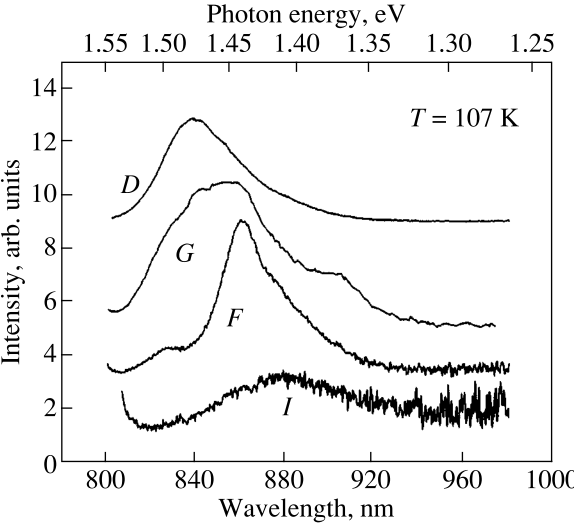

Fig. 6. A demonstration set of the spectra of background impurity–defect luminescence of the material under study (points D, F, G, and I within the single-crystal grain, see Fig. 1).

how these precipitates form during the growth process. It can only be stated with confidence that neither isolated dislocations nor twin boundaries (points C, E, and I in Fig. 1) act as the nucleation centers. A slight nonsystematic increase in the impurity-band intensity was observed in the neighborhood of the grain boundaries. In the spectra of grain-inside regions, only an intense edge band is typically present. However, these regions are also not entirely free of defects. Analyzing the spectra of these regions (points D, F, G, and H in Fig. 1) recorded on a considerably expanded sensitivity scale, we observed weak bands peaked at 1.49, 1.47, 1.44, 1.41, and 1.36 eV under our experimental conditions). A demonstration set of the corresponding spectra is shown in Fig. 6. These bands are apparently related to the radiative transitions to different levels of the acceptors with an energy E_v + 0.15 eV [1, 16], which, thus, form a weak impurity–defect background in the spectra of the crystals under study.

To examine the response of the ensemble of crystal impurities and defects to thermal treatment, the samples were subjected to annealing at 700°C in an atmosphere of saturated Cd vapor. Such a treatment leads to a 100-fold increase in the intensity of all spectral bands. In addition, a new band appears at ~1.41 eV; unfortunately, it overlaps strongly with the other bands and they cannot be analyzed separately. In general, these changes were typical of the spectra from any point on the crystal surface. Thus, on the one hand, the annealing noted causes a substantial decrease in the density of nonradiative recombination centers in the material; on the other hand, it causes the formation of new impurity–defect centers. However, the former effect is so strong that it makes it possible to observe crystal luminescence at room temperature; specifically, the edge band peaked at 1.502 eV (this band is due to the conduction-to-valence band transitions and the exciton transition with its phonon replicas [17]).

4. CONCLUSION

Thus, we demonstrated that microphotoluminescence can be efficiently used to study the impurity and defect content and the structure of CdTe crystals grown by nonequilibrium techniques, including low-temperature synthesis from deeply purified components with the subsequent purification of the compound being grown under the conditions of congruent sublimation, gas-dynamic vapor flow, and high-rate low-temperature condensation. A key feature of the studies performed was the need for local analysis of the material obtained. Although the material possesses a polycrystalline structure with grains 1–2 mm in size, it exhibits strong low-temperature exciton luminescence with rather uniform intensity distribution over the bulk of the ingots. It is evident, however, that, due to the large deviation from equilibrium during the growth, the background impurities are distributed inhomogeneously; there is a tendency toward accumulation of impurities and defects in regions, about 100-μm-size, with a high density of certain impurities (chlorine). The detailed mechanism of this phenomenon is not yet understood. It can be said with confidence that neither isolated dislocations nor twin boundaries act as the nucleation centers. A slight nonsystematic increase in the impurity-band intensity was observed in the spectra recorded from regions close to the grain boundaries. Apparently, the accumulation of impurities in these regions leads to some purification of the grain bulk from impurity- and defect-related recombination centers. The luminescent properties of the crystals can be enhanced considerably by long-term annealing in a Cd-vapor atmosphere. The influence of the grain boundaries and other aggregations of extended defects on the ensemble of impurities and defects in the crystals under study will be considered in detail in a subsequent publication.

ACKNOWLEDGMENTS

We are grateful to Prof. A.A. Gippius and Prof. V.S. Bagaev for useful comments and their interest in this study.

The study was supported by the Russian Foundation for Basic Research (project nos. 01-02-16500 and 00-02-17521) and the Program of Support of the Leading Scientific Schools of the Russian Federation (project no. 00-15-96568).

REFERENCES

1. K. Zanio, *Semiconductors and Semimetals*, Ed. by R. K. Willardson and A. C. Beer (Academic, New York, 1978), Vol. 13.
2. A. V. Kvit, Yu. V. Klevkov, S. A. Medvedev, *et al.*, Fiz. Tekh. Poluprovodn. (St. Petersburg) **34**, 19 (2000) [Semiconductors **34**, 17 (2000)].
3. Y. Klevkov and S. Medvedieff, Brevet (France), No. 2782932.
4. A. M. Gukasyan, V. V. Ushakov, A. A. Gippius, and A. V. Markov, Fiz. Tekh. Poluprovodn. (St. Petersburg) **26**, 525 (1992) [Sov. Phys. Semicond. **26**, 296 (1992)].
5. T. Schmidt, K. Lischka, and W. Zulehner, Phys. Rev. B **45**, 8989 (1992).
6. T. Taguchi, J. Shirafuji, and Y. Inuishi, Jpn. J. Appl. Phys. **12**, 1558 (1973).
7. B. Furgolle, M. Hoclet, M. Vandevyver, *et al.*, Solid State Commun. **14**, 1237 (1974).
8. C. E. Barnes and K. Zanio, J. Appl. Phys. **46**, 3959 (1975).
9. C. B. Norris and C. E. Barnes, Rev. Phys. Appl. **12**, 219 (1977).
10. W. Stadler, D. M. Hofmann, H. C. Alt, *et al.*, Phys. Rev. B **51**, 10619 (1995).
11. G. Brunthaler, W. Jantsch, U. Kaufmann, and J. Schneider, J. Phys. C **1**, 1925 (1989).
12. D. M. Hofmann, P. Omling, H. G. Grimmeiss, *et al.*, Phys. Rev. B **45**, 6247 (1992).
13. J. E. Espinosa, J. M. Gracia, H. Navarro, *et al.*, J. Lumin. **28**, 163 (1983).
14. J. Lee, N. C. Giles, D. Rajavel, and C. J. Summers, J. Appl. Phys. **78**, 5669 (1995).
15. D. Grecu, A. D. Compaan, U. Jayamaha, and D. H. Rose, J. Appl. Phys. **88**, 2490 (2000).
16. M. Samimi, B. Biglary, M. Hage-Ali, *et al.*, Nucl. Instrum. Methods Phys. Res. A **283**, 243 (1989).
17. J. Lee, N. C. Giles, D. Rajavel, and C. J. Summers, Phys. Rev. B **49**, 1668 (1994).

Translated by M. Skorikov

Semiconductors, Vol. 37, No. 9, 2003, pp. 1047–1052. Translated from Fizika i Tekhnika Poluprovodnikov, Vol. 37, No. 9, 2003, pp. 1072–1077.
Original Russian Text Copyright © 2003 by Bobrovnikova, Vilisova, Ivonin, Lavrent'eva, Preobrazhenskiĭ, Putyato, Semyagin, Subach, Toropov.

ELECTRONIC AND OPTICAL PROPERTIES OF SEMICONDUCTORS

Effect of Growth Conditions on Incorporation of Si into Ga and As Sublattices of GaAs During Molecular-Beam Epitaxy

I. A. Bobrovnikova*, M. D. Vilisova, I. V. Ivonin**, L. G. Lavrent'eva**, V. V. Preobrazhenskiĭ***, M. A. Putyato***, B. R. Semyagin***, S. V. Subach*, and S. E. Toropov****

**Kuznetsov Physicotechnical Institute, pl. Revolyutsii 1, Tomsk, 634050 Russia*
e-mail:bia@ic.tsu.ru
***Tomsk State University, Tomsk, 634050 Russia*
****Institute of Semiconductor Physics, Siberian Division, Russian Academy of Sciences, pr. Akademika Lavrent'eva 13, Novosibirsk, 630090 Russia*
Submitted December 5, 2002; accepted for publication December 17, 2002

Abstract—The effect of dopant concentration and growth-surface crystallographic orientation on the incorporation of Si into Ga and As sublattices was investigated during GaAs molecular-beam epitaxy. The epitaxial layers (epilayers) were grown on GaAs substrates with (100), 2°(100), 4°(100), and 8°(100) orientations at a temperature of 520°C and with (111)A, 2°(111)A, 2°(111)A, 5°(111)A, 6°(111)A, and 8°(111)A (where A = Ga) orientations at a temperature of 480°C. The Si-dopant concentration was varied within 10^{17}–10^{19} cm^{-3}. Through electrical and photoluminescent methods of investigation, the Si impurity was found to occur at the sites of both GaAs-layer sublattices not only as simple donors and acceptors (Si_{Ga} and Si_{As}), but also as Si_{Ga}–Si_{As}, Si_{Ga}–V_{Ga}, and Si_{As}–V_{As} complexes. The concentration of Si impurity in various forms depends on the doping level of the layers and on the growth-surface orientation. Amphoteric properties of Si manifest themselves more prominently on the (111)A face than on the (100) one. It is shown that impurity defects form at the stage of layer crystallization and depend on the growth-surface structure. © *2003 MAIK "Nauka/Interperiodica".*

1. INTRODUCTION

The development of microelectronics and nanoelectronics requires that the technology of molecular-beam epitaxy (MBE) constantly be improved. The properties of doped epilayers are affected profoundly by specific features of impurity incorporation into the layers, which, in turn, depends on the growth conditions and the growth-surface crystallographic orientation. The surface orientation is known [1–8] to strongly affect the electrical and optical properties of the layers, the formation of intrinsic and impurity defects, and, in the case of doping GaAs with the Si amphoteric impurity, can change the impurity distribution between the Ga and As sublattices. However, the mechanism of this phenomenon is poorly studied. In this paper, we report results from investigating the effect of the dopant concentration and the growth-surface crystallographic orientation on the incorporation of Si into the Ga and As sublattices during GaAs molecular-beam epitaxy.

2. EXPERIMENTAL

GaAs layers 1 μm thick were grown using the Katun' MBE facility on GaAs substrates with (100), 2°(100), 4°(100), and 8°(100) orientations at a temperature of 520°C and with (111)A, 2°(111)A, 5°(111)A, 6°(111)A, and 8°(111)A (where A = Ga) orientations at a temperature of 480°C. The ratio between the As and Ga fluxes was equal to 20. The growth rate governed by the Ga flux was constant (1 μm/h). The Si concentration in the (100) layers was varied within 10^{17}–10^{19} cm^{-3} by adjusting the Si-source temperature. When growing the layers on substrates with other orientations, the Si-source temperature was held constant and corresponded to an Si concentration $N_{Si} \approx 10^{18}$ cm^{-3} in the layers.

The electrical parameters of the layers were determined by measuring the conductivity and the Hall effect. Photoluminescence (PL) spectra were measured at 77 K; they were exsited by an LG-75 laser at a wavelength of 635 nm, and the emission was detected by a germanium photodetector. The concentration N_i of optically active centers was estimated (accurate to a constant factor) from the formula [9, 10]

$$N_i \approx CnI_i/I_{cv}, \quad (1)$$

where n is the electron concentration, I_i is the PL-band intensity corresponding to a given type of defects, I_{cv} is the edge-emission intensity, and C is the constant for an ith type of centers. This formula is derived on the basis of calculations performed in [11] for the radiative-recombination deep-level centers in n-GaAs and can be used under low-temperature conditions and low excitation level. Such an estimate makes it possible to elimi-

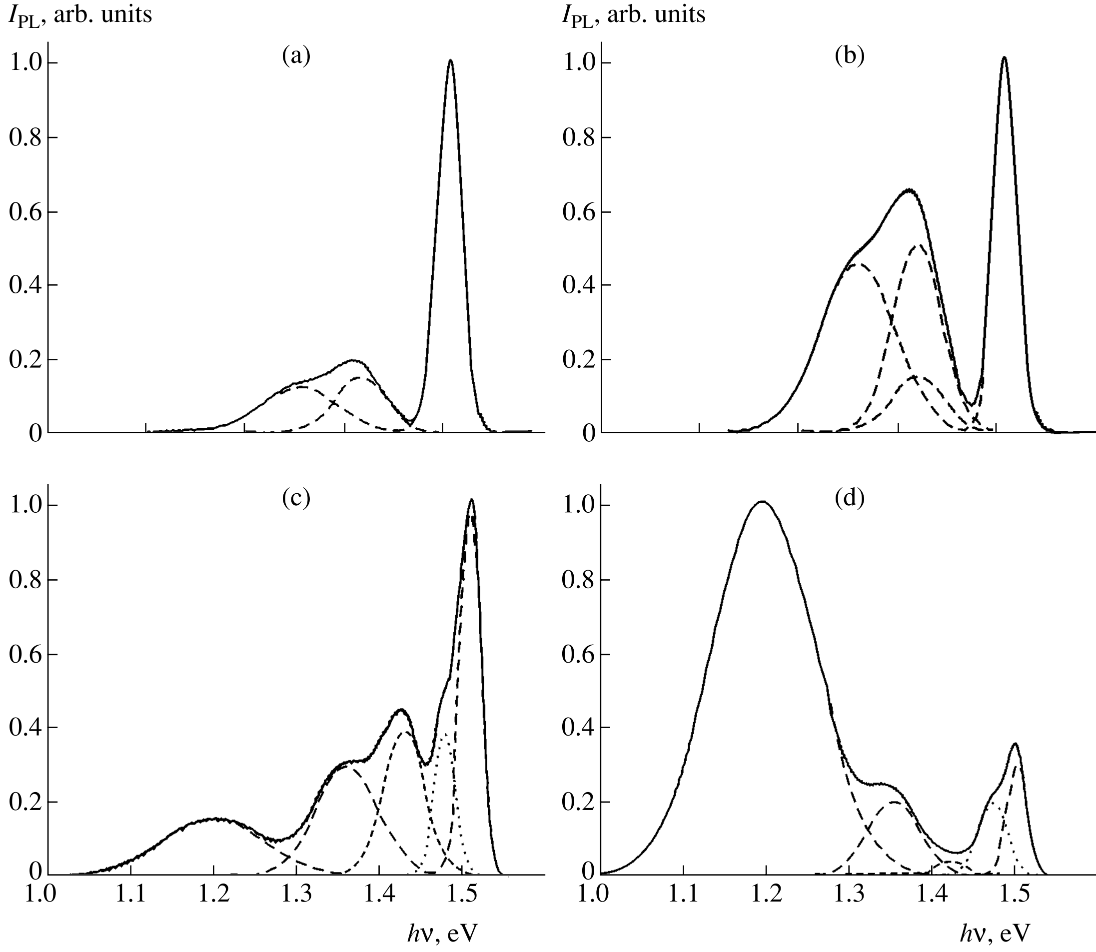

Fig. 1. Photoluminescence spectra of (100) GaAs epilayers doped to the concentrations of n = (a) 0.3, (b) 1, (c) 3, and (d) 7 × 10^{18} cm^{-3}.

nate the influence of the nonradiative-recombination centers.

3. RESULTS AND DISCUSSION

3.1. Doping-Level Effect on Incorporation of Si into GaAs Layers

The measurements showed that all the doped GaAs epilayers are of n-type. The electron concentration in the (100) layers varies from 10^{17} to 10^{19} cm^{-3} with increasing Si flux.

The photoluminescent properties of GaAs layers grown on the (100) face depend heavily on the Si-doping level. In PL spectra from layers with an electron concentration $n \approx 10^{17}$–10^{18} cm^{-3}, there are three emission bands: an edge band with a peak energy of 1.51 eV and two emission bands in the impurity region of the spectrum with peaks at 1.36 and 1.43–1.44 eV (Fig. 1a). The intensity of the “impurity” bands increases with increasing Si concentration (Fig. 1b). In the spectra from layers with $n > 2 \times 10^{18}$ cm^{-3}, the impurity region involves the emission bands with peaks at 1.2 and 1.48 eV (Fig. 1c), whose intensity increases with the Si concentration in the layers. For the electron concentration $n \gtrsim 7 \times 10^{18}$ cm^{-3}, the 1.2-eV emission band is dominant in the spectra from the layers (Fig. 1d).

The emission bands under consideration were identified by comparison with known published data. The emission in the 1.2-eV region is characteristic of Si-doped n-GaAs and related to the Si_{Ga}–V_{Ga} defects [11–15]. The 1.36-eV band is conventionally attributed to an Si_{As}–V_{As} complex involving an impurity atom at the As site and an As vacancy. This band is most commonly encountered in spectra of p-GaAs layers grown with relatively low ratios between As and Ga fluxes [5, 6, 13]. The band with the 1.48-eV peak is most likely caused by the Si_{Ga}–Si_{As} defect [5, 16].

The data on the nature of the emission band in the 1.43- to 1.44-eV region are contradictory. This band is associated with the transitions from the conductivity band to acceptor levels of V_{Ga} and Ga_{As} intrinsic defects

[6], or to those of Si_{As} impurity defects [8]. In any event, it is generally accepted that the emission band in the 1.43- to 1.44-eV region corresponds to an elementary acceptor defect. In our opinion, the existence of Ga_{As} antisite defects in the investigated layers is improbable because the MBE proceeds under the conditions where there is As excess. The Ga vacancy in GaAs is conventionally considered to be nonradiative-recombination centers. In addition, we did not observe the band under consideration in the PL spectra of undoped GaAs layers. On this basis, we assume that the emission band in the 1.43- to 1.44-eV region is caused by Si_{As} defects.

Thus, the results of electrical and photoluminescent investigations indicate that the GaAs layers involve the Si impurity at sites of both sublattices both in the elementary form and in the form of complexes with intrinsic defects. The concentration of Si in various forms depends on the doping level of the layers. Because all the investigated layers were of *n* type, we may conclude that Si atoms occupy predominantly the Ga sites Si_{Ga} in the layers and manifest themselves as shallow-level donors. For the impurity concentration $n > 10^{17}$ cm^{-3}, the Si atoms occupy not only the Ga sites, but also the As ones exhibiting amphoteric properties. In this case, the impurity atoms at the As sites can be present both in the form of elementary acceptors Si_{As} and in the form of more complicated defects—the complexes with intrinsic defects of the Si_{As}–V_{As} type (the PL bands of 1.43 and 1.36 eV, respectively). The concentration of these defects increases linearly as the doping level rises (Fig. 2). For an impurity concentration $n > 2 \times 10^{18}$ cm^{-3} in the layers, the Si_{Ga}–V_{Ga} complexes, which involve an Si atom at the Ga site and a Ga vacancy, and also the Si_{Ga}–Si_{As} pairs (the 1.2- and 1.48-eV bands, respectively) appear and begin to prevail. As can be seen from Fig. 2, the concentration of these complexes increases more sharply with rising doping level (almost quadratically). In heavily Si-doped layers ($n > 7 \times 10^{18}$ cm^{-3}), the Si_{Ga}–V_{Ga} complexes become the predominant type of impurity defects, along with the Si_{Ga} donors.

3.2. Effect of Growth-Surface Orientation on Incorporation of Si into GaAs Layers

The electrical parameters of GaAs layers grown on variously oriented substrates for a constant Si flux are listed in the table. It can be seen that the electron concentration in the (100) layers is somewhat higher than that in the (111)A layers (A stands for Ga) and amounts to 1.2×10^{18} and 9.2×10^{17} cm^{-3}, respectively. It should be noted that this distinction in the electron concentration cannot be associated with the various temperatures of layer growth on the (111)A and (100) surfaces because, according to the published data [12], growth-temperature variation from 425 to 520°C does not influence the electron concentration in Si-doped layers.

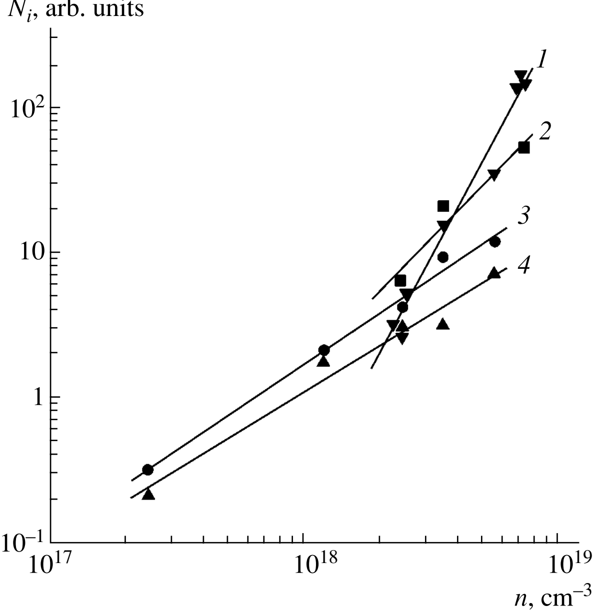

Fig. 2. Concentration of (*1*) Si_{Ga}–V_{Ga}, (*2*) Si_{Ga}–Si_{As}, (*3*) Si_{As}, and (*4*) Si_{As}–V_{As} defects as a function of the doping level of the (100) GaAs layers.

The measurements of the photoluminescent characteristics of the layers showed that the same PL bands are observed in the spectra of GaAs epilayers with all of the orientations as those for the (100) layers with a similar doping level; we observe, bands peaked at 1.51, 1.36, and 1.43–1.44 eV. The intensity of these bands strongly depends on the growth-surface orientation. As an example, we show the PL spectra for the (100) and (111)A layers in Fig. 3. It can be seen that the "impurity"-emission intensity is higher in the region of 1.3–1.4 eV for the (111)A face than for the (100) one. In addition, the intensities are comparable in magnitude for both impurity bands in the spectra of the (100) layers, whereas it is the short-wave emission in the region of 1.43 eV which is dominant for the (111)A layers.

The experimental data obtained indicate that the concentration of the Si impurity incorporated in various

Charge-carrier concentration in GaAs layers

Surface orientation	Electron concentration, 10^{18} cm^{-3}
(100)	1.2
2°(100)	1.3
4°(100)	1.2
8°(100)	1.4
(111)A	0.92
5°(111)A	0.90
6°(111)A	0.92
8°(111)A	0.86

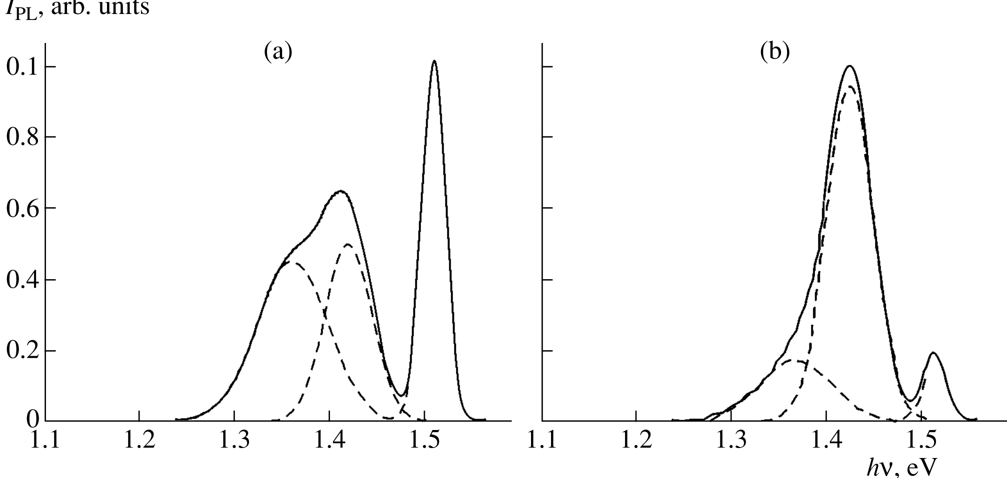

Fig. 3. Photoluminescence spectra of GaAs epilayers with the orientation (a) (100) and (b) (111)A. In these layers, the electron concentration amounts to 1.2×10^{18} and 9.2×10^{17} cm^{-3}, respectively.

forms into the GaAs layers substantially depends on the growth-surface orientation. For the (111)A face, the electron concentration in layers, i.e., the Si_{Ga}-defect concentration (see table), is lower as compared with the (100) face, whereas in the As sublattice, the defect concentration, primarily, that of Si_{As} defects, increases (the intensity of the corresponding PL bands increases, see Fig. 3). According to data from electrical measurements, the degree of compensation in the layers also increases (from 0.35 to 0.5). These results indicate that the amphoteric properties of Si manifest themselves more distinctly for the (111)A face than for the (100) one.

The existence of an orientation dependence for the impurity-defect concentration in GaAs layers indicates that their formation depends on the growth-surface structure. The distinctions in the structures of the singular (100) and (111)A faces are associated with the difference in the density of free chemical bonds on the surface. It is in this context that the more pronounced amphoteric properties of Si in GaAs layers with a (111)A face, with those with a (100) face, are explained in a number of studies [2–8]. According to the reasoning in these works, as the (111)A face with one dangling bond per atom brings about unfavorable conditions for the dissociation of As molecules and to incorporating As atoms into the crystal (as compared with the (100) face with two dangling bonds per atom), Si atoms can compete more efficiently with As atoms being incorporated into the As sites. Thus, a higher acceptor concentration is conventionally observed on the (111)A face as compared with other orientations, which is consistent with our experiments.

The investigation of the effect of small-angle deflections φ from the singular faces on properties of GaAs layers showed that the misorientation of the layers only weakly influences (see table) the electron concentration, i.e., the concentration of simple impurity defects Si_{Ga} in the Ga sublattice.

At the same time, according to the photoluminescent measurements, the impurity-defect concentration in the As sublattice depends heavily on the deflection angle φ. In Fig. 4, we show the orientation dependences of concentration for Si_{As} acceptors and Si_{As}–V_{As} complexes. It can be seen that the concentration of simple Si_{As} defects in the As sublattice is highest in both singular faces and decreases with misorientation; i.e., the conventional faceting effect is observed.

The dependence of the Si_{As}–V_{As}-complex concentration on the deflection angle has a different character near the (100) and (111)A faces. The concentration of these defects is highest on the (100) face and decreases when deviating from it. In the case of deflection from the (111)A singular face, the concentration of the complexes varies only slightly: first, it increases somewhat and then decreases.

For the deflection from a singular face, the surface acquires a profile which consists of steps with terraces having indices of the face from which the deflection takes place and with vertical portions having indices of the face in the direction of which the misorientation occurs. The terrace size (the spacing λ between the steps) can be calculated using the expression

$$N_{st}h = \tan\varphi,$$

where $N_{st} = 1/\lambda$ is the density of steps and h is their height, amounting to 2.82 Å for the deflection from the (100) face and 3.26 Å for that from the (111)A face. In Fig. 4a (curve *1*), we show the calculated dependence $\lambda(\varphi)$. It can be seen that the spacing λ between the steps decreases with increasing angle of deflection from a singular face, which correlates with the trend of dependences for the concentration of the Si_{As} and Si_{As}–V_{As} defects on φ in a larger portion of the range. Such a cor-

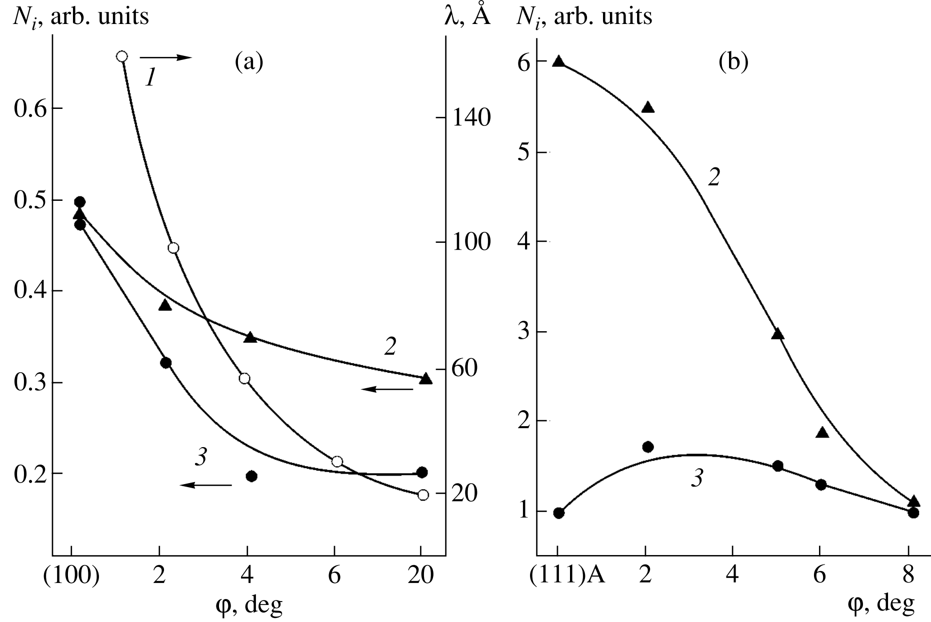

Fig. 4. (*1*) Calculated distance λ between the steps, (*2*) Si_{As}-defect concentration, and (*3*) Si_{As}–V_{As}-defect concentration as functions of the angle φ of deflection from the singular face: (a) from the (100) face towards the (111)A face, and (b) from the (111)A face towards the (100) face.

relation means that the formation of impurity defects in the As sublattice is primarily governed by the processes occurring on the growth-surface terraces.

Thus, the results obtained in this study indicate that a considerable fraction of the Si impurity is incorporated into the lattice during GaAs molecular-beam epitaxy in the form of complexes with intrinsic point defects. The mechanism of formation of the complexes in the GaAs epilayers grown by vapor epitaxy, i.e., under conditions of reasonably low growth temperatures, is not conclusively established. The dependence of the concentration of complexes on the growth-surface orientation points to the fact that they are formed at the layer-crystallization stage. Previously, when investigating the processes of growing and doping GaAs in chloride and MOC-hydride systems, we suggested a mechanism for the formation of impurity–vacancy complexes as a result of entrapping the adsorbed diatomic impurity molecules. This mechanism is likely quite common for all impurities forming stable diatomic molecules, which was corroborated by the thermodynamic calculations of the composition of adsorbed layers and by the experimental data on the kinetics of entrapping S, Te, Sn, and Ge impurities [9, 10, 17, 18]. A similar complex-formation mechanism can be assumed to also take place for the growth of layers during molecular-beam epitaxy. A low MBE temperature and a pronounced segregation of the impurity at the interface between a crystal and an adsorbed layer increase the probability of both the formation of complexes in the adsorbed layer and their incorporation into the growing layer without preliminary dissociation. To clarify this issue, further investigations are necessary, in particular, the calculation of adsorbed-layer composition in MBE systems.

4. CONCLUSIONS

The results obtained in this study enable us to conclude the following.

(i) During GaAs molecular-beam epitaxy, Si atoms are incorporated into the lattice not only in the form of Si_{Ga} simple donors, but also as Si_{As} elementary acceptors and more complicated defects: Si_{Ga}–Si_{As}, Si_{Ga}–V_{Ga}, and Si_{As}–V_{As} complexes.

(ii) The concentration of various impurity defects in the layers depends on the doping level and the growth-surface orientation.

(iii) The amphoteric properties of Si are more pronounced on the (111)A face than on the (100) face.

(vi) The impurity defects are formed at the crystallization stage and determined by the growth-surface structure.

ACKNOWLEDGMENTS

This study was supported by the Russian Foundation for Basic Research, project no. 01-02-17280.

REFERENCES

1. Y. Okano, H. Seto, H. Katahama, *et al.*, Jpn. J. Appl. Phys. **28**, L151 (1989).
2. F. Piazza, L. Pavesi, M. Henini, and D. Johnston, Semicond. Sci. Technol. **7**, 1504 (1992).

3. A. Chin, P. Martin, P. He, *et al.*, Appl. Phys. Lett. **59**, 1899 (1991).
4. W. I. Wang, E. E. Mendez, T. S. Kuan, and L. Esaki, Appl. Phys. Lett. **47**, 826 (1985).
5. G. B. Galiev, V. G. Mokerov, É. R. Lyapin, *et al.*, Fiz. Tekh. Poluprovodn. (St. Petersburg) **35**, 421 (2001) [Semiconductors **35**, 409 (2001)].
6. L. Pavesi, M. Henini, and D. Johnston, Appl. Phys. Lett. **66**, 2846 (1995).
7. T. Ohachi, J. M. Feng, K. Asai, *et al.*, Microelectron. J. **30**, 471 (1999).
8. V. G. Mokerov, G. B. Galiev, Yu. V. Slepnev, and Yu. V. Khabarov, Fiz. Tekh. Poluprovodn. (St. Petersburg) **32**, 1320 (1998) [Semiconductors **32**, 1175 (1998)].
9. I. A. Bobrovnikova, L. G. Lavrentieva, M. P. Rusaikin, and M. D. Vilisova, J. Cryst. Growth **123**, 529 (1992).
10. I. A. Bobrovnikova, L. G. Lavrent'eva, and S. E. Toropov, Fiz. Tekh. Poluprovodn. (Leningrad) **20**, 1701 (1986) [Sov. Phys. Semicond. **20**, 1065 (1986)].
11. K. D. Glinchuk, K. Lukat, and A. V. Prokhorovich, in *Optoelectronics and Semiconductor Technology*, Ed. by S. V. Svechnikov (Naukova Dumka, Kiev, 1982), No. 1, p. 39.
12. K. S. Zhuravlev, D. I. Lubyshev, V. P. Migal', *et al.*, in *Abstracts of 8th All-Union Conference on Crystal Growth* (Khar'kov, 1992), Vol. 1, p. 218.
13. Nguen Hong Ky and F. K. Reinhart, J. Appl. Phys. **83**, 718 (1998).
14. E. W. Williams, Phys. Rev. **168**, 922 (1968).
15. N. S. Averkiev, A. A. Gutkin, M. A. Reshchikov, and V. E. Sedov, Fiz. Tekh. Poluprovodn. (St. Petersburg) **30**, 1123 (1996) [Semiconductors **30**, 595 (1996)].
16. Y. Imura, D. Yui, and M. Kawabe, in *Extended Abstracts of the 18th International Conference on Solid State Devices and Materials* (Tokyo, 1986), p. 623.
17. L. G. Lavrent'eva, I. A. Bobrovnikova, and M. D. Vilisova, Izv. Vyssh. Uchebn. Zaved., Mater. Élektron. Tekh., No. 4, 35 (1998).
18. A. E. Kunitsyn, V. V. Chaldyshev, S. P. Vul', *et al.*, Fiz. Tekh. Poluprovodn. (St. Petersburg) **33**, 1187 (1999) [Semiconductors **33**, 1080 (1999)].

Translated by V. Bukhanov

Semiconductors, Vol. 37, No. 9, 2003, pp. 1053–1056. Translated from Fizika i Tekhnika Poluprovodnikov, Vol. 37, No. 9, 2003, pp. 1078–1081.
Original Russian Text Copyright © 2003 by Abramov, Gorbatyĭ.

ELECTRONIC AND OPTICAL PROPERTIES OF SEMICONDUCTORS

Intervalley Redistribution of Electrons at Low Temperatures and the Magnetodiode Effect

A. A. Abramov* and I. N. Gorbatyĭ

Moscow State Institute of Electronic Engineering (Technical University), Moscow, 103498 Russia

**e-mail: gpd@gf.miee.ru*

Submitted December 2, 2002; accepted for publication December 17, 2002

Abstract—The *I–V* characteristics of silicon *p–i–n* structures were measured in a magnetic field transverse to the current at a temperature of 77 K. The special features of the *I–V* characteristics and the magnetosensitivity at low temperatures are attributed to the superposition of the anisotropic dimensional effects caused by the Lorentz force and by the intervalley redistribution of electrons. This redistribution can, in turn, be caused by field heating of electrons (the Sasaki effect) in the semiconductor bulk or by violation of the mutual compensation for transverse electron fluxes belonging to various valleys near the semiconductor surface. *© 2003 MAIK "Nauka/Interperiodica".*

In a *p–i–n* structure placed in a magnetic field transverse to the current ($\mathbf{B} \perp \mathbf{J}$, $\mathbf{B}$ is the magnetic induction vector directed along the z axis and $\mathbf{J}$ is the current density vector directed along the x axis), the charge carrier deflection by the Lorentz force to a particular lateral surface of the *p–i–n* structure causes the magnetodiode effect, which manifests itself in the dependence $J(B)$. If the surface recombination rates (SRRs) S_p^+ and S_p^- at the Hall face of the *i*-region (at $y \pm d$) differ, the magnetosensitivity (MS) in a weak magnetic field is, as a rule, polar at room temperature ($\Delta J/\Delta B$ is of opposite sign at $B > 0$ and $B < 0$) [1–3]. The current MS is positive ($\Delta J/\Delta B > 0$) when the magnetic field deflects carriers from the surface with a high SRR and forces them to the surface with a low SRR. In this case, an increase in the magnetic field results in a decrease in the carrier recombination rate averaged over the cross section at rather small $|E_xB|$ ($\mathbf{E}$ is the electric field vector), which causes an increase in the injection current. However, a further increase in $|E_xB|$ brings about intense accumulation of carriers at the surface with a low SRR; as a result, the average recombination rate increases and the current begins to decrease with the magnetic field. Therefore, the MS becomes nonpolar. Such a magnetodiode effect is well explained within the drift theory [1, 4–6].

At liquid-nitrogen and liquid-helium temperatures, a number of special features in the magnetodiode effect [7, 8] are observed in the *p–i–n* structures fabricated from multivalley semiconductors (such as Ge and Si). Figure 1 shows the experimental current-voltage (*I–V*) characteristics of silicon n^+–p–p^+ structures at 77 K. The structures under study have the same design as in [8]. The samples were formed on pure *p*-Si (111) wafers of thickness $2d = 200$–400 µm with a resistivity $\rho \approx 20$ kΩ cm and bulk lifetime of charge carriers $\tau \approx 500$ µs at $T = 300$ K. At the top surface of the wafers, n^+ and p^+ regions spaced by $w = 300$–800 µm were formed by ion-implantation doping. These regions comprised n^+–p and p^+–p junctions, which provided double injection in the corresponding n^+–p–p^+ structures. The *I–V* characteristics were measured at $T = 77$–300 K in various magnetic fields. The magnetic field $B_z \equiv B$ parallel to the wafer surface and perpendicular to the current lines acted in two directions: at $B < 0$, carriers were deflected by the magnetic field to the top surface of the wafer (at $y = d$) and to the opposite side ($y = -d$) at $B > 0$. To prevent heating of the semiconductor sample, a pulsed measuring technique was used.

We note the following special features of these *I–V* characteristics. First, the *I–V* characteristic includes a pronounced sublinear portion at $B = 0$. Second, the MS features are usual at $B < 0$. In contrast to the situation

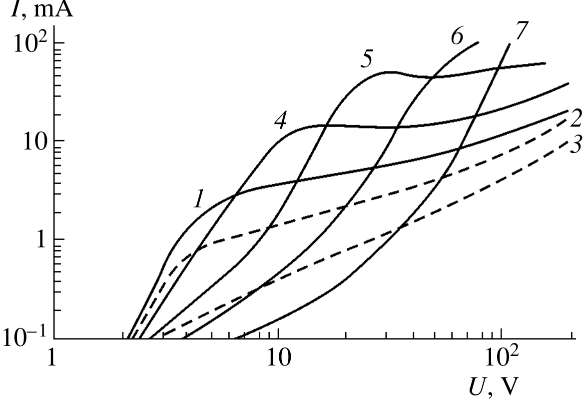

Fig. 1. Experimental *I–V* characteristics of the silicon n^+–p–p^+ structure at $T = 77$ K under magnetic fields $B = 0$ (*1*), 0.05 (*2*), 0.19 (*3*), –0.05 (*4*), –0.125 (*5*), –0.19 (*6*), and –0.63 (*7*) T.

taking place at room temperature, in this case, the polar MS arises only at rather high voltages. This effect was discussed in [8]; however, it could be seen in the *I–V* characteristics of germanium structures studied at T = 77 K as early as 1968 (see [7]).

In [8], it was assumed that the low-temperature features in the *I–V* characteristics and the MS of the *p–i–n* structures can be caused by the following factors:

(i) the intervalley redistribution of electrons (IVRE) near the semiconductor wafer surfaces and

(ii) the IVRE due to field heating of electron gas (the Sasaki effect).

Let us discuss these assumptions.

The surface IVRE was studied for the first time in [9, 10] for the monopolar [9] and then for the bipolar case (at uniform photogeneration) [10]. Since the semiconductor layer surfaces confine the anisotropic drift (transverse to the current) of electrons that belong to various valleys, the electron density at the semiconductor surface increases or decreases in specific valleys. The consequences of such a surface IVRE in a bipolar semiconductor are as follows [10]:

(i) an increase in the effective surface recombination rate and

(ii) the conductivity anisotropy in the surface semiconductor layers, whose thickness depends on the electric field and the intervalley relaxation rates.

In [11], the results of [10] were generalized to the case of *p–i–n* structures with double injection. In [12], in addition to the injection and the surface IVRE, deflection of carriers by an external magnetic field was also taken into account. The calculations of [12] showed that the surface IVRE could indeed give rise to the *I–V* characteristics and MS, which were similar to those shown in Fig. 1 and observed previously [7, 8]. However, we note that this requires very specific conditions at the semiconductor wafer surfaces. It is hardly probable that such conditions were present in the experimental samples [7, 8]. Furthermore, estimations show that field heating of electron gas undeniably took place in the experiments under consideration; this was disregarded in the theory [12].

Under conditions of field heating of charge carriers, the multivalley semiconductor conductivity, as is known, becomes anisotropic (the Sasaki effect [13, 14]). This conductivity anisotropy is associated with the intervalley redistribution of carriers caused by dissimilar heating of electrons by an electric field in different valleys. In the case of field heating of electron gas, the theoretical analysis of the double injection currents becomes very complicated. In this case, the kinetic and relaxation parameters of a semiconductor depend on the electron gas temperature, which is, in turn, controlled by the electric field. Since the field E is nonuniform in the case of double injection, a spatial dependence of the semiconductor kinetic and relaxation parameters arises, and the terms caused by the electron-temperature gradient appears in the continuity equations. The problems of electron density and temperature determination in various valleys are interrelated. Solving these problems requires knowledge of the temperature dependences of the relaxation, recombination, and transport coefficients, but data for these are lacking. Therefore, we simplify the further analysis of the *I–V* characteristics of the *p–i–n* structure with the simultaneous consideration of the Sasaki effect and the Lorentz force. The purpose of this analysis is to reveal qualitatively the features of the *I–V* characteristics of the *p–i–n* structure under conditions where the conductivity anisotropy is caused by field heating of carriers and their deflection, by an external magnetic field.

Let us analyze the *I–V* characteristics and MS using the concept of the effective carrier lifetime τ_{eff}, which can be introduced under certain assumptions in many specific models of double-injection currents. For example, in the drift mode of the *I–V* characteristic of the *p–i–n* structure, $J(U)$ is defined using τ_{eff} by the following equations:

$$wJ = e\mu_n\mu_p(n_T - p_T)\int_0^{E_w}\tau_{\mathrm{eff}}E_x dE_x,$$
$$UJ = e\mu_n\mu_p(n_T - p_T)\int_0^{E_w}\tau_{\mathrm{eff}}E_x^2 dE_x. \quad (1)$$

Here, U is the voltage, p_T and n_T are equilibrium concentrations of holes and electrons in the i-region, $\mu_{p,n}$ are their mobilities, and $E_w = E_x(w)$. In the situation where the IVRE and field heating of carriers are insignificant, it is possible to obtain a sufficiently exact expression for the effective lifetime, which defines the dependence of τ_{eff} on the semiconductor sample thickness, the carrier lifetime, the surface recombination rates, and electric and magnetic fields (see, e.g., [5, 6]). At equal surface recombination rates, $S_p^+ = S_p^-$, a good approximation for τ_{eff} is given by

$$\tau_{\mathrm{eff}} = \frac{\tau_{\mathrm{eff}}^0}{\sqrt{1 + (E_x/E_B)^2}}, \quad (2)$$

where τ_{eff}^0 is the effective lifetime at $B = 0$, and the characteristic field E_B is inversely proportional to the magnetic field induction ($E_B \propto 1/B$).

If the surface IVRE is taken into account (with no field heating of electrons), the expression for τ_{eff} depends also on the times of intervalley relaxation in the bulk and the relaxation rates at the semiconductor surface. This expression, in some extreme cases, can also be approximated by expressions similar to formula (2) (see [12], where specific expressions for τ_{eff} are given, as well as results of some calculations).

When analyzing the *I–V* characteristics of the *p–i–n* structure with simultaneous consideration of the Lorentz force and the Sasaki effect, we use an approximate expression for τ_{eff}. Substituting this expression into Eq. (1) makes it possible to take into account the superposition of transverse fluxes of carriers due to the IVRE in a strong electric field and the deflection by the Lorentz force. By analogy with formula (2), as such an expression, we take the dependence of τ_{eff} on E_x and B in the form

$$\tau_{eff} = \frac{\tau_{eff}^0}{\sqrt{1 + [(E/E_B) - (E/E_S)^{\gamma}]^2}}, \quad (3)$$

where E_S is a characteristic field such that heating of electron gas, the IVRE and, hence, the Sasaki anisotropy become significant at $E > E_S$. The parameter γ defines the development rate of the Sasaki anisotropy with the field E. Substituting expression (3) into Eqs. (1) and reducing the relations obtained to a dimensionless form, we obtain

$$i_S = \int_0^{\varepsilon_w} \frac{\varepsilon d\varepsilon}{\sqrt{1 + (\beta_S\varepsilon - \varepsilon^{\gamma})^2}},$$
$$u_S i_S = \int_0^{\varepsilon_w} \frac{\varepsilon^2 d\varepsilon}{\sqrt{1 + (\beta_S\varepsilon - \varepsilon^{\gamma})^2}}, \quad (4)$$

where

$$i_S = \frac{Jw}{e\mu_n\mu_p(n_T - p_T)\tau_{eff}^0 E_S^2},$$

$$u_S = \frac{U}{wE_S}, \quad \varepsilon = \frac{E}{E_S}, \quad \beta_S = \frac{E_S}{E_B}$$

are the dimensionless current, voltage, electric field, and magnetic induction. Figure 2 shows the dependences $i_S(U)$ calculated by the above formulas for the various magnetic fields and $\gamma = 3/2$.

At $B = 0$ and low voltages, the dependence of the current on the voltage is quadratic, since the semiconductor mode of double injection takes place. As the voltage increases, the Sasaki anisotropy begins to manifest itself. Due to the transverse anisotropic drift, carriers are accumulated near one of the lateral surfaces of the sample and actively recombine. The effective lifetime decreases with voltage, and the dependence of the current on the voltage becomes weaker (sublinear).

The magnetic field also causes surface accumulation of electron–hole plasma. As the induction vector reverses its direction, the direction of the Lorentzian drift is also reversed. At $B > 0$, the anisotropic effects caused by the magnetic field and the Sasaki effect give rise to the transverse drift of carriers in opposite directions at $B > 0$ and $B < 0$.

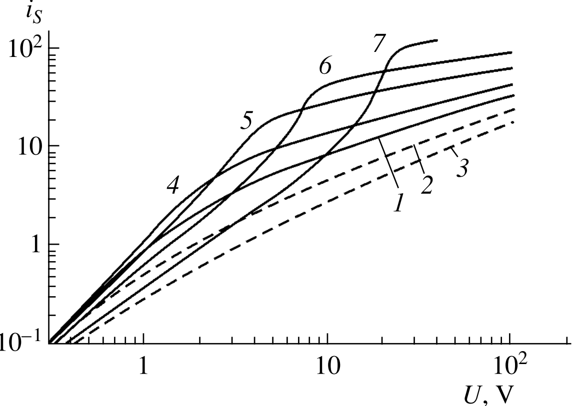

Fig. 2. *I–V* characteristics of the *p–i–n* structure under various magnetic fields (relative units) at $\beta_S = 0$ (*1*), 2 (*2*), 5 (*3*), –1 (*4*), –2 (*5*), –3 (*6*), and –5 (*7*).

At $B > 0$, the Lorentzian drift and the Sasaki anisotropy enhance the surface accumulation of carriers with the voltage and magnetic field. In this case, the current decreases with B at any voltage. At $B < 0$, the nonmonotonic dependence of the current on the magnetic field takes place. At a fixed voltage U, the highest current is attained in the magnetic field $B_C(U)$ that, to a great extent, causes compensation for the Sasaki anisotropy. At $B < B_C$, the Sasaki effect is dominant and carriers are accumulated at one *i*-region surface. At $B > B_C$, the Lorentzian drift is dominant and carriers are accumulated at the opposite surface.

We now consider the *I–V* characteristics at a fixed magnetic induction $B < 0$. At low voltages, the semiconductor conductivity anisotropy is controlled by the magnetic field. As $|BE_x|$ increases, the Lorentzian drift and the surface accumulation of carriers are enhanced. In this case, the recombination rate increases, the effective lifetime is shortened, and the quadratic dependence of the current on the voltage becomes linear. At rather high voltages, the Sasaki anisotropy becomes significant, which initially decreases carrier accumulation at the surface and, hence, increases the effective lifetime. At $\varepsilon^{\gamma - 1} = \beta_S$, the anisotropic effects caused by the magnetic and electric fields cancel each other out; as a result, the current drastically increases at $u_S \approx \beta_S^{1/(\gamma - 1)}$. A further voltage increase causes carrier accumulation at the opposite surface of the semiconductor wafer. As a result, the effective lifetime is abruptly shortened and the rise in current with voltage is retarded.

Although the above interpretation of the experimental *I–V* characteristics of planar *p–i–n* structures at low temperatures is not rigorous, it nevertheless provides insight into the causes of significant differences in these *I–V* characteristics at $T = 300$ and 77 K.

REFERENCES

1. Z. S. Gribnikov, G. I. Lomova, and V. A. Romanov, Phys. Status Solidi **28**, 815 (1968).
2. T. Yamada, in *Proceedings of IX International Conference on Physics of Semiconductors* (Moscow, 1968), Vol. 2, p. 711.
3. V. I. Stafeev and É. I. Karakushan, *Magnetodiodes* (Nauka, Moscow, 1975).
4. H. Pfleiderer, Solid-State Electron. **15**, 335 (1972).
5. A. A. Abramov and A. U. Fattakhdinov, Fiz. Tekh. Poluprovodn. (Leningrad) **13**, 2144 (1979) [Sov. Phys. Semicond. **13**, 1254 (1979)].
6. L. S. Gasanov and I. N. Gorbatii, Phys. Status Solidi A **59**, 401 (1980).
7. K. Miyazaki and J. Yamaguchi, Jpn. J. Appl. Phys. **7**, 1210 (1968).
8. L. S. Gasanov, Fiz. Tekh. Poluprovodn. (Leningrad) **15**, 2416 (1981) [Sov. Phys. Semicond. **15**, 1404 (1981)].
9. É. I. Rashba, Zh. Éksp. Teor. Fiz. **48**, 1427 (1965) [Sov. Phys. JETP **21**, 954 (1965)].
10. Z. S. Gribnikov, Fiz. Tekh. Poluprovodn. (Leningrad) **3**, 1821 (1969) [Sov. Phys. Semicond. **3**, 1543 (1969)].
11. A. A. Abramov and I. N. Gorbatyĭ, Izv. Vyssh. Uchebn. Zaved., Élektron., No. 6, 41 (2000).
12. A. A. Abramov and I. N. Gorbatyĭ, Fiz. Tekh. Poluprovodn. (St. Petersburg) **36**, 847 (2002) [Semiconductors **36**, 793 (2002)].
13. W. Sasaki, M. Shibuya, and K. Mizuguchi, J. Phys. Soc. Jpn. **13**, 456 (1958).
14. K. Seeger, *Semiconductor Physics* (Springer, Berlin, 1974; Mir, Moscow, 1977).

Translated by A. Kazantsev

Semiconductors, Vol. 37, No. 9, 2003, pp. 1057–1060. Translated from Fizika i Tekhnika Poluprovodnikov, Vol. 37, No. 9, 2003, pp. 1082–1084.
Original Russian Text Copyright © 2003 by Aliev.

Electrical and Thermoelectric Properties of p-Ag_2Te in the β Phase

F. F. Aliev

Institute of Physics, Azerbaijan National Academy of Sciences, Baku, 370143 Azerbaijan
Submitted December 2, 2002; accepted for publication December 17, 2002

Abstract—The conductivity σ, Hall coefficient R, and thermoelectric power α_0 of p-Ag_2Te were studied in the temperature range of 300–550 K. Inconsistency between the signs of R and α_0 was observed at 420–550 K. These results are interpreted within the two-phase model with spherical constant energy surfaces. It is established that the inconsistency between the R and α_0 signs is due to the emergence of the scattering mechanisms with the parameters r_{0ac}, r_{00}, and r_{0d} an increase of about 50% in the ratio of the effective electron and hole masses as a result of the transition $\alpha \longrightarrow \beta$. *© 2003 MAIK "Nauka/Interperiodica".*

Recently, we have published a paper [1] devoted to the temperature dependences of the Hall coefficient $R(T)$, conductivity $\sigma(T)$, and thermoelectric power $\alpha_0(T)$ in p-Ag_2Te in the temperatures range of 4–300 K. The experimental data on $R(T)$, $\sigma(T)$, and $\alpha_0(T)$ were interpreted within the model with two carrier types. In [2, 3] it was shown that the transition $\alpha \longrightarrow \beta$ in Ag_2Te is accompanied by additional transitions $\alpha \longrightarrow \alpha'$ $\beta' \longrightarrow \beta$ approximately according to the scheme $\alpha_{385} \longrightarrow \alpha'_{405} \longrightarrow \beta'_{420} \longrightarrow \beta_{440}$. To gain insight into the influence of the phase transition on the electrical and thermoelectric properties of Ag_2Te, we studied a number of p-type samples in the temperatures range of 300–550 K. The samples were prepared using conventional technology [1].

The results of the study show that the $R(T)$ and $\alpha_0(T)$ signs are unchanged before the transition $\alpha' \longrightarrow \beta'$, and the material exhibits n-type conduction in both effects. After the transition, the R sign is unchanged, while the α_0 sign changes from n to p; i.e., the R and α_0 signs become inconsistent (Fig. 1). The establishment of the causes of the inconsistency in the R and α_0 sign requires complex calculations taking into account the possible scattering mechanisms in order to ascertain the entire change in the effective carrier masses.

In [4], it was shown that the transition $\alpha \longrightarrow \beta$ in Ag_2Te was accompanied by an increase in the number of silver vacancies in interstices which played the role of acceptor centers. Therefore, the conduction is mixed in the indicated temperature range.

To establish the cause of the difference between the R and α_0 signs, we carried out calculations within the two-band model with spherical constant-energy surfaces. The expressions for σ, R, and α_0 in the range of mixed conduction can be written as functions of the ratio of hole and electron conductivity components ($a = \sigma_p/\sigma_n$, see [5])

$$\sigma = \sigma_i \frac{b^{1/2}(a+1)}{a^{1/2}(b+1)}, \qquad (1)$$

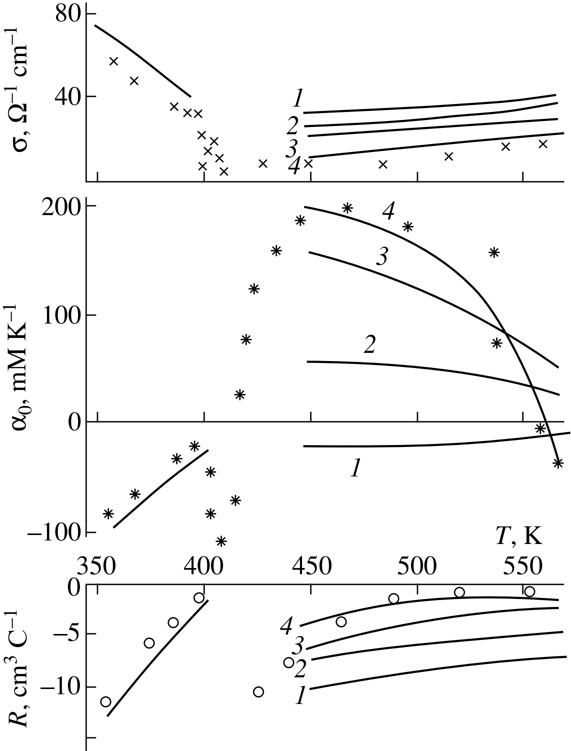

Fig. 1. Temperature dependences of the conductivity σ, thermoelectric power α_0, and Hall coefficient in p-Ag_2Te. Solid lines are plotted for (*1*) r_{0i}, r_{0ac}, $m_{n\beta} = 0.03$, $m_{p\beta} = 0.12$; (*2*) r_{0ac}, r_{00}, $m_{n\beta} = 0.03$, $m_{p\beta} = 0.12$; (*3*) r_{0ac}, r_{00}, r_{0d}, $m_{n\beta} = 0.03$, $m_{p\beta} = 0.12$; (*4*) r_{0ac}, r_{00}, r_{0d}, $m_{n\beta} = 0.03$, $m_{p\beta} = 0.18$.

1063-7826/03/3709-1057$24.00 © 2003 MAIK "Nauka/Interperiodica"

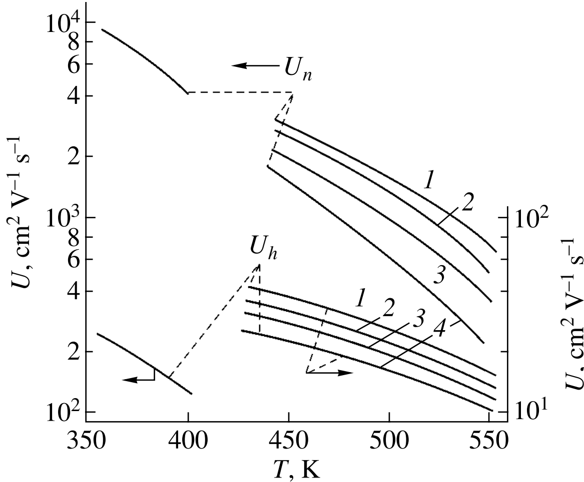

Fig. 2. Temperature dependences of the electron (U_n for a nonparabolic band) and hole (U_p for a parabolic band) mobilities. The notation is the same as in Fig. 1.

$$R = \frac{A}{n_i e}\frac{(ab)^{1/2}(a/b-1)}{(a+1)^2}, \quad (2)$$

$$\alpha_0 = \frac{k_0}{2e}\left[\frac{\varepsilon_0(a-1)}{(a+1)} + \chi - \ln a\right], \quad (3)$$

where $\sigma_i = en_i(U_n + U_p)$; $b = \frac{U_n}{U_p}$; $\varepsilon_0 = \left(\frac{\varepsilon_g}{k_0 T}\right) + r_n + r_p$, $\chi = r_p - r_n + \ln\left[b\left(\frac{m_n}{m_p}\right)^{3/2}\right]$; n_i is the intrinsic carrier concentration; U_n, U_p, m_n, and m_p are the mobilities and effective masses of electrons and holes; A is the Hall factor (for a parabolic and nonparabolic bands, $A = \frac{F_{3/2}F_{2r+1/2}}{(F_{r+1})^2}$ and $A = I^0_{3/2,0}I^0_{2r+1/2,4}(I^0_{r+1,2})^2$, respectively, where $F_r(\mu^*)$ and $I^m_{n,k}(\mu^*, \beta)$ are the one- and two-parameter Fermi integrals; $\beta_0 = k_0T/\varepsilon_g$ is the parameter characterizing the degree of nonparabolicity of the band; $\mu^* = \mu/k_0T$ is the reduced chemical potential [6]); and r_n and r_p are the scattering coefficients.

The temperature dependence of the mobility is given by

$$U = \frac{e}{m^*}\tau(T), \quad (4)$$

where m^* is the effective mass of carriers and τ is the relaxation time.

The parameters U_n and U_p entering formulas (1)–(3) were calculated as follows.

In the case of two scattering mechanisms with the parameters r_{0i} and r_{0ac}, the effective relaxation time is written as (see [1])

$$\tau_{eff} = \frac{\tau_{0i}(T)\tau_{0ac}(T)\left(\frac{\varepsilon}{k_0T}\right)^{r_{0ac}-1/2}}{\tau_{0i}(T) + \tau_{0ac}(T)\left(\frac{\varepsilon}{k_0T}\right)^{r_{0ac}-r_{0i}}}. \quad (5)$$

To determine $\tau_{0i}(T)$, we use the following formula:

$$\tau_{0i}(T) = \frac{\chi_0(2m_n)^{1/2}(k_0T)^{3/2}}{\pi e^4 N_i F}, \quad (6)$$

where χ_0 is the crystal permittivity,

$$F = \ln(1+\xi) - \frac{\xi}{1+\xi}, \quad \xi = 4k^2 r_s, \quad (7)$$

r_s is the screening length, which, for nondegenerate semiconductors, is given by

$$r_s = \frac{\chi_0 k_0 T}{4\pi e^2 n_0}, \quad (8)$$

n_0 is the charge-carrier density $p = \frac{(2m_pk_0T)^{3/2}}{3\pi^2\hbar^3}F_{3/2}(\mu^*)$ for the parabolic valence band and $n = \frac{(2m_nk_0T)^{3/2}}{3\pi^2\hbar^3}I^0_{3/2}(\mu^*, \beta_0)$ for the nonparabolic conduction band; the dispersion relation of electrons in β-Ag_2Te obeys the Kane model [7]), and N_i is the impurity ion concentration [6].

The expression for $\tau_{0ac}(T)$ for the standard and nonstandard bands is written as (see [1])

$$\tau_{0ac}(T) = \frac{9\pi}{2}\frac{\rho U_0^2\hbar^4}{C^2(2m_nk_0T)^{3/2}}\left(\frac{\varepsilon}{k_0T}\right)^{-1/2},$$
$$\tau_{0ac}(T) = \frac{9\pi}{2}\frac{\rho U_0^2\hbar^4}{C^2(2m_nk_0T)^{3/2}}, \quad (9)$$

where ρ is the crystal density, C is the constant of the interaction between carriers and lattice vibrations, and U_0 is the velocity of sound in the crystal. It was ascertained that C is related to the deformation-potential constant $E_d = \frac{2}{3}C$ [1]. We take into account the values $\chi_{0\beta} = 14$, $\rho_\beta = 7.64$ kg cm^{-3}, $U_{0\beta} = 3.5 \times 10^5$ cm/s, $E_d = 10$ eV, $m_{n\beta} = 0.03$ [7], and $m_p\beta = 0.12$ [8], as well as $\mu \approx -\frac{\varepsilon_g}{2} + \frac{3}{4}k_0T\ln\frac{m_n}{m_p}$ (disregarding a small deviation). After calculating $\tau_{0i}(T)$, F, ξ, r_s, and $\tau_{0ac}(T)$ taking into account their numerical values in formula (5), $\tau_{eff}(I)$ was determined. Then, using formula (4), $U_n(T)$ and

$U_p(T)$ were determined for the nonparabolic and parabolic bands, respectively (Fig. 2, curves *1*).

The intrinsic carrier concentration n_i is calculated using the formula

$$n_i = 4.9 \times 10^{15}\left(\frac{m_{n\beta}m_{p\beta}}{m_0^2}\right)^{3/4} T^{3/2}\exp\left(-\frac{\varepsilon_g}{2k_0T}\right), \quad (10)$$

where $\varepsilon_g = 0.12$ eV [7].

Substituting the values of U_n, U_p, n_β, p_β, n_i, and ε_g into formulas (1)–(3), we obtain $\sigma(T)$, $R(T)$, and $\alpha_0(T)$ (Fig. 1, curve *1*).

The calculations show that the consideration of the contribution of scattering by impurity ions (this contribution is insignificant) and by acoustic lattice vibrations does not result in the agreement of experimental and calculated curves (Fig. 1, curve *1*). Therefore, the contribution of carrier scattering by optical lattice vibrations is taken into account in the calculation. At $k_0T \gg \hbar\omega$, in the case of a parabolic band, the relaxation time in the case of scattering by optical phonons is given by (see [6])

$$\tau_{00}(T) = \frac{\sqrt{2}}{4\pi}\frac{M\Omega_0(\hbar\omega_0)^2}{e^4(m_pk_0T)^{1/2}}\left(\frac{\varepsilon}{k_0T}\right)^{1/2}, \quad (11)$$

where $M = \frac{m_1m_2}{m_1+m_2}$ is the reduced mass of ions in the unit cell, Ω_0 is the unit cell volume, and ω_0 is the limiting frequency of longitudinal optical phonons. Taking into account the values of $\tau_{00}(T)$ in formula (4), we determine U_{00} (Fig. 2, curve *2*).

In the case of a nonparabolic band and scattering by optical phonons, U_{00} is given by

$$U_{00} = \frac{3^{1/3}M\Omega_0\omega_0^2h^3n^{1/3}}{16\pi^{4/3}ee^*k_0Tm_n^2}\frac{1}{f_{op}}, \quad (12)$$

where e^* is the effective charge and f_{op} is the factor accounting for the influence of nonparabolicity on the scattering probability [9].

In the case of mixed scattering mechanisms with the parameters r_{0ac} and r_{00}, the carrier mobility is written as

$$U = \left(\frac{1}{U_{0ac}} + \frac{1}{U_{00}}\right)^{-1}. \quad (13)$$

Having taken into account these scattering mechanisms, the calculations using formulas (1)–(3) qualitatively comply with the experimental data (Fig. 1, curve *2*). An analysis of the above calculations shows that the quantitative agreement of experimental and calculated curves requires taking into account new scattering centers in formula (13).

In [4], it was shown that abrupt changes in the kinetic coefficients of Ag_2Te during the transition $\alpha \longrightarrow \beta$ are caused not only by changes in the band parameters, but also by the densities of electrically active and neutral defects. Andre and Simon [10] reason that Ag_2Te is characterized by Frenkel defects with Ag atoms at interstices, which manifest themselves due to Ag atoms statistically arranged in the corresponding sublattice. As follows from the conclusions of [4, 10, 11], the run of $\sigma(T)$, $R(T)$, and $\alpha_0(T)$ at $T > 420$ K is also associated with point defects generated during the transition $\alpha \longrightarrow \beta$. Therefore, formula (13) can additionally account for the contribution of the mobility U_{0d} calculated using the relaxation time for the mechanism of scattering by point defects in the case of the parabolic band as (see [6])

$$\tau_{0d}(T) = \frac{\pi\hbar^4}{(2m_nk_0T)^{1/2}m_nV_0^2N_d}\left(\frac{\varepsilon}{k_0T}\right)^{-1/2}, \quad (14)$$

where V_0 is the constant characterizing the δ potential amplitude and N_d is the point defect density, which is determined in [11]. Substituting formula (14) into relation (4), $U_{0d}(T)$ was determined. In this case, U for all of the scattering mechanisms is defined as

$$U = \left(\frac{1}{U_{0ac}} + \frac{1}{U_{00}} + \frac{1}{U_{0d}}\right)^{-1}. \quad (15)$$

The calculations show that the consideration of formula (15) (Fig. 1, curve *3*) at $m_{p\beta} = 0.18$ leads to a total agreement of the experimental and calculated curves $\sigma(T)$, $R(T)$, and $\alpha_0(T)$ (Fig. 1, curve *4*).

As the results of calculations show, each new scattering mechanism taken into account in the calculation, as well as an increase in the effective mass of holes, promotes convergence of the experimental and calculated curves. Scattering of charge carriers by phonons in the case of p-type conduction is important as well. In this case, the $m_{p\beta}$ maximum increases by 50% (as $m_{n\beta}/m_{n\alpha}$ in [7]); however, this increase has a more significant effect on $\alpha_0(T)$ than on $\sigma(T)$ and $R(T)$. We can see from formulas (2) and (3) that the conditions $p > n$ and $U_n > U_p$ yield $nU_n^2 > pU_p^2$; it then follows from formula (2) that $R < 0$; i.e., sign n is dominant in $R(T)$. Since $m_p > m_n$, formula (3) yields $\alpha_0(T) > 0$ and sign p is dominant.

Thus, the disagreement of the Hall coefficient and thermoelectric power signs in p-Ag_2Te in the temperature range of 420–550 K is accompanied by combination of the scattering mechanisms with the parameters r_{0ac}, r_{0p}, and r_{0d}, as well as a 50% increase in the effective mass of electrons and holes as a result of the transition $\alpha \longrightarrow \beta$.

REFERENCES

1. F. F. Aliev, É. M. Kerimova, and S. A. Aliev, Fiz. Tekh. Poluprovodn. (St. Petersburg) **36**, 932 (2002) [Semiconductors **36**, 869 (2002)].
2. S. A. Aliev, F. F. Aliev, and G. P. Pashaev, Izv. Ross. Akad. Nauk, Neorg. Mater. **29**, 1073 (1993).
3. S. A. Aliev, F. F. Aliev, and Z. S. Gasanov, Fiz. Tverd. Tela (St. Petersburg) **40**, 1693 (1998) [Phys. Solid State **40**, 1540 (1998)].
4. S. A. Aliev and F. F. Aliev, Izv. Akad. Nauk SSSR, Neorg. Mater. **25**, 241 (1989).
5. V. M. Berezin, G. P. Vyatkin, V. N. Konev, and P. I. Karikh, Fiz. Tekh. Poluprovodn. (Leningrad) **18**, 312 (1984) [Sov. Phys. Semicond. **18**, 194 (1984)].
6. B. M. Askerov, *Kinetic Effects in Semiconductors* (Nauka, Leningrad, 1970).
7. S. A. Aliev and F. F. Aliev, Izv. Akad. Nauk SSSR, Neorg. Mater. **21**, 1869 (1985).
8. S. A. Aliev and F. F. Aliev, Izv. Akad. Nauk SSSR, Neorg. Mater. **24**, 341 (1988).
9. T. A. Aliev, F. M. Gashimzade, S. A. Aliev, *et al.*, Fiz. Tekh. Poluprovodn. (Leningrad) **5**, 323 (1971) [Sov. Phys. Semicond. **5**, 274 (1971)].
10. A. Andre and C. Simon, J. Phys. Chem. **42**, 95 (1983).
11. F. F. Aliev, Dokl. Akad. Nauk Azerb. **56** (1–3), 85 (2000).

Translated by A. Kazantsev

Semiconductors, Vol. 37, No. 9, 2003, pp. 1061–1062. Translated from Fizika i Tekhnika Poluprovodnikov, Vol. 37, No. 9, 2003, pp. 1085–1086.
Original Russian Text Copyright © 2003 by Nemov, Kozhanova, P. Seregin, N. Seregin, Shamshur.

Local Symmetry and Electronic Structure of Tin Atoms in $(Pb_{1-x}Sn_x)_{1-z}In_zTe$ Lattices

S. A. Nemov*, Yu. V. Kozhanova*, P. P. Seregin*, N. P. Seregin, and D. V. Shamshur*****

**St. Petersburg State Technical University, Politekhnicheskaya ul. 29, St. Petersburg, 195251 Russia*

***Institute of Analytical Instrumentation, Russian Academy of Sciences, Rizhskii pr. 26, St. Petersburg, 198103 Russia*

****Ioffe Physicotechnical Institute, Russian Academy of Sciences, Politekhnicheskaya ul. 26, St. Petersburg, 194021 Russia*

Submitted December 10, 2002; accepted for publication December 17, 2002

Abstract—Mössbauer spectroscopy of the ^{119}Sn isotope has shown that the superconducting transition in $(Pb_{1-x}Sn_x)_{1-z}In_zTe$ solid solutions is not accompanied by a change in the local symmetry of tin atoms or in their electronic structure. © *2003 MAIK "Nauka/Interperiodica".*

Superconductivity with a critical temperature $T_c \approx$ 4 K, which is extremely high for semiconductors and depends on the tin concentration, was revealed in the $(Pb_{1-x}Sn_x)_{1-z}In_zTe$ solid solutions with $x \approx 0.8$ and $z \approx$ 0.16–0.20 [1]. This finding cannot currently be explained within any version of microscopic theory of superconductivity. One cannot rule out the possibility that the phenomenon of superconductivity in these semiconductors is related to resonance levels created by the indium impurity in the valence band of the crystals [2].

Mössbauer spectroscopy is a promising tool for studying the electronic structure of solids. The parameters of Mössbauer spectra (the isomer shift and quadrupole splitting) allow reliable determination of the charge state of the centers studied and the symmetry of their local environment, whereas, by measuring the temperature dependence of the centroid S of a Mössbauer spectrum, both above and below the superconducting-transition temperature T_c, one can investigate the formation of Cooper pairs.

We undertook a Mössbauer study of the $(Pb_{1-x}Sn_x)_{1-z}In_zTe$ solid solutions using the ^{119}Sn isotope with the purpose of detecting possible changes in the local symmetry of tin sites and the electronic structure of tin atoms, as well as of following the process of Cooper pair formation.

The solid solutions $(Pb_{0.5}Sn_{0.5})_{0.84}In_{0.16}Te$ ($T_c \approx 4$ K), $Pb_{0.5}Sn_{0.5}Te$ ($T_c < 1.8$ K), $(Pb_{0.4}Sn_{0.6})_{0.84}In_{0.16}Te$ ($T_c \approx$ 4 K), $Pb_{0.4}Sn_{0.6}Te$ ($T_c < 1.8$ K), $(Pb_{0.4}Sn_{0.6})_{0.97}In_{0.03}Te$ ($T_c < 1.8$ K), and the compound SnTe ($T_c < 1.8$ K) were prepared by melting the starting components of semiconductor-grade purity in evacuated quartz cells, with their subsequent annealing at 650°C for 120 h. X-ray analysis showed all the samples to be single-phase (with an NaCl-type structure). The ^{119}Sn Mössbauer spectra were obtained with an SM 2201 commercial spectrometer at 295, 195, 78, 4.2, and 2 K, with the source ($Ca^{119}SnO_3$) maintained at 295 K. The width of the spectrum of this source with a $CaSnO_3$ absorber (surface density 0.1 mg/cm^2 for ^{119}Sn) was 0.78(1) mm/s, and this value was assumed to be the instrumental width of the ^{119}Sn spectral line.

The ^{119}Sn Mössbauer spectra of all the $(Pb_{1-x}Sn_x)_{1-z}In_zTe$ samples consisted of individual lines (Fig. 1), whose full widths at half maximum W_{exp} were close to the instrumental width of the spectra (W_{exp} varied from 0.96 to 1.04 mm s^{-1}, depending on the sample composition). The transition of an alloy to the superconduct-

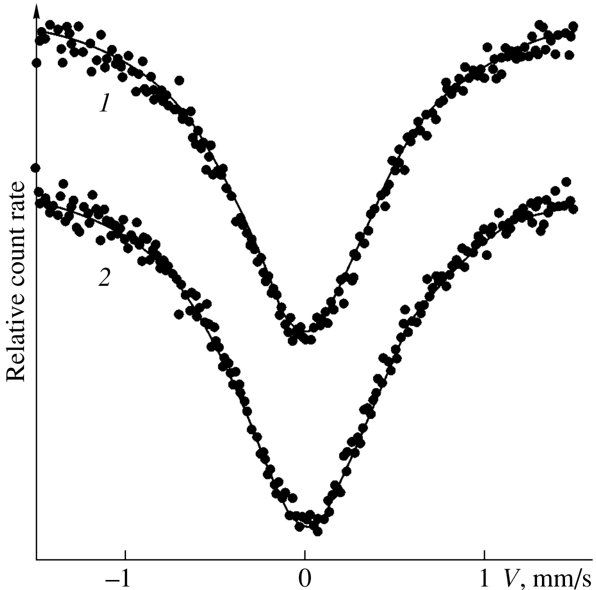

Fig. 1. ^{119}Sn Mössbauer spectra of the $(Pb_{0.5}Sn_{0.5})_{0.84}In_{0.16}Te$ solid solution ($T_c \approx 4$ K) measured at (*1*) 4.2 and (*2*) 2 K. The isomer shifts are specified relative to the spectrum measured at 4.2 K.

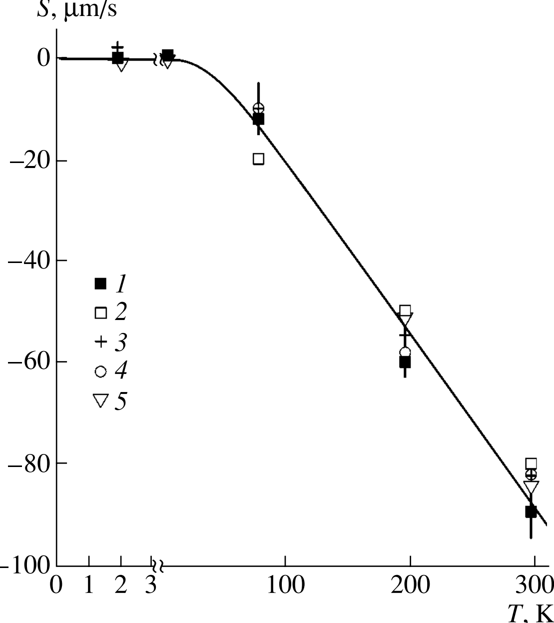

Fig. 2. Temperature dependences of the centroid S of the ^{119}Sn Mössbauer spectra measured for the solid solutions (*1*) $(Pb_{0.4}Sn_{0.6})_{0.84}In_{0.16}Te$, (*2*) $Pb_{0.5}Sn_{0.5}Te$, (*3*) $(Pb_{0.4}Sn_{0.6})_{0.84}In_{0.16}Te$, (*4*) $Pb_{0.4}Sn_{0.6}Te$, and (*5*) $(Pb_{0.4}Sn_{0.6})_{0.97}In_{0.03}Te$, related to its values at 4.2 K. The solid line shows the theoretical temperature dependence of S calculated for the case of a second-order Doppler shift at $\theta = 130$ K.

ing state does not noticeably affect W_{exp}. Thus, we may conclude that the transition of the $(Pb_{1-x}Sn_x)_{1-z}In_zTe$ solid solutions to the superconducting state does not entail any change in the local symmetry of their cation lattice sites.

The isomer shift of Mössbauer spectra is governed by the chemical nature of atoms in the local environment of the Mössbauer probe. Since a variation in the composition of the $(Pb_{1-x}Sn_x)_{1-z}In_zTe$ solid solution leaves the nearest environment of tin atoms unchanged, the constancy of the ^{119}Sn Mössbauer isomer shift, which, for all of the compositions, coincides within experimental error with that of the SnTe compound, does not come as a surprise.

The phenomenon of superconductivity is known to be based on formation of a Bose condensate of Cooper pairs, which is described by a common coherent wave function, so that the distribution of electron density over the lattice sites of a superconductor measured at temperatures above and below the superconducting-transition temperature should be different [3]. Since the isomer shift of Mössbauer spectra depends on the electron density at the probe nucleus, one can detect the formation of the Bose condensate from the temperature dependence of the centroid S of the Mössbauer spectrum of a superconductor at $T < T_c$ [4]. We should bear in mind that, in the absence of phase transitions, the temperature dependence of S, governed by a second-order Doppler shift, can be written in terms of the Debye model in the form [5]

$$\left(\frac{\delta D}{\delta T}\right)_P = -\frac{3kE_0}{2Mc^2}F\left(\frac{T}{\theta}\right), \qquad (1)$$

where k is the Boltzmann constant, E_0 is the energy of the isomer transition, M is the probe-nucleus mass, c is the speed of light in vacuum, θ is the Debye temperature, and $F(T/\theta)$ is the Debye function. Deviation of an experimental dependence $S(T)$ from the relation of type (1) should indicate a change in the electron density of the crystal at the Mössbauer probe sites in the crystal, which is due to the Bose condensation.

Figure 2 shows experimental (symbols) and theoretical (solid lines plotted using Eq. (1)) temperature dependences of the centroid of the ^{119}Sn spectra obtained for the $(Pb_{1-x}Sn_x)_{1-z}In_zTe$ solid solutions. Within the temperature range studied (above and below the superconducting-transition temperature), the experimental dependences $S(T)$ are seen to be well fitted by the second-order Doppler shift for the Debye temperature $\theta = 130$ K.

Thus, we can conclude that ^{119}Sn Mössbauer spectroscopy reveals changes neither in the local site symmetry nor in the electronic structure of atoms in $(Pb_{1-x}Sn_x)_{1-z}In_zTe$ solid solutions at the superconducting transition.

ACKNOWLEDGMENTS

This study was supported by the Russian Foundation for Basic Research, project no. 02-02-17306.

REFERENCES

1. R. V. Parfeniev, D. V. Shamshur, and M. F. Shakhov, J. Alloys Compd. **219**, 313 (1995).
2. S. A. Nemov and Yu. I. Ravich, Usp. Fiz. Nauk **168**, 817 (1998) [Phys. Usp. **41**, 735 (1998)].
3. J. R. Schrieffer, *Theory of Superconductivity* (Benjamin, New York, 1964; Mir, Moscow, 1965).
4. N. P. Seregin and P. P. Seregin, Zh. Éksp. Teor. Fiz. **118**, 1421 (2000) [JETP **91**, 1230 (2000)].
5. D. L. Nagy, in *Mössbauer Spectroscopy of Frozen Solutions*, Ed. by A. Vértes and D. L. Nagy (Akadémiai Kiadó, Budapest, 1990; Mir, Moscow, 1998).

Translated by G. Skrebtsov

Semiconductors, Vol. 37, No. 9, 2003, pp. 1063–1069. Translated from Fizika i Tekhnika Poluprovodnikov, Vol. 37, No. 9, 2003, pp. 1087–1093.
Original Russian Text Copyright © 2003 by Kamilov, Stepurenko, Kovalev.

Phenomena of the Collective Behavior of Autosolitons in a Dissipative Structure in InSb

I. K. Kamilov, A. A. Stepurenko, and A. S. Kovalev

Institute of Physics, Dagestan Scientific Center, Russian Academy of Sciences, ul. 26 Bakinskikh Komissarov 94, Makhachkala, 367003 Dagestan, Russia

Submitted July 1, 2002; accepted for publication December 24, 2002

Abstract—It is shown that the behavior of autosolitons can be considered as the behavior of an ensemble of interacting solitary localized states in the electron–hole plasma. Investigations revealed transitions from the modes of chaotic oscillations of a current in the external circuit of a sample, which are caused by the motion of autosolitons, to regular oscillations, and from regular oscillations to other regular oscillations through bifurcation by doubling the period with increasing the excitation level of the electron–hole plasma. It is concluded that the system which consists of an ensemble of interacting autosolitons possesses the property of self-organization. It is shown that the autosolitons, which travel through the sample in an external longitudinal magnetic field as strong as 13.6×10^3 A/m, also exhibit synergetic behavior in a dissipative structure in InSb. © *2003 MAIK "Nauka/Interperiodica".*

It is shown theoretically [1–17] and experimentally that localized regions with an extreme concentration and temperature of charge carriers, so-called autosolitons, both in the form of layers of current (longitudinal autosolitons) and in the form of layers of a strong electric field (transverse autosolitons) can emerge in the nonequilibrium excited electron-hole plasma. The plasma may be generated either by impact ionization or injection in *n*-GaAs [8, 9], or by photogeneration in Ge [10], as well as by Joule heating in InSb [11, 12].

According to previous numerical calculations [13–17], the kinetics of formation of autosolitons in the electron–hole plasma of semiconductors and their evolution are very diverse. The generation of autosolitons in the electron–hole plasma when the sample is inhomogeneous has been considered [13]. In an electric field, the autosolitons sequentially travel through the sample and are destroyed when they reach the end of the sample. As a result, jumps in current appear and manifest themselves as relaxation oscillations of the current in the external circuit of the sample. The period T of these oscillations is governed by the delay time t_d of the emergence of autosolitons at the inhomogeneity $T = t_d(E)$. At the same time, $T = \mathcal{L}/v_{AC}$ and $\mathcal{L} > L$, where $\mathcal{L}$ is the sample length, L is the ambipolar diffusion length of charge carriers, v_{AC} is the velocity of autosolitons, $v_{AC} \propto \mu E$, μ is the ambipolar carrier mobility, and E is the strength of the electric field applied to the sample. With varying E, the velocity of autosolitons and the delay time t_d vary, which leads to changes in the oscillation frequency of the current in the sample circuit. On reaching a certain E value, the distance $\mathcal{L}_c$ between the autosolitons will become close to L. In the case $\mathcal{L}_p \leq L$, an interaction of the transfer type becomes possible between travelling autosolitons generated at the inhomogeneity [1, 10]. Due to this circumstance, a random sequence of travelling autosolitons emerges in the sample; this sequence leads to stochastic oscillations in the external circuit of the sample. The natural presence of several inhomogeneities in the sample, even with differing magnitudes, may lead to the emergence of several sequences of autosolitons travelling through the sample, which gives rise to a complex pattern of oscillations of the current in the external circuit of the sample.

Transverse autosolitons, which are formed in the electron–hole plasma excited in the sample subjected to an electric field, comprise regions with an increased electric-field strength. On reaching a certain excitation level, i.e., certain electric-field strength, impact ionization sets in these regions [13–17]. Depending on the generation and recombination rates, as well as on the excitation level, the autosoliton deforms or divides. In the external circuit of the sample, such a situation manifests itself in the form of current oscillations with doubled frequency. The impact ionization in autosolitons should be more easily observed in one-valley semiconductors, in which impact ionization sets in at carrier temperatures lower than those for intervalley transitions.

The motion of transverse autosolitons emerging in the electron–hole plasma in a semiconductor which is in an external electric field may be accompanied by their pulsation. Analysis of computational investigations [17] shows that two phases may be recognized during pulsations, namely, an increase in the amplitude of an autosoliton and its slight narrowing, and a decrease in the amplitude of an autosoliton and its slight broadening. The frequency of occurring pulsations $\omega \propto \tau_r^{-1}$, where τ_r is the characteristic recombina-

1063-7826/03/3709-1063$24.00 © 2003 MAIK "Nauka/Interperiodica"

tion time. With an increase in the level of electron–hole plasma heating, the amplitude of pulsations of autosolitons increases steadily. For a certain level of heating of the electron–hole plasma, the amplitude of pulsations reaches a magnitude such that the pulsating autosoliton divides into two autosolitons scattering from each other. These autosolitons, in their turn, also divide when they are far enough apart from one another. Due to a sequence of such divisions, the sample is filled by interacting autosolitons.

Taking into account the aforesaid, we may conclude that we are dealing with a cooperative system of autosolitons with a natural tendency toward self-organization. It seems likely that the periodic relaxation oscillations of the current should be observed in the external circuit of the sample. With increasing voltage applied to the sample, they become chaotic and then take the form of regular oscillations again. Bifurcations are possible via doubling of the period of oscillations and other complex scenarios of development, which reflect the collective behavior of travelling autosolitons.

A classical object for the experimental investigation of the cooperative behavior of travelling autosolitons is the well-known InSb semiconductor. This is a polar one-valley semiconductor with a narrow band gap E_g = 0.17 eV; effective masses of electrons and holes $m_e^* = 0.013m_0$ and $m_p^* = 0.6m_0$; a ratio of electron and hole mobilities $b = \mu_e/\mu_p \approx 100$; and Θ = 264 K. The time of the electron-energy relaxation due to scattering at phonons τ_{ef} depends on the energy as $\tau_{ef} \propto E^{-1/2}$, whereas the time of the electron-momentum relaxation due to scattering at holes, as at charged centers, $\tau_p \propto E^{3/2}$ [1, 18]. The condition of stratification of the hot nonequilibrium electron–hole plasma $\alpha + s > 0$ [1] for InSb ($\alpha = 3/2$, $s = -1/2$, $\alpha + s = 1 > 0$) is satisfied. At temperatures above 150 K, the InSb samples acquire intrinsic conduction [18], which permits one to generate the nonequilibrium electron–hole plasma at a relatively low dissipated power under Joule heating. Further strengthening of the electric field applied to the sample leads to heating of the nonequilibrium electron–hole plasma, which makes the formation of autosolitons possible.

It was shown that the formation of autosolitons was accompanied by current oscillations, which have several modes [11, 12]. The frequency and amplitude for each mode varied with a certain regularity for each mode as the electric field applied to the sample increased. Further investigations allowed us to find modes of more complex oscillations of the current, which were clear signs of the self-organization of a dissipative structure in InSb.

The purpose of this study is to investigate the dynamics of the development of a dissipative structure in InSb upon varying the excitation level; to identify the oscillations of the current observed with corresponding autosolitons, whose kinetics of formation and travelling was described previously [13–17]; and to reveal the mechanisms of the self-organization phenomena for autosolitons in the dissipative structure in InSb. For investigations, InSb crystals with a hole density $p = (2–4) \times 10^{12}$ cm^{-3} and mobility $\mu_p \approx 4000–7000$ cm^2/V s at T = 77 K were used.

In this paper, experimental results for the following samples are reported:

InSb-*d*2 ($p = 1.5 \times 10^{12}$ cm^{-3}, μ_p = 5200 cm^2/V s) with dimensions l = 6.9 mm, a = 2.2 mm, b = 1.1 mm, and resistance R = 19.2 kΩ;

InSb-*b*1-2 ($p = 4 \times 10^{12}$ cm^{-3}, μ_p = 7000 cm^2/V s) with dimensions l = 4.9 mm, a = 2.2 mm, b = 1.4 mm, and resistance R = 9.16 kΩ;

InSb-*b*5-2 ($p = 1.8 \times 10^{12}$ cm^{-3}, μ_p = 5060 cm^2/V s) with dimensions l = 6.1 mm, a = 2.3 mm, b = 1.4 mm, and resistance R = 9.16 kΩ.

The nonequilibrium electron–hole plasma in the samples was generated using Joule heating by a rectangular voltage pulse with a duration of 2.5 ms and a repetition frequency of 10 Hz. The electron–hole plasma generated was excited by the same voltage pulse. Owing to this, longitudinal autosolitons emerged in the form of a filament of the current and transverse autosolitons emerged in the form of layers of a strong electric field. Since the electron–hole plasma is not symmetric for InSb ($m_p^* > m_e^*$), these layers move in the electric field from the cathode to the anode, causing oscillations of the current in the external circuit of the sample. The change of the current in the sample circuit was recorded using an oscilloscope and was stored in computer memory using an analog–digital converter. The data recorded were subjected to computer processing.

Figure 1 shows the oscillograms of oscillations of the current in the external circuit of the InSb-*d*2 sample. The oscillations are caused by the travelling of transverse autosolitons through the sample. The phase portraits and power spectra upon varying the voltage applied to the sample from U_a = 48.4 V to U_a = 52.9 V are also shown in Fig. 1.

The kinetics of formation of an autosoliton and its motion through the sample are in rather good agreement with the results of the theoretical investigation [13]. The demonstrated pattern of regular oscillations of the current may be presented as a sequence of travelling autosolitons after their formation at the inhomogeneity and detachment from it. In this case, $\mathcal{L}_c > L$. The phase portrait (attractor) comprises a limiting cycle. The shape of the phase portrait indicates that the oscillations of the current are far from harmonic; most likely, they are relaxational. It can be seen from Fig. 1b that the shape of the phase portraits varies. This means that the autosolitons, when travelling, undergo deformation both at the leading edge and at the trailing edge with increasing excitation level. The frequency of oscillations of the current decreases, and a second harmonic emerges even for the highest voltage in the electric field

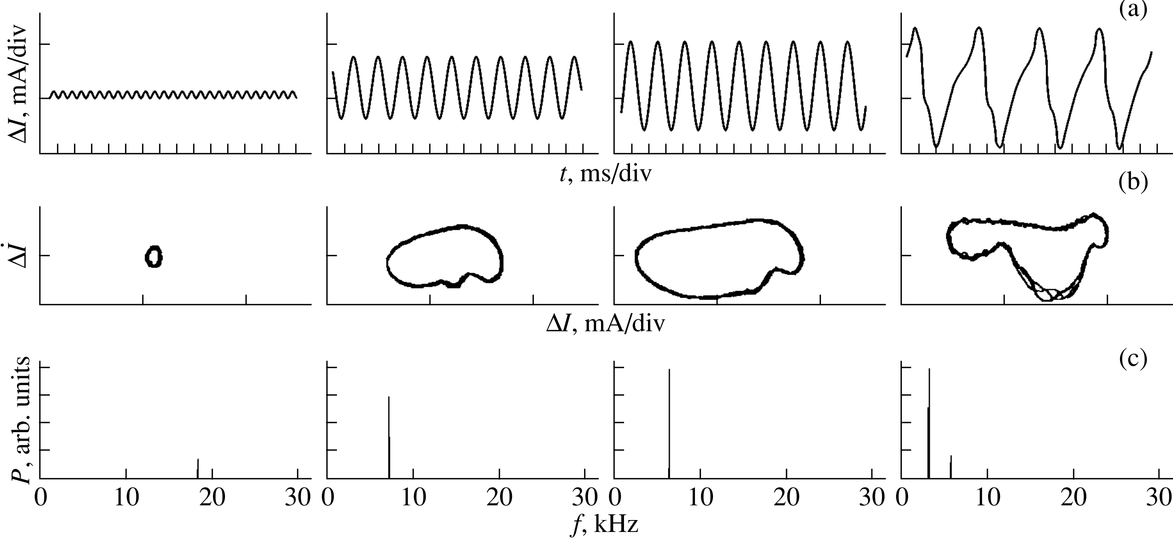

Fig. 1. (a) Oscillograms of oscillations of the current in the sample InSb-d2, (b) phase portraits, and (c) power spectra. U_a = 48.4–52.9 V.

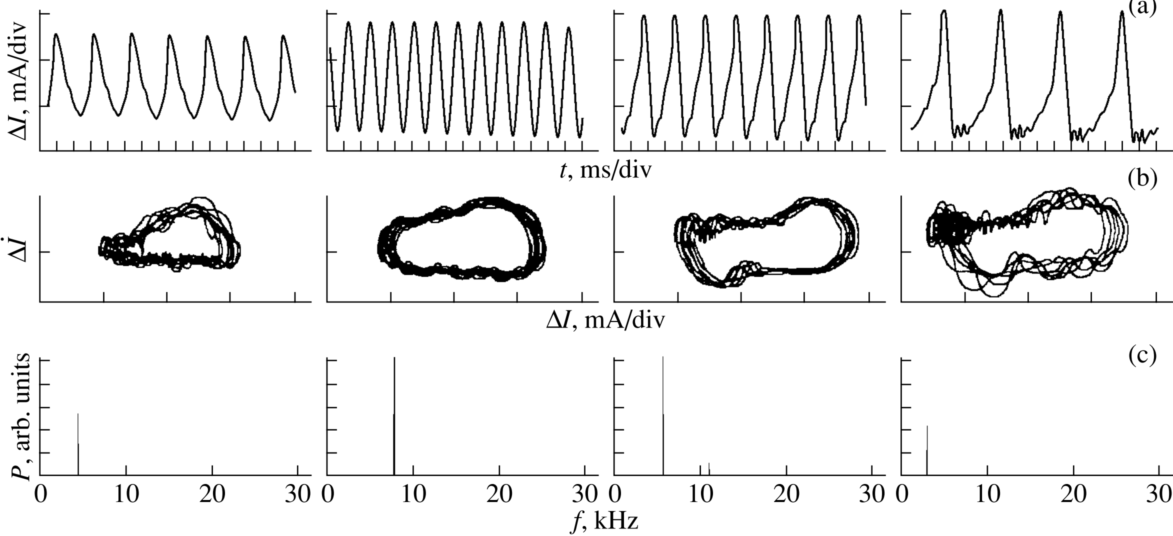

Fig. 2. (a) Oscillograms of oscillations of the current in the sample InSb-b5-2, (b) phase portraits, and (c) power spectra.

range for this mode. At this voltage, the current oscillations, their phase portrait, and the power spectrum of these oscillations manifest the tendency of autosolitons to divide. The mode of current oscillations under consideration possesses a certain regularity of the development dynamics with increasing level of excitation of the electron–hole plasma, which was described previously [12]; i.e., the oscillation frequency decreases, whereas the amplitude rises. This mode is the most frequently encountered mode in all investigations of autosolitons in InSb.

Another mode of oscillations of the current often encountered with another regularity of development is the mode for which variation in the frequency with increasing excitation of the electron–hole plasma has a positive extremum. Figure 2 presents the oscillograms of oscillations of the current in the external circuit of the InSb-b5-2 sample with precisely the mentioned regularity of dynamics of the development with increasing excitation of the electron–hole plasma. Phase portraits and power spectra with varying voltage applied to the sample from U_a = 56.7 V to U_a = 58.5 V are also shown in Fig. 2.

It can be seen from oscillograms of current oscillations and from phase portraits that the autosolitons are noticeably deformed both at the leading and trailing edges of the pulse, although the regularity of oscillations is retained. As in the mode described above, the

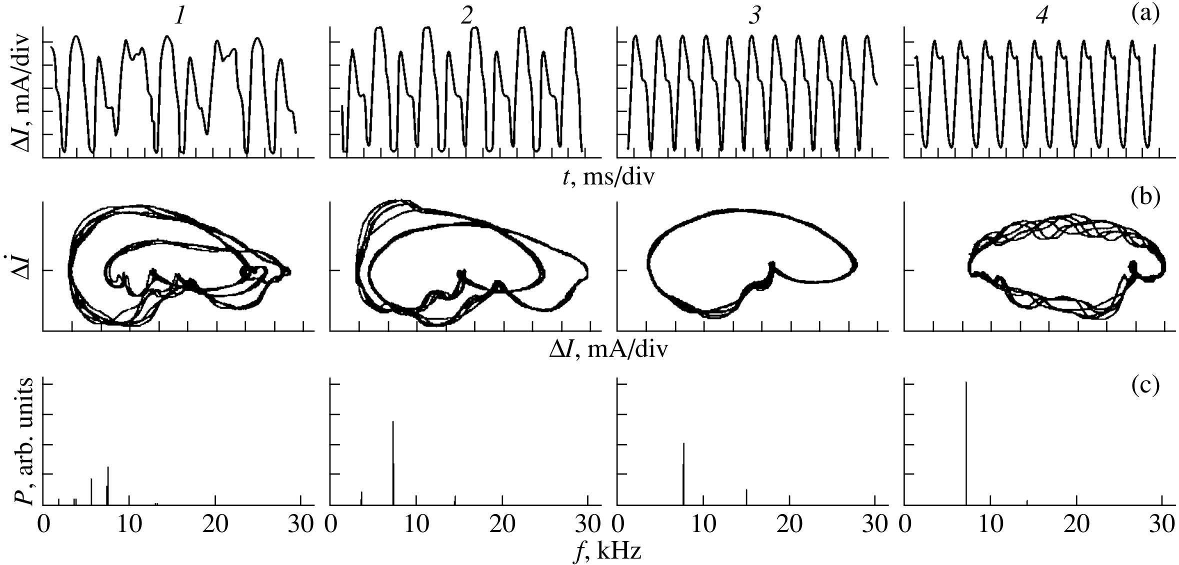

Fig. 3. (a) Oscillograms of the current oscillations in the sample InSb-*d*2, (b) phase portraits, and (c) power spectra. U_a = 56.2–60.0 V.

phase portrait comprises a limiting cycle with a configuration which varies with increasing excitation level of the electron–hole plasma. In the power spectra of oscillations, a single peak is present. With increasing electron–hole plasma excitation, the frequency position of this peak initially shifts to the right, reaches a maximum frequency ($f \approx 8$ kHz), and then shifts to the left down to $f \approx 3$ kHz.

For $\mathcal{L}_c \leq L$, interaction emerges between the autosolitons formed at the inhomogeneity. This may lead to violation of the regularity of the sequence of travelling autosolitons. With increasing excitation level of the electron–hole plasma, the violation of the regularity of the sequence or random sequence of autosolitons travelling in the electron–hole plasma may also self-organize into a regular sequence.

Figure 3 presents the oscillograms of current oscillations in the external circuit of the InSb-*d*2 sample, as well as phase portraits and power spectra with varying the voltage applied to the sample from U_a = 56.2 to 60.0 V.

For the voltage U_a = 56.2 V, variation in the current (oscillogram *1*) in the external circuit of the sample comprises a set of relaxational oscillations. The phase portrait includes a limiting cycle, there are four periods, and the spectral distribution of the power consists of four peaks. With increasing voltage (the excitation level of the electron–hole plasma), the oscillations are ordered, the number of periods of the limiting cycle is retained, and redistribution occurs in the power spectrum. Even for the voltage U_a = 56.8 V, the bifurcations emerge in the current oscillations and manifest themselves in the doubling of the period (oscillogram *3*). In the phase portrait, the limiting cycle and two periods are retained, whereas two peaks are retained in the power spectrum. For the voltage U_a = 59.6 V, the oscillations become regular. The phase portrait is represented by a single period of the limiting cycle, and the power spectrum consists of a single peak. With a further increase in voltage, the peak top bifurcates, which may be indicative of local breakdown due to impact ionization at the autosoliton center [14, 15].

Figure 4 presents the oscillograms of oscillations of the current in the external circuit of the InSb-*b*1-2 sample, phase portraits, and power spectra with varying the voltage applied to the sample from U_a = 28.4 to 28.95 V.

For a voltage U_a = 28.4 V, the oscillations of the current in the external circuit correspond to an irregular sequence of travelling autosolitons (oscillogram *1* in Fig. 4), which have the tendency to divide. The phase portrait contains the limiting cycle, two periods, and a single peak prevails in the power spectrum. For the voltage U_a = 28.5 V (oscillogram *2*), the regularity of oscillations is enhanced, and the tendency of autosolitons to divide is also enhanced. In the next oscillogram *3*, the emergence of three periods of oscillations of the current can be seen. This circumstance is also reflected in the phase portrait and in the power spectrum of oscillations. We may state that the sequential division of autosolitons occurs. For the voltage U_a = 28.9 V, all autosolitons which form the initial sequence divide. The oscillations of the current become regular, the phase portrait consists of a single period of the limiting cycle, and a single peak is present in the power spectrum of oscillations.

The division of autosolitons may be caused by different circumstances. As was already noted, impact ionization is quite possible in InSb [14]. The transverse autosolitons comprise regions depleted of carriers, while, in the electric field, they comprise regions with an increased electric-field strength as well. The condi-

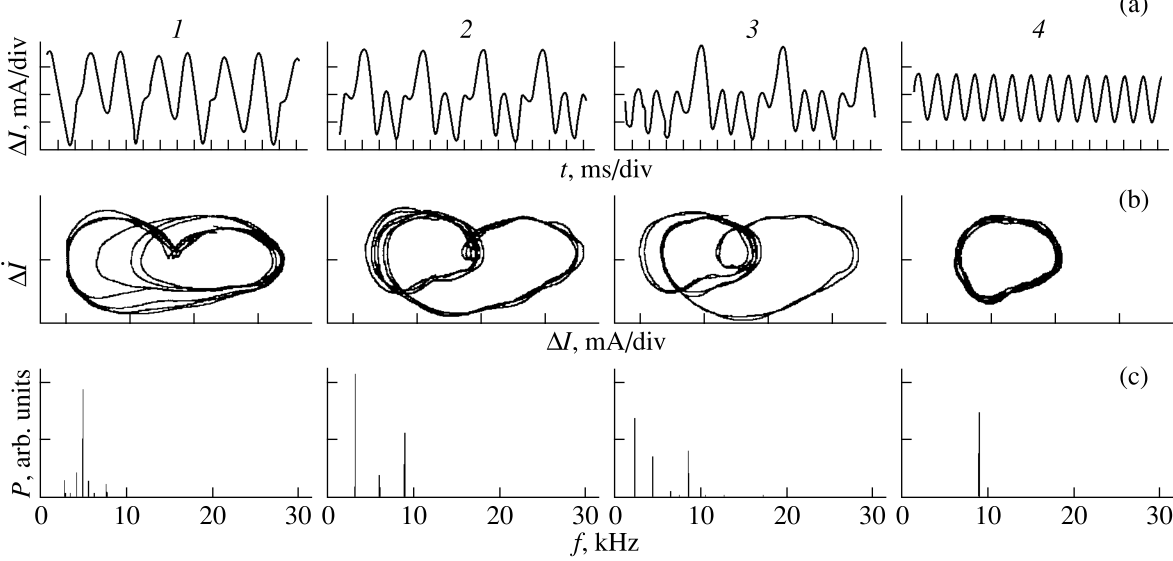

Fig. 4. (a) Oscillograms of the current oscillations in the sample InSb-*b*1-2, (b) phase portraits, and (c) power spectra.

tions for the realization of the impact ionization in the local region of the autosoliton are more than sufficient. When the electric field reaches the magnitude sufficient for impact ionization by in the autosoliton, local breakdown may occur at its center [14, 15], i.e., an avalanche-like increase in the carrier density at the autosoliton center. This will lead to the extension of the autosoliton. With a further increase in the voltage applied to the sample, i.e., an increase in the excitation level of the electron–hole plasma, a broad autosoliton can be more easily divided than restored. The autosolitons do not divide individually, but by constituting a certain collective system of interacting autosolitons, for which the property of self-organization is inherent. Another circumstance which causes the division of the autosoliton is its pulsation with increasing heating level of the electron–hole plasma, which was mentioned above.

An investigation of the behavior of the ensemble of interacting autosolitons in a dissipative structure under the action of an external longitudinal magnetic field H as strong as 13.6×10^3 A/m was carried out (the sample InSb-*b*5-2). As a result, it was found that the effect of the magnetic field within the limits of 0–629 A/m on the behavior of autosolitons for $U_a = U_1 = \text{const} = 35.93$ V is similar to the effect of the electric field within the limits $U_a = 35.93$–39.16 V for $H = 0$. The oscillograms shown in Fig. 5a illustrate the dynamics of variations in the current oscillations in the external circuit as a result of the motion of autosolutions through the sample with increasing electric field. The similar oscillograms in Fig. 5b correspond to $U_1 = \text{const}$ and an external magnetic field in the range from 0 to 629 A/m. It can be seen from Figs. 5a and 5b that the time realization of instabilities, their phase portraits, and the power spectra are identical. With a further increase in the electric field (for $H = 0$), the oscillations vanish. However, with a continuing increase in the magnetic field (for $U_1 = \text{const}$), current instabilities emerge again. These instabilities are indicative of the certain self-organization of travelling autosolitons (Fig. 5c). It can be seen that, in the range of magnetic fields $(3.6–13.1) \times 10^3$ A/m, the oscillations of the current in the sample circuit undergo evolution from regular oscillations through stochastic ones to other regular oscillations, including the bifurcation stage by doubling the period.

The effect of an external magnetic field on the behavior of both separate autosolitons and their ensemble is determined by the decisive contribution of thermomagnetic effects [19, 20]. The longitudinal magnetic field, owing to a large temperature gradient (~10^5 K/cm) in the localized region of the longitudinal autosoliton, induces a considerable transverse potential difference due to the Nernst–Ettingshausen effect. The sign of this difference depends on the direction of the magnetic field. Under the effect of this potential difference, the autosolitons, which travel through the sample, shift to a cold or hot region of the electron–hole plasma, which has a radial temperature gradient. As a result, the variations in the frequency and amplitude of the current oscillations, which are caused by autosolitons travelling through the sample, will be different depending on the direction of the applied magnetic field. As the electric-field strength increases (for $H = 0$), the electron–hole plasma is heated, which is one of the causes of the variations in the oscillation frequency in the external circuit of the sample [12]. Similar behavior of the frequency and amplitude of these oscillations is also observed as the external longitudinal magnetic field increases from zero to small values in one of the directions (at $U_1 = \text{const}$). The external magnetic field does not affect the energy state of the electron–hole plasma. Therefore, the special features of variations in the

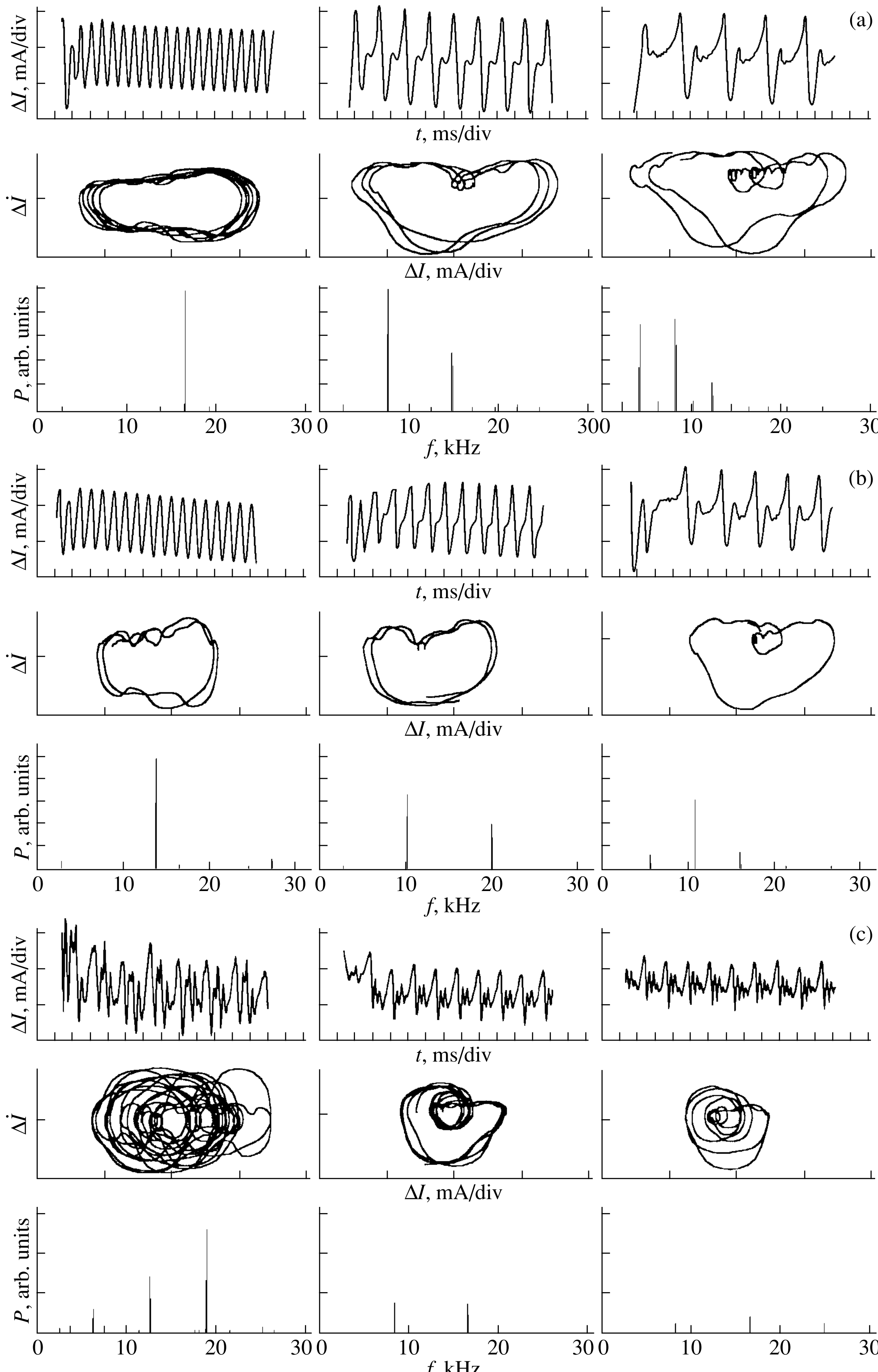

Fig. 5. (a) Oscillograms of the current oscillations in the external circuit of the sample InSb-*b*5-2, phase portraits, and power spectra of these oscillations in the absence of a magnetic field; (b), (c) oscillograms of oscillations of the current, phase portraits, and power spectra of these oscillations in the magnetic field in the ranges of 0–629 A/m and (3.6–13.1) × 10^3 A/m, respectively.

parameters of the current oscillations for stronger external magnetic fields substantially differ from those for increasing the electric field strength (for $H = 0$). This distinction also determines the corresponding behavior of interacting autosolitons excited in the electron–hole plasma.

The investigations of behavior of other modes of current oscillations in the external circuit of the sample 13.6×10^3 A/m, which are caused by autosolitons travelling through the sample, also reveal synergetic behavior of autosolitons in the dissipative structure in InSb.

Thus, it is shown experimentally that the kinetics of formation and the dynamics of the development of autosolitons in the electron–hole plasma correspond to the notions described in theoretical studies. The behavior of autosolitons may be considered as the behavior of an ensemble of interacting autosolitons in a dissipative structure rather than as the behavior of separate objects. Owing to the investigations, the transition from stochastic oscillations to regular ones and from regular oscillations to other regular oscillations is found. The transition passes through the stage of bifurcation, which corresponds to the doubling of the excitation period of the electron–hole plasma. It is also demonstrated that the complete division of stochastic autosolitons occurs via the sequential division of these autosolitons. In the external circuit of the sample, this evolution manifests itself in the emergence of two, three, and four periods of oscillations of the current.

On the basis of the results obtained, we may conclude that a system which consists of an ensemble of interacting autosolitons possesses the property of self-organization.

ACKNOWLEDGMENTS

This study was supported by the Russian Foundation for Basic Research, project no. 01-02-16195.

REFERENCES

1. B. S. Kerner and V. V. Osipov, Zh. Éksp. Teor. Fiz. **71**, 1542 (1976) [Sov. Phys. JETP **44**, 807 (1976)].
2. B. S. Kerner and V. V. Osipov, Pis'ma Zh. Éksp. Teor. Fiz. **41**, 386 (1985) [JETP Lett. **41**, 473 (1985)].
3. B. S. Kerner and V. V. Osipov, Pis'ma Zh. Éksp. Teor. Fiz. **18**, 122 (1973) [JETP Lett. **18**, 70 (1973)].
4. B. S. Kerner and V. V. Osipov, Fiz. Tekh. Poluprovodn. (Leningrad) **13**, 891 (1979) [Sov. Phys. Semicond. **13**, 523 (1979)].
5. B. S. Kerner and V. V. Osipov, Fiz. Tverd. Tela (Leningrad) **21**, 2342 (1979) [Sov. Phys. Solid State **21**, 1348 (1979)].
6. B. S. Kerner and V. V. Osipov, Fiz. Tekh. Poluprovodn. (Leningrad) **13**, 721 (1979) [Sov. Phys. Semicond. **13**, 424 (1979)].
7. A. L. Dubitskiĭ, B. S. Kerner, and V. V. Osipov, Fiz. Tverd. Tela (Leningrad) **28**, 1290 (1986) [Sov. Phys. Solid State **28**, 725 (1986)].
8. B. S. Kerner and V. F. Sinkevich, Pis'ma Zh. Éksp. Teor. Fiz. **36**, 359 (1982) [JETP Lett. **36**, 436 (1982)].
9. B. S. Kerner, V. V. Osipov, M. T. Romanenko, and V. F. Sinkevich, Pis'ma Zh. Éksp. Teor. Fiz. **44** (2), 77 (1986) [JETP Lett. **44**, 97 (1986)].
10. M. N. Vinoslavskiĭ, Fiz. Tverd. Tela (Leningrad) **31** (8), 315 (1989) [Sov. Phys. Solid State **31**, 1461 (1989)].
11. A. A. Stepurenko, Fiz. Tekh. Poluprovodn. (St. Petersburg) **28**, 402 (1994) [Semiconductors **28**, 243 (1994)].
12. I. K. Kamilov and A. A. Stepurenko, Phys. Status Solidi B **194**, 643 (1996).
13. V. V. Gafiĭchuk, B. S. Kerner, V. V. Osipov, and I. V. Tyslyuk, Fiz. Tverd. Tela (Leningrad) **31** (8), 46 (1989) [Sov. Phys. Solid State **31**, 1304 (1989)].
14. A. L. Dubitskiĭ, B. S. Kerner, and V. V. Osipov, Fiz. Tekh. Poluprovodn. (Leningrad) **20**, 1195 (1986) [Sov. Phys. Semicond. **20**, 755 (1986)].
15. A. L. Dubitskiĭ, B. S. Kerner, and V. V. Osipov, Fiz. Tverd. Tela (Leningrad) **28**, 1290 (1986) [Sov. Phys. Solid State **28**, 725 (1986)].
16. V. V. Gafiĭchuk, B. S. Kerner, V. V. Osipov, and A. G. Yuzhanin, Fiz. Tekh. Poluprovodn. (Leningrad) **22**, 2051 (1989) [Sov. Phys. Semicond. **22**, 1298 (1989)].
17. V. V. Gafiĭchuk, B. S. Kerner, V. V. Osipov, and T. M. Shcherbachenko, Fiz. Tekh. Poluprovodn. (Leningrad) **25**, 1696 (1991) [Sov. Phys. Semicond. **25**, 1020 (1991)].
18. C. Hilsum and A. C. Rose-Innes, *Semiconducting III–V Compounds* (Pergamon Press, Oxford, 1961; Inostrannaya Literatura, Moscow, 1963), p. 323.
19. I. K. Kamilov, A. A. Stepurenko, and A. S. Kovalev, J. Phys.: Condens. Matter **10**, 9477 (1998).
20. I. K. Kamilov, A. A. Stepurenko, and A. S. Kovalev, Fiz. Tekh. Poluprovodn. (St. Petersburg) **34**, 433 (2000) [Semiconductors **34**, 418 (2000)].

Translated by N. Korovin

Semiconductors, Vol. 37, No. 9, 2003, pp. 1070–1075. Translated from Fizika i Tekhnika Poluprovodnikov, Vol. 37, No. 9, 2003, pp. 1094–1099.
Original Russian Text Copyright © 2003 by Balagurov.

On the Nernst Coefficient of Binary Composites in a Weak Magnetic Field

B. Ya. Balagurov

Emanuel Institute of Biochemical Physics, Russian Academy of Sciences, ul. Kosygina 4, Moscow, 119991 Russia

e-mail: balagurov@deom.chph.ras.r

Submitted December 9, 2002; accepted for publication December 30, 2002

Abstract—Thermogalvanomagnetic properties of two-component isotropic composites are considered in the linear (in the magnetic field **H** and thermoelectric power α) approximation. It is shown that the effective Nernst coefficient contains the three-parameter function Φ, which can be expressed in terms of the electric field and the temperature gradient in a medium at $\mathbf{H} = 0$ and $\alpha = 0$. This allows estimation of Φ by numerical methods.
© 2003 MAIK "Nauka/Interperiodica".

1. INTRODUCTION

In the theory of steady-state transport phenomena in inhomogeneous media, it seems that the problem of thermogalvanomagnetic properties of these systems is the most general. It is obvious that this problem is also the most complex, since its solution causes even more intricate problems than in the consideration of the thermoelectric or galvanomagnetic properties of inhomogeneous media. Nevertheless, in the case of two-dimensional isotropic two-component systems, a complete solution to this problem can be found using symmetry transformations (see [1]). The isomorphism relations obtained in [1] make it possible to express the effective thermogalvanomagnetic characteristics of such systems in terms of the properties of components and the dimensionless effective conductivity f determined without a magnetic field and disregarding the thermoelectric effects.

The field and current transformation used in [1] is valid only for two-dimensional systems and is not extended to three-dimensional ($D = 3$) ones. There is no sufficiently general symmetry transformation in the latter case, which does not allow application of the approach [1] and makes doubtful the possibility of solving this problem by alternative methods without simplifying assumptions. Certain simplifications can arise when imposing some restrictions on the properties of components (see Section 3). The problem also becomes much easier under the conditions of a weak magnetic field **H** and thermoelectric coupling (i.e., a low thermoelectric coefficient α), which often take place in actual experiments.

In this paper, we consider the thermogalvanomagnetic properties of isotropic two-component media in the approximation which is linear in the magnetic field **H** and the thermoelectric coefficient α. A phenomenological approach based on consequences from certain partial symmetry transformations was used to determine the Hall component structure in the effective tensor of the thermoelectric power. It is shown that the effective Nernst coefficient includes a three-parameter function Φ which is theoretically noncalculable. A solution of the dc equations by expansion in powers of **H** and α allowed us to express Φ in terms of the electric field and the temperature gradient in a medium at $\mathbf{H} = 0$ and $\alpha = 0$. (We note that some of these results are presented in the brief report [2] without derivation.) It was indicated that the numerical tabulation of the dimensionless conductivity b and the function Φ using the approximation linear in **H** and α would yield a description of all basic electrical characteristics of isotropic binary composites.

2. PRELIMINARIES

Let us first discuss the formulation of the problem and introduce necessary notation. To calculate the effective thermogalvanomagnetic characteristics of an inhomogeneous medium, we should solve the set of dc equations (see [3])

$$\operatorname{div}\mathbf{j} = 0. \quad \operatorname{curl}\mathbf{E} = 0; \quad \operatorname{div}\mathbf{q} = 0, \quad \operatorname{curl}\mathbf{G} = 0; \quad \mathbf{G} = -\nabla T, \tag{1}$$

where **E** is the electric-field strength, **j** is the electric current density, $T = T(\mathbf{r})$ is the temperature of the medium at the point **r**, and **q** is the heat flux density divided by the average sample temperature (see [1]). In the problem which is linear in **E** and **G**, the constitutive equations are written as

$$\mathbf{j} = \hat{\boldsymbol{\sigma}}(\mathbf{r})\mathbf{E} + \hat{\gamma}(\mathbf{r})\mathbf{G}, \quad \mathbf{q} = \hat{\gamma}(\mathbf{r})\mathbf{E} + \hat{\chi}(\mathbf{r})\mathbf{G}; \quad \hat{\gamma} = \hat{\sigma}\hat{\alpha}, \quad \hat{\chi} = \bar{T}^{-1}\hat{\kappa} + \hat{\sigma}\hat{\alpha}^2, \tag{2}$$

where $\hat{\sigma}(\mathbf{r})$, $\hat{\kappa}(\mathbf{r})$, and $\hat{\alpha}(\mathbf{r})$ are the tensors of the conductivity, heat conductivity, and thermoelectric power of the medium, and $\bar{T}$ is the average sample temperature.

1063-7826/03/3709-1070$24.00 © 2003 MAIK "Nauka/Interperiodica"

The effective characteristics of a medium are defined in the conventional way,

$$\langle \mathbf{j} \rangle = \hat{\sigma}_e \langle \mathbf{E} \rangle + \hat{\gamma}_e \langle \mathbf{G} \rangle, \quad \langle \mathbf{q} \rangle = \hat{\gamma}_e \langle \mathbf{E} \rangle + \hat{\chi}_e \langle \mathbf{G} \rangle;$$
$$\hat{\gamma}_e = \hat{\sigma}_e \hat{\alpha}_e, \quad \hat{\chi}_e = \bar{T}^{-1} \hat{\kappa}_e + \hat{\sigma}_e \hat{\alpha}_e^2, \tag{3}$$

where $\langle \ldots \rangle$ means averaging over the sample volume V,

$$\langle (\ldots) \rangle = \frac{1}{V} \int_V (\ldots) d\mathbf{r} \tag{4}$$

at $V \longrightarrow \infty$.

For an isotropic system in a magnetic field $\mathbf{H}$, the conductivity tensor $\hat{\sigma}$ is given by

$$\hat{\sigma} = \begin{pmatrix} \sigma_x & \sigma_a & 0 \\ -\sigma_a & \sigma_x & 0 \\ 0 & 0 & \sigma_z \end{pmatrix}, \tag{5}$$

where it is assumed that $\mathbf{H}$ is directed along the z axis. To simplify the subsequent formulas, the designations $\sigma_x = \sigma_{xx} = \sigma_{yy}$, $\sigma_z = \sigma_{zz}$, and $\sigma_a = \sigma_{xy} = -\sigma_{yx}$ are introduced into (5), respectively, for the lateral, longitudinal, and Hall components of the conductivity tensor. The tensors $\hat{\kappa}$, $\hat{\alpha}$, hence, the tensors $\hat{\gamma}$, $\hat{\chi}$ have a form similar to expression (5). In the case of a two-component medium, the tensors $\hat{\sigma}(\mathbf{r})$, $\kappa(\mathbf{r})$, and $\alpha(\mathbf{r})$ assume the constant values $\hat{\sigma}_1$, $\hat{\kappa}_1$, $\hat{\alpha}_1$, and $\hat{\sigma}_2$, $\hat{\kappa}_2$, $\hat{\alpha}_2$ in the first and second components, respectively.

Thus, in the theory of thermogalvanomagnetic properties of three-dimensional isotropic two-component media, it is necessary to determine nine effective characteristics: σ_{xe}, σ_{ze}, σ_{ae}, κ_{xe}, κ_{ze}, κ_{ae}, α_{xe}, α_{ze}, α_{ae}. Each is a multiparameter function depending on the concentration p and the quantities $\hat{\sigma}_1$, $\hat{\sigma}_2$, $\hat{\kappa}_1$, $\hat{\kappa}_2$, $\hat{\alpha}_1$, $\hat{\alpha}_2$, i.e., at least on 19 arguments. In such a general formulation, the problem is extraordinarily complex and its solution is hardly possible without simplifying assumptions. In this paper, we consider the case of $\mathbf{H} \longrightarrow 0$, when the Hall components σ_{ai}, κ_{ai}, and α_{ai} are small. It is also assumed that the thermoelectric effects are weak, which formally corresponds to $\hat{\alpha}_i \longrightarrow 0$ (or $\hat{\gamma} \longrightarrow 0$).

In a weak magnetic field ($\mathbf{H} \longrightarrow 0$), the parameter σ_a is linear in $\mathbf{H}$, while the corrections to σ_x and σ_z are quadratic. Therefore, in the approximation linear in $\mathbf{H}$ (to which we hereafter restrict the analysis), it should be assumed that $\sigma_x = \sigma_z = \sigma$, where σ is the scalar conductivity of a medium at $\mathbf{H} = 0$. In a similar way, at $\mathbf{H} \longrightarrow 0$, the parameters κ_a, α_a (hence, χ_a, γ_a) are linear in $\mathbf{H}$, and $\kappa_x = \kappa_z = \kappa$, $\alpha_x = \alpha_z = \alpha$ in the same approximation. In the absence of thermoelectric effects ($\hat{\alpha} = 0$, $\hat{\gamma} = 0$), the system conductivity at $\mathbf{H} = 0$ can be written as

$$\sigma_e = \sigma_1 f(p, \sigma_2/\sigma_1), \tag{6}$$

where f is the dimensionless effective conductivity of a medium, and p is the concentration (an occupied volume fraction) of the first component. For the effective Hall component σ_{ae} at $\mathbf{H} \longrightarrow 0$, we have (see [4, 5])

$$\sigma_{ae} = \sigma_{a2} + (\sigma_{a1} - \sigma_{a2})\varphi_\sigma; \quad \varphi_\sigma = \varphi(p, \sigma_2/\sigma_1), \tag{7}$$

where φ is a two-parameter function depending on the medium's properties at $\mathbf{H} = 0$ (see [4, 5]). The heat-conductivity problem (at $\hat{\alpha} = 0$) differs from the electrical-conductivity problem only in the notation, so that

$$\kappa_e = \kappa_1 f(p, \kappa_2/\kappa_1); \tag{8}$$

$$\kappa_{ae} = \kappa_{a2} + (\kappa_{a1} - \kappa_{a2})\varphi_\kappa; \quad \varphi_\kappa = \varphi(p, \kappa_2/\kappa_1), \tag{9}$$

where the functions f and φ are the same as in relations (6) and (7).

Before proceeding to the determination of the tensor $\hat{\alpha}_e$ (or $\hat{\gamma}_e$), we consider the consequences of the invariance of Eqs. (1) and (2) under some partial transformations of fields and currents.

3. SYMMETRY TRANSFORMATIONS

3.1. It is easy to verify that Eqs. (1) retain their form under a symmetry transformation which generalizes all the factors considered in [5, 6]:

$$\mathbf{E} = \mathbf{E}', \quad \mathbf{j} = \mathbf{j}' + \hat{A}_a \mathbf{E}' + \hat{B}_a \mathbf{G}';$$
$$\mathbf{G} = \mathbf{G}', \quad \mathbf{q} = \mathbf{q}' + \hat{C}_a \mathbf{E}' + \hat{D}_a \mathbf{G}', \tag{10}$$

where $\hat{A}_a$, $\hat{B}_a$, $\hat{C}_a$, and $\hat{D}_a$ are the antisymmetric tensors which are independent of coordinates: $A_a^{\alpha\beta} = -A_a^{\beta\alpha}$, etc. For a "primed" system, the constitutive equations retain (at $\hat{B}_a = \hat{C}_a$) form (2), where

$$\hat{\sigma}'(\mathbf{r}) = \hat{\sigma}(\mathbf{r}) - \hat{A}_a, \quad \hat{\gamma}'(\mathbf{r}) = \hat{\gamma}(\mathbf{r}) - \hat{B}_a,$$
$$\hat{\chi}'(\mathbf{r}) = \hat{\chi}(\mathbf{r}) - \hat{D}_a. \tag{11}$$

Similar relations are also valid for the effective characteristics of the initial ($\hat{\sigma}_e$, $\hat{\gamma}_e$, $\hat{\chi}_e$) and primed ($\hat{\sigma}'_e$, $\hat{\gamma}'_e$, $\hat{\chi}'_e$) systems,

$$\hat{\sigma}_e = \hat{\sigma}'_e + \hat{A}_a, \quad \hat{\gamma}_e = \hat{\gamma}'_e + \hat{B}_a, \quad \hat{\chi}_e = \hat{\chi}'_e + \hat{D}_a. \tag{12}$$

We now consider a two-component medium, setting $\hat{A}_a = \hat{\sigma}_{a2}$, $\hat{B}_a = \hat{\gamma}_{a2}$, and $\hat{D}_a = \hat{\chi}_{a2}$, where $\hat{\sigma}_{a2}$, $\hat{\gamma}_{a2}$, and $\hat{\chi}_{a2}$ are the antisymmetric components of the tensors $\hat{\sigma}_2$, $\hat{\gamma}_2$, and $\hat{\chi}_2$. Then, in a primed system, the Hall components with subscripts 2 and 1 are written as

$\sigma'_{a2} = 0$, $\gamma'_{a2} = 0$, $\chi'_{a2} = 0$ and $\sigma'_{a1} = \sigma_{a1} - \sigma_{a2}$, $\gamma'_{a1} = \gamma_{a1} - \gamma_{a2}$, $\chi'_{a1} = \chi_{a1} - \chi_{a2}$. Thus, the parameters $\hat{\sigma}'_e$, $\hat{\gamma}'_e$, and $\hat{\chi}'_e$ depend on the Hall components only as the differences $\sigma_{a1} - \sigma_{a2}$, $\gamma_{a1} - \gamma_{a2}$, and $\chi_{a1} - \chi_{a2}$. According to relations (12), this means that the quantities σ_{xe}, σ_{ze}, $\sigma_{ae} - \sigma_{a2}$, γ_{xe}, γ_{ze}, $\gamma_{ae} - \gamma_{a2}$, χ_{xe}, χ_{ze}, $\chi_{ae} - \chi_{a2}$ in the initial system also depend only on $\sigma_{a1} - \sigma_{a2}$, $\gamma_{a1} - \gamma_{a2}$, and $\chi_{a1} - \chi_{a2}$. We note that expressions (7) and (9) satisfy these conditions.

3.2. Let us show that the problem of thermogalvanomagnetic properties can be solved in two particular cases by reducing it to the problem of the conductivity and heat conductivity calculated disregarding the thermoelectric effects.

Let the tensor $\hat{\gamma}$ be given by

$$\hat{\gamma}(\mathbf{r}) = \alpha\hat{\sigma}(\mathbf{r}), \quad (13)$$

where α is independent of coordinates. Using the transformations (cf. [6, 7])

$$\begin{gathered} \mathbf{j} = \mathbf{j}'', \quad \mathbf{E} + \alpha\mathbf{G} = \mathbf{E}'', \\ \mathbf{q} = \alpha\mathbf{j}'' + \bar{T}^{-1}\mathbf{q}'', \quad \mathbf{G} = \mathbf{G}'', \end{gathered} \quad (14)$$

we reduce the initial problem to two independent problems

$$\begin{gathered} \operatorname{div}\mathbf{j}'' = 0, \quad \operatorname{curl}\mathbf{E}'' = 0, \quad \mathbf{j}'' = \hat{\sigma}(\mathbf{r})\mathbf{E}'', \\ \langle\mathbf{j}''\rangle = \hat{\sigma}_e\langle\mathbf{E}''\rangle; \\ \operatorname{div}\mathbf{q}'' = 0, \quad \operatorname{curl}\mathbf{G}'' = 0, \quad \mathbf{q}'' = \hat{\kappa}(\mathbf{r})\mathbf{G}'', \\ \langle\mathbf{q}''\rangle = \hat{\kappa}_e\langle\mathbf{G}''\rangle, \end{gathered} \quad (15)$$

from which it follows that the effective tensors of electrical conductivity $\hat{\sigma}_e$ and heat conductivity $\hat{\kappa}_e$ have the same form as at $\hat{\alpha} = 0$. Substituting the expressions for $\mathbf{j}''$ and $\mathbf{E}''$ from relations (14) into $\langle\mathbf{j}''\rangle = \hat{\sigma}_e\langle\mathbf{E}''\rangle$, we obtain $\langle\mathbf{j}\rangle = \hat{\sigma}_e\langle\mathbf{E}\rangle + \alpha\hat{\sigma}_e\langle\mathbf{G}\rangle$, from which

$$\hat{\gamma}_e = \alpha\hat{\sigma}_e. \quad (16)$$

Averaging of the heat-flux density $\mathbf{q} = \alpha\mathbf{j}'' + \bar{T}^{-1}\mathbf{q}''$ also yields the same result. We note that from relation (16) it follows that

$$\hat{\alpha}_e = \alpha\hat{1}, \quad \hat{1} = \begin{pmatrix} 1 & 0 \\ 0 & 1 \end{pmatrix}.$$

Now we consider the case when the tensor $\hat{\gamma}$ is proportional to the tensor $\hat{\chi}$,

$$\hat{\gamma}(\mathbf{r}) = \beta\hat{\chi}(\mathbf{r}), \quad (17)$$

where β is independent of coordinates. Using the transformations

$$\begin{gathered} \mathbf{j} = \mathbf{j}''' + \beta\mathbf{q}''', \quad \mathbf{E} = \mathbf{E}'''; \quad \mathbf{q} = \mathbf{q}''', \\ \mathbf{G} + \beta\mathbf{E} = \mathbf{G}''' \end{gathered} \quad (18)$$

we again reduce the problem to two independent problems,

$$\operatorname{div}\mathbf{j}''' = 0, \quad \operatorname{curl}\mathbf{E}''' = 0, \quad \mathbf{j}''' = \hat{\sigma}'''(\mathbf{r})\mathbf{E}''',$$

$$\hat{\sigma}'''(\mathbf{r}) = \hat{\sigma}(\mathbf{r}) - \beta^2\hat{\chi}(\mathbf{r}), \quad \langle\mathbf{j}'''\rangle = \hat{\sigma}'''_e\langle\mathbf{E}'''\rangle; \quad (19)$$

$$\operatorname{div}\mathbf{q}''' = 0, \ \operatorname{curl}\mathbf{G}''' = 0, \ \mathbf{q}''' = \hat{\chi}(\mathbf{r})\mathbf{G}''', \ \langle\mathbf{q}'''\rangle = \hat{\chi}_e\langle\mathbf{G}'''\rangle.$$

The substitution of the expressions for $\mathbf{q}'''$ and $\mathbf{G}'''$ from relation (18) into $\langle\mathbf{q}'''\rangle = \hat{\chi}_e\langle\mathbf{G}'''\rangle$ yields $\langle\mathbf{q}\rangle = \beta\hat{\chi}_e\langle\mathbf{E}\rangle + \hat{\chi}_e\langle\mathbf{G}\rangle$, from which

$$\hat{\gamma}_e = \beta\hat{\chi}_e. \quad (20)$$

According to relations (19), the quantity $\hat{\chi}_e$ can be obtained from the heat conductivity tensor $\hat{\kappa}_e$ calculated disregarding the thermoelectric effects, using the replacements $\kappa_1 \longrightarrow \chi_1$ and $\kappa_2 \longrightarrow \chi_2$. The conductivity tensor $\hat{\sigma}_e$ is determined using the relation $\hat{\sigma}_e = \hat{\sigma}'''_e + \beta^2\hat{\chi}_e$.

Notwithstanding the comparative simplicity, results (16) and (20) play an important role in the phenomenological analysis (see Section 4).

4. PHENOMENOLOGICAL CONSIDERATION

As shown in [5], in the problem of galvanomagnetic properties of two-component media, the structure of the effective conductivity tensor (at $\mathbf{H} \longrightarrow 0$) can be determined from symmetry considerations. Such a phenomenological approach is found to be also useful in the study of thermogalvanomagnetic properties of inhomogeneous media. First, we consider the thermoelectric power α_e at $\mathbf{H} = 0$.

4.1. In the case of isotropic two-component systems, the parameter α_e in the approximation linear in α should have the form

$$\alpha_e = \alpha_1\Psi_1 + \alpha_2\Psi_2, \quad (21)$$

where the coefficients Ψ_1 and Ψ_2 depend only on the properties of the medium at $\alpha = 0$; i.e., they are three-parameter functions: $\Psi_i = \Psi_i(p; \sigma_2/\sigma_1, \kappa_2/\kappa_1)$.

Expression (21) is valid at any α_1 and α_2; therefore, it should satisfy the conditions imposed on α_e by relations (16) and (20) (with the proper choice of α_1 and α_2). Setting $\alpha_1 = \alpha_2 = \alpha$, we conclude that relation (21) transforms into $\alpha_e = \alpha$ if $\Psi_1 + \Psi_2 = 1$. Therefore, denoting Ψ_2 by Ψ, relation (21) yields

$$\alpha_e = \alpha_1 - (\alpha_1 - \alpha_2)\Psi. \quad (22)$$

In the approximation linear in α, it follows from relations (17) and (20) that expression (22) should transform into $\alpha_e = (\kappa_e/\sigma_e)\beta\bar{T}^{-1}$ at $\alpha_i = (\kappa_i/\sigma_i)\beta\bar{T}^{-1}$ (where $i = 1, 2$). From this condition, we define the function Ψ as

$$\Psi = \left(\frac{\kappa_1}{\sigma_1} - \frac{\kappa_e}{\sigma_e}\right)\Big/\left(\frac{\kappa_1}{\sigma_1} - \frac{\kappa_2}{\sigma_2}\right). \quad (23)$$

The substitution of expression (23) into (22) yields the final form

$$\alpha_e = \alpha_1 + \frac{\sigma_1\sigma_2(\alpha_1 - \alpha_2)}{\sigma_1\kappa_2 - \sigma_2\kappa_1}\left(\frac{\kappa_1}{\sigma_1} - \frac{\kappa_e}{\sigma_e}\right). \quad (24)$$

Expression (24) coincides with the exact result obtained by an alternative method in [6] (see also [8]). In expressions (23) and (24), σ_e and κ_e are the effective electrical and heat conductivities, calculated disregarding the thermoelectric effects, so that these conductivities are given by formulas (6) and (8). We note an important detail: the three-parameter function $\Psi(p; \sigma_2/\sigma_1, \kappa_2/\kappa_1)$ is reduced to the two-parameter functions $f(p, \sigma_2/\sigma_1)$ and $f(p, \kappa_2/\kappa_1)$ using relation (23). It is this circumstance that makes it possible to develop a consistent theory of the critical dynamics of the thermoelectric power (see [6, 9]).

4.2. We now consider the Hall component of the tensor $\hat{\gamma}_e$. In the approximation linear in $\mathbf{H}$ and $\hat{\gamma}$ (i.e., $\hat{\alpha}$), the parameter γ_{ae} should have the form

$$\gamma_{ae} = \gamma_{a2} + (\gamma_{a1} - \gamma_{a2})\Psi + (\sigma_{a1} - \sigma_{a2})(\gamma_1\Phi_1 + \gamma_2\Phi_2) + (\kappa_{a1} - \kappa_{a2})(\gamma_1\Phi_3 + \gamma_2\Phi_4). \quad (25)$$

Here, the dependence of γ_{ae} on γ_{ai}, σ_{ai}, and κ_{ai} is written according to the requirements following from symmetry transformation (10). The coefficients Φ, Φ_1, Φ_2, Φ_3, and Φ_4 depend only on the medium's properties at $\mathbf{H} = 0$ and $\alpha = 0$; i.e., the are three-parameter functions: $\Phi = \Phi(p; \sigma_2/\sigma_1, \kappa_2/\kappa_1)$, etc.

According to expressions (13) and (16), expression (25) should transform into $\gamma_{ae} = \alpha\sigma_{ae}$ at $\gamma_i = \alpha\sigma_i$ and $\gamma_{ai} = \alpha\sigma_{ai}$. From this condition, taking into account expressions (7), we have

$$\Phi + \sigma_1\Phi_1 + \sigma_2\Phi_2 = \varphi_\sigma, \quad \sigma_1\Phi_3 + \sigma_2\Phi_4 = 0. \quad (26)$$

Then, it follows from relations (17) and (20) that γ_{ae} should have the form $\gamma_{ae} = \beta\kappa_{ae}/\bar{T}$ at $\gamma_i = \beta\kappa_i/\bar{T}$ and $\gamma_{ai} = \beta\kappa_{ai}/\bar{T}$. In this case, expressions (25) and (9) yield

$$\kappa_1\Phi_1 + \kappa_2\Phi_2 = 0, \quad \Phi + \kappa_1\Phi_3 + \kappa_2\Phi_4 = \varphi_\kappa. \quad (27)$$

Determining functions Φ_1, Φ_2, Φ_3, and Φ_4 from relations (26) and (27), we finally obtain

$$\gamma_{ae} = \gamma_{a2} + (\gamma_{a1} - \gamma_{a2})\Phi - (\sigma_{a1} - \sigma_{a2})\frac{\gamma_1\kappa_2 - \gamma_2\kappa_1}{\sigma_1\kappa_2 - \sigma_2\kappa_1}(\Phi - \varphi_\sigma) + (\kappa_{a1} - \kappa_{a2})\frac{\gamma_1\sigma_2 - \gamma_2\sigma_1}{\sigma_1\kappa_2 - \sigma_2\kappa_1}(\Phi - \varphi_\kappa), \quad (28)$$

where the quantities φ_σ and φ_κ are defined according to expressions (7) and (9) and are considered as known (the basic properties of the function $\varphi(p, h)$ are considered in [5]). The effective Nernst coefficient N_e is expressed in terms of γ_{ae} from relation (28) as

$$N_e = -\frac{1}{H}\frac{\gamma_{ae}}{\sigma_e}. \quad (29)$$

We note that result (28) is given in [2] without derivation.

Thus, the phenomenological approach allows determination of the general form of the quantity γ_{ae} (in the approximation linear in $\mathbf{H}$ and α) within a new unknown function Φ. In expression (28), the dependence γ_{ae} is separated in explicit form from all the thermogalvanomagnetic characteristics of the components. The dependence of γ_{ae} on the main parameters p, σ_2/σ_1, and κ_2/κ_1 is contained in the functions φ_σ and φ_κ. Unfortunately, it is impossible to reduce the three-parameter function Φ to two-parameter ones in the general case. Currently, this circumstance does not allow a consistent description of the critical behavior of γ_{ae} at any values of the parameters involved in the problem. It is required to apply numerical methods to preliminarily study the function $\Phi(p; \sigma_2/\sigma_1, \kappa_2/\kappa_1)$ and to elucidate its critical behavior, which can be rather complex (cf. the thermoelectric power [6, 9]). However, the mentioned reduction of the function Φ and, hence, the consistent description of the critical behavior of γ_{ae}, can be carried out in two extreme cases (see Section 5).

5. BASIC PROPERTIES OF THE FUNCTION Φ

The value of γ_{ae} can also be determined ab initio, i.e., by direct solution of Eqs. (1) and (2). In this case, solutions to the common problems of electrical and heat conductivities of a medium at $\mathbf{H} = 0$ and $\alpha = 0$ are considered to be known. The effective thermogalvanomagnetic characteristics of the system are sought using the perturbation theory by a power expansion in $\mathbf{H}$ and α. Previously, a similar method was applied to consider galvanomagnetic [5] and thermoelectric [10] properties of inhomogeneous media.

Let us introduce the notation $\mathbf{E}^{(\nu)}(\mathbf{r})$, $\mathbf{G}^{(\nu)}(\mathbf{r})$ and $\mathbf{j}^{(\nu)}(\mathbf{r})$, $\mathbf{q}^{(\nu)}(\mathbf{r})$ for the fields and the current densities in the medium, determined with the given $\langle\mathbf{E}^{(\nu)}\rangle$ and $\langle\mathbf{G}^{(\nu)}\rangle$, where the superscript ν indicates that the average field is directed along the ν axis. For these quantities, a

number of identities valid at $V \longrightarrow \infty$ (cf. [5, 10]) can be proven,

$$\langle \mathbf{E}^{(\mu)}\mathbf{j}^{(\nu)}\rangle = \langle \mathbf{E}^{(\mu)}\rangle\langle \mathbf{j}^{(\nu)}\rangle, \quad \langle \mathbf{G}^{(\mu)}\mathbf{q}^{(\nu)}\rangle = \langle \mathbf{G}^{(\mu)}\rangle\langle \mathbf{q}^{(\nu)}\rangle;$$
$$\langle [\mathbf{E}^{(\mu)}, \mathbf{G}^{(\nu)}]\rangle = [\langle \mathbf{E}^{(\mu)}\rangle, \langle \mathbf{G}^{(\nu)}\rangle]. \tag{30}$$

The square brackets signify the vector product.

According to formula (28), it is sufficient to consider the case of $\sigma_{ai} = 0$ and $\kappa_{ai} = 0$ to determine the unknown function Φ. Let us take advantage of this circumstance to simplify the problem. In the approximation linear in $\mathbf{H}$ and α, using the method of [5, 10], from identity (30) we obtain expression (28) for γ_{ae} (with $\sigma_{ai} = 0$ and $\kappa_{ai} = 0$) with

$$\Phi = \langle [\mathbf{E}_0^{(\mu)}, \mathbf{G}_0^{(\nu)}]_z - [\mathbf{E}_0^{(\nu)}, \mathbf{G}_0^{(\mu)}]\rangle^{(1)}$$
$$\times \{[\langle \mathbf{E}_0^{(\mu)}\rangle, \langle \mathbf{G}_0^{(\nu)}\rangle]_z - [\langle \mathbf{E}_0^{(\nu)}\rangle, \langle \mathbf{G}_0^{(\mu)}\rangle]_z\}^{-1} (\nu \neq \mu). \tag{31}$$

The subscript z at the square brackets signifies that the z component of the vector product is considered. In expression (31), $\mathbf{H}$ and α in the parameters $\mathbf{E}_0(\mathbf{r})$ and $\mathbf{G}_0(\mathbf{r})$ should be set equal to zero. Integration in

$$\langle (\ldots)\rangle^{(1)} = \frac{1}{V}\int_{V_1} (\ldots) d\mathbf{r}$$

is carried out over the volume of the first component.

Thus, formula (31) yields the expression for the function Φ in terms of the field strengths $\mathbf{E}_0(\mathbf{r})$ and $\mathbf{G}_0(\mathbf{r})$ determined at $\mathbf{H} = 0$ and $\alpha = 0$, i.e., via solutions of standard problems on the electrical and heat conductivities. In the numerical study of the function Φ, it is convenient to direct the μ and ν axes along x and y, respectively. In this case, formula (31) is identical to the expression for Φ given in [2]. We note that the replacement $\sigma_i \rightleftarrows \kappa_i$ is equivalent to the permutation $\mathbf{E}_0(\mathbf{r}) \rightleftarrows \mathbf{G}_0(\mathbf{r})$; hence, it follows from formula (31) that

$$\Phi(p; \sigma_2/\sigma_1, \kappa_2/\kappa_1) = \Phi(p; \kappa_2/\kappa_1, \sigma_2/\sigma_1). \tag{32}$$

According to [5], the functions φ_σ and φ_κ are given by

$$\varphi_\sigma = \frac{\langle [\mathbf{E}_0^{(\mu)}, \mathbf{E}_0^{(\nu)}]_z\rangle^{(1)}}{[\langle \mathbf{E}_0^{(\mu)}\rangle, \langle \mathbf{E}_0^{(\nu)}\rangle]_z}, \quad \varphi_\kappa = \frac{\langle [\mathbf{G}_0^{(\mu)}, \mathbf{G}_0^{(\nu)}]_z\rangle^{(1)}}{[\langle \mathbf{G}_0^{(\mu)}\rangle, \langle \mathbf{G}_0^{(\nu)}\rangle]_z}, \tag{33}$$

where $\langle(\ldots)\rangle^{(1)}$ is the same as in expression (31). A comparison of formulas (33) and (31) shows that

$$\varphi_\sigma = \Phi(p; \sigma_2/\sigma_1, \sigma_2/\sigma_1),$$
$$\varphi_\kappa = \Phi(p; \kappa_2/\kappa_1, \kappa_2/\kappa_1); \tag{34}$$

i.e., φ_σ and φ_κ are two limiting values of the function $\Phi(p; \sigma_2/\sigma_1, \kappa_2/\kappa_1)$.

When $\kappa_1 = \kappa_2$, $\mathbf{G}_0^{(\nu)}(\mathbf{r})$ is independent of the coordinates and equal to $\langle \mathbf{G}_0^{(\nu)}\rangle$. Since (see, e.g., [5])

$$\langle \mathbf{E}_0^{(\nu)}\rangle^{(1)} = \frac{\sigma_e - \sigma_2}{\sigma_1 - \sigma_2}\langle \mathbf{E}_0^{(\nu)}\rangle$$

at $\kappa_1 = \kappa_2$, we find from expression (31) that

$$\Phi(p; h, 1) = \frac{f-h}{1-h}, \quad h = \frac{\sigma_2}{\sigma_1}. \tag{35}$$

In this case, similarly to [5], a consistent theory of the critical behavior of γ_{ae}, hence, of the effective Nernst coefficient N_e, can be developed.

When the Viedemann–Franz law

$$\frac{\kappa_1}{\sigma_1} = \frac{\kappa_2}{\sigma_2}$$

is satisfied, expression (28) contains mathematical indeterminacies such as zero divided by zero by virtue of relations (34). To evaluate these indeterminate forms, we note that at $\delta h \longrightarrow 0$ it follows from definitions (31) and (33) that

$$\Phi(p; h, h+\delta h) - \varphi(p, h) = \frac{1}{2}\frac{\partial \varphi}{\partial h}\delta h. \tag{36}$$

Therefore, having set $\kappa_2/\kappa_1 = h + \delta h$ (where $h = \sigma_2/\sigma_1$), from expression (28) in the limit $\delta h \longrightarrow 0$, we obtain

$$\gamma_{ae} = \gamma_{a2} + (\gamma_{a1} - \gamma_{a2})\varphi(p, h)$$
$$-\frac{1}{2}\sigma_2(\alpha_1 - \alpha_2)\left(\frac{\sigma_{a1} - \sigma_{a2}}{\sigma_1} + \frac{\kappa_{a1} - \kappa_{a2}}{\kappa_1}\right)\frac{\partial \varphi(p, h)}{\partial h}. \tag{37}$$

According to formula (37), the critical behavior of γ_{ae} in this case is governed by the function $\varphi(p, h)$, whose properties near the percolation threshold were considered in [5]. We note that, for the lattice model, the function $\varphi(p, h)$ and its derivative $\partial\varphi(p, h)/\partial h$ were calculated and tabulated in graphic form in a wide domain of variability of the arguments p and h (see [11, 12]).

According to [3], in the approximation linear in $\mathbf{H}$, thermogalvanomagnetic phenomena in isotropic media are characterized by three coefficients:

$$R = \frac{1}{H}\frac{\sigma_a}{\sigma^2}, \quad L = \frac{\kappa_a}{H}, \quad N = -\frac{1}{H}\frac{\gamma_a}{\sigma}, \tag{38}$$

to which the thermoelectric power α, as well as the electrical conductivity σ and the heat conductivity κ, should be added. According to the results of [5, 6, 10], as well as those of this study, the effective quantities σ_e, κ_e, α_e, R_e, L_e, and N_e can be written in terms of two functions f and Φ undeterminable theoretically. Therefore, tabulation of these functions by numerical methods will allow a description of the entire set of electrophysical properties of isotropic two-component media (composites) in the approximation linear in $\mathbf{H}$ and α.

We also note that a number of correlations can be established between various effective characteristics of these media (see, e.g., [1, 5, 9]).

6. TWO-DIMENSIONAL CASE

As indicated above, the problem of thermogalvanomagnetic properties of two-dimensional two-component isotropic systems has an exact solution at any **H** and α (see [1]). Therefore, it is of significant interest to test the methods under consideration by this exactly solvable example in the approximation linear in **H** and α.

The methods of [5] can be applied to prove the identity

$$\langle [\mathbf{j}^{(\mu)}, \mathbf{q}^{(\nu)}]_z \rangle = [\langle \mathbf{j}^{(\mu)} \rangle, \langle \mathbf{q}^{(\nu)} \rangle]z, \quad (39)$$

which is valid for two-dimensional systems. Let us write expression (39) and the last equation in set (30) at $\mathbf{H} = 0$ and $\alpha = 0$ as sums over individual components,

$$\sigma_1\kappa_1\langle [\mathbf{E}_0^{(\mu)}, \mathbf{G}_0^{(\nu)}]_z \rangle^{(1)} + \sigma_2\kappa_2\langle [\mathbf{E}_0^{(\mu)}, \mathbf{G}_0^{(\nu)}]_z \rangle^{(2)} = \sigma_e\kappa_e[\langle \mathbf{E}_0^{(\mu)} \rangle, \langle \mathbf{G}_0^{(\nu)} \rangle]_z, \quad (40)$$

$$\langle [\mathbf{E}_0^{(\mu)}, \mathbf{G}_0^{(\nu)}]_z \rangle^{(1)} + \langle [\mathbf{E}_0^{(\mu)}, \mathbf{G}_0^{(\nu)}]_z \rangle^{(2)} = [\langle \mathbf{E}_0^{(\mu)} \rangle, \langle \mathbf{G}_0^{(\nu)} \rangle]_z,$$

where $\langle (\ldots) \rangle^{(i)}$ is the integral over the volume of the ith component, divided by the sample volume V. Having determined the value of $\langle [\mathbf{E}_0^{(\mu)}, \mathbf{G}_0^{(\nu)}]_z \rangle^{(1)}$ from Eqs. (40), we determine the function Φ from formula (31),

$$\Phi(p; \sigma_2/\sigma_1, \kappa_2/\kappa_1) = \frac{\sigma_e\kappa_e - \sigma_2\kappa_2}{\sigma_1\kappa_1 - \sigma_2\kappa_2}; \quad (41)$$

using (41) and taking into account expressions (34), we obtain

$$\varphi_\sigma = \frac{\sigma_e^2 - \sigma_2^2}{\sigma_1^2 - \sigma_2^2}, \quad \varphi_\kappa = \frac{\kappa_e^2 - \kappa_2^2}{\kappa_1^2 - \kappa_2^2}, \quad (42)$$

which is consistent with the data reported in [5]. Writing the functions φ_σ, φ_κ, and Φ in the form

$$\varphi_\sigma = 1 + \frac{\sigma_e^2 - \sigma_1^2}{\sigma_1^2 - \sigma_2^2}, \quad \varphi_\kappa = 1 + \frac{\kappa_e^2 - \kappa_1^2}{\kappa_1^2 - \kappa_2^2},$$

$$\Phi = 1 + \frac{\sigma_e\kappa_e - \sigma_1\kappa_1}{\sigma_1\kappa_1 - \sigma_2\kappa_2}$$

and substituting them into formula (28), we obtain an expression for γ_{ae} that is identical to formula (29) in [1].

REFERENCES

1. B. Ya. Balagurov, Fiz. Tverd. Tela (Leningrad) **28**, 2068 (1986) [Sov. Phys. Solid State **28**, 1156 (1986)].
2. B. Ya. Balagurov, Fiz. Tverd. Tela (Leningrad) **30**, 3501 (1988) [Sov. Phys. Solid State **30**, 2013 (1988)].
3. L. D. Landau and E. M. Lifshitz, *Course of Theoretical Physics*, Vol. 8: *Electrodynamics of Continuous Media*, 3rd ed. (Nauka, Moscow, 1992; Pergamon, New York, 1984).
4. D. J. Bergman and D. Stroud, Phys. Rev. B **32**, 6097 (1985).
5. B. Ya. Balagurov, Zh. Éksp. Teor. Fiz. **93**, 1888 (1987) [Sov. Phys. JETP **66**, 1079 (1987)].
6. B. Ya. Balagurov, Zh. Éksp. Teor. Fiz. **85**, 568 (1983) [Sov. Phys. JETP **58**, 331 (1983)].
7. B. Ya. Balagurov, Fiz. Tekh. Poluprovodn. (Leningrad) **16**, 259 (1982) [Sov. Phys. Semicond. **16**, 1204 (1982)].
8. V. Halpern, J. Phys. C **16**, L217 (1983).
9. B. Ya. Balagurov, Fiz. Tekh. Poluprovodn. (Leningrad) **20**, 1276 (1986) [Sov. Phys. Semicond. **20**, 805 (1986)].
10. B. Ya. Balagurov, Fiz. Tekh. Poluprovodn. (Leningrad) **21**, 1978 (1987) [Sov. Phys. Semicond. **21**, 1198 (1987)].
11. B. Ya. Balagurov and V. A. Kashin, Zh. Éksp. Teor. Fiz. **110**, 1001 (1996) [JETP **83**, 553 (1996)].
12. B. Ya. Balagurov and V. A. Kashin, Zh. Éksp. Teor. Fiz. **121**, 770 (2002) [JETP **94**, 664 (2002)].

Translated by A. Kazantsev

Semiconductors, Vol. 37, No. 9, 2003, pp. 1076–1079. Translated from Fizika i Tekhnika Poluprovodnikov, Vol. 37, No. 9, 2003, pp. 1100–1103.
Original Russian Text Copyright © 2003 by Kazanskiĭ, Forsh, Khabarova, Chukichev.

ELECTRONIC AND OPTICAL PROPERTIES OF SEMICONDUCTORS

Effect of Electron Irradiation on Optical and Photoelectric Properties of Microcrystalline Hydrogenated Silicon

A. G. Kazanskiĭ*, P. A. Forsh, K. Yu. Khabarova, and M. V. Chukichev

Moscow State University, Moscow, 119899 Russia

**e-mail: kazanski@phys.msu.su*

Submitted January 10, 2003; accepted for publication January 21, 2003

Abstract—The effect of irradiation with 40 keV electrons on the spectral dependence of the absorption coefficient and on the conductivity and photoconductivity of μ*c*-Si:H was studied. An increase in the absorption coefficient in the defect-related spectral range ($h\nu < 1.2$ eV) and a decrease in photoconductivity of μ*c*-Si:H films were observed after irradiation. The initial parameters were restored by annealing the films at 180°C for 1 h. It was assumed that the changes observed result from the formation of metastable defects of the dangling bond type at boundaries of microcrystalline columns in μ*c*-Si:H films subjected to electron irradiation. An inverse proportional dependence of photoconductivity on the concentration of defects formed under electron irradiation of μ*c*-Si:H films was obtained. © *2003 MAIK "Nauka/Interperiodica".*

In recent years, microcrystalline hydrogenated silicon (μ*c*-Si:H) has been regarded as a material that can serve as an alternative to amorphous hydrogenated silicon (*a*-Si:H), which is widely used in various optoelectronic devices and, in particular, solar cells. This is largely due to the fact that, in contrast to *a*-Si:H, μ*c*-Si:H films do not change their properties upon prolonged exposure to light.

Studying the effect of irradiation with fast electrons on the properties of μ*c*-Si:H films is of interest for determining the efficiency of operation of devices based on this material under the action of high-energy particles (electrons, protons). Studies of this kind also yield information about the influence exerted by defects appearing under irradiation with, in particular, electrons on the photoelectric and optical properties of the material. According to [1], the threshold of defect formation during irradiation of crystalline silicon with fast electrons (hundreds of kiloelectronvolts) greatly exceeds that during irradiation of *a*-Si:H (several kiloelectronvolts). The effect of irradiation with high-energy (1 MeV) electrons on the parameters of μ*c*-Si:H films was studied in [2, 3]. It was found that the absorption coefficient at photon energies $h\nu = (0.8–1.2)$ eV increases and photoconductivity decreases because of the growing concentration of defects in the material. At the same time, μ*c*-Si:H films have a complex structure consisting of the crystalline and amorphous phases and containing a considerable amount of hydrogen atoms. Therefore, it seems of interest to analyze the influence exerted on the optical and photoelectric properties of μ*c*-Si:H films by their irradiation with electrons whose energies (tens of kiloelectronvolts) are known to be lower than the threshold of defect formation in crystalline silicon. This was the subject of the present study.

Investigations were made on ≈1-μm-thick μ*c*-Si:H films grown by chemical vapor deposition from plasma generated under cyclotron resonance conditions (ECRCVD) [4]. The substrate (quartz) temperature was 325°C. Magnesium contacts were deposited onto the film surface by vacuum evaporation. The dark conductivity (σ_d) of films obtained at room temperature was $8 \times 10^{-7}\ \Omega^{-1}\ \text{cm}^{-1}$. The films were irradiated with electrons (energy 40 keV, flux $3 \times 10^{13}\ \text{cm}^{-2}\ \text{s}^{-1}$) at room temperature. The total irradiation dose was $3 \times 10^{17}\ \text{cm}^{-2}$. The photoconductivity ($\Delta\sigma_{ph}$) was measured under illumination of the films with photons ($h\nu = 1.8$ eV, intensity $6 \times 10^{14}\ \text{cm}^{-2}\ \text{s}^{-1}$). All measurements were done in a vacuum at a residual pressure of 10^{-3} Pa.

Figure 1 shows spectral dependences of the relative absorption coefficient, $\alpha_{cpm}(h\nu)/\alpha_{cpm}(1.8\ \text{eV})$, obtained using the constant photocurrent method for a μ*c*-Si:H film before (curve *1*) and after (curve *2*) its irradiation. The spectral dependences obtained are typical of μ*c*-Si:H with a high content of the crystalline phase (>70%) [5, 6]. As seen in the figure, irradiation of μ*c*-Si:H with 40-keV electrons leads to a substantial increase in the absorption coefficient of μ*c*-Si:H in the absorption "tail" region ($h\nu < 1.2$ eV). According to [6, 7], the absorption at these photon energies is determined by states associated with defects in μ*c*-Si:H. Correspondingly, the result obtained indicates that irradiation with 40-keV electrons increases the concentration of defects in μ*c*-Si:H. The authors' measurements demonstrated that raising the temperature of irradiated samples leads to a decrease in absorption in the defect-related spectral range and, correspondingly, to anneal-

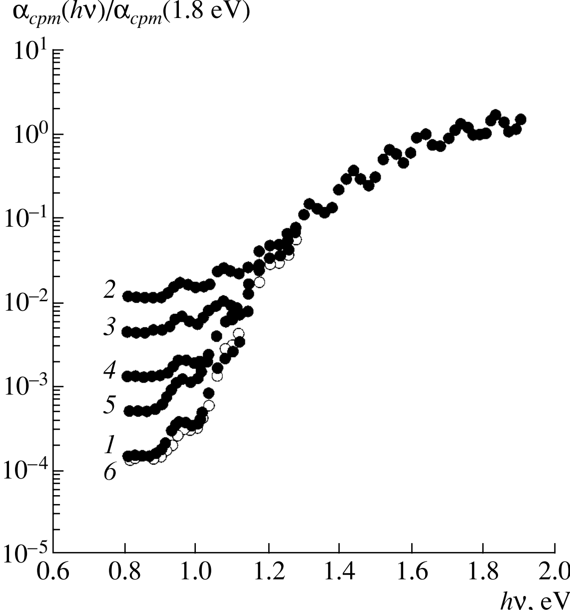

Fig. 1. Spectral dependences of the relative absorption coefficient ($\alpha_{cpm}(h\nu)/\alpha_{cpm}(1.8\text{ eV})$) of μc-Si:H films: (*1*) before electron irradiation; (*2*) after irradiation; after irradiation and at (*3*) 110, (*4*) 165, and (*5*) 180°C annealing for 5 min; (*6*) after irradiation and annealing at 180°C for 1 h.

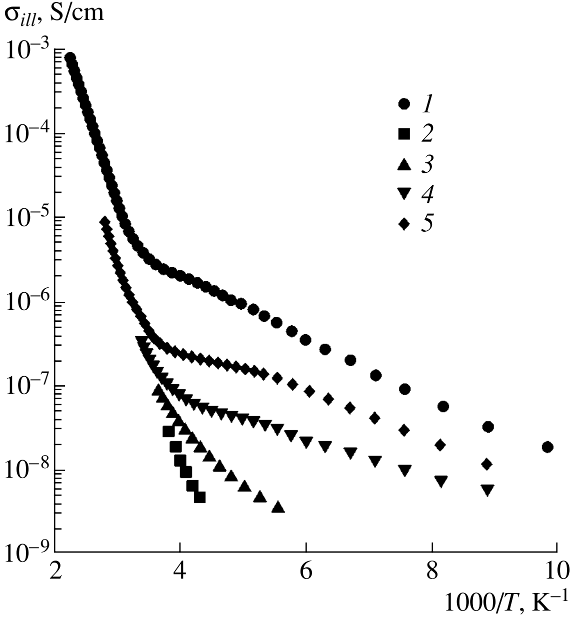

Fig. 2. Temperature dependences of the total conductivity of illuminated μc-Si:H films ($\sigma_{ill} = \Delta\sigma_{ph} + \sigma_d$): (*1*) before electron irradiation; (*2*) after irradiation; and after irradiation and annealing at (*3*) 110, (*4*) 165, and (*5*) 180°C for 5 min.

ing-out of defects induced in μc-Si:H by electron irradiation. As an illustration, Fig. 1 shows spectral dependences $\alpha_{cpm}(h\nu)/\alpha_{cpm}(1.8\text{ eV})$ measured at room temperature for an irradiated film after its annealing for 5 min at various temperatures. The initial absorption at photon energies lower than 1.2 eV is restored after annealing of the irradiated film at 180°C for 1 h (curve *6*).

Figure 2 shows temperature dependences of the total conductivity of an illuminated film ($\sigma_{ill} = \Delta\sigma_{ph} + \sigma_d$) measured before irradiation of the film with electrons, after electron irradiation, and after electron irradiation and annealing at various temperatures for 5 min. It can be seen that electron irradiation of an unirradiated film leads to a decrease in σ_{ill} and annealing of an irradiated film, to an increase in σ_{ill}. Room-temperature measurements demonstrated that electron irradiation has virtually no effect on the dark conductivity σ_d and makes the photoconductivity $\Delta\sigma_{ph}$ nearly 2 orders of magnitude lower. The value of $\Delta\sigma_{ph}$ was restored after annealing of an irradiated film at 180°C for 1 h.

The results presented here show that irradiation of μc-Si:H with 40-keV electrons leads to the formation of metastable defects in the material. It is noteworthy that annealing of the defects generated as a result of irradiation begins at relatively low temperatures. This is illustrated by Fig. 3, which shows the behavior of the relative photoconductivity $\Delta\sigma_{ph}/\Delta\sigma_{ph}^A$ and the absorption coefficient in the defect-related spectral range, $\alpha_{cpm}(0.8\text{ eV})/\alpha_{cpm}^A(0.8\text{ eV})$, with the temperature of annealing (5 min) of irradiated films. Here, the quantities $\Delta\sigma_{ph}^A$ and $\alpha_{cpm}^A(0.8\text{ eV})$ correspond to data for an

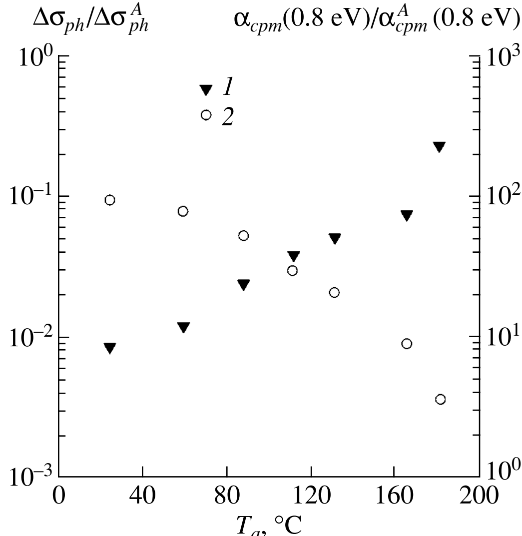

Fig. 3. (*1*) Relative photoconductivity ($\Delta\sigma_{ph}/\Delta\sigma_{ph}^A$) and (*2*) absorption coefficient ($\alpha_{cpm}(0.8\text{ eV})/\alpha_{cpm}^A(0.8\text{ eV})$) of irradiated μc-Si:H films vs. the temperature of their annealing for 5 min.

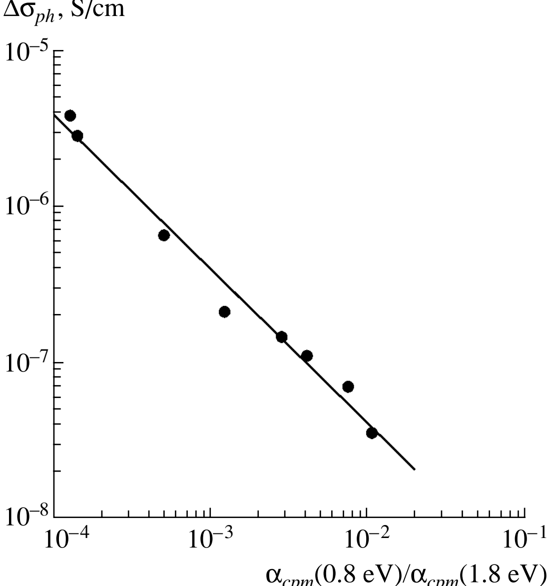

Fig. 4. Dependence of the photoconductivity ($\Delta\sigma_{ph}$) of a μ*c*-Si:H film at room temperature on the relative absorption coefficient in the defect-related spectral range (α_{cpm}(0.8 eV)/α_{cpm}(1.8 eV)).

unirradiated μ*c*-Si:H film. The initial values of $\Delta\sigma_{ph}$ and α_{cpm}(0.8 eV) are restored after annealing of an irradiated film at 180°C for 1 h. It should be noted that the dependence of the absorption coefficient in the defect-related spectral range on the annealing temperature, which is shown for an irradiated μ*c*-Si:H film in Fig. 3, is close to a similar dependence for the concentration of defects created by electron irradiation in *a*-Si:H films [8]. This indicates that the mechanisms of generation and annealing of metastable defects induced by electron irradiation in μ*c*-Si:H films, on the one hand, and *a*-Si:H films, on the other, are the same.

As seen in Fig. 3, the absorption coefficient in the defect-related spectral range and, correspondingly, the defect concentration decrease with increasing annealing temperature. At the same time, the photoconductivity grows. A correlation between the photoconductivity and the absorption coefficient in the defect-related range is shown in Fig. 4. It can be seen that the dependence of $\Delta\sigma_{ph}$ on α_{cpm}(0.8 eV)/α_{cpm}(1.8 eV) is nearly inversely proportional (as shown by the solid line in Fig. 4). This indicates that the defects generated by electron irradiation serve as the main recombination centers for nonequilibrium carriers and determine the photoconductivity of μ*c*-Si:H at room temperature.

Now, the possible nature of defects generated in μ*c*-Si:H by electron irradiation and possible mechanisms of their formation will be considered. It is known [9] that the structure of μ*c*-Si:H consists of microcrystals several to tens of nanometers in size, which are combined into columns extending perpendicularly to the substrate surface, with the diameters of these columns ranging from tens to hundreds of nanometers. The amorphous phase and pores may be present at column boundaries. In the opinion of Lips *et al.* [10] and Finger *et al.* [11], the basic defects in μ*c*-Si:H are dangling bonds of silicon, which are mainly found at column boundaries. It has been assumed [12] that the states associated with these defects contribute to absorption in μ*c*-Si:H at $h\nu < 1.2$ eV. Thus, the increase in the absorption in the defect-related spectral range, observed by the authors of the present study (see Fig. 1), points to an increase in the concentration of dangling bonds as a result of irradiation of μ*c*-Si:H with 40-keV electrons. Also, the dependence of the photoconductivity on the absorption coefficient in the defect-related range (see Fig. 4) confirms the assumption [13, 14] that recombination of nonequilibrium carriers in μ*c*-Si:H at room temperature proceeds via localized states associated with dangling bonds at column boundaries.

It may be assumed that, as in the case of *a*-Si:H, the rupture of bonds between hydrogen and silicon atoms is the main mechanism of defect formation in μ*c*-Si:H during irradiation with electrons with energies of tens of kiloelectronvolts [8]. In the opinion of Tanaka [15], the main portion of hydrogen that passivates dangling bonds in μ*c*-Si:H is situated at column boundaries. Therefore, the rupture of silicon–hydrogen bonds must lead to a higher concentration of dangling bonds at column boundaries and, correspondingly, to stronger absorption in the defect-related spectral range and lower photoconductivity.

Thus, the investigation performed demonstrated that, even though no photoinduced changes in properties are observed in μ*c*-Si:H (in contrast to *a*-Si:H), irradiation of μ*c*-Si:H with low-energy (tens of kiloelectronvolts) electrons leads, as in the case of *a*-Si:H, to the generation of metastable defects, which affect the optical and photoelectric parameters of the material.

We thank Prof. W. Fuhs and Dr. M. Birkholtz for providing us with the μ*c*-Si:H films.

REFERENCES

1. H. Shade and J. I. Pankove, J. Phys. (Suppl. 10) (Paris) **42**, C4-327 (1981).
2. W. Bronner, M. Mehring, and R. Bruggemann, Phys. Rev. B **65**, 165212-1 (2002).
3. R. Bruggemann, W. Bronner, and M. Mehring, Solid State Commun. **119**, 23 (2001).
4. I. Beckers, N. H. Nickel, W. Pilz, and W. Fuhs, J. Non-Cryst. Solids **227**, 847 (1998).
5. D. Han, D. Yue, J. D. Lorentzen, *et al.*, J. Appl. Phys. **87**, 1882 (2000).

6. N. Beck, J. Meier, J. Fric, *et al.*, J. Non-Cryst. Solids **198–200**, 903 (1996).
7. N. Beck, P. Torres, J. Fric, *et al.*, Mater. Res. Soc. Symp. Proc. **452**, 761 (1997).
8. M. Stutzmann, in *Amorphous and Microcrystalline Semiconductor Devices*, Vol. 2: *Material and Device Physics*, Ed. by J. Kanicki (Artech House, Boston, 1991), p. 129.
9. D. Ruff, H. Mell, L. Toth, *et al.*, J. Non-Cryst. Solids **227**, 1011 (1998).
10. K. Lips, P. Kanschat, D. Will, *et al.*, J. Non-Cryst. Solids **227**, 1021 (1998).
11. F. Finger, J. Muller, C. Malten, *et al.*, J. Non-Cryst. Solids **266**, 511 (2000).
12. A. Poruba, M. Vanecek, J. Meier, and A. Shah, J. Non-Cryst. Solids **299–302**, 536 (2002).
13. A. G. Kazanskiĭ, H. Mell, E. I. Terukov, and P. A. Forsh, Fiz. Tekh. Poluprovodn. (St. Petersburg) **36**, 41 (2002) [Semiconductors **36**, 38 (2002)].
14. K. V. Kougiya and E. I. Terukov, Fiz. Tekh. Poluprovodn. (St. Petersburg) **35**, 643 (2001) [Semiconductors **35**, 615 (2001)].
15. K. Tanaka, Mater. Res. Soc. Symp. Proc. **452**, 3 (1997).

Translated by M. Tagirdzhanov

Semiconductors, Vol. 37, No. 9, 2003, pp. 1080–1084. Translated from Fizika i Tekhnika Poluprovodnikov, Vol. 37, No. 9, 2003, pp. 1104–1108.
Original Russian Text Copyright © 2003 by Vavilova, Vinokurov, Kapitonov, Murashova, Nevedomskiĭ, Poletaev, Sitnikova, Tarasov, Shamakhov.

ELECTRONIC AND OPTICAL PROPERTIES OF SEMICONDUCTORS

Optical and Structural Properties of InGaAsP Miscibility-Gap Solid Solutions Grown by MOVPE on GaAs(001) Substrates

L. S. Vavilova, D. A. Vinokurov, V. A. Kapitonov, A. V. Murashova, V. N. Nevedomskiĭ, N. K. Poletaev, A. A. Sitnikova, I. S. Tarasov, and V. V. Shamakhov

Ioffe Physicotechnical Institute, Russian Academy of Sciences, St. Petersburg, 194021 Russia

e-mail: tarasov@hpld.ioffe.ru

Submitted January 16, 2003; accepted for publication January 21, 2003

Abstract—Optical and structural properties of InGaAsP solid solutions grown by MOVPE at 600°C on GaAs(001) substrates are studied. The photoluminescence spectra of InGaAsP solid solutions with a composition corresponding to the miscibility gap contain a main band and an additional auxiliary band. It is established that both bands are related to band-to-band radiative transitions; i. e., the studied layer includes two solid solutions with different compositions and different band gaps. It is shown that the observed high-energy shift of the additional band with an increasing level of excitation is governed by the nanometer size of domains in the corresponding solid solution. This conclusion is consistent with the results of TEM study, which revealed the presence of a periodic structure comprised of alternating domains with different compositions. This structure of alternating domains extends along the [100] and [010] directions with a characteristic period of 10 nm. © *2003 MAIK "Nauka/Interperiodica".*

INTRODUCTION

In recent decades, a system of In–Ga–As–P solid solutions have been widely and successfully used in the production of optoelectronic devices, such as lasers and light-emitting diodes. This system of solid solutions is known to feature a fairly wide miscibility gap. The layers of solid solutions whose composition falls within the miscibility gap are characterized by unique optical, electrical [1, 2], and structural [3, 4] properties, which distinguish them from homogeneous solid solutions and point to an emergence of a new complicated object: a periodic domain structure. Despite a number of interesting recent publications devoted to this topic, the crystallization of InGaAsP solid solutions, as well as the properties of periodic domain structures, still leave room for investigation. This situation is apparently due to the fact that the self-organization of domain structures in semiconductors is a comparatively new field in modern solid-state physics.

This study further contributes to previous [5–8] investigations of epitaxial films of InGaAsP solid solutions grown within the miscibility gap. A combined study of the objects in question by means of the photoluminescence (PL) technique and transmission and scanning electron microscopy (TEM and SEM) enabled the determination of their optical and structural properties.

EXPERIMENTAL

The experimental samples were grown by metal-organic vapor phase epitaxy (MOVPE) on GaAs(001) substrates at 600°C. They comprised two layers grown on the GaAs(001) substrate: an $In_{0.47}Ga_{0.53}P$ ternary solid solution and an InGaAsP quaternary solid solution. The expected compositions of the InGaAsP solid solutions varied along the GaAs isoperiodic line. The thickness of the layers ranged from 300 to 500 nm.

The study of the optical properties of samples included an analysis of their PL spectra obtained at different temperatures and excitation levels. The structure of the epitaxial InGaAsP layers was investigated using a PHILIPS EM 420 transmission electron microscope with an accelerating voltage of 80–120 kV. A CamScan S4-90FE scanning electron microscope was used to study the natural and cleaved surfaces of the samples. The layer boundaries at the cleaved surfaces were preliminarily determined by etching in an $H_2SO_4 : H_2O_2 : H_2O$ (1 : 1 : 50) sulfuric acid solution for 1 min.

RESULTS AND DISCUSSION

According to the results of our previous studies [1, 5, 9] and the data available from the literature, the miscibility gap of $In_{1-x}Ga_xAs_{1-y}P_y$ solid solutions grown on GaAs(001) substrates at conventional temperatures between 650 and 800°C encompasses the compositions $0.5 < y < 0.95$ lying along the GaAs isoperiodic line. The immiscibility of components in such a solid solution is mainly shown by a number of special features appearing in the characteristics of the grown layers, such as the broadening of the edge-emission band in the PL spectrum, a decrease in the mobility of charge carriers, a change in the surface morphology, etc. Taken together, these data point to certain inhomo-

1063-7826/03/3709-1080$24.00 © 2003 MAIK "Nauka/Interperiodica"

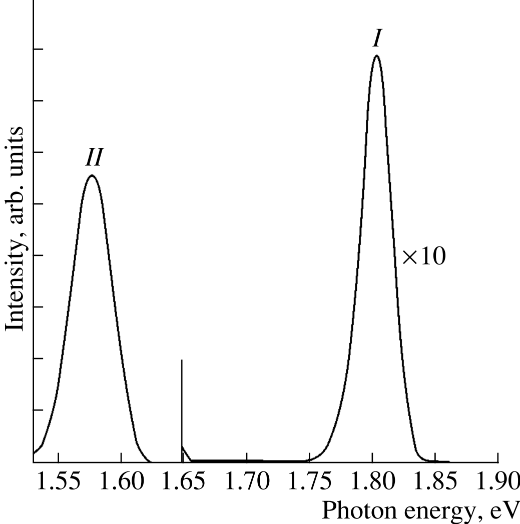

Fig. 1. The PL spectrum of InGaAsP solid solution grown at 600°C on GaAs(001) by MOVPE (sample *X*2536). The spectrum is measured at 77 K and the excitation level is 0.5 kW/cm^2. The expected composition $x = 0.65$ and $y = 0.7$ is within the miscibility gap at the growth temperature specified. Peaks *I* and *II* correspond to the main and the additional bands, respectively.

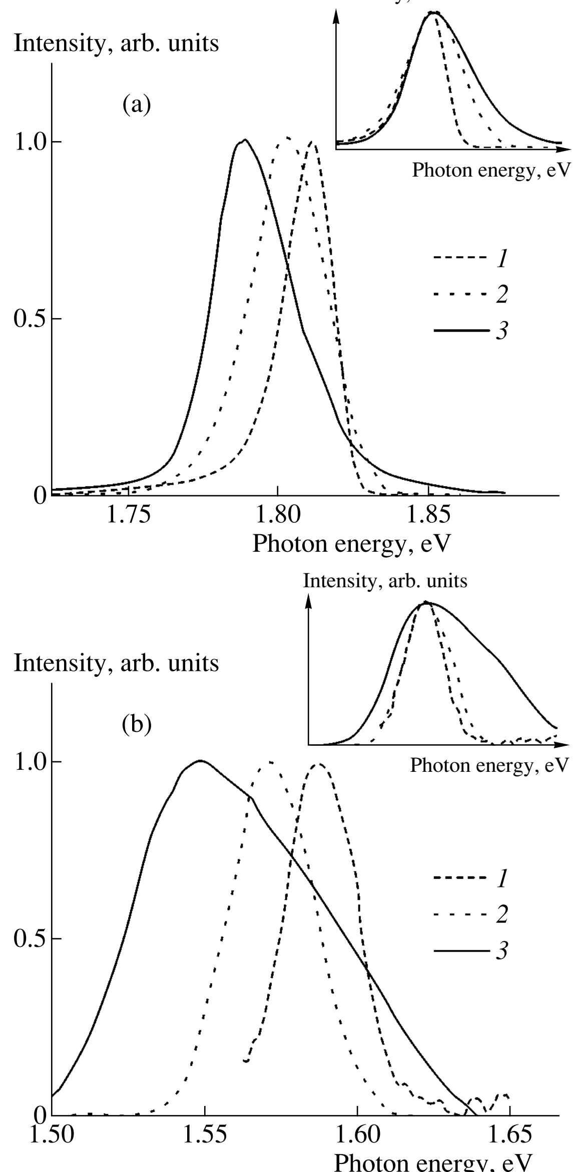

Fig. 2. (a) The main and (b) the additional bands in the PL spectrum of InGaAsP solid solution composed within the miscibility gap (sample *X*2536) as measured at a temperature of (*1*) 2, (*2*) 77, and (*3*) 300 K. The spectra are normalized to the maximum of the signal.

geneities in the composition of the solid solution inside the epitaxial layer.

The most interesting feature observed in the optical properties of InGaAsP solid solutions grown on GaAs(001) substrates within the miscibility gap is the presence of an additional PL band. Similar spectra were described in [1, 9, 10], but no clear physical interpretation was given to the appearance of the additional peak. By way of example, a spectrum exhibiting two peaks is shown in Fig. 1 for the epilayer of $In_{1-x}Ga_xAs_{1-y}P_y$ solid solutions with the expected composition $x = 0.65$ and $y = 0.7$. At a growth temperature of 600°C, this composition falls within the miscibility gap. Along with the peak corresponding to the band gap of the solid solution with the expected composition ($h\nu_1 = 1.81$ eV) (Fig. 1), there is another peak lying in the low-energy spectral region ($h\nu_2 = 1.59$ eV). In what follows, these two bands will be referred to as main and additional, respectively.

As is typical of edge emission [10], the position of the peak of the main band remains constant as the excitation intensity grows from 0.05 to 2.5 kW/cm^2. The attribution of the main band to band-to-band transitions is also supported by its behavior with an increase in temperature from 2 to 300 K. It is seen from Fig. 2a that an increase in temperature from 2 to 300 K results in asymmetric broadening on the high-energy side of the band. The inset to Fig. 2a shows the main-band spectra measured at 2, 77, and 300 K and brought together by shifting the 77 and 300 K curves along the horizontal axis by the value of the temperature-induced change in the band gap. This procedure makes evident the almost exact coincidence between the low-energy falloff of the spectra and an appreciable extension of its high-energy wing with temperature. Such extension is typical of edge emission, because it stems from a temperature change in the distribution of free carriers in the bands. It should be noted that, on the high-energy side, the shape of the spectra deviates from a Maxwellian one. In addition, the main band width turns out to somewhat exceed theoretical estimates. As was shown in [1], these facts are indicative of fluctuations in the solid-solution composition.

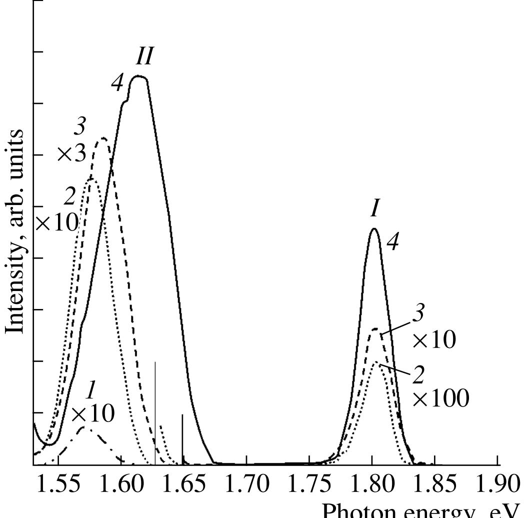

Fig. 3. The PL spectra of InGaAsP solid solution composed within the miscibility gap (sample *X*2536) as measured at 77 K and an excitation level of (*1*) 0.05, (*2*) 0.2, (*3*) 0.5, and (*4*) 2.5 kW/cm^2. Peaks *I* and *II* correspond to the main and additional bands, respectively.

A similar temperature behavior is observed for the additional band. It is seen from Fig. 2b that the additional band asymmetrically broadens (predominantly, on the high-energy side) with temperature, just like the main peak. This observation makes it possible to attribute the additional band also to band-to-band radiative transitions. Therefore, two solid solutions with different compositions and band gaps are present inside the InGaAsP layer. However, unlike the main band, the additional band shifts to higher energies with an increase in the excitation level (Fig. 3). It is seen also that the integrated intensity of the additional band grows more slowly than that of the main band. At a sufficiently high excitation level, even saturation of the additional peak occurs; i.e., two distinct bands in the spectra of some samples are replaced by a wide main band with a "tail" that is extended far to lower energies. At the excitation level used in the experiment, this situation is only possible if the domains in the narrow-band material are of nanometer size. This conclusion can be substantiated by the following considerations.

It is well known that the quantum efficiency of luminescence in double heterostructures based on InGaAsP solid solutions decreases with increasing excitation level due to Auger recombination, which starts to compete with the radiative recombination [11, 12]. A simple estimate for undoped InGaAsP solid solutions with a band gap of 1.2–1.9 eV suggests that the Auger recombination rate ($G_A = Rn^3$) becomes comparable to the band-to-band radiative recombination rate ($G_r = Bn^2$) [11] at the nonequilibrium carrier concentration $n \approx 10^{20}$ cm^{-3} (300 K). Here, we used the values of the Auger-recombination coefficient R and the bulk radiative recombination coefficient B from studies [11–15]. Considering the aforesaid, we can evaluate the excitation level that corresponds to the discussed situation with the saturation of PL intensity. In the steady state, the generation rate of nonequilibrium carriers may be taken equal to their recombination rate on the assumption that their concentration appreciably exceeds the equilibrium value ($n \gg n_0$):

$$nV1/\tau = I_0(1 - \exp(-\alpha d))S_0, \quad (1)$$

where n is the nonequilibrium carrier concentration, $V = S_0 d$ is the volume of illuminated material, τ is the total lifetime of carriers ($1/\tau = 1/\tau_r + 1/\tau_A$, $\tau_r = 1/Bn$, and $\tau_A = 1/Rn^2$), I_0 is the illumination intensity, α is the absorption coefficient, d is the layer thickness, and S_0 is the illuminated area. In the case under study, $G_r = G_A$, which corresponds to $n \approx 10^{20}$ cm^{-3}, the characteristic time of radiative recombination τ_r is equal to the characteristic time of nonradiative Auger recombination τ_A. With a further increase in the nonequilibrium carrier concentration, Auger recombination prevails. Using the values typical of semiconductors, $R \approx 10^{-30}$–10^{-31} cm^6 s^{-1} [11–15], $\alpha \approx 10^5$ cm^{-1} [16, 17] and the experimental value $d \approx 0.5$ μm, we obtain the value of I_0 at which the leveling off of the intensity of the edge-emission band sets in ($I_0 \approx 10^{24}$–10^{25} cm^{-2} s^{-1}). In our experiments, the highest excitation level P was 8 kW/cm^2; for the argon laser used in experiment (wavelength $\lambda = 488$ nm, photon energy 2.54 eV), this corresponds to the pump intensity $I_0' = P/E \approx 10^{22}$ cm^{-2} s^{-1}. This value is lower than I_0 obtained from Eq. (1) by 10^3 times, which indicates that we cannot observe the leveling off of the intensity of band-to-band emission from the material bulk under our experimental conditions. However, if we associate the additional band with radiative transitions in nanometer-size domains, the leveling off of its intensity can be explained by the fact that nonequilibrium carriers rapidly occupy all the allowed states, whose number in a nanometer-sized domain is considerably smaller than that in the bulk material. This explanation is consistent with the observed spectral shift of the additional band at higher excitation levels. The structural properties of layers of InGaAsP solid solutions with a composition corresponding to the miscibility gap give additional evidence of the presence of nanometer-size domains in these layers.

Figure 4 shows a TEM image of the studied InGaAsP layer obtained in a 220-type reflection from a sample prepared in planar geometry. A small-scale modulation of intensity in the [100] and [010] directions with a characteristic period of 10 nm is well seen. This type of contrast is related [3, 4] to the modulation of the lattice parameter and, hence, to the modulation of the solid-solution composition, since the distribution of contrast in the 220-reflection image represents the distribution of stresses over the sample. In other words, the layer consists of alternating domains with different solid-solution compositions and lattice parameters. The

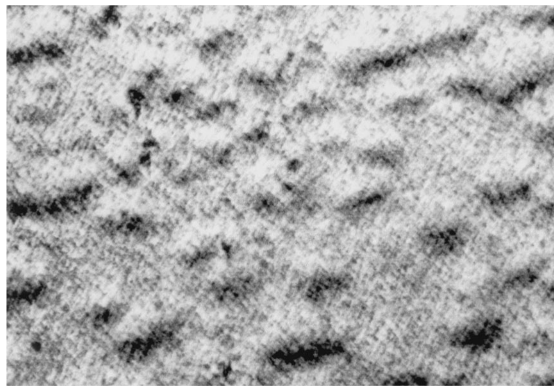

Fig. 4. Dark-field TEM image (g = 220) of a planar (001) section of InGaAsP solid solution composed within the miscibility gap (sample X2536).

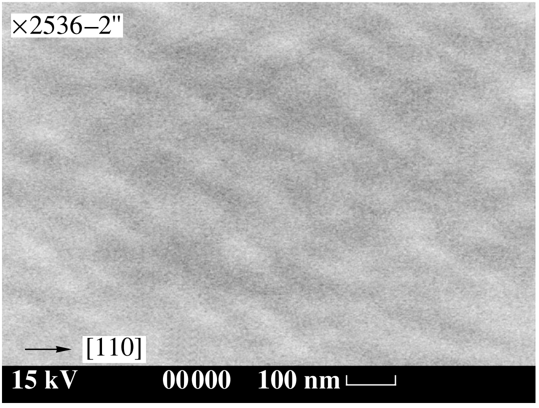

Fig. 5. SEM image of the surface of InGaAsP solid solution composed within the miscibility gap (sample X2536). The sample is rotated around the [110] axis by 20°.

changes in the properties of solid solutions occur within a distance such that the domains can be considered as nanometer-size objects. The presence of nanometer-size domains inside the studied layer explains the observed behavior of the additional PL band at different levels of excitation. The fact that an increase in the excitation leads to neither a change in the position of the band nor the leveling off of its intensity suggests that the wide-gap solid solution inside the layer exists not only in the form of nanometer-size domains but also as bulk material. This conclusion does not contradict TEM data, since the image is formed by only a thin (50–100 nm) upper part of the sample and does not incorporate complete information about the layer with a thickness of 300–500 nm.

Along with the small-scale contrast, the TEM image shows a nonperiodic large-scale contrast in the form of 100-nm-size grains. A similar surface profile was revealed by the SEM study of the sample (Fig. 5). This circumstance allows us to attribute the grain-shaped contrast in the TEM image to the surface profile. However, the nature of large-scale contrast is not conclusively established and there may be several other factors contributing to the formation of this contrast. Nevertheless, we ascertain that the special features in the PL spectra of InGaAsP epitaxial films grown within a miscibility gap on GaAs(001) substrates are related to the small-scale contrast appearing in their TEM images.

We also studied epitaxial films of InGaAsP solid solutions whose compositions lie outside the miscibility gap and found that they exhibit properties of homogeneous solid solutions. The PL spectra of such layers contain a single band whose peak corresponds to the expected composition of a solid solution. By analyzing the spectrum shape, we established that the high-energy wing of the curves is described by the Maxwell-distribution function to a high accuracy. The shifts of peak positions with temperature varying from 77 to 300 K are compared to the experimental data presented in [10] for the PL spectra of homogeneous InGaAsP solid solutions on GaAs(001) substrates. The peak positions remain unchanged with an increase in the excitation level. This behavior is indicative of edge emission. In the TEM images of layers obtained beyond the miscibility gap, the distribution of contrast features only unordered fluctuations, which gives additional evidence of the absence of periodic modulation in the composition of these layers.

CONCLUSION

A comparison was made between the optical and the structural properties of InGaAsP solid solutions grown on GaAs(001) substrate whose composition falls within the miscibility gap under the given conditions of growth. The results indicate that the special features in the PL spectra of such layers originate from the presence of a periodic structure of alternating nanosized domains with two different compositions, band gaps, and the lattice parameters of a solid solution. The range of compositions corresponding to the growth of domain structures, as well as their type and parameters, are in good agreement with the results predicted by the theory of the instability of solid solutions [15–19]. Thus, we attributed the formation of nanostructures to the decomposition of unstable solid solutions.

ACKNOWLEDGMENTS

This study was supported by the Russian Foundation for Basic Research (project no. 01-02-17842) and INTAS (grant no. 0175wp).

REFERENCES

1. S. Mukai, J. Appl. Phys. **54**, 2635 (1983).
2. E. Kuphal, J. Cryst. Growth **67**, 441 (1984).
3. O. Ueda, S. Isozumi, and S. Komiya, Jpn. J. Appl. Phys. **23**, L241 (1984).
4. A. G. Norman and G. R. Booker, J. Appl. Phys. **57**, 4715 (1985).

5. N. A. Bert, L. S. Vavilova, I. P. Ipatova, *et al.*, Fiz. Tekh. Poluprovodn. (St. Petersburg) **33**, 544 (1999) [Semiconductors **33**, 510 (1999)].
6. L. S. Vavilova, V. A. Kapitonov, D. A. Livshits, *et al.*, Fiz. Tekh. Poluprovodn. (St. Petersburg) **34**, 325 (2000) [Semiconductors **34**, 319 (2000)].
7. L. S. Vavilova, V. A. Kapitonov, A. V. Murashova, and I. S. Tarasov, Fiz. Tekh. Poluprovodn. (St. Petersburg) **34**, 1307 (2000) [Semiconductors **34**, 1255 (2000)].
8. V. N. Nevedomskiĭ, N. A. Bert, A. V. Murashova, *et al.*, in *Proceedings of 18th Russian Conference on Electron Microscopy, EM'2000* (Chernogolovka, Russia, 2000), p. 60.
9. A. Knauer, G. Erbert, S. Gramlich, *et al.*, J. Electron. Mater. **24**, 1655 (1995).
10. S. Mukai, M. Matsuzaki, and J. Shimada, Jpn. J. Appl. Phys. **19**, L505 (1980).
11. D. Z. Garbuzov, V. V. Agaev, Z. N. Sokolova, *et al.*, Fiz. Tekh. Poluprovodn. (Leningrad) **18**, 1069 (1984) [Sov. Phys. Semicond. **18**, 665 (1984)].
12. D. Z. Garbuzov, V. P. Chalyĭ, A. E. Svelokuzov, *et al.*, Fiz. Tekh. Poluprovodn. (Leningrad) **22**, 657 (1988) [Sov. Phys. Semicond. **22**, 410 (1988)].
13. V. P. Varshni, Phys. Status Solidi **19**, 459 (1967).
14. V. P. Varshni, Phys. Status Solidi **20**, 9 (1967).
15. D. Z. Garbuzov and V. B. Khalfin, Preprint No. 652, FTI AN SSSR (Physicotechnical Inst., USSR Academy of Sciences, 1980).
16. T. S. Moss, G. J. Burrell, and B. Ellis, *Semiconductor Opto-Electronics* (Butterworths, London, 1973; Mir, Moscow, 1976).
17. S. M. Sze, *Physics of Semiconductor Devices*, 2nd ed. (Wiley, New York, 1981; Mir, Moscow, 1984), Vol. 1.
18. B. DeCremoux, P. Hirth, and J. Ricciardi, Inst. Phys. Conf. Ser. **56**, 115 (1981).
19. G. B. Stringfellow, J. Cryst. Growth **58**, 194 (1982).
20. K. Onabe, Jpn. J. Appl. Phys. **21**, 797 (1982); Jpn. J. Appl. Phys. **21**, L323 (1982).
21. I. P. Ipatova, V. G. Malyshkin, A. Yu. Maslov, and V. A. Shchukin, Fiz. Tekh. Poluprovodn. (St. Petersburg) **27**, 285 (1993) [Semiconductors **27**, 158 (1993)].
22. V. A. Shchukin and A. N. Starodubtsev, in *Extended Abstracts of 26th International Symposium on Compound Semiconductors* (Berlin, 1999), WeP-5.

Translated by A. Sidorova

Semiconductors, Vol. 37, No. 9, 2003, pp. 1085–1089. Translated from Fizika i Tekhnika Poluprovodnikov, Vol. 37, No. 9, 2003, pp. 1109–1113.
Original Russian Text Copyright © 2003 by Serezhkin, Shesterkina.

SEMICONDUCTORS STRUCTURES, INTERFACES, AND SURFACES

Carrier Multiplication in Silicon *P–N* Junctions

Yu. N. Serezhkin and A. A. Shesterkina
Mordovian State University, Bol'shevistkaya ul. 68, Saransk, 430000 Russia
e-mail: Serezhkin_YN@mail.ru
Submitted November 5, 2002; accepted for publication November 21, 2002

Abstract—The dependences of carrier multiplication factors M on the voltage applied to p–n Si junctions with an avalanche breakdown voltage of 10–3000 V are considered. Analytical expressions for the approximation of these dependences for electrons, holes, and generation current are suggested. In the range of varying the multiplication factors of 1.01–3.0, the relative rms error of approximation ($M - 1$) is several percent. This is more than an order of magnitude more accurate compared with the approximation by the widely known Miller–Moll expression. It is assumed that the analytical expressions of the form suggested will be suitable for the approximation of dependences of multiplication factors on the voltage applied for most semiconductor materials.
© 2003 MAIK "Nauka/Interperiodica".

The carrier multiplication in reverse-biased p–n junctions governs, to a large extent, many properties of semiconductor devices, namely, bipolar transistors, thyristors, avalanche photodiodes, etc. The quantitative characteristics of multiplication are the multiplication factors for charge carriers and the generation current of a p–n junction.

In a general case, the multiplication factors for electrons and holes $M_{n,p}$ are the complex implicit functions of the applied voltage [1]:

$$M_{n,p} = 1/(1 - J_{n,p}), \quad (1)$$

$$J_n = \int_0^L \alpha_n \exp\left(-\int_0^x (\alpha_n - \alpha_p)dx'\right)dx, \quad (2)$$

$$J_p = \int_0^L \alpha_p \exp\left(\int_x^L (\alpha_n - \alpha_p)dx'\right)dx, \quad (3)$$

where α_n and α_p are the coefficients of the impact ionization for electrons and holes, respectively; and L is the width of the space charge region of the p–n junction. For most semiconductors, the dependences of α_n and α_p on the electric-field strength E are given by

$$\alpha(E) = A\exp(-(b/E)^m), \quad (4)$$

where $m = 1$ or 2. The corrections b and A are determined experimentally. For such a dependence, the multiplication factors can be calculated only by numerical methods. However, in order to analyze the operation of devices and to calculate their parameters, it is desirable to have simpler and explicit $M(U)$ dependences.

The first approximate expression of such kind was suggested by Miller [2] and was modified afterwards by Moll [3]; this expression is written as

$$M = \left(1 - \left(\frac{1}{f}\frac{U}{U_B}\right)^n\right)^{-1}, \quad (5)$$

where U_B is the avalanche breakdown voltage of the p–n junction; and f and n are parameters which depend on the type of charge carriers multiplied, the p–n junction type, and its breakdown voltage.

However, it was later found that this expression describes the dependences $M(U)$ well only in rare cases. For example, it describes inadequately the electron multiplication in the Si p–n junctions. Other approximate expressions were also used [4–7]. However, their accuracy was also poor. In addition, the expressions suggested were not substantiated at all. Only in one case was the expression derived on the basis of another approximate expression [7]. However, this expression is applicable to relatively large multiplication factors, and it is complicated for practical usage.

Let us consider a particular case of equality of the ionization coefficients for electrons and holes. For $\alpha_n(E) = \alpha_p(E)$, the ionization integrals (2) and (3) are substantially simplified and can be expressed in terms of transcendent functions. For Si, $m = 1$; in this case,

$$J = ALE_2(z) \quad (6)$$

for abrupt p–n junctions, and

$$j = AL(z/2)\exp(-z/2)(K_1(z/2) - K_0(z/2)) \quad (7)$$

for gradient p–n junctions [1]. Here, $E_2(z)$ is an exponential second-kind integral, $K(z/2)$ is the modified Bessel function for an imaginary argument, and $z = b/E_m$. Analysis shows that, as is typical for multiplication of charge carriers, the highest field strength in the

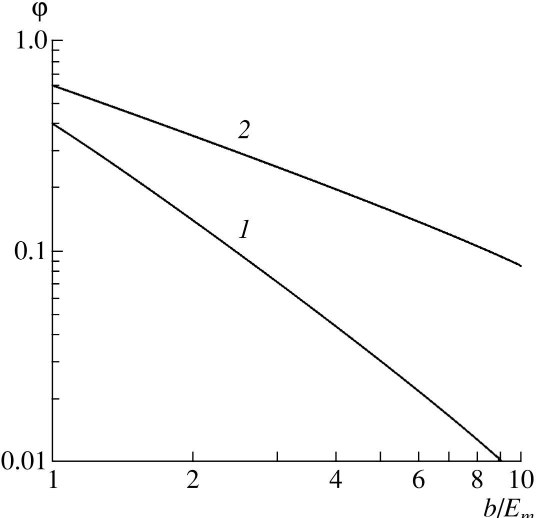

Fig. 1. Function φ for (*1*) abrupt and (*2*) gradient *p–n* junctions.

p–n junctions E_m for most of semiconductors is considerably less than the parameter *b* up to the breakdown fields. Therefore, the argument *z* for the aforementioned functions considerably exceeds unity, especially for $U \ll U_B$. Using the properties of these functions for large argument values [8], ionization integrals (6) and (7) can be represented in the form

$$J = B_{\varphi}(z)\alpha(z),$$

where $\varphi(z)$ is a function which varies slowly with the field strength, and $\alpha(z)$ is the ionization coefficient. The dependences $\varphi(z)$ for $z > 1$ are shown in Fig. 1. As can be seen from Fig. 1, these functions can be represented by power dependences in a rather wide range of variations in *z*. For a specific *p–n* junction, the highest field strength usually increases by no more than a factor of two as *M* varies from 1.01 to ∞. Therefore, to approximate the ionization integrals, the following expression can be used:

$$J = (U_B/U)^k \exp(-a((U_B/U)^{\chi} - 1)). \quad (8)$$

Here, $\chi = 1/2$ for abrupt *p–n* junctions and 2/3 for gradient ones, respectively; and *k* and *a* are the parameters of the approximation. If $\alpha_n(E) \neq \alpha_p(E)$, the approximation is more accurate the larger the b/E_m ratio and the smaller the difference between ionization coefficients for electrons and holes. In Si, at the breakdown voltage, $z > 1.5$ even for the *p–n* junctions operating at lowest voltages. However, the ionization coefficients for electrons and holes are different, and their ratio depends on the field strength. This ratio varies approximately from 1.1 to 20 as the field strength varies from 8×10^5 to 2.5×10^5 V/cm.

For the analysis of the applicability of expression (8), the ionization integrals and multiplication factors were calculated from relationships (1)–(3) by numerical methods. The ionization coefficients for electrons and holes were taken in the form (4) for $m = 1$ as $A = 6.3 \times 10^5$ cm^{-1}, $b = 1.23 \times 10^6$ V/cm for electrons, and $A = 1.74 \times 10^6$ cm^{-1}, $b = 2.18 \times 10^6$ V/cm for holes. These values are considered as most plausible for Si at present [9].

The highest operating voltage for bipolar transistors in a circuit with a common emitter and a reverse blocking voltage of thyristors is determined by the criterion $\alpha_0 M = 1$. Here, α_0 is the current gain for a corresponding transistor with no allowance made for the multiplication of charge carriers. On the basis of this criterion, we determined the parameters of the approximation *k* and *a* from the range of varying *M* from 1.01 to 3, which is of greater interest for the analysis of the properties of bipolar transistors and thyristors. The parameters were determined by the least-squares method after the linearization of expression (8) by taking the logarithm. The abrupt and gradient *p–n* junctions with a breakdown voltage from 10 to 3000 V were analyzed.

It turned out that expression (8) approximates the dependences $M(U)$ much more accurately than does relationship (5) by Miller–Moll. The accuracy of the approximation may be improved if we vary the χ parameter along with the *k* and *a* parameters. However, when determining the parameters *k*, *a*, and χ by the least-squares method, the parameter χ changes its sign for a certain breakdown voltage and passes through zero. In this case, the parameters *k* and *a* increase sharply and tend toward infinity. This is very inconvenient for describing the dependence of *k* and *a* on the avalanche-breakdown voltage.

The analysis demonstrated that, for the breakdown voltage range under investigation, it is possible to choose other values of the parameter χ that differ from those derived above and which are also independent of the breakdown voltage. The best values for Si in our case are $\chi = -1/2$ for electrons and $\chi = -4$ for holes and generation current for both abrupt and gradient junctions. Therefore, the following relationships were chosen finally for the approximation of multiplication factors:

$$1/M_n(U) = 1 - (U/U_B)^k \exp[-a((U/U_B)^{1/2} - 1)] \quad (9)$$

and

$$1/M_{p,g}(U) = 1 - (U/U_B)^k \times \exp[-a((U/U_B)^4 - 1)]. \quad (10)$$

In Table 1, the results of the approximation of the $M_n(U)$ dependence for the *p–n* junction with a donor-impurity concentration in the base $N_d = 10^{15}$ cm^{-3} are listed as an example. The calculated value of the breakdown voltage $U_B = 267.85$ V. The parameters of the approximation were $k = 9.845$ and $a = 18.160$.

The results of approximating according to the Miller–Moll formula (5) ($f = 0.80$, $n = 3.52$) are also given in Table 1. The relative rms error of the approximation for $(M_n - 1)$ from formula (9) was about 3% in

Table 1. Results of approximation of multiplication factors for electrons in an abrupt p^+–n junction with $N_d = 10^{15}$ cm^{-3}

U, B	U/U_B	$M_n - 1$				
		the values calculated according to expressions (1) and (2)	approximation according to expression (9)	error, %	approximation according to expression (5)	error, %
56.93	0.2125	0.0045	0.0043	–5.1	0.0097	115
69.40	0.2591	0.0131	0.0127	–3.2	0.0197	51
86.52	0.3230	0.0389	0.0388	–0.2	0.0437	12.2
106.91	0.3991	0.1036	0.1048	1.1	0.0966	–6.8
130.21	0.4861	0.2495	0.2521	1.0	0.2139	–14.3
151.78	0.5667	0.4969	0.4973	0.1	0.4329	–12.9
163.38	0.6100	0.7008	0.6969	–0.5	0.6433	–8.2
175.71	0.6560	0.9999	0.9883	–1.2	1.0224	2.3
183.91	0.6866	1.2651	1.2457	–1.5	1.4603	15.4
192.79	0.7198	1.6362	1.6059	–1.8	2.3406	43.1
199.80	0.7459	2.0131	1.9727	–2.0	3.8656	92.1
212.65	0.7939	2.9971	2.9382	–2.0	90.5	2920

the range of M_n varying from 1.01 to 3, whereas for the Miller–Moll relationship the error is larger than 40%.

Table 2 represents the results of approximation and relative rms error δ for $(M_p - 1)$ for the range of M_p varying from 1.01 to 3 for holes in gradient p–n junctions. As can be seen from Table 2, expression (10) approximates the multiplication factors for holes very well.

In general, the multiplication factors for gradient p–n junctions are approximated more accurately compared with those for abrupt junctions, for holes more accurately than for electrons, and for low-voltage p–n junctions more accurately than for high-voltage p–n junctions. All these tendencies are explained well if the differences in the b/E_m and α_n/α_p ratios are taken into account. The closer α_n/α_p is to unity at the breakdown voltage and the larger the b/E_m, the more valid are the assumptions based on which the approximation formula for multiplication factors is obtained.

Figures 2 and 3 show the dependences of the approximation parameters on the avalanche breakdown voltage of the p–n junction. For the n^+–p junctions, the dependences k and a differ only slightly from the corresponding curves for the p^+–n junctions and are not shown in Figs. 2 and 3. As can be seen from Fig. 2, the parameter a for electrons for all breakdown voltages differs from zero, which is indicative of the inadequacy of the Miller–Moll expression for the approximation of the $M_n(U)$ dependence. However, it can be seen from Fig. 3 that, for holes and a generation current in the range U_B = 30–50 V, $a = 0$. In this range, the Miller–Moll relationship is quite acceptable for the approximation of the $M_p(U)$ dependence. These rather smooth curves can be approximated by power polynomials. However, in order to retain the accuracy of the approximation, the degree of polynomials should be no less than three; i.e.,

$$k, a = C_0 + C_1 \ln U_B + C_2(\ln U_B)^2 + C_3(\ln U_B)^3,$$

where U_B is expressed in volts.

The coefficients of corresponding polynomials are given in Table 3. Of course, if we take different values of parameters A and b for the ionization coefficients $\alpha_n(E)$ and $\alpha_p(E)$, these coefficients will change. However, the approximation accuracy of multiplication factors by expressions (9) and (10) will remain high. If we narrow the range of variation in the breakdown voltage, the approximation accuracy may become even higher.

The approximate expressions obtained and the approximation parameters for the multiplication factors of electrons, holes, and generation current in Si p–n junc-

Table 2. Parameters of approximation for multiplication factors of holes in a gradient junction

grad$\lvert N_a - N_d \rvert$, cm^{-4}	U_{br}, B	a	k	δ, %
10^{16}	3488.72	–5.729	4.925	0.003
10^{17}	1346.06	–3.622	7.166	0.003
10^{18}	531.22	–2.120	7.991	0.003
10^{19}	215.59	–1.081	7.875	0.002
10^{20}	90.69	–0.389	7.177	0.002
10^{21}	40.00	0.054	6.172	0.007
10^{22}	18.85	0.332	5.067	0.020
10^{23}	9.79	0.486	3.946	0.045

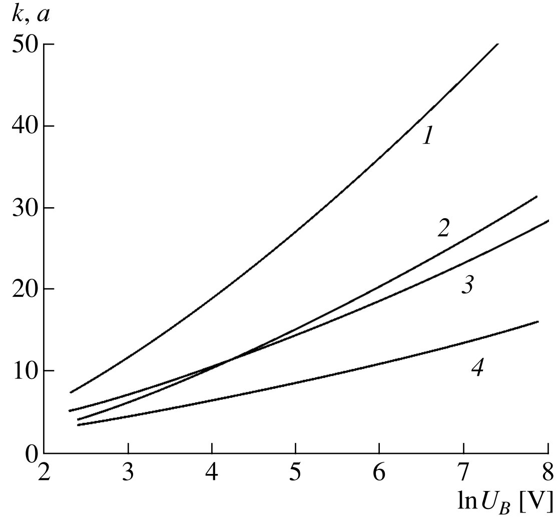

Fig. 2. Approximation parameters k and a for the electron multiplication: (*1*), (*2*) a for the gradient and abrupt p^+–n junctions, respectively; (*3*), (*4*) k for the gradient and abrupt p^+–n junctions, respectively.

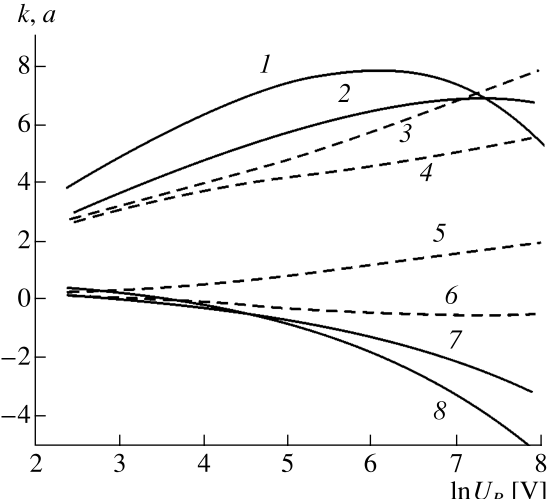

Fig. 3. Approximation parameters k and a for the multiplication of holes and generation current. Solid lines denote the multiplication for holes, and dashed lines denote the multiplication for the generation current. The upper group of curves, k: (*1*), (*3*) a gradient p–n junction, (*2*), (*4*) an abrupt p^+–n junction. The lower group of curves, a: (*5*), (*8*) a gradient p–n junction, (*6*), (*7*) an abrupt p^+–n junction.

tions allow one to describe the $M(U)$ dependences in the range of breakdown voltages from 10 to 3000 V with a high accuracy.

On the basis of assumptions concerning substantiation of the approximate formula, we may expect that expression (8) for the ionization integral will be applicable to many other semiconductor materials. Specifically, for GaAs and GaP, where $\alpha_n(E) = \alpha_p(E)$, and for Ge, where $\alpha_p(E) \approx 2\alpha_n(E)$, the approximation accuracy may be even higher. Expression (8) may also be applicable to cases where the ionization coefficients do not follow formula (4) exactly, since the dependences $\alpha(E)$ for most semiconductors are qualitatively similar.

Table 3. Coefficients in approximate formulas for parameters k and a

Multiplication	Junction type	Parameter	C_0	C_1	C_2	C_3
Electrons	p^+–n	k	-3.958×10^{-2}	1.051	1.345×10^{-1}	-1.165×10^{-3}
		a	–2.607	1.784	3.970×10^{-1}	-9.346×10^{-3}
	n^+–p	k	-4.972×10^{-1}	1.319	9.432×10^{-2}	-2.213×10^{-4}
		a	–3.588	2.673	2.659×10^{-1}	4.221×10^{-3}
	Gradient	k	-4.666×10^{-1}	1.687	2.682×10^{-1}	-3.800×10^{-3}
		a	–3.383	2.987	7.000×10^{-1}	-1.668×10^{-3}
Holes	p^+–n	k	9.504×10^{-1}	6.157×10^{-1}	1.786×10^{-1}	-2.032×10^{-2}
		a	7.324×10^{-1}	-2.458×10^{-1}	3.817×10^{-2}	-8.677×10^{-3}
	n^+–p	k	1.155	2.640×10^{-1}	2.630×10^{-1}	-2.802×10^{-2}
		a	8.519×10^{-1}	-2.823×10^{-1}	6.060×10^{-2}	-1.147×10^{-2}
	Gradient	k	1.647	2.876×10^{-1}	4.498×10^{-1}	-5.332×10^{-2}
		a	1.086	-3.801×10^{-1}	9.534×10^{-2}	-1.851×10^{-2}
Generation current	p^+–n	k	-5.685×10^{-1}	1.979	-2.829×10^{-1}	-1.692×10^{-2}
		a	2.734×10^{-1}	1.528×10^{-1}	-8.412×10^{-2}	6.964×10^{-3}
	n^+–p	k	7.411×10^{-1}	5.283×10^{-1}	7.316×10^{-4}	5.472×10^{-4}
		a	-2.268×10^{-1}	1.753×10^{-1}	2.615×10^{-2}	-1.741×10^{-3}
	Gradient	k	1.497	5.199×10^{-1}	3.637×10^{-2}	2.996×10^{-4}
		a	7.644×10^{-1}	-4.244×10^{-1}	1.223×10^{-1}	-5.933×10^{-3}

REFERENCES

1. I. V. Grekhov and Yu. N. Serezhkin, *Avalanche Breakdown of p–n Junctions in Semiconductors* (Énergiya, Leningrad, 1980).
2. S. L. Miller, Phys. Rev. **99**, 1234 (1955).
3. J. L. Moll, J. L. Su, and A. C. M. Wang, IEEE Trans. Electron Devices **5**, 420 (1970).
4. J. Maserjian, J. Appl. Phys. **30**, 1613 (1959).
5. P. G. Dermenzhi, V. A. Kuz'min, N. N. Kryukova, V. I. Mamonov, and V. Ya. Pavlik, *Calculation of Power Semiconductor Devices*, Ed. by V. A. Kuz'min (Énergiya, Moscow, 1980).
6. V. P. Grigorenko, P. G. Dermenzhi, V. A. Kuz'min, and T. T. Mnatsakanov, *Simulation and Automated of Design of Power Semiconductor Devices* (Énergoatomizdat, Moscow, 1988).
7. V. A. Kholodnov, Fiz. Tekh. Poluprovodn. (St. Petersburg) **30**, 1051 (1996) [Semiconductors **30**, 558 (1996)].
8. *Handbook of Mathematical Functions*, Ed. by M. Abramowitz and I. A. Stegun, 2nd ed. (Dover, New York, 1971; Nauka, Moscow, 1979).
9. A. S. Kyuregyan and S. N. Yurkov, Fiz. Tekh. Poluprovodn. (Leningrad) **23**, 1819 (1989) [Sov. Phys. Semicond. **23**, 1126 (1989)].

Translated by N. Korovin

Semiconductors, Vol. 37, No. 9, 2003, pp. 1090–1092. Translated from Fizika i Tekhnika Poluprovodnikov, Vol. 37, No. 9, 2003, pp. 1114–1116.
Original Russian Text Copyright © 2003 by Ivanov, Petrov, Tonkikh, Tsyrlin, Ustinov.

LOW-DIMENSIONAL SYSTEMS

Dependence of the Binding Energy of *A*(+) Centers on Quantum-Well Width in GaAs/AlGaAs Structures

Yu. L. Ivanov, P. V. Petrov, A. A. Tonkikh, G. É. Tsyrlin, and V. M. Ustinov

Ioffe Physicotechnical Institute, Russian Academy of Sciences, Politekhnicheskaya ul. 26, St. Petersburg, 194021 Russia

Submitted December 9, 2002; accepted for publication December 17, 2002

Abstract—The luminescence of GaAs/AlGaAs multiple-quantum-well structures with different well widths, containing *A*(+) centers, was studied to determine the dependence of the center binding energy on quantum-well width. It is shown that the binding energy of the *A*(+) centers increases markedly with decreasing well width, becoming ten times greater in 10-nm-wide wells than in the bulk material. The binding energy of *A*(+) centers was found to depend on their concentration. © *2003 MAIK "Nauka/Interperiodica".*

1. INTRODUCTION

The investigation of positively charged acceptors, the so-called *A*(+) centers, in GaAs/AlGaAs quantum wells begin in [1–3]. The energy position and the Bohr radius of the *A*(+) centers were established by measurements of the Hall effect [1] and low-temperature hopping transport over the *A*(+) band [2]. The binding energy of *A*(+) centers in 15-nm-thick quantum wells was found to be considerably higher than that for the bulk material. A study of the luminescence properties of *A*(+) centers was carried out [3]. It showed that the luminescence line related to the *A*(+) centers is due to the radiative transition of nonequilibrium electrons to an *A*(+) center, a process similar to the radiative capture of nonequilibrium electrons by a conventional acceptor center. This permits one to use luminescence data for determining the *A*(+)-center binding energy.

This communication reports on a luminescence analysis of quantum-well structures with *A*(+) centers for different well widths; it is aimed at the comprehensive investigation of the dependence of the *A*(+)-center binding energy on quantum-well width.

2. EXPERIMENTAL TECHNIQUE AND DATA PROCESSING

The samples were grown by MBE in an ÉP1203 setup on the singular (001) surface of semiinsulating GaAs substrates. The structures were grown at a constant substrate temperature of 580°C. The growth rates for GaAs and $Al_{0.35}Ga_{0.65}As$ layers were 0.2 and 0.3 nm/s, respectively. During growth, the structures were selectively doped with beryllium to a bulk hole concentration of 10^{17} cm^{-3} in GaAs. Each sample represented a set of ten GaAs quantum wells separated by 20-nm-thick AlGaAs barriers. The well width varied from 7 to 18 nm. In addition, for better confinement of the carriers in the quantum-well region, AlGaAs cap layers, 100 and 250 nm thick, were grown on the substrate and surface sides, respectively. Stationary *A*(+) centers in the quantum wells were produced by so-called double selective doping [4] (simultaneous doping of the quantum wells and the barriers). To do this, a 2-nm-wide layer at the center of each well and a 3-nm-wide layer at the center of each intermediate barrier were doped, whereas, in the barriers at the edges of first and last wells, 1.5-nm-thick layers were doped. Hall measurements of the bulk hole concentration in GaAs:Be and $Al_{0.35}Ga_{0.65}As$:Be samples suggested that this doping scheme provides approximately equal concentrations of impurity centers in the wells and the barriers. This gives rise to occupation of the levels of impurity centers in the wells by holes from the impurity centers in the barriers, i.e., to the formation of the *A*(+) centers. This method of quantum-well doping [5] does not, however, exclude a certain probability of finding some unoccupied *A*(0) centers.

An LGN-215 He–Ne laser was used for photoluminescence excitation. The samples were directly immersed in liquid helium. A pump light was injected into a sample, and the luminescence signal was extracted using a glass fiber providing a maximum pump light intensity of about 10 mW/mm^2. The sample luminescence was analyzed by a DFS-12 spectrometer interfaced to a nitrogen-vapor-cooled FÉU-62 photomultiplier. The spectra were taken in the photon-counting mode.

A typical photoluminescence spectrum of the structures under study contained two peaks, one of them due to the *A*(+)-center emission, and the other, to the recombination of excitons bound to neutral acceptors. A free-exciton peak may sometimes be observed. The amplitudes of the first two peaks depend linearly on the pump intensity. Both of these peaks are fairly broad, from 2–3 to 10 meV. The peak width increases with decreasing quantum-well size, which can be affributed both to the increasing relative fluctuation of the quantum-well width and to the fact that the dependence of the binding

1063-7826/03/3709-1090$24.00 © 2003 MAIK "Nauka/Interperiodica"

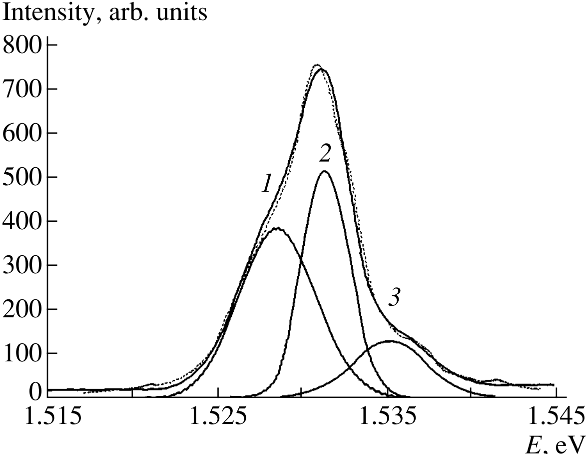

Fig. 1. Illustration of a spectral unfolding into Gaussian constituents. The peaks are due to (*1*) $A(+)$-center recombination, (*2*) a bound exciton, and (*3*) a free exciton.

energy on the position of the center in the well becomes significant for narrow wells. This gives rise to the problem of correct peak discrimination in the cases when the spacing between the peaks is comparable to their halfwidth. To establish the correct position of the luminescence peaks due to $A(+)$ centers and excitons, the spectra were first filter-smoothed by a fast Fourier transform. Following this procedure, the parameters of the Gaussian peaks were refined by successive least-squares iterations. Figure 1 illustrates this processing by the example of the spectrum of a sample with 18-nm-wide quantum wells recorded at 24 K. We readily see that the processing employed allows us to determine of the peak positions with a high accuracy.

In narrow [3], 10- to 15-nm-wide wells, the energy of the free-electron–$A(+)$-center transition is lower than the luminescence energy of the bound exciton. The binding energy of the $A(+)$ center is higher because of the stronger confining effect the well width exerts on the $A(+)$-center wave function of the. The reverse is true for a bulk material; specifically, the energy of the fransition of a free electron to the $A(+)$ center is higher than that of bound-exciton luminescence. (The $A(+)$-center binding energy is low.) Therefore, as the quantum-well width increases, the spacing between these peaks decreases, with the result that, in broad wells, the free-electron–$A(+)$-center transition energy becomes greater than the bound-exciton luminescence energy. To identify these peaks, the Gaussian unfolding procedure was complemented by determining the temperature dependence of the intensity of the corresponding peaks. This method is based on the observation that a bound-exciton peak disappears rapidly with increasing temperature because of the low binding energy between the exciton and the neutral center, whereas the intensity of the free-electron–$A(+)$-center radiative transitions decreases weakly. The above reasoning is illustrated by Fig. 2 for the cases of a "narrow" (Fig. 2a) and a "wide"

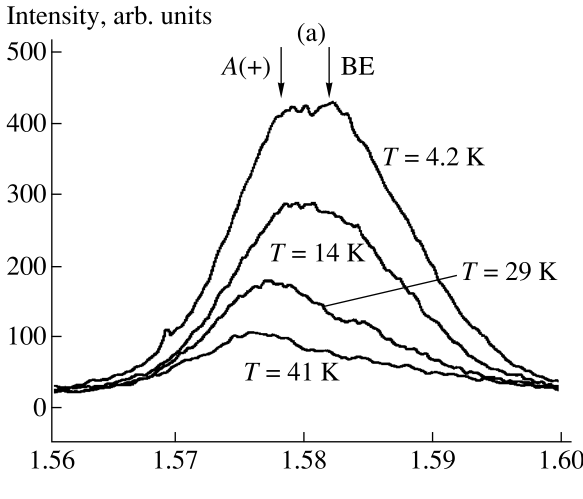

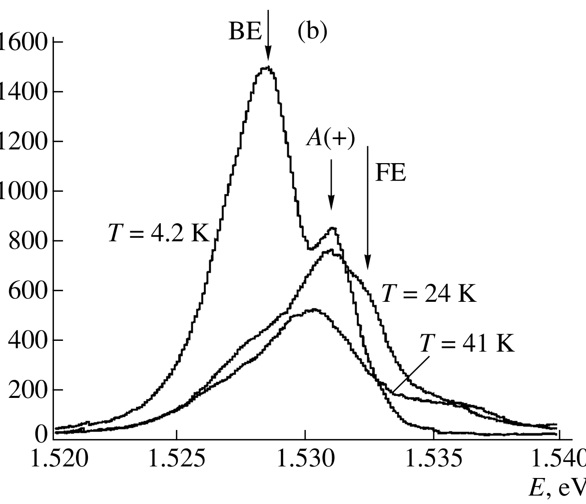

Fig. 2. Photoluminescence spectra of (a) sample *F*-335 with a well width of 70 Å and (b) sample *F*-338 with a well width of 180 Å, which were recorded at the specified temperatures. BE and FE denote the bound, and free excitons, respectively.

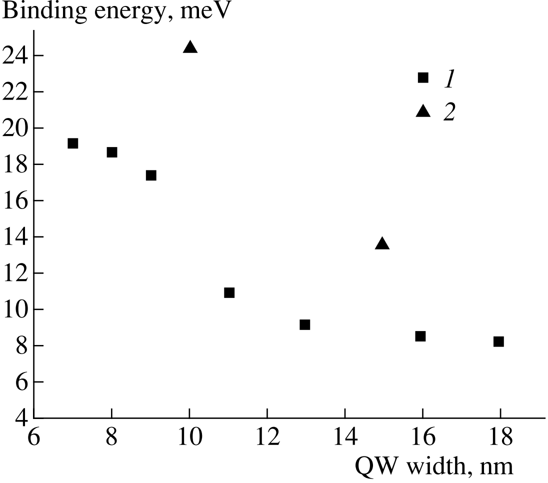

Fig. 3. (*1*) Dependence of the $A(+)$-center binding energy on quantum-well width and (*2*) data obtained for samples with a higher $A(+)$-center concentration [3].

(Fig. 2b) quantum well. We readily see that, while the right-hand wing of the common peak disappears with increasing temperature for "narrow" wells, for "broad" wells, it is the left-hand wing that fades with increasing temperature.

The binding energy of the $A(+)$ center was found by adding the energy difference between the $A(+)$ and bound-exciton peaks to the binding energy of the exciton bound to a neutral acceptor, which is available in the literature. The results are shown in Fig. 3. The binding energy of the $A(+)$ centers derived from the luminescence measurements is seen to increase with decreasing quantum-well width.

3. DISCUSSION

The results obtained in this study can be summarized as follows.

First, the binding energy in quantum wells of the width of interest, which is determined by photoluminescence, is indeed many times larger than the value reported for the bulk GaAs material [6]. This fact, described already in [1], is related to the large localization length of the $A(+)$ center, which is comparable to the quantum-well width and experiences the strong confining effect of the well.

Second, as the width of a well decreases, its confining effect on the $A(+)$-center wave function grows, which increases the center binding energy. The localization length of $A(+)$ centers in a 15-nm-wide quantum well was estimated to be 11 nm [2]. It is at these quantum-well widths where the binding energy in for samples under study is observed to increase (Fig. 3).

Third, the dependence of the binding energy of $A(+)$ centers on their concentration, derived by the photoluminescence technique, may be considered established. Figure 3 plots the measured binding energies [3] for samples with a higher $A(+)$-center concentration, $(4–6) \times 10^{17}$ cm^{-3}. The binding energy of $A(+)$ centers determined for these samples from photoluminescence measurements turned out to be higher than that for samples with a concentration of 10^{17} cm^{-3}. The reasons for the increase in the $A(+)$-center binding energy at higher doping levels are not completely understood. This phenomenon may be due to the potential fluctuations (irregularity of the band edges) as a result of the $A(+)$centers in a well being charged. It is also possible that the increase in the $A(+)$ binding energy at high concentrations of centers could be caused by the second Hubbard band as a whole. Note that the volume concentration of $A(+)$ centers of 10^{17} cm^{-3} chosen in this study may not be low enough, so that the $A(+)$ binding energy will not depend on the concentration of these centers. These issues require further study.

ACKNOWLEDGMENTS

This study was supported by the Russian Foundation for Basic Research (project no. 01-02-17912) and by the program "Optical and Nonlinear-Optical Properties of Nanostructures" (project no. 40.072.1.1.1175).

REFERENCES

1. N. V. Agrinskaya, Yu. L. Ivanov, V. M. Ustinov, and D. A. Poloskin, Fiz. Tekh. Poluprovodn. (St. Petersburg) **35**, 571 (2001) [Semiconductors **35**, 550 (2001)].
2. N. V. Agrinskaya, V. I. Kozub, Yu. L. Ivanov, *et al.*, Zh. Éksp. Teor. Fiz. **120**, 480 (2001) [JETP **93**, 424 (2001)].
3. Yu. L. Ivanov, N. V. Agrinskaya, P. V. Petrov, *et al.*, Fiz. Tekh. Poluprovodn. (St. Petersburg) **36**, 993 (2002) [Semiconductors **36**, 929 (2002)].
4. S. Huant, S. P. Najda, and B. Etienne, Phys. Rev. Lett. **65**, 1486 (1990).
5. D. Larsen, Phys. Rev. B **47**, 16333 (1993).
6. B. I. Shklovskiĭ and A. L. Éfros, *Electronic Properties of Doped Semiconductors* (Nauka, Moscow, 1979; Springer, New York, 1984).

Translated by G. Skrebtsov

Semiconductors, Vol. 37, No. 9, 2003, pp. 1093–1099. Translated from Fizika i Tekhnika Poluprovodnikov, Vol. 37, No. 9, 2003, pp. 1117–1122.
Original Russian Text Copyright © 2003 by Borisenko.

LOW-DIMENSIONAL SYSTEMS

Scattering of Electrons at Impurity Ions at Low Temperatures in a Superlattice with Doped Quantum Wells

S. I. Borisenko

Kuznetsov Physicotechnical Institute, pl. Revolyutsii 1, Tomsk, 634050 Russia

e-mail: sib@elefot.tsu.ru

Submitted November 11, 2002; accepted for publication December 19, 2002

Abstract—The longitudinal and transverse mobilities of electrons in a superlattice with doped quantum wells, limited by scattering of the electrons at impurity ions, are calculated. The case of low temperatures and low densities of charge carriers is considered. The Conwell–Weisskopf hypothesis of the minimum scattering angle is used to solve the Boltzmann equation for a nondegenerate electron gas in the region of weak screening of the Coulomb potential of impurity ions. The numerical calculations are performed for the symmetric superlattice $GaAs/Al_{0.36}Ga_{0.64}As$ with a period of 10 nm and an electron concentration of 10^{14} cm^{-3} at $T = 20$ K. © *2003 MAIK "Nauka/Interperiodica".*

1. INTRODUCTION

As is known, scattering of electrons and holes by impurity ions at low temperatures is one of the main scattering mechanisms not only for bulk semiconductors, but also for low-dimensional heterostructures based on them. The effect of this scattering mechanism on the electron mobility in individual quantum wells (QWs) has been widely investigated [1–9]. Superlattices (SLs) composed of QWs have been studied much less [10, 11]. Most studies devoted to SLs are aimed at investigating the electrical properties of a degenerate electron gas that arises due to the selective doping of the layers which serve as potential barriers in the structures considered (such structures are used to design high-electron-mobility transistors (HEMTs)) [12]. Few, if any, studies are devoted to the analysis of the transport properties of a nondegenerate electron gas in SLs, which appears as a result of uniform doping or doping of QWs. As is known, SLs composed of QWs are used in fabrication of infrared photodetectors operating on intersubband transitions [13, 14]. It is difficult to take into account the scattering by impurity ions in terms of the Brooks–Herring theory because of weak screening of the Coulomb potential of ions caused by low concentrations of free charge carriers and their low velocities. All these factors result in very large integrated scattering cross sections, thus hindering numerical calculations of the transport cross section, which governs the relaxation time for the charge-carrier momentum. In bulk semiconductors with an isotropic parabolic spectrum, this problem is solved in terms of the Conwell–Weisskopf hypothesis of the finite value of the integrated scattering cross section, which is controlled by the average distance between impurity ions. For low-dimensional semiconductor structures, such as superlattices consisting of quantum wells, this problem has not been considered yet.

In this study formulas, in terms of the Born approximation for the scattering probability, are obtained with the use of the Boltzmann equation and the components of the relaxation-time tensor and the mobility of nondegenerate electrons in the lower miniband are calculated for the case of scattering by impurity ions in a symmetric $GaAs/Al_{0.36}Ga_{0.64}As$ SL with doped QWs. Calculations were performed for a sample with an electron concentration $n = 10^{14}$ cm^{-3} and a superlattice period of 10 nm at $T = 20$ K. In solving the Boltzmann equation and calculating the scattering probability, the Conwell–Weisskopf approximation for the minimum scattering angle and the Debye screening for the Coulomb potential of ions were taken into account. The effect of taking into account the Conwell–Weisskopf approximation on the calculated relaxation time and electron mobility is analyzed.

2. BASIC FORMULAS

The calculation of the probability of scattering of electrons by impurity ions in an SL with doped QWs was performed in the Born approximation by the formula

$$w(\mathbf{k}, \mathbf{k}') = \frac{2\pi e^4 Z^2 N_I}{\hbar \varepsilon_0^2 \varepsilon^2 V} \sum_{n, n' = -N_z/2}^{N_z/2} S_n^* S_{n'} W(\mathbf{q}_n) W(\mathbf{q}_{n'}) \times \frac{\sin\left[\pi \frac{a}{d}(n - n')\right]}{\pi \frac{a}{d}(n - n')} \delta(E(\mathbf{k}') - E(\mathbf{k})), \tag{1}$$

where

$$S_n = \frac{1}{d}\int_{-d/2}^{d/2} e^{i\frac{2\pi n}{d}z}|u_0(z)|^2 dz, \quad W(\mathbf{q}) = \frac{1}{\mathbf{q}^2 + \alpha^2},$$

$$E(\mathbf{k}) = E = E_\perp + \frac{\Delta}{2}[1 - \cos(k_z d)], \quad E_\perp = \frac{\hbar^2 k_\perp^2}{2m_\perp},$$

$\mathbf{k}$ and $\mathbf{k}'$ are the wave vectors of the initial and final states of an electron in the lower miniband; $\mathbf{q}_n = \mathbf{k}' - \mathbf{k} + \frac{2\pi n}{d}\mathbf{e}_z$; $\mathbf{e}_z$ is the unit vector along the SL axis; $-\frac{N_z}{2} < n < \frac{N_z}{2}$; N_z is the number of the SL periods, which is assumed to be infinitely large; Δ is the width of the lower miniband; a and d are the width of a QW and the period of the SL, respectively; eZ and $N_I = aN_I^{QW}/d$ are the charge and the average concentration of impurity ions in the SL, respectively; N_I^{QW} is the concentration of impurity ions in a QW; α is the Debye screening factor; ε is the static permittivity; and $u_0(z)$ is the periodic part of the envelope of the Bloch function $u_{k_z}(z)$ at $k_z = 0$. Formula (1) is obtained in the random-phase approximation for the case of uniform impurity distribution over a QW, on the assumption that the permittivity is distributed uniformly over the SL and that the function $u_{k_z}(z)$ depends weakly on k_z.

The additional nonequilibrium term in the distribution function of electrons was calculated in the form

$$g(\mathbf{k}) = e\frac{\partial f_0}{\partial \varepsilon}\sum_i \tau_i(\mathbf{k})F_i \mathbf{v}_i(\mathbf{k}), \tag{2}$$

where F_i are the components of the strength of a constant electric field, $\mathbf{v}(\mathbf{k}) = \nabla_{\mathbf{k}}E/\hbar$ is the velocity of an electron, and $f_0(\varepsilon)$ is the equilibrium Fermi–Dirac function. By analogy with the solution to the linearized Boltzmann equation for elastic scattering mechanisms in the approximation of the parabolic dispersion relation for charge carriers, the function $\tau_i(\mathbf{k})$ will be referred to in the usual way as the relaxation time. For calculating these functions with the use of the linearized Boltzmann equation, we derived the integral equations

$$\tau_\perp(\mathbf{k}) = \tau_0(\mathbf{k})\left\{\sum_{\mathbf{k}'} w(\mathbf{k}, \mathbf{k}')\tau_\perp(\mathbf{k}')\frac{k_\perp k'_\perp}{k_\perp^2} + 1\right\}, \tag{3}$$

$$\tau_\parallel(\mathbf{k}) = \tau_0(\mathbf{k})\left\{\sum_{\mathbf{k}'} w(\mathbf{k}, \mathbf{k}')\tau_\parallel(\mathbf{k}')\frac{\sin(k'_z d)}{\sin(k_z d)} + 1\right\}, \tag{4}$$

where

$$\tau_0^{-1}(\mathbf{k}) = \sum_{\mathbf{k}'} w(\mathbf{k}, \mathbf{k}') \tag{5}$$

is the total probability of scattering of an electron from the state with the wave vector $\mathbf{k}$ per unit time. Using the formula for the scattering probability (1) and disregarding all the terms in the sum in formula (1), except for $n = n' = 0$, we can represent Eqs. (3) and (4) in the form

$$\frac{\tau_\perp(E_\perp, \theta)}{\tau_0(E_\perp, \theta)} = C_I\int_{-\pi}^{+\pi}\int_{-1}^{\beta}\frac{\tau_\perp(E'_\perp, \theta')\sqrt{E'_\perp/E_\perp}\,\Theta(E'_\perp)x\,dx\,d\theta'}{\sqrt{1 - x^2}(A - Bx)^2} + 1, \tag{6}$$

$$\frac{\chi_\parallel(E_\perp, \theta)}{\tau_0(E_\perp, \theta)} = C_I\int_{-\pi}^{+\pi}\int_{-1}^{\beta}\frac{\chi_\parallel(E'_\perp, \theta')\Theta(E'_\perp)\,dx\,d\theta'}{\sqrt{1 - x^2}(A - Bx)^2} + \sin\theta, \tag{7}$$

where

$$A = E'_\perp + E_\perp + t^2(\theta' - \theta)^2 + \zeta^2,$$

$$B = 2(E'_\perp E_\perp)^{1/2},$$

$$\frac{1}{\tau_0(E_\perp, \theta)} = C_I\int_{-\pi}^{+\pi}\int_{-1}^{\beta}\frac{\Theta(E'_\perp)\,dx\,d\theta'}{\sqrt{(1 - x^2)(A - Bx)^2}}, \tag{8}$$

$$E'_\perp = E_\perp + \frac{\Delta}{2}(\cos\theta' - \cos\theta),$$

$$\chi_\parallel(E_\perp, \theta) = \tau_\parallel(E_\perp, \theta)\sin\theta, \tag{9}$$

$$C_I = 2\left(\frac{e^2 Z}{4\pi\varepsilon_0\varepsilon}\right)^2\frac{\hbar N_I}{m_\perp d}, \quad t^2 = \frac{\hbar^2}{2m_\perp d^2}, \quad \zeta^2 = \frac{\hbar^2\alpha^2}{2m_\perp}$$

is the transverse energy of the final state; $x = \cos\varphi$, φ is the angle between $k_\perp$ and $k'_\perp$; $\theta = k_z d$; and $\Theta(E_\perp)$ is the theta function, which is nonzero and equal to unity at positive values of the argument. After integration over x, which leads to the analytical expressions (see Appendix 1), formulas (6)–(8) are reduced to single integrals. If, at a specified value of $\mathbf{k}$, the integrated effective scattering cross section S_α^* calculated with regard to the screening of the Coulomb potential did not exceed the quantity

$$S_{\max}^* = \frac{\pi}{4}N_I^{-2/3},$$

the parameter β was assumed to be unity. According to the Brooks–Herring theory, this value of β corresponds to the possibility of scattering of an electron by an individual impurity ion from the specified state at any value of the impact parameter i.e., it corresponds to the description in terms of the single-particle scattering theory. If this condition is not satisfied, then according

to the Conwell–Weisskopf theory, when integrating over the angles in formulas (6)–(8) we have to take into account the presence of the minimum impact parameter or minimum scattering angle δ of the vector $\mathbf{k}$ with vector $\mathbf{k}'$. This angle is determined from the condition for the equality of the integrated effective cross section to the maximum value

$$S^*_{\max} = S^*_{\alpha} = [N_I \mathbf{v}(\mathbf{k})\tau_0(\mathbf{k})]^{-1} \tag{10}$$

at

$$\frac{k'_\perp k_\perp x + k'_z k_z}{k'k} \le \cos\delta. \tag{11}$$

The joint solution of Eqs. (8) and (10) with consideration of condition (11) makes it possible to determine the parameter β as a function of the transverse energy $E_\perp$ and the parameter θ. In the case of bulk semiconductors with an isotropic parabolic energy spectrum of electrons, the introduction of the minimum scattering angle, according to formulas (10) and (11), into the Brooks–Herring theory leads to the formula for the dependence of the relaxation time on the energy E, which can be referred to as the generalized Brooks–Herring and Conwell–Weisskopf formula (see Appendix 2):

$$\frac{1}{\tau_I(E)} = \frac{e^4 Z^2 N_I E^{-3/2}}{16\pi\varepsilon_0^2\varepsilon_s^2\sqrt{2m^*}}\left[\ln\left(\frac{1+\eta}{1+\eta\gamma}\right) - \frac{\eta(1-\gamma)}{(1+\eta)(1+\eta\gamma)}\right], \tag{12}$$

where

$$\gamma = \sin^2\left(\frac{\delta}{2}\right) = \frac{\eta(\eta C^2 - 1) - 1}{\eta(\eta C^2 + \eta + 1)}\Theta(\eta^2 C^2 - \eta - 1),$$
$$C = \frac{e^2 Z N_I^{1/3}}{4\pi\varepsilon_0\varepsilon E}, \quad \eta = \frac{4E}{\zeta^2}. \tag{13}$$

Equations (6) and (7) are nonlinear integral equations with two variables $E_\perp$ and θ. In the approximation of quasi-two-dimensional electron gas ($\Delta \ll k_0 T$) and at $\Delta = 0$ in formulas (6)–(9), the integral equations transform into equations with one variable θ, which parametrically depend on $E_\perp$. Equations (6) and (7) were solved numerically by an iterative procedure. The solution to these equations obtained in terms of the quasi-two-dimensional approximation by the difference method [15] was used as a zero-order approximation.

The electron mobility was calculated by the formulas

$$\mu_{xx} = \mu_{yy} = \mu_\perp = e\langle\tau_\perp\rangle/m_\perp,$$
$$\mu_{zz} = \mu_\parallel = e\langle\tau_\parallel\rangle/\langle m_\parallel\rangle, \tag{14}$$

where

$$\langle\tau_\perp\rangle = \frac{\int_0^\infty [-f'_0(E_\perp)]\tau_\perp(E_\perp)E_\perp dE_\perp}{\int_0^\infty f_0(E_\perp)dE_\perp}, \tag{15}$$

$$\langle\tau_\parallel\rangle = \frac{\int_0^\infty [-f'_0(E_\perp)]\tau_\parallel(E_\perp)d\varepsilon_\perp}{\int_0^\infty [-f'_0(E_\perp)]dE_\perp}, \tag{16}$$

$$\tau_\perp(E_\perp) = \frac{1}{\pi}\int_0^\pi \tau_\perp(E_\perp, \theta)d\theta,$$

$$\tau_\parallel(E_\perp) = \frac{2}{\pi}\int_0^\pi \tau_\parallel(E_\perp, \theta)\sin^2(\theta)d\theta, \tag{17}$$

$$\frac{1}{\langle m_\parallel\rangle} = \frac{1}{2}\left(\frac{\Delta d}{2\hbar}\right)^2 \frac{\int_0^\infty [-f'_0(E_\perp)]dE_\perp}{\int_0^\infty f_0(E_\perp)dE_\perp} \tag{18}$$

is the inverse longitudinal effective electron mass averaged over energy.

3. NUMERICAL ANALYSIS

The relaxation time and the electron mobility governed by scattering of electrons by impurity ions were calculated for the symmetric composite $GaAs/Al_{0.36}Ga_{0.64}As$ superlattice with doped 5-nm-wide quantum wells at $T = 20$ K. In the calculations, the following parameters were used for GaAs and for the $Al_xGa_{1-x}As$ [16] alloy: $m_\perp = m^* = 0.066m_0$ and $\varepsilon = 13.18$. The width of the lower miniband $\Delta = 7.1$ meV, which was calculated for the specified SL by the method described in [17], significantly exceeds the average value of the energy of nondegenerate electrons with a concentration $n = N_I = 10^{14}$ cm^{-3} at a value of the Fermi level equal to $-5k_0T$. The results of calculating the components of the relaxation-time tensor and the mobility in the Brooks–Herring approximation ($\alpha \ne 0$, $\beta = 1$; approximation 1); the Conwell–Weisskopf approximation ($\alpha = 0$, $\beta < 1$; approximation 2); and the generalized Brooks–Herring and Conwell–Weisskopf approximation ($\alpha \ne 0$, $\beta \le 1$; approximation 3) are listed in the table. The values of the longitudinal mobility listed were obtained at $\langle m_\parallel\rangle = 0.30m_0$. According to the table, the calculated values of the transverse relaxation

Average values of the components of the relaxation-time tensor and the mobilities of electrons in the superlattice

Approximation	$\langle\tau_\perp\rangle$, ps	$\langle\tau_\parallel\rangle$, ps	$\mu_\perp$, $m^2 V^{-1} s^{-1}$	$\mu_\parallel$, $m^2 V^{-1} s^{-1}$	τ_{GaAs}, ps
1	13	30	34	17	13
2	15	36	40	21	15
3	15	38	41	22	16

time averaged over energy are close to the corresponding values for bulk GaAs and depend weakly on the approximation used. The averaged values of the longitudinal relaxation time calculated in different approximations differ more significantly. As one might expect, the calculation method based on the generalized approximation yields the largest values of the relaxation time and mobility. We should note that, at the temperature considered, the values of mobility governed by scattering of electrons by impurity ions with the concentration noted are close to the corresponding values governed by inelastic scattering at acoustic phonons in an SL calculated by the procedure suggested in [18]: $\mu_\perp = 50$ $m^2/(V\ s)$ and $\mu_\parallel = 13$ $m^2/(V\ s)$.

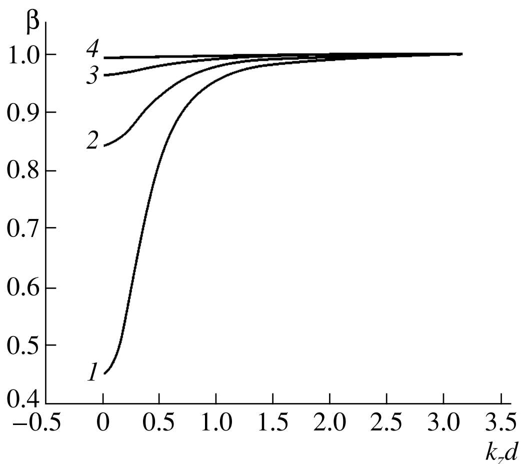

Fig. 1. Dispersion of the parameter β over the longitudinal wave vector. The ratio $E_\perp/k_0T$ is (*1*) 0.5, (*2*) 1, (*3*) 2, and (*4*) 4.

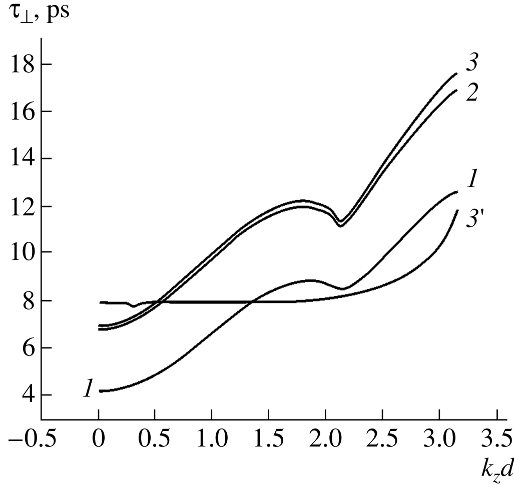

Fig. 2. Dispersion of the transverse relaxation time over the longitudinal wave vector calculated in the approximations (*1*) 1, (*2*) 2, and (*3*) 3, respectively (see table); (*3*') represents the results of calculation using the quasi-two-dimensional approximation.

Figure 1 shows the dispersion of the parameter β over the longitudinal wave vector calculated in terms of the generalized approximation for different values of the transverse energy. It can be seen from Fig. 1 that a noticeable dispersion of this parameter, as should be expected, occurs at small values of the total energy (the sum of longitudinal and transverse energies) of an electron.

Figures 2 and 3 show, respectively, the dispersions of the transverse relaxation time and the function $\chi_\parallel$ over the longitudinal wave vector calculated by formulas (6) and (9) at $E_\perp = k_0T$ in approximations 1 (curves *1*), 2 (curves *2*), and 3 (curves *3*). The variance of the functions noted is nonmonotonic, which is due to the dispersion of the energy of longitudinal motion along k_z. This statement follows from the shape of the dependence of the functions noted calculated in generalized approximation 3 using the quasi-two-dimensional approximation for the electron gas (curves *3*').

The dispersions of the transverse and longitudinal relaxation times over the energy of transverse motion averaged over the longitudinal wave vector (see formulas (16)) are shown in Figs. 4 and 5, respectively. It follows from Fig. 4 that the dispersion of the transverse relaxation time calculated in different approximations is almost the same and close to the dispersion of the relaxation time calculated by formula (12) for bulk GaAs (Fig. 5, curve *4*). For the longitudinal relaxation time (Fig. 5), the dispersions calculated in different approximations differ noticeably. In addition, according to Fig. 5, a significant difference between the values of the longitudinal relaxation time for the SL and for bulk GaAs is also observed.

In accordance with formulas (6), (7), and (10), the function $\tau_0^{-1}(\mathbf{k})$, which is defined by formulas (5) and (8) and represents the total probability of scattering of an electron from the state with the wave vector **k**, plays an important role in the calculations of the relaxation time. The dispersion of this function over the longitudinal wave vector at $E_\perp = k_0T$, calculated in different approximations, is shown in Fig. 6. According to Fig. 6, the value of this function calculated in the Conwell–

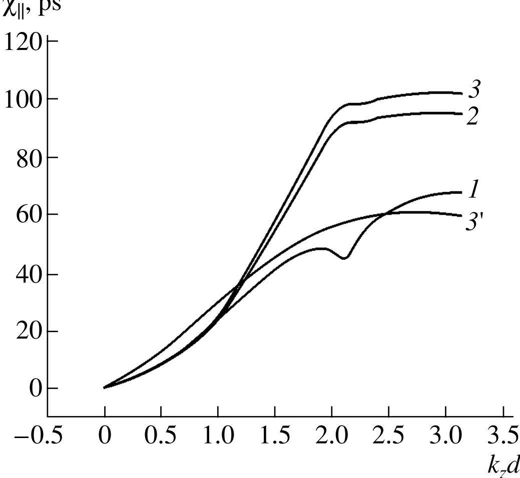

Fig. 3. Dispersion of the function $\chi_{\|}$ over the longitudinal wave vector calculated in the approximations (*1*) 1, (*2*) 2, and (*3*) 3, respectively (see table); (*3*') represents the results of calculation using the quasi-two-dimensional approximation.

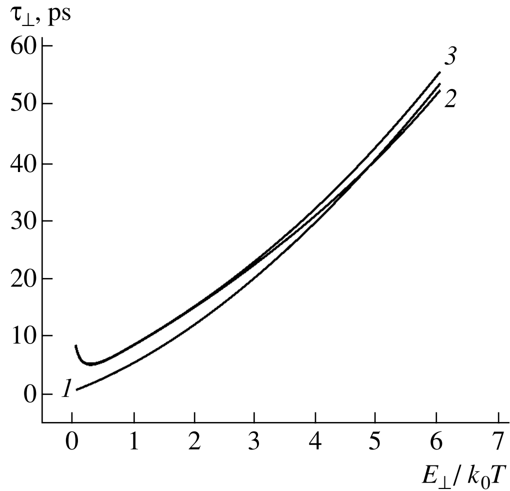

Fig. 4. Dispersion of the transverse relaxation time over the energy of the transverse motion averaged over the longitudinal wave vector. Designations (*1*–*3*) are the same as in Fig. 2.

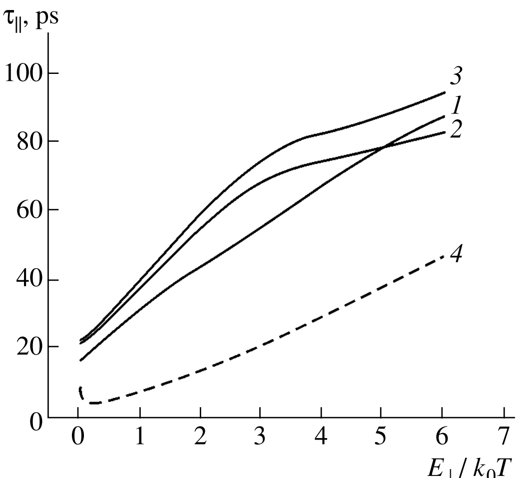

Fig. 5. Dispersion of the longitudinal relaxation time over the energy of the transverse motion averaged over the longitudinal wave vector. Designations (*1*–*3*) are the same as in Fig. 2. (*4*) Represents the results of calculations for bulk GaAs (12).

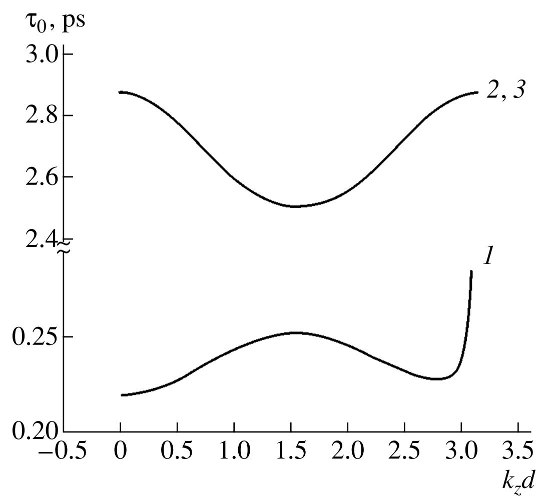

Fig. 6. Dispersion of the function $\tau_0(\mathbf{k})$ over the longitudinal wave vector. Designations (*1*–*3*) are the same as in Fig. 2.

Weisskopf and generalized approximations (curves *2* and *3*, respectively) exceeds the corresponding value calculated in the Brooks–Herring approximation (curve *1*) by an order of magnitude.

4. CONCLUSION

The analysis performed showed that the calculation of the longitudinal and transverse relaxation times for nondegenerate electron gas in a superlattice carried out in the Conwell–Weisskopf approximation with allowance made for weak screening of the Coulomb potential of impurity atoms in the Debye approximation yields results similar to those obtained in the Brooks–Herring approximation. Notably, the average value of the transverse relaxation time is similar to the corresponding value for a bulk semiconductor in which a quantum well is formed. This fact is related to the strong dependence of the Fourier component of the Coulomb potential on the wave vector in the region of small wave vectors in the case of weak Debye screening.

We should note that the results obtained are qualitative in view of the following. The temperature considered is out of the temperature range where the Born

approximation may be applied with confidence to the calculation of the scattering probability. At the same time, the applicability of the Boltzmann equation is justified by small values of the impurity concentration. As a result of an increase in temperature, accompanied by enhanced scattering of electrons by phonons, the scattering by impurity ions begins to play an important role at higher concentrations of ions and electrons, which, in turn, removes the problem of the applicability of the Born approximation, as well as the problem of weak screening of the Coulomb potential of impurity ions.

APPENDIX 1

The integrand in formula (6), which depends on x, has a fairly simple form, which allows us to reduce the integral over x to the analytical expression

$$\int_{-1}^{\beta}\frac{xdx}{\sqrt{1-x^2}(A-Bx)^2} = -\frac{1}{A^2-B^2}\left[\frac{A\sqrt{1-\beta^2}}{A-\beta B} + i\frac{B}{\sqrt{A^2-B^2}}\ln\left(\frac{B-\beta A+i\sqrt{(A^2-B^2)(1-\beta^2)}}{A-\beta B}\right)\right], \quad \text{(A.1,1)}$$

where

$$A = E'_{\perp}+E_{\perp}+t^2(\theta'-\theta)^2+\zeta^2, \quad B = 2\sqrt{E'_{\perp}E_{\perp}}.$$

The integrals in formulas (7) and (8) can be transformed similarly:

$$\int_{-1}^{\beta}\frac{dx}{\sqrt{1-x^2}(A-Bx)^2} = -\frac{1}{A^2-B^2}\left[\frac{B\sqrt{1-\beta^2}}{A-\beta B} + i\frac{A}{\sqrt{A^2-B^2}}\ln\left(\frac{B-\beta A+i\sqrt{(A^2-B^2)(1-\beta^2)}}{A-\beta B}\right)\right]. \quad \text{(A.1,2)}$$

At $\beta = 1$ (the case of a finite scattering cross section due to the screening of the Coulomb potential), the right-hand side of formula (A.1,1) is simplified considerably:

$$\int_{-1}^{1}\frac{xdx}{\sqrt{1-x^2(A-Bx)^2}} = \frac{\pi B}{(A^2-B^2)^{3/2}}, \quad \text{(A.1,3)}$$

$$\int_{-1}^{1}\frac{dx}{\sqrt{1-x^2(A-Bx)^2}} = \frac{\pi A}{(A^2-B^2)^{3/2}}. \quad \text{(A.1,4)}$$

APPENDIX 2

As is known [19], in the Born approximation, the probability of scattering of an electron at the screened potential of an impurity ion in a bulk semiconductor has the form

$$w(\mathbf{k},\mathbf{k}') = \frac{2\pi e^4Z^2N_I}{\hbar\varepsilon_0^2\varepsilon^2V}\frac{1}{[(\mathbf{k}'-\mathbf{k})^2+\alpha^2]^2}\delta(E(\mathbf{k}')-E(\mathbf{k})). \quad \text{(A.2,1)}$$

In the case of an isotropic parabolic energy spectrum of electrons, the integrated effective scattering cross section S_α^* calculated for an electron with the energy E, with regard to (A.2,1) and the minimum scattering angle δ, has the analytical form

$$S_\alpha^*(E,\delta) = \frac{1}{v(E)N_I}\sum_{\mathbf{k}'}w(\mathbf{k},\mathbf{k}') = 2\pi A_1^2 \times\int_{\delta}^{\pi}\frac{\sin(\theta)d\theta}{[\eta^{-1}+\sin^2(\theta/2)]^2} = 4\pi A_1^2\eta\left(\frac{1}{1+\eta\gamma}-\frac{1}{1+\eta}\right), \quad \text{(A.2,2)}$$

where

$$A_1 = \frac{e^2Z}{16\pi\varepsilon_0\varepsilon E}.$$

The other designations are the same as in formula (12). Formula (12) for the relaxation time is derived in the ordinary way by calculating the transport effective cross section $\sigma_c(E,\delta)$:

$$\frac{1}{\tau_I(E)} = N_Iv(E)\sigma_c(E,\delta). \quad \text{(A.2,3)}$$

Here, by definition,

$$\sigma_c(E,\delta) = \frac{1}{v(E)N_I}\sum_{\mathbf{k}'}\left(1-\frac{\mathbf{k}'\mathbf{k}}{k^2}\right)w(\mathbf{k},\mathbf{k}') = 2\pi A_1^2\int_{\delta}^{\pi}\frac{[1-\cos\theta]\sin(\theta)d\theta}{[\eta^{-1}+\sin^2(\theta/2)]^2} = 8\pi A_1^2\left\{\ln\left(\frac{1+\eta}{1+\eta\gamma}\right)-\frac{1}{1+\eta\gamma}+\frac{1}{1+\eta}\right\}. \quad \text{(A.2,4)}$$

Assuming that $S_\alpha^*(E,0) > S_{\max}^*$ and equating (A.2,2) to $S_{\max}^*$, we obtain yields formula (13) for the parameter $\gamma > 0$. In the opposite case, γ should be assumed as zero, which corresponds to the case of $\delta = 0$. In this case, formula (12) transforms into the known Brooks–Herring formula. With an electron concentration $n \longrightarrow 0$, the parameter $\eta \longrightarrow \infty$ and formulas (12) and (13) transform into the known formulas of the Conwell–Weisskopf theory [20] for the relaxation time and the minimum scattering angle. Hence, the relaxation time calculated by formula (12) is the longest relative to the

relaxation time calculated by the Brooks–Herring and Conwell–Weisskopf formulas.

REFERENCES

1. J. Lee, H. N. Spector, and V. K. Arora, J. Appl. Phys. **54**, 6995 (1983).
2. A. Gold and V. T. Dolgopolov, Phys. Rev. B **33**, 1076 (1986).
3. A. Gold, Phys. Rev. B **35**, 723 (1987).
4. J. L. Thobel, L. Baudry, F. Dessenne, *et al.*, J. Appl. Phys. **73**, 233 (1993).
5. I. Kaoru and M. Toshinobu, Phys. Rev. B **47**, 3771 (1993).
6. J. Tutor, J. A. Bermudez, and F. Comas, Phys. Rev. B **47**, 3690 (1993).
7. V. M. Borzdov, S. G. Mulyarchik, and A. V. Khomich, Pis'ma Zh. Tekh. Fiz. **23** (12), 77 (1997) [Tech. Phys. Lett. **23**, 935 (1997)].
8. V. Piazza, P. Casarini, D. F. Silvano, *et al.*, Phys. Rev. B **57**, 10017 (1998).
9. S. K. Sarkar and D. Chattopadhyay, Phys. Rev. B **62**, 15331 (2000).
10. S.-R. E. Yang and S. D. Sarma, Phys. Rev. B **37**, 10090 (1988).
11. A. B. Henriques, P. L. Souza, and B. Yavich, Phys. Rev. B **64**, 45319 (2001).
12. *Molecular Bean Epitaxy and Heterostructures*, Ed. by L. L. Chang and K. Ploog (Martimus Nishoff, Amsterdam, 1985; Mir, Moscow, 1989).
13. B. F. Levin, K. K. Choi, C. G. Bethea, *et al.*, Appl. Phys. Lett. **50**, 1092 (1987).
14. K. K. Choi, B. F. Levin, C. G. Bethea, *et al.*, Appl. Phys. Lett. **50**, 1814 (1987).
15. N. N. Kalitkin, *Numerical Methods* (Nauka, Moscow, 1978), Chap. 14, p. 455.
16. Landolt–Börnstein, *Numerical Date and Functional Relationships in Science and Technology*, Ed. by O. Madelung (Springer, Berlin, 1987), New Ser. 3, Vol. 22a.
17. S. I. Borisenko and G. F. Karavaev, Fiz. Tekh. Poluprovodn. (St. Petersburg) **32**, 607 (1998) [Semiconductors **32**, 544 (1998)].
18. S. I. Borisenko, Fiz. Tekh. Poluprovodn. (St. Petersburg) **36**, 1445 (2002) [Semiconductors **36**, 1360 (2002)].
19. B. B. K. Ridley, *Quantum Processes in Semiconductors* (Clarendon Press, Oxford, 1982; Mir, Moscow, 1986).
20. E. M. Conwell and V. F. Weisskopf, Phys. Rev. **77**, 388 (1950).

Translated by Yu. Sin'kov

Semiconductors, Vol. 37, No. 9, 2003, pp. 1100–1103. Translated from Fizika i Tekhnika Poluprovodnikov, Vol. 37, No. 9, 2003, pp. 1123–1126.
Original Russian Text Copyright © 2003 by Gastev, Emel'yanov, Sobolev, Andreev, Krasil'nik, Shmagin.

LOW-DIMENSIONAL SYSTEMS

Effective Cross Section for Photoluminescence Excitation and Lifetime of Excited Er^{3+} Ions in Selectively Doped Multilayer Si:Er Structures

S. V. Gastev*, A. M. Emel'yanov*, N. A. Sobolev*, B. A. Andreev, Z. F. Krasil'nik*, and V. B. Shmagin****

**Ioffe Physicotechnical Institute, Russian Academy of Sciences, St. Petersburg, 194021 Russia*

***Institute for Physics of Microstructures, Russian Academy of Sciences, Nizhni Novgorod, 603095 Russia*

**e-mail: nick@sobolev.ioffe.ru*

Submitted January 17, 2003; accepted for publication January 21, 2003

Abstract—The effective cross section for photoluminescence (PL) excitation and lifetime of erbium ions in an excited state have been determined in Si:Er/Si/Si:Er/Si…/Si structures fabricated by sublimation molecular beam epitaxy. The obtained results show that a considerable enhancement of PL intensity from erbium ions in selectively doped silicon, compared with that doped uniformly, is not related to changes in the radiative lifetime, effective cross section for excitation, or lifetime of erbium ions in the excited state. © *2003 MAIK "Nauka/Interperiodica".*

INTRODUCTION

Studies of photoluminescence (PL) in semiconductor structures doped with rare-earth elements are aimed at designing new light emitters for optoelectronic applications. Numerous publications have been devoted to the luminescence of Er ions in Si (see, e.g., [1–17]). Topical problems here are the raising of the emission intensity of Er ions and the excitation efficiency. Nowadays, a high intensity of Er-ion PL at low temperatures is obtained in Er-doped Si layers produced by molecular-beam epitaxy (MBE) [4–7]. Studies of structures fabricated by sublimation MBE (SMBE) have shown that in periodically doped structures, where the layers of pure Si alternate with Er-doped Si (Si:Er) layers, the intensity of Er-ion PL can be significantly raised in comparison with uniformly doped structures [7, 13]. The PL intensity increase in these structures can be attributed both to an increase in the concentration of excited optically active centers and a decrease in the radiative lifetime (τ_{rad}) of Er^{3+} ions as compared with that in uniformly doped structures. This conclusion follows from the fact that the PL intensity is directly proportional to the number of excited Er ions and inversely proportional to τ_{rad} [3, 8]. No answer has been hitherto obtained to the question of which of these factors is the principal one. The parameters characterizing the efficiency of the radiative energy conversion, namely the effective cross-section of Er-ion PL excitation and the effective lifetime of Er ions in the excited state, have not been determined either.

The goal of the present study is the determination of the effective cross-section of Er-ion PL excitation, kinetics of Er-ion PL decay in periodically doped Si:Er structures, and the revealing of the most probable of the above-listed sources that causes the PL intensity to rise in periodically doped structures compared with uniformly doped ones.

2. EXPERIMENT

Epitaxial Si:Er/Si/Si:Er/…/Si structures were SMBE-fabricated on (100) Si:B substrates of 10 Ω cm resistivity [7]. Alternating Si:Er epitaxial layers with an Er concentration of $\sim 10^{18}$ cm^{-3} (according to SIMS data for uniformly doped layers grown in similar conditions) and of 4.5 nm thickness and undoped Si layers of 19 nm thickness were formed by sublimation of, respectively, polycrystalline Si:Er wafers and single-crystal Si (1000 Ω cm resistivity) heated by electric current. The substrate temperature was 570°C. A structure comprised 94 Si:Er/Si periods.

PL was excited at the temperature of 78 K with an argon laser $\lambda = 488$ nm. An electromechanical modulator with a switching time of <30 μs was used for the amplitude modulation of radiation. The emission from the structure surface was focused by a system of lenses onto the entrance slit of a monochromator and detected at its output with an uncooled InGaAs diode with a resolution of $\Delta\lambda = 3$ nm in the $\lambda = 1.0$–1.65 μm range. In the measurements of the PL decay kinetics, the characteristic response time of the detector and the recording system did not exceed 5 μs.

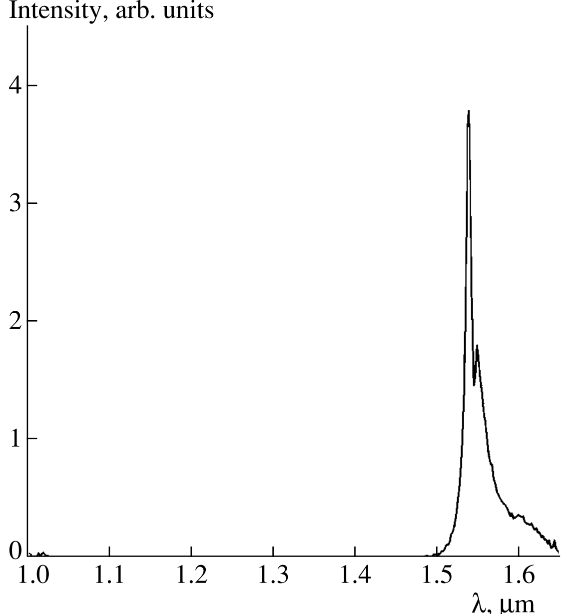

Fig. 1. The PL spectrum of a structure at 78 K.

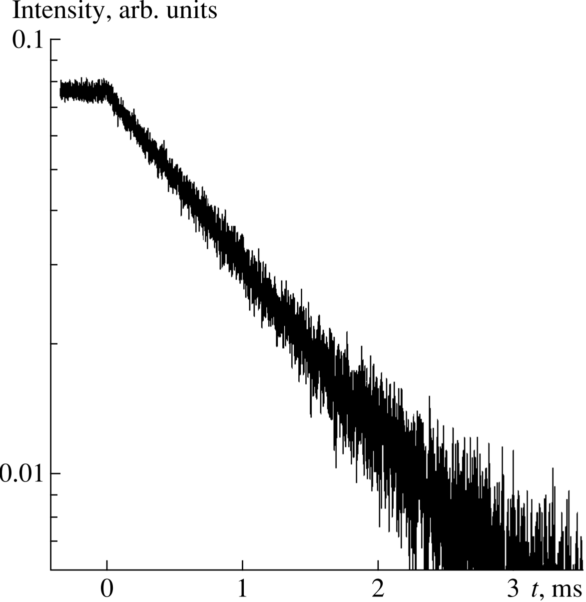

Fig. 3. The PL intensity as a function of time after switching off the sample irradiation with an argon laser of 10 mW power.

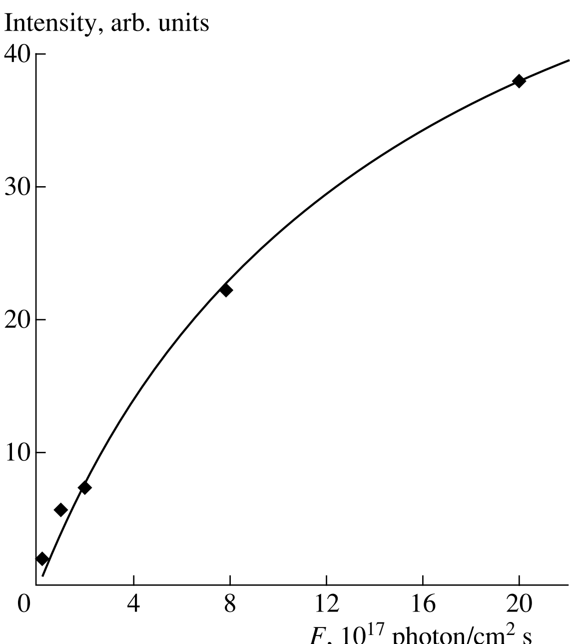

Fig. 2. The intensity of the $\lambda = 1.538$ μm PL peak at 78 K vs. the flux F of photons from an argon laser penetrating into the sample.

3. RESULTS AND DISCUSSION

Figure 1 shows the PL spectrum of a structure at a temperature of 78 K. In the spectral range under study, the spectrum contains only a single peak at $\lambda \approx 1.54$ μm, which is associated with radiative transitions of electrons between the levels $^4I_{13/2}$ (first excited state) and $^4I_{15/2}$ (ground state) of Er^{3+} ions split by a crystal field. The PL spectra of these samples were studied earlier with a BOMEM DA3.36 Fourier spectrometer with 0.5 cm^{-1} resolution at 4.2 K (see [16], sample no. 64). It was established that (i) the dominating center is the well-known Er–oxygen complex (Er-01 center, with the most intense transitions at 6507 and 6472 cm^{-1}) and (ii) that the so-called $D1$ lines, attributed to edge dislocations and characterized by the temperature-dependent spectral position [17] (by contrast to Er-related lines), are absent.

With the intensity of exciting light rising, the PL intensity increases and tends toward a constant value. Figure 2 shows the experimental dependence of the Er PL intensity at 78 K on the flux F of photons which are emitted by the argon laser and penetrate into the sample. The value of F was determined with account taken of the losses in the optical path and reflection from the Si surface. The PL intensity dependence on F can be described by the expression [8]

$$PL = A\sigma_{\mathrm{eff}}\tau F/(1 + \sigma_{\mathrm{eff}}\tau F), \qquad (1)$$

where σ_{eff} is the effective cross-section for PL excitation; τ is the lifetime of Er ions in the excited state; and A is a constant independent of σ_{eff}, τ, and F. For the curve fitting the experimental data in Fig. 2, the value of $\sigma_{\mathrm{eff}}\tau$, determined from (1), was $\sim 6.8 \times 10^{-19}$ cm^2 s.

To independently determine the lifetime of Er ions in the excited state and further calculate the value of σ_{eff}, we studied the kinetics of PL decay. Figure 3 shows the PL intensity as a function of time t for an argon laser emission power of 10 mW. The instant $t = 0$ corresponds to switching off of the sample irradiation with the argon laser. As is known (see, e.g., [8, 9]), the

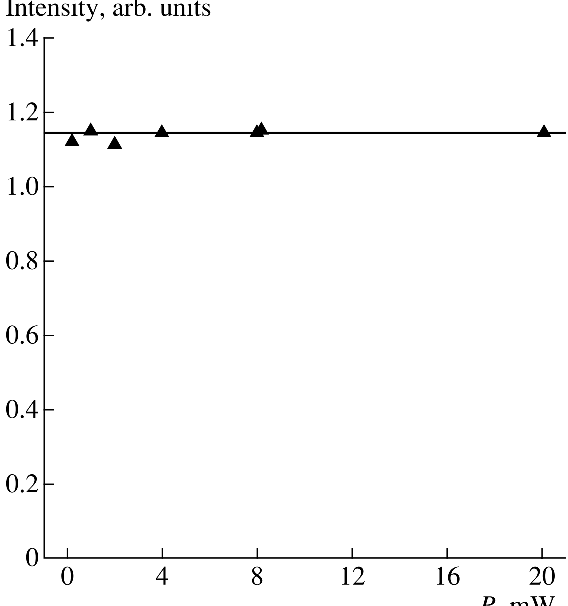

Fig. 4. The time constant of the Er-ion PL decay as a function of the Ar laser emission power *P*.

decay rate of the concentration N^*_{Er} of excited Er ions after switching off of the laser beam is described by

$$dN^*_{\text{Er}}/dt = -N^*_{\text{Er}}/\tau. \quad (2)$$

The solution to Eq. (2) has the form

$$N^*_{\text{Er}} = N^*_{\text{Er}}\exp(-t/\tau), \quad (3)$$

where N_{Er} is the initial concentration of excited Er ions. Since the luminescence intensity is directly proportional to N^*_{Er}, the time constant τ_d of the PL signal decay after switching off the argon laser equals the lifetime of Er ions in the excited state. As seen in Fig. 3, the kinetics of the luminescence decay is well described by an exponential function with a single time constant. Figure 4 shows the dependence of τ_d on the intensity of the argon laser radiation. The value of τ_d is virtually independent of the laser power in the range under study; it equals ~1.14 ± 0.03 ms. This value is close to the maximum lifetime ($\tau_{\max} \approx 2$ ms) of Er ions in the excited state, which was observed in unselectively doped Si at $T = 15$ K [10]. The maximum τ is usually obtained at rather low temperatures; it varies within ~1–2 ms in different studies of uniformly doped Si [10–12]. It is noteworthy that τ is virtually constant at temperatures at which free carriers are frozen out (see, e.g., [11]). Since all the hitherto studied effective mechanisms of nonradiative de-excitation of Er^{3+} ions in Si presume a temperature-dependent τ, it is widely believed that, in all probability, $\tau_{\max} \approx \tau_{rad}$. The value of τ obtained at $T = 78$ K in the present study differs from $\tau_{\max}$ ($T = 15$ K) by less than a factor of 2 and is very close to the decay time of the PL signal (1.3 ms at $T = 78$ K) [14] in SMBE-grown uniformly doped Si:Er epitaxial layers. At the same time, the PL intensity was raised by nearly an order of magnitude owing to selective doping [7, 13]. The obtained result shows that the reduction of the radiative lifetime of the Er^{3+} ion is not the principal reason for the increase in the PL intensity in periodically doped Si, compared with uniformly doped material.

Based on the obtained $\sigma_{\text{eff}}\tau$ and τ values, we calculated σ_{eff} as $\sim 0.6 \times 10^{-15}$ cm^2 at $T = 78$ K, an argon laser emission power up to 20 mW, and a light beam cross-section of 1.5 mm. The values in the literature of the effective cross-section for Er^{3+} ion excitation in uniformly doped single-crystal Si layers determined for the case of low temperatures and low excitation power P are $\sigma_{\text{eff}} = 3 \times 10^{-15}$ cm^{-2} ($T \approx 15$ K, $P < 1$ mW, light beam diameter 1 mm) [10] and $\sigma_{\text{eff}} = 5.2 \times 10^{-15}$ cm^2 ($T \approx 4$ K, $P \approx 10$ μW) [11]. Taking into account the reduction of the effective cross-section for excitation with an increase of temperature and pumping power [10, 11], we believe that the value of σ_{eff} in periodically doped SMBE structures is close to that in uniformly doped structures.

4. CONCLUSION

The effective cross-section for PL excitation and the lifetime of Er ions in the excited state in periodic Si:Er/Si/Si:Er/Si…/Si structures doped in SMBE-process have been measured for the first time. The obtained data show that a considerable increase in the Er-ion PL intensity in periodically doped Si, in comparison with uniformly doped Si, is not related to changes in the radiative lifetime, effective cross section for excitation, or lifetime of erbium ions in the excited state.

ACKNOWLEDGMENTS

This study was supported in part by the Russian Foundation for Basic Research (project nos. 02-02-16374 and 02-02-16773); the Russian Foundation for Basic Research and Office for Scientific and Technical Cooperation, Austria (grant no. 01-02-02000 OSTC_a); and INTAS (grant no. 2001-0194).

REFERENCES

1. N. A. Sobolev, Fiz. Tekh. Poluprovodn. (St. Petersburg) **29**, 1153 (1995) [Semiconductors **29**, 595 (1995)].
2. A. Polman, J. Appl. Phys. **82**, 1 (1997).
3. S. Coffa, G. Franzo, and F. Priolo, MRS Bull., No. 23, 25 (1998).
4. J. Stimmer, A. Reitinger, E. Neufeld, *et al.*, Thin Solid Films **294**, 220 (1997).
5. R. Serna, J. H. Shin, M. Lohmeier, *et al.*, J. Appl. Phys. **79**, 2658 (1996).

6. W.-X. Ni, K. B. Joelsson, C. X. Du, *et al.*, Appl. Phys. Lett. **70**, 3383 (1997).
7. B. Andreev, V. Chalkov, O. Gusev, *et al.*, Nanotechnology **13**, 97 (2002).
8. M. S. Bresler, O. B. Gusev, P. E. Pak, *et al.*, Fiz. Tverd. Tela (St. Petersburg) **43**, 601 (2001) [Phys. Solid State **43**, 625 (2001)].
9. S. Coffa, G. Franzo, and F. Priolo, Appl. Phys. Lett. **69**, 2077 (1996).
10. F. Priolo, G. Franzo, S. Coffa, and A. Carnera, Phys. Rev. B **57**, 4443 (1998).
11. J. Palm, F. Gan, B. Zheng, *et al.*, Phys. Rev. B **54**, 17603 (1996).
12. P. B. Klein and G. S. Pomrenke, Electron. Lett. **24**, 1503 (1988).
13. B. A. Andreev, Z. F. Krasil'nik, M. V. Stepikhova, *et al.*, in *Proceedings of 26th International Conference on Physics of Semiconductors, Edinburgh, 2002* (2003).
14. B. A. Andreev, Z. F. Krasil'nik, V. P. Kuznetsov, *et al.*, Fiz. Tverd. Tela (St. Petersburg) **43**, 979 (2001) [Phys. Solid State **43**, 1012 (2001)].
15. O. B. Gusev, M. S. Bresler, P. E. Pak, and I. N. Yassievich, Phys. Rev. B **64**, 075302 (2001).
16. M. Stepikhova, B. Andreev, V. Kuznetsov, *et al.*, Solid State Phenom. **82–84**, 629 (2002).
17. N. A. Sobolev, O. B. Gusev, E. I. Shek, *et al.*, Appl. Phys. Lett. **72**, 3326 (1998).

Translated by D. Mashovets

Semiconductors, Vol. 37, No. 9, 2003, pp. 1104–1106. Translated from Fizika i Tekhnika Poluprovodnikov, Vol. 37, No. 9, 2003, pp. 1127–1130.
Original Russian Text Copyright © 2003 by Semenova, Zhukov, Vasil'ev, Mikhrin, Kovsh, Ustinov, Musikhin, Blokhin, Gladyshev, Ledentsov.

Metamorphic Modulation-Doped InAlAs/InGaAs/InAlAs Heterostructures with High Electron Mobility Grown on GaAs Substrates

E. S. Semenova*, A. E. Zhukov, A. P. Vasil'ev, S. S. Mikhrin, A. R. Kovsh, V. M. Ustinov, Yu. G. Musikhin, S. A. Blokhin, A. G. Gladyshev, and N. N. Ledentsov

Ioffe Physicotechnical Institute, Russian Academy of Sciences, St. Petersburg, 194021 Russia

**e-mail: esemenova@mail.ioffe.ru*

Submitted February 3, 2003; accepted for publication February 4, 2003

Abstract—Metamorphic modulation-doped InGaAs/InAlAs heterostructures have been MBE-grown on GaAs substrates. The optimization of low-temperature growth conditions for a graded-composition buffer layer made it possible to reduce the amount of structural defects in the active layers of the structure. The electron mobility in the 2D channel of metamorphic structures grown under optimum conditions (8100 cm^2/V s at 300 K) noticeably exceeds the values achievable in strained InGaAs/AlGaAs heterostructures on GaAs substrates. *© 2003 MAIK "Nauka/Interperiodica".*

Modulation-doped InGaAs/InAlAs heterostructures (MDHS) grown by epitaxy on InP substrates are widely used in microelectronics in the fabrication of low-noise high-speed transistors [1]. The advantage of this system of materials over InGaAs/AlGaAs on GaAs substrate is the possibility of using layers with a higher In content (typically, ~50% for InP substrate in contrast to ~20% for GaAs) and the resulting higher conduction band offset at the channel–barrier heterointerface and lower electron effective mass. These factors make it possible to obtain in MDHS a higher density ($>2 \times 10^{12}$ instead of $\sim 1 \times 10^{12}$ cm^{-2}) and mobility (>10000 instead of ~6000 cm^2/V s) of electrons in the 2D gas formed near the heterointerface. However, significant drawbacks of InP substrates as compared with GaAs, such as smaller size of commercially available wafers, high fragility, and high cost, hinder the manufacture of devices based on InP substrates. This raises interest in so-called metamorphic structures on GaAs substrates, where the application of specific growth technology for the In(Ga)AlAs buffer layer allows the transition from the GaAs to the InP lattice constant in such a way that the majority of dislocations do not propagate in the growth direction, being confined to the transition layer [2–6]. At the same time, fabrication on GaAs substrates of metamorphic structures with transport and structural characteristics competitive with those of MDHS on InP substrates is complicated by incomplete suppression of dislocation threading to the active layers of the structure and emergence of a surface microprofile [5].

In the present study, we have optimized the growth conditions for MDHS based on metamorphic InAlAs/InGaAs/InAlAs structures on GaAs substrates, so as to reduce the amount of defects and obtain a high carrier mobility.

The structures were grown in a Riber 32P MBE machine. The growth process was monitored directly during layer deposition by means of reflection high-energy electron diffraction (RHEED). The composition and structural perfection of layers were studied by high-resolution X-ray diffraction. The density and mobility of carriers were measured by the van der Pauw method in a BioRad installation at temperatures of 77 and 300 K. The obtained structures were studied also by scanning and transmission electron microscopy (SEM and TEM) to determine the surface morphology and the degree of relaxation of layers in a structure.

Due to significant lattice mismatch (~3.5%) between InP and GaAs, the direct epitaxial growth of comparatively thick structurally perfect layers with a lattice constant coinciding with that of InP is impossible, because, in this situation, the relaxation of elastic strains is accompanied by the formation of dislocations threading across the entire thickness of the epitaxial layer. As an example, Fig. 1a shows a cross-sectional TEM image of an InGaAs layer (with an In content of ~30%) on GaAs. In this study, InAlAs with an In content varying linearly from 10 to 58% served as the buffer layer. The structures under study comprise the following set of layers: an InAlAs buffer layer of 0.9 μm thickness is deposited onto a semi-insulating GaAs substrate; then, an $In_{0.52}Al_{0.48}As$ layer of 0.4 μm thickness is deposited and a structure with 2D electron gas is formed on this layer; the structure comprises an $In_{0.53}Ga_{0.47}As$ channel of 40 nm thickness, an $In_{0.52}Al_{0.48}As$ spacer (5 nm), a doped n-$In_{0.52}Al_{0.48}As$ barrier layer (10 nm), an $In_{0.52}Al_{0.48}As$ subgate layer (15 nm), and an n-$In_{0.53}Ga_{0.47}As$ contact layer of 7 nm thickness.

1063-7826/03/3709-1104$24.00 © 2003 MAIK "Nauka/Interperiodica"

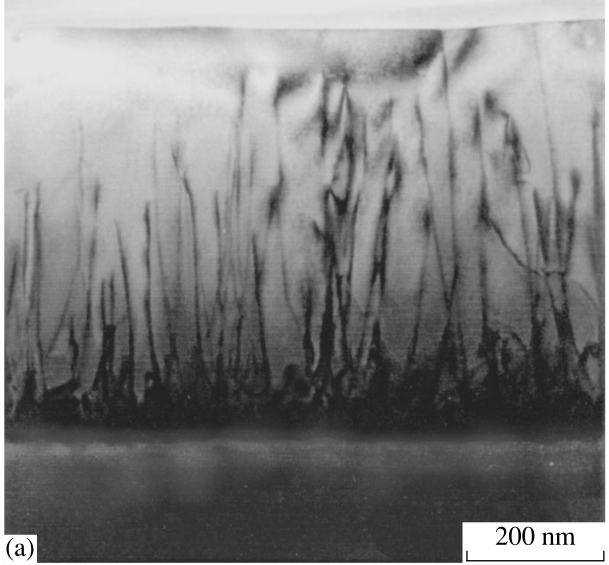

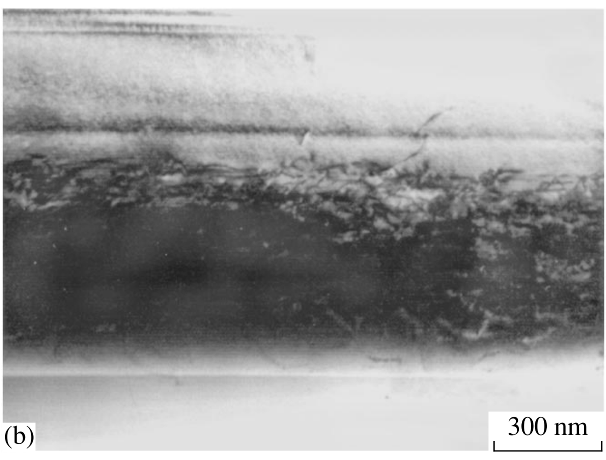

Fig. 1. Cross-sectional TEM images of structures on GaAs substrates: (a) $In_{0.3}Al_{0.7}As$ layer and (b) InAlAs/InGaAs/InAlAs MDHS on GaAs substrate with a metamorphic graded layer.

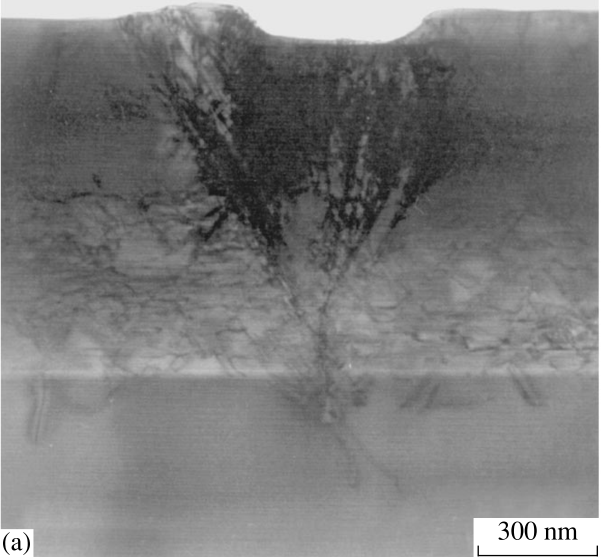

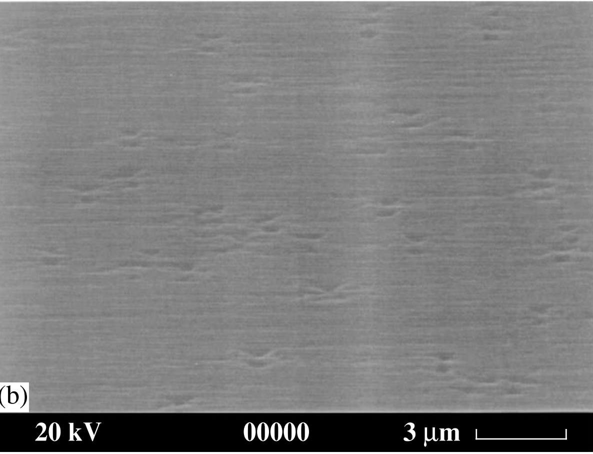

Fig. 2. InAlAs/InGaAs/InAlAs MDHS with a metamorphic graded layer on GaAs substrate: (a) cross-sectional TEM image of a structure with a stacking fault and (b) SEM image of the structure surface.

We have found that using a sufficiently low temperature (≤400°C) during the deposition of the buffer layer makes it possible to "confine" the majority of dislocations to within the buffer layer and to prevent their propagation into upper layers, which is clearly seen in the cross-sectional TEM image (Fig. 1b). It is noteworthy that the morphology of the growing surface is to a large extent dependent on the substrate temperature during the deposition of the buffer layer. It was found that when temperatures are too low, ~350°C, growth occurs in the 3D mode, which is indicated by a spotty RHEED pattern. However, the situation changes significantly when the temperature is raised to 400°C. Immediately after the start of deposition of the graded buffer layer, a (1 × 1) surface reconstruction is observed, but the rods show markedly thickened parts indicating the 3D growth mode. During the low-temperature growth of $In_{0.52}Al_{0.48}As$, the RHEED pattern changes; specifically, the thickened parts gradually disappear. During subsequent growth and upon termination of growth for raising the substrate temperature, a striped diffraction pattern of (4 × 1) surface reconstruction is observed.

Thus, the use of optimal growth conditions allowed us to both suppress the threading of dislocations and to obtain atomic-smooth interfaces necessary for the reduction of the scattering by the roughness of the heterointerface, which makes the carrier mobility in 2D electron gas higher. At the same time, the problem of stacking fault formation in the course of the growth of the buffer layer has not been completely resolved (Fig. 2a). These defects arise due to high dislocation density at the initial stage of growth; in contrast to dislocations by themselves, they are not confined to within the buffer layer, but thread across the entire structure thickness and form specific morphological features on

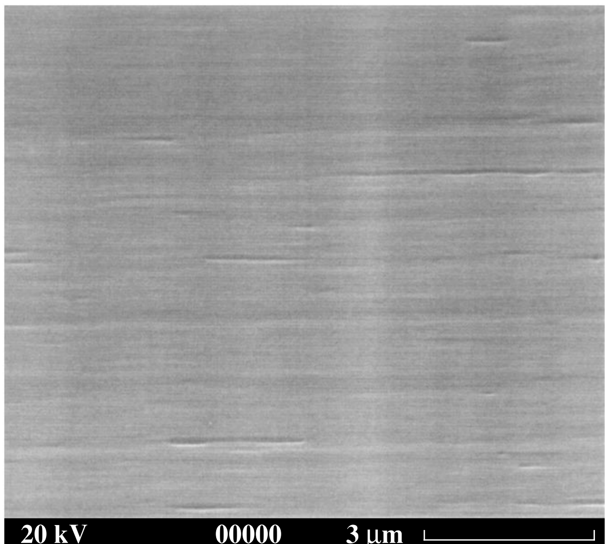

Fig. 3. SEM image of the surface of InAlAs/InGaAs/InAlAs MDHS grown on GaAs substrate under optimized growth conditions.

the surface (Fig. 2b). The formation of this type of defect can significantly affect the transport properties of a structure by lowering the carrier mobility due to additional scattering. The methods for suppressing this type of defect remain poorly studied yet. As the first step, we have investigated the influence of the pressure of arsenic on the density of stacking faults in the structure. Under standard growth conditions, when the As flux exceeds the total flux of Group III elements by a factor of 2–4, the resulting surface is corrugated, with a large amount of stacking faults formed (Fig. 2b). It was established, however, that the surface becomes smoother and the density of stacking faults decreases when the As flux is reduced. The best result was achieved under the deposition conditions where the As flux was equal to the total flux of metals (Fig. 3). The mobility and density of electrons in the optimized structure were, respectively, 8100 cm^2/V s and 1.2×10^{12} cm^{-2} at 300 K. At 77 K, the mobility was 33100 cm^2/V s. In a similar structure grown on InP substrate without a buffer layer, the electron mobility was 11050 cm^2/V s at an electron density of 1.9×10^{12} cm^{-2} at 300 K, and at 77 K the mobility was 51670 cm^2/V s. Evidently, the larger number of defects in the structure with a metamorphic buffer leads to lower carrier mobility; however, despite this circumstance, the obtained parameters exceed the values reached in InGaAs/AlGaAs/GaAs structures.

The optimization of the design of the metamorphic graded buffer in MDHS grown on GaAs substrates allowed us to prevent dislocation propagation into the active layers of a structure. The optimization of growth conditions made it possible to suppress the formation of stacking faults in these structures. This enabled us to fabricate on GaAs substrates InAlAs/InGaAs/InAlAs MDHS lattice-matched with InP, with electrical characteristics (an electron mobility of 8100 cm^2/V s, a density of 1.2×10^{12} cm^{-2} at 300 K) comparable with the parameters of similar structures on InP substrates and exceeding those for InGaAs/AlGaAs/GaAs structures. We believe that further optimization of the design of metamorphic modulation-doped InAlAs/InGaAs/InAlAs heterostructures lattice-matched with InP will considerably improve the transport properties of structures based on GaAs substrates.

We are grateful to V.M. Busov for SEM and M.V. Baidakova for XRD studies.

This study was supported by the program "Physics of Solid-State Nanostructures," the Russian Foundation for Basic Research, and the Joint Scientific Program of the Ioffe Physicotechnical Institute and Nanosemiconductors Gmbh, Germany.

REFERENCES

1. L. D. Nguyen, L. E. Larson, and U. K. Mishra, Proc. IEEE **80**, 494 (1992).
2. W. E. Hoke, P. J. Lemonias, and J. J. Mosca, J. Vac. Sci. Technol. B **17**, 1131 (1999).
3. M. Zaknoune, B. Bonte, and C. Gaquiere, IEEE Electron Device Lett. **19** (9), 345 (1998).
4. G. Wang, Y. Chen, and W. J. Scha, IEEE Trans. Electron Devices **35**, 818 (1988).
5. M. Behet, K. van der Zanden, and G. Borghs, Appl. Phys. Lett. **73**, 2760 (1998).
6. T. Mishima, K. Higuchi, and M. Mori, J. Cryst. Growth **150**, 1230 (1995).

Translated by D. Mashovets

Semiconductors, Vol. 37, No. 9, 2003, pp. 1107–1113. Translated from Fizika i Tekhnika Poluprovodnikov, Vol. 37, No. 9, 2003, pp. 1131–1137.
Original Russian Text Copyright © 2003 by Mamakin, Yunovich, Wattana, Manyakhin.

PHYSICS OF SEMICONDUCTOR DEVICES

Electrical Properties and Luminescence Spectra of Light-Emitting Diodes Based on InGaN/GaN Heterostructures with Modulation-Doped Quantum Wells[1]

S. S. Mamakin*, A. É. Yunovich*^, A. B. Wattana, and F. I. Manyakhin****

**Department of Physics, Moscow State University, Moscow, 119992 Russia*

***Moscow Institute of Steel and Alloys, Moscow, 117936 Russia*

^e-mail: yunovich@scon175.phys.msu.su

Submitted September 2, 2002; accepted for publication September 6, 2002

Abstract—The distribution of charged centers $N(w)$, quantum efficiency, and electroluminescence spectra of blue and green light-emitting diodes (LED) based on InGaN/AlGaN/GaN *p–n* heterostructures were investigated. Multiple InGaN/GaN quantum wells (QW) were modulation-doped with Si donors in GaN barriers. Acceptor and donor concentrations near the *p–n* junction were determined by the heterodyne method of dynamic capacitance to be about $N_A \geq 1 \times 10^{19}$ cm$^{-3} \gg N_D \geq 1 \times 10^{18}$ cm^{-3}. The $N(w)$ functions exhibited maxima and minima with a period of 11–18 (±2–3 nm) nm. The energy diagram of the structures has been constructed. The shifts of spectral peaks with variation of current ($J = 10^{-6}$–3×10^{-2} A) are smaller (13–12 meV for blue and 20–50 meV for green LEDs) than the corresponding values for the diodes with undoped barriers (up to 150 meV). This effect is due to the screening of piezoelectric fields in QWs by electrons. The dependence of quantum efficiency on current correlates with the charge distribution and specific features in the current–voltage characteristics. © *2003 MAIK "Nauka/Interperiodica".*

1. INTRODUCTION

The mechanisms of radiative recombination in light-emitting diodes (LEDs) based on InGaN/AlGaN/GaN heterostructures with quantum wells (QW) are dependent on strong electric fields in the structures. These fields are due not only to the doping of both constituents of the *p–n* junction, but also to piezoelectric and spontaneous polarization of the structure of hexagonal crystals [1–3].

The direction of the electric field of polarization in InGaN QWs is opposite to the field of the *p–n* junction if the structures are grown by epitaxy on a surface with Ga-polarity. This field separates electrons and holes in QWs if the well width is comparable or exceeds the exciton radius. In this case, the luminescence is dependent on the quantum-confinement Stark effect; this effect reduces the probability of radiative recombination [4–5]. The polarization field in GaN and AlGaN barriers is parallel to the field of the *p–n* junction, so that the total electric field in the structures reaches values of about 10^6 V cm^{-1}. Such strong fields are responsible for tunneling effects in heterostructures based on GaN [6, 7].

If the barriers in multiple quantum wells (MQW) are doped with donors, electrons pass from donors to QWs. They screen the surface charges at heterointerfaces, so that the electric fields in the structures may decrease substantially. The influence of the Stark effect decreases; tunnel leakage currents are simultaneously diminished. Thus, the quantum efficiency of emission can be considerably raised in LEDs with modulation-doped QWs, as shown by Gardner *et al.* [1].

The goal of the present study is the investigation of mechanisms of radiative recombination in InGaN/AlGaN/GaN *p–n* heterostructures with modulation-doped MQWs. The experimental methods used earlier in the study of GaN LEDs [6–11] were applied in the study of LEDs fabricated by LumiLeds Lighting Co. [1, 12, 13].

2. EXPERIMENTAL METHODS

Blue and green LEDs based on $In_xGa_{1-x}N/Al_yGa_{1-y}$/GaN heterostructures grown by MOCVD on sapphire substrates were studied. An *n*-GaN base layer was doped with Si, $N_D \approx (1–2) \times 10^{18}$ cm^{-3}. Four periods of $In_xGa_{1-x}N$ QWs (2.5–3 nm) separated with GaN barriers (12–14 nm) were grown on the base layer. The In content was in the limits of $x = 0.10–0.15$ and $x = 0.17–0.22$ for blue and green diodes, respectively. The barriers were doped with Si donors, $N_D \approx (1–1.5) \times 10^{18}$ cm^{-3}.

[1] This study was reported in part at the All-Russia Conference "Nitrides of Gallium, Indium, and Aluminum: Structures and Devices" (Moscow State University, November, 2001), MRS Spring Meeting (San Francisco, USA, April 2002), and the International Conference "Optics, Optoelectronics, and Technology," (Ul'yanovsk, Russia, June 2002).

1063-7826/03/3709-1107$24.00 © 2003 MAIK "Nauka/Interperiodica"

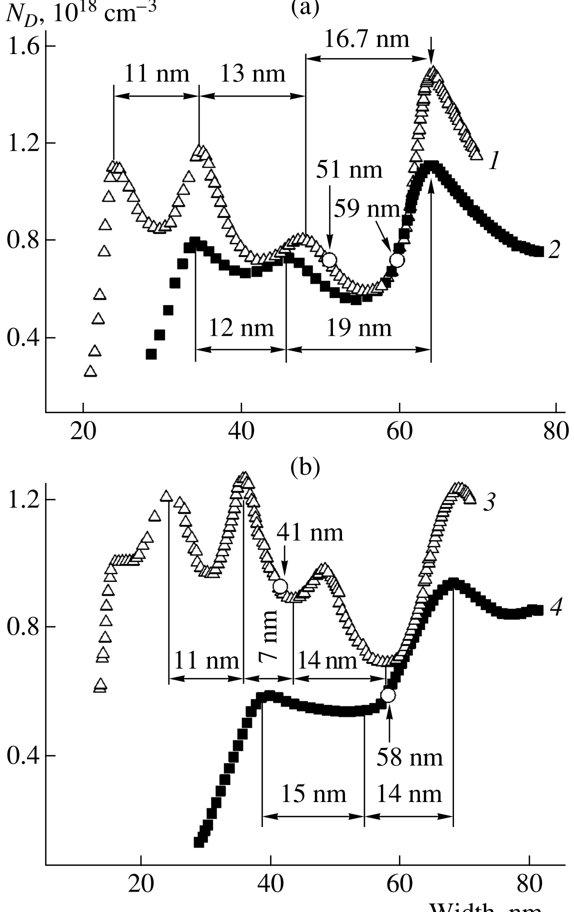

Fig. 1. The distribution of charged centers in the space charge region. (a) For two blue LEDs; circles indicate the w_0 values at $V = 0$. Maximum concentration for diode no. 1 is $N_D = 1.5 \times 10^{18}$ cm^{-3} at $z = 65$ nm, efficiency 8.7% at $J = 0.5$ mA; for diode no. 2 $N_D = 1.1 \times 10^{18}$ cm^{-3} at $z = 64$ nm, efficiency 6.4% at $J = 2$ mA. (b) For two green LEDs; circles indicate the w_0 values at $V = 0$. Maximum concentration for diode no. 3 is $N_D = 1.3 \times 10^{18}$ cm^{-3} at $z = 36$ nm, efficiency 4.4% at $J = 10$ mA; for diode no. 4 $N_D = 9.3 \times 10^{17}$ cm^{-3} at $z = 68$ nm, efficiency 3.1% at $J = 3$ mA.

A *p*-AlGaN layer of 50–80 nm thickness and a top GaN layer were doped with Mg, $N_A \approx (1–2) \times 10^{19}$ cm^{-3}. The LEDs fabricated from these structures had an area $S = 4.66 \times 10^{-4}$ cm^{-2} and a plastic dome 5 mm in diameter.

We studied 40 LED samples; detailed data were obtained for four samples of each series in the range of currents $J = 10^{-7}$–3×10^{-2} A at room temperature. The procedure for measuring the luminescence spectra and electrical properties of LEDs has been described elsewhere [6–11]. The external quantum efficiency of emission $\eta_e(J)$ and the power efficiency $\eta_p(J)$ of the LEDs were determined from measurements of the emission power.

3. EXPERIMENTAL RESULTS

3.1. Distribution of Charged Centers in the Active Region of the Structures

The dependence of differential capacitance on voltage, $C(V) = (dV/dQ)$, and the derivative of this dependence (d^2V/dQ^2) were measured by the heterodyne method of dynamic capacitance [8, 9]. The distribution of charged centers $N(w)$ and the space charge region thickness w were calculated using the relations

$$w = \varepsilon\varepsilon_0 S/(dV/dQ); \; N(w) = (\varepsilon\varepsilon_0 S^2)(d^2V/dQ^2). \quad (1)$$

The dielectric constant was taken to be $\varepsilon = 9.0$ in the calculations. It is worth noting that only absolute values of w and N, but not the character of $N(w)$ distribution, depend on ε and S.

Figures 1a and 1b show $N(w)$ distributions for two blue and two green LEDs. Clearly pronounced maxima and minima of $N(w)$ correspond to modulation doping of MQWs with a period of 11–18 nm. The amplitude of oscillations varied from sample to sample; it was higher for larger $N_{max}(w)$ values. The values of the space charge region width w_0 at $V = 0$ are denoted in figures and listed in the table (section I). A discussion of these results with technologists [1, 13] has revealed that variations of $N(w)$ distributions result from uncontrollable growth conditions.

3.2. Current–Voltage Characteristics

Current–voltage (*I–V*) characteristics of blue and green LEDs are shown in Figs. 2a and 2b. They exhibit a portion corresponding to tunneling (leakage) current at low voltages ($V < V_1 \approx 1.9$–2.1 V for blue and $V < V_1 \approx 1.6$–1.9 V for green LEDs). With rising V, an exponential increase of current in the range $J = 0.1$–10 mA corresponds to the injection of minority carriers, i.e., holes, into the active region of a structure with MQWs. In this range, the derivative of $V_J = dV/d(\ln J)$ curves equals $V_J = 40$–75 mV and $V_J = 80$–100 mV for blue and green LEDs, respectively. The region of high voltages V is affected by the series resistance R_s, which depends on current J:

$$J = J_0 \exp[e(V - JR_s(J))]/(mkT). \quad (2)$$

Minimum values of the “nonideality factor” $m = V_J(e/kT)$ for blue and green LEDs are listed in the table (II). In the range of high currents, *I–V* characteristics were also represented as power dependences:

$$J = A(V - V_2)^{\nu}, \quad (2a)$$

with the exponent ν between 1.5 and 3.5 (table, (II)).

3.3. Emission Power and Power Efficiency of LEDs

The dependence of power P and power efficiency ($\eta_p = P/JV$) of LEDs on current was nonmonotonic, with a maximum $\eta_p = \eta_{max}$ in the range $J = 1$–10 mA

LED parameters

No.	Parameter	Blue				Green			
		*b*067	*b*169	*b*093	*b*026	*g*029	*g*176	*g*188	*g*038
I	$w_0(10^{-6})$, cm	1.26	2.07	2.1	2.85	2.85	1.35	2.55	1.68
	$N_i(10^{17})$, cm^{-3}	2.43	1.11	2.8	3.45	1.4	6.22	2.0	4.0
	φ_{kn}, V	1.33	0.906	0.816	0.66	0.49	0.87	0.704	1.05
II	ν	1.5	3.0	2.0	1.8	2.5	2.3	3.5	2.8
	$m = dV/d(\ln J)(e/kT)(\min)$	1.7	1.9	1.7	3.0	4.1	3.8	2.8	3.3
	$U_{\min}$, V	2.0	2.4	2.45	2.5	2.1	2.8	2.2	2.2
	φ_{kJ}, V	2.2	1.8	2.0	1.9	1.35	1.7	1.8	1.9
	$e\varphi_k$, $(F_n - F_p)$, eV	3.07	3.08	2.92	3.32	3.22	3.45	3.00	3.31
III	$\eta_{\max}$, %	4.8	10.5	8.8	6.5	2.9	4.4	5.9	4
	($J_{\max}$, mA)	3	3	0.5	2	2	10	2	3
	η, % (J = 10 mA)	4.4	8.9	6.1	5.4	2.4	4.4	4.4	3.7
IV	$\hbar\omega_{\max}$, eV (J = 20 mA)	2.784	2.678	2.655	2.618	2.421	2.413	2.380	2.349
	$\Delta\hbar\omega_{\max}$, meV ($J = 10^{-6} \Rightarrow 2 \times 10^{-2}$ A)	–2	–3	5	14	42	48	19	17
	$\Delta(\hbar\omega)_{1/2}$, eV	0.13	0.11	0.12	0.12	0.13	0.15	0.14	0.14
	E_1, meV (J = 20 mA)	–31	–35	–35	–35	–31	–40	–39	–39
	E_0, meV (J = 20 mA)	59	52	54	60	50	54	54	53

(Figs. 3a and 3b, table (III)). The values of $\eta_{\max}$ are also presented in Fig. 1 for comparison with $N(w)$ distributions. It is necessary to note that high values of $\eta_{\max}$ corresponded to heavier doping of the barriers and clearly pronounced periodic variations in $N(w)$. These values exceed the $\eta_{\max}$ values observed in LED structures without modulation-doping [9–11] by nearly a factor of 2.

3.4. Luminescence Spectra of LEDs

Figures 4a and 4b show the electroluminescence (EL) spectra of blue and green LEDs in a wide range of dc currents. Similarly to previously studied LEDs without modulation-doping [9–11], the spectra show exponential falloff on both sides. The characteristic energy of the high-energy fall is $E_1 = mkT$ of about 35 meV ($m \approx 1.3$). The characteristic energy on the low-energy side, E_0, was about 55 meV. The FWHM of spectra were 115–120 and 135–140 meV for the blue and green LEDs, respectively (Figs. 4a and 4b, table (IV)).

The shift of spectral peaks $\hbar\omega_{\max}$ to shorter wavelengths under varying current ($J = 10^{-6}$–2×10^{-2} A) was comparatively small: for diodes presented in Figs. 4a, 4b, it was 5 and 50 meV for blue and green LEDs, respectively. These values are considerably less than in the LEDs with undoped MQWs (up to 150 meV) studied earlier [9–11]. At high current, the spectra of blue LEDs demonstrate a slight shift to longer wavelengths, which is related to heating (table (IV)). As shown in Fig. 4a for one of the blue LEDs, no long-wavelength spectral bands related to tunneling emission are observed in the low-energy range; the signal is determined only by noise.

4. DISCUSSION

4.1. Distribution of Charged Centers in Heterostructures

Periodic variations of the distribution of charged centers in modulation-doped heterostructures with QWs were studied earlier for the case of GaAs/AlGaAs structures [14, 15]. However, for nanometer-scale InGaN/GaN structures (Fig. 1), these variations are observed, as far as we know, for the first time. Therefore, it is necessary to discuss the physical meaning and the precision of the determination of coordinates in Fig. 1. The thickness of the carrier depleted space-charge region, w, can be determined from the measurements of the dynamic capacitance to within the Debye screening length:

$$L_{Dn} = [\varepsilon\varepsilon_0(kT/e)/en_0]^{1/2}, \quad (3)$$

where n_0 is the electron density on the side of the more lightly doped n-constituent of the p–n heterojunction. In our case, $L_{Dn} \approx 2.5$ nm. That is why the experiment shows smooth $N(w)$ curves with the period d = 12–15 nm instead of steplike dependences associated with the sharp doping profile of the barriers. The values of $N(w)$,

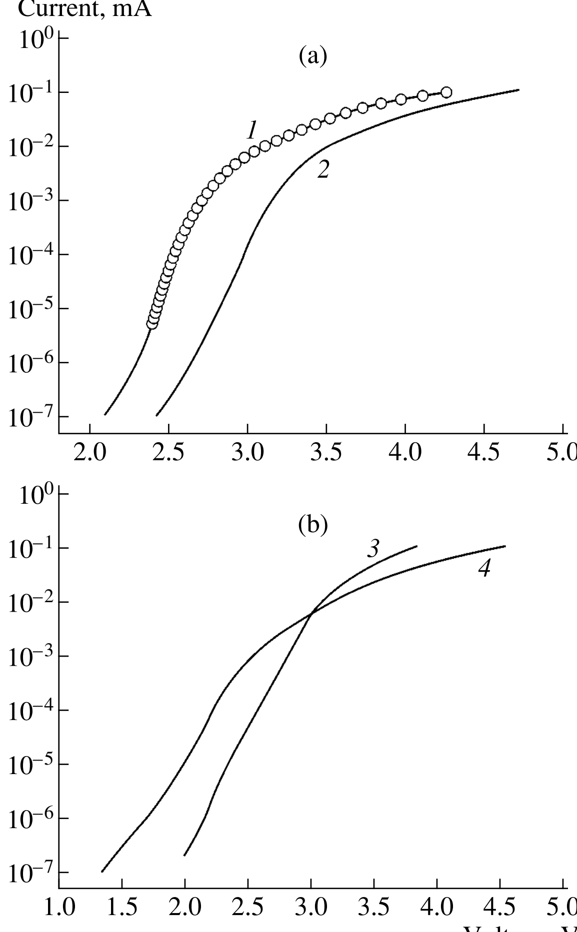

Fig. 2. *I–V* characteristics of (a) blue and (b) two green LEDs. Points in Fig. 2a represent the result of fitting to the curves by Eq. (2), with the model parameters: $V_J = mkT/e$ = 0.0398 V, J_0 = 0.0104 A, R_s = 1.685 Ω, k = 4.113, ϕ_k = 2.668 V.

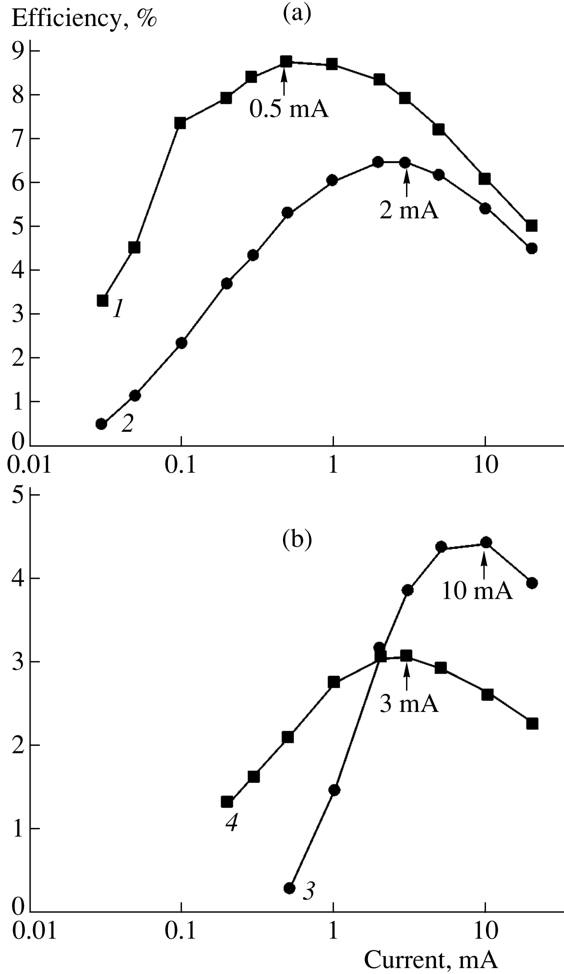

Fig. 3. The power efficiency of LEDs as a function of current for (a) two blue and (b) two green LEDs.

i.e., the reduced concentration of charged impurities, correspond to the donor concentration $N_D(z)$ on the n-side of the junction to within the ratio of concentrations on two sides of the p–n junction, $N_D/N_A \approx 0.1$. This means that $N_D(z)$ is higher than $N(w)$ in Fig. 1, and the distance z in MQWs is smaller than the abscissa w in Fig. 1:

$$N_D(z) = N(w)(1 + N_D/N_A);\quad dz = dw/(1 + N_D/N_A). \tag{4}$$

Taking into account the above considerations, we conclude that the distribution of charges depends on the specifics of growth conditions. The space-charge layer thickness w_0 (circles in Fig. 1) varied from sample to sample in the limit from 40 to 60 nm. The higher the $N(w)$ value, the smaller its period. The experiments described indicate that MQWs are located on the n-side of the structure, and, under equilibrium conditions, they are partially filled with electrons.

4.2. Energy Diagram

We now integrate the Poisson equation for the potential Ψ,

$$d^2\Psi/dz^2 = (-e/\varepsilon\varepsilon_0)N_D(z),$$

with the $N(w)$ distribution known from the experiment and taking into account Eq. (4). The boundary conditions are as follows: in the point $z = w_0$, the potential Ψ relative to the homogeneous n-region equals $\psi_{n_0} = -kT/e$ and the electric field $E_{(z = w_0)} = -d\Psi/dz = -kT/eL_{D_n}$. The first integral yields the distribution of field E_z from the point w_0 ($V = 0$) to the point w_1, where $N_D(z)$ is negligible (Fig. 1), and the field equals

$$(d\Psi/dz)_{w_1} = -E_{w_1} = (-e/\varepsilon\varepsilon_0)\int_{w_1}^{w_0 + L_{Dn}} N_D^+(z)dz. \tag{5}$$

The second integral yields the distribution of the potential $\Psi(z)$ in the same interval and the value of the contact potential in the point w_1 in the n-region, φ_{kn} (table, (I)).

Due to the neutrality of the system as a whole, the total charge of acceptors (from deep inside the p-region to the doping boundary w_2) equals the total donor charge with the opposite sign. Therefore, the electric induction vectors $\mathbf{D} = \varepsilon\mathbf{E}$ in points w_1 and w_2 must be equal:

$$\varepsilon_2(d\Psi/dz)_{w_2} = -\varepsilon_2 E_{w_2}$$
$$= -\varepsilon_1 E_{w_1} = (+e/\varepsilon_0)\int_{-L_{Dp}}^{w_2} N_A^-(z)dz. \quad (6)$$

Rigorous calculations considering the difference in ε values in different layers of the structure and polarization fields are beyond the scope of the present study; we assumed that $\varepsilon_1 \approx \varepsilon_2$.

The distribution of charged Mg acceptors, $N_A^-(z)$, which is hardly controllable technologically, was not determined in our experiments. Acceptors in the p-region can be partly compensated by donors (the donor concentration $N_{Dp} \approx (1\text{–}5) \times 10^{17}$ cm^{-3}). The Mg level is comparatively deep (ΔE_A = 160 meV at $N_A \approx 10^{19}$ cm^{-3}); and in theoretical calculations it is necessary to take into consideration the incomplete ionization, so that the density of holes in the p-region $p_0 \approx (1\text{–}3) \times 10^{17}$ cm^{-3}. Under these assumptions, the first integral of the Poisson equation from deep inside the p-region to the point w_2 yields the relation between φ_{pk} and $(d\Psi/dz)_{w_2}$:

$$\left(\frac{d\Psi}{dz}\right)_{w_2} = +\frac{kT}{ep_0^{1/2}L_{Dp}}\left\{p_0\left[1-\exp\left(-\frac{e\varphi_{pk}}{kT}\right)\right] + (N_A - N_{D_p})\frac{e\varphi_{pk}}{kT} + N_A \ln\frac{1+g\exp\left(-\frac{e\varphi_{pk}}{kT}\right)}{1+g\exp\frac{e(\Psi_A-\Psi_0)}{kT}}\right\}^{1/2}, \quad (7)$$

where $p_0 = N_v\exp(-e\Psi_0/kT)$ and $e\Psi_0 = F_p - E_{v0}$ are the density of holes and the Fermi level position in the p-region, $\Psi_A = \Delta E_A/kT$, $g = 4$ is the degeneracy factor of the acceptor level, and $L_{Dp} = [2\varepsilon\varepsilon_0(kT/e)/ep_0]^{1/2}$ is the screening length in the p-region. Calculations have shown that the sum $(\varphi_{pk} + \varphi_{kn})$ is less than the contact potential $\varphi_k \approx 3.0\text{–}3.3$ eV determined from the N_A and N_D concentrations on both sides of the junction and from the I–V characteristics (see below). This implies that, in the middle of the structure, there exists a neutral compensated i-layer with a width $w_i = w_2 - w_1$, in which the equilibrium potential drop equals

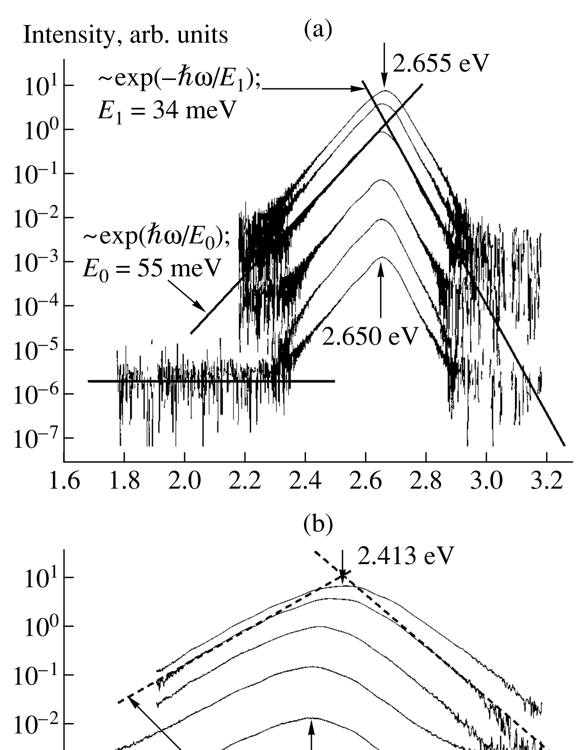

Fig. 4. Spectra of LEDs: (a) blue no. 1 in the range of currents from 10 μA to 20 mA, and (b) green no. 3 in the range of currents from 0.5 to 20 mA.

$$\varphi_i = \varphi_k - (\varphi_{kn} + \varphi_{kp}). \quad (8)$$

Assuming that the potential varies linearly in the i-layer, we can calculate the parameters of the energy diagram of the structure, as was done in [9, 11]. In contrast to these studies, where MQWs were located in the i-region, in our case they are on the border of the n-region and the point w_0 is fixed at a definite coordinate in MQW. Figure 5 shows the thus-obtained diagram for a blue LED.

The quantitative disagreement between the diagram in Fig. 5 and the data presented in Fig. 1 and in the table requires further analysis. If the potential drop in the i-layer is calculated using the linear function

$$\varphi_i = (-E_{w1})w_i, \quad (9)$$

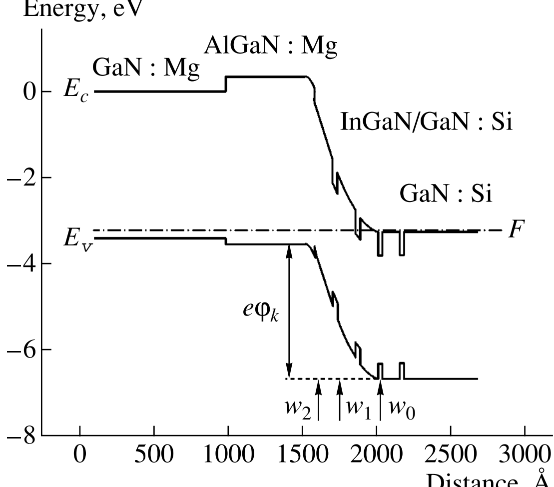

Fig. 5. Energy-band diagram of structures with modulation-doped MQWs for a blue diode.

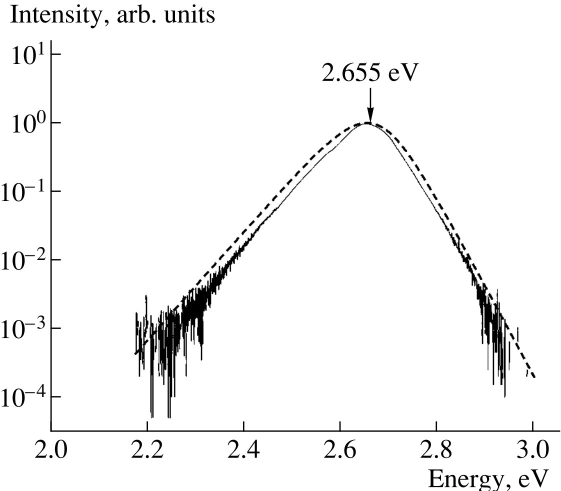

Fig. 6. A comparison of spectra with those yielded by the model of recombination in 2D-structures with exponential density-of-state tails. Points: fitting to spectra in terms of the model [9, 11]; parameters: E_{max} = 2.652 ± 0.011 eV, E_g = 2.655_8 ± 0.0005 eV, E_0 = 0.054 eV, $E_1 = mkT$ = 0.033 ± 0.0004 eV, ΔF_p = 0.029_1 eV.

where w_i is taken from the experimental data, the result is lower than that calculated from relation (8) by approximately 1.2–1.6 V (see table, (II)).

4.3. Current–Voltage Characteristics

An analytical description of *I–V* characteristics must take into account the presence of the *i*-layer and the dependence of the series resistance on current. If the *i*-layer resistance decreases at high currents, then some part of the current can be described by the quadratic dependence on voltage across this layer (see the theories of double injection [16]).

In this case, Eq. (2) for the empirical description of *I–V* characteristics includes four independent fitting parameters (V_J, R_s, k, and φ_{kJ}):

$$V = V_J \ln(J/J_1) + kJ^{1/2} + JR_s + \varphi_{kJ}. \qquad (10)$$

The parameter J_1 describes the injection component of current, and k the quadratic one. An example of description by Eq. (9), which disregards tunneling leakage at small J, is shown in Fig. 2a. The physical meaning of the parameter φ_{kJ} is the potential holes must overcome to be injected into the active MQW layer; this parameter and the combination of parameters φ_{kJ} are mutually interdependent. The parameter $-V_J\ln(J_1)$ is considerably smaller than the contact potential φ_k (see table, (II)) determined from the extrapolation of *I–V* characteristics (Fig. 2a) to the voltage $V - JR_s(J) \approx mkT$.

4.4. LED Efficiency

As shown in [1–5], piezoelectric fields in InGaN/GaN structures cause the spatial separation of electrons and holes in QWs. Therefore, the doping of barriers with donors and the screening of these fields by electrons should enhance the probability of radiative recombination in QWs. This is one of the reasons for the observed enhancement of the efficiency η_P of the LEDs under study as compared with the LEDs without modulation-doping studied earlier.

A decrease in the total electric field in the barriers reduces the probability of nonradiative tunneling currents. This factor also raises the quantum efficiency of emission. It is important that the maximum of η_P at currents J = 1–10 mA (the density $j = J/S \approx$ 2–20 A/cm^2) demonstrates the possibility of raising the power of LEDs at the same j by extending the area S.

4.5. Luminescence Spectra

The central result of the spectral studies is that the shift of $\hbar\omega_{max}$ peaks with current rising is smaller than that observed in LEDs without MQW doping. This fact confirms the screening of the fields of piezoelectric and spontaneous polarization by electrons [1]. The shift of $\hbar\omega_{max}$ in [7–11] was related mainly to the screening of fields by injected electrons.

The model of recombination in 2D-structures with the density-of-state tails induced by the potential fluctuations [7–11] describes the exponential fall of spectra, but the spectra are narrower than predicted by theory (Fig. 6). This difference demands further analysis that takes into account the piezoelectric effects.

The lack of a spectral band related to tunneling emission can be accounted for by the screening of piezoelectric fields upon modulation-doping and by the decrease in efficient electric fields in *p–n* heterostructures.

5. CONCLUSIONS

(1) The heterodyne method of dynamic capacitance yields information about the periodic distribution of charge, $N(w)$, in modulation-doped InGaN/GaN *p–n* heterostructures with QWs. The doping of barriers in MQWs with Si_D in the range $(1–2) \times 10^{18}$ cm^{-3} correlates with the enhancement of the LED efficiency.

(2) The calculation of the electric field and potential distribution from $N(w)$ shows that the active layer of a MQW is localized at the *n*-border of the space charge region. This indicates the presence of a compensated *i*-layer in a *p–i–n* structure.

(3) To explain the *I–V* characteristics of LEDs, the variation of the series resistance of structures due to double injection of carriers into the *i*-layer must be taken into account.

(4) The maximum power efficiency of LEDs at currents $J = 1–10$ mA ($j = J/S \approx 2–20$ mA/cm^2) demonstrates the possibility of raising the power at the same j by means of increasing S.

(5) The shifts of spectral peaks with varying current in LEDs with modulation-doped MQWs are significantly smaller than in undoped LEDs. This result indicates that electrons coming from donors screen the piezoelectric fields in QWs. This fact is important for LED application in white-light emitters.

ACKNOWLEDGMENTS

We are grateful to S. Stockman, M. Misra, W. Goetz, N. Gardner (LumiLeds Lighting Co.) for providing the samples used in our study and discussing the results, and to V.E. Kudryashov and S.S. Obydena for assistance with the experiments.

This study was supported by the Russian Foundation for Basic Research (project no. 00-02-16418) and by the Ministry of Industry, Science, and Technology of the Russian Federation (Contract no. 108-23(00)).

REFERENCES

1. N. Gardner, C. Kocot, W. Goetz, *et al.*, in *Book of Abstracts: 4th International Conference on Nitride Semiconductors* (Denver, 2001), PM B6.1, p. 38.
2. P. Lefebre, J. Allegre, B. Gil, *et al.*, Phys. Rev. B **59**, 15363 (1999).
3. F. Bernardini and V. Fiorentini, Phys. Rev. B **57**, R9427 (1998).
4. S. F. Chichibu, S. P. DenBaars, K. Wada, *et al.*, Mater. Sci. Eng. **59**, 298 (1999).
5. A. Hangleiter, J. S. Im, H. Kollmer, *et al.*, MRS Internet J. Nitride Semicond. Res. **4S11**, G6.20 (1999).
6. V. E. Kudryashov, K. G. Zolina, A. N. Kovalev, *et al.*, Fiz. Tekh. Poluprovodn. (St. Petersburg) **31**, 1304 (1997) [Semiconductors **31**, 1123 (1997)].
7. A. N. Kovalev, F. I. Manyakhin, V. E. Kudryashov, *et al.*, Fiz. Tekh. Poluprovodn. (St. Petersburg) **32**, 63 (1998) [Semiconductors **32**, 54 (1998)].
8. V. E. Kudryashov, A. N. Turkin, A. É. Yunovich, *et al.*, Fiz. Tekh. Poluprovodn. (St. Petersburg) **33**, 445 (1999) [Semiconductors **33**, 429 (1999)].
9. V. E. Kudryashov, S. S. Mamakin, A. N. Turkin, *et al.*, Fiz. Tekh. Poluprovodn. (St. Petersburg) **35**, 861 (2001) [Semiconductors **35**, 827 (2001)].
10. A. E. Yunovich, V. E. Kudryashov, S. S. Mamakin, *et al.*, Phys. Status Solidi A **176**, 125 (1999).
11. A. E. Yunovich and V. E. Kudryashov, Phys. Status Solidi B **228**, 141 (2001).
12. F. I. Manyakhin, A. B. Vattana, S. S. Mamakin, and A. É. Yunovich, in *Abstracts of All-Russia Conference on Gallium, Aluminum, and Indium Nitrides: Structures and Devices* (Mosk. Gos. Univ., Moscow, 2001), p. 27.
13. A. E. Yunovich, S. S. Mamakin, F. I. Manyakhin, *et al.*, in *Abstracts of MRS Spring Meeting 2002* (San Francisco, 2002), K2.4.
14. P. N. Broukov, T. Benyattou, and G. Guillot, J. Appl. Phys. **80**, 864 (1996).
15. P. Blood, Semicond. Sci. Technol. **1**, 7 (1986).
16. É. I. Adirovich, P. M. Karageorgiĭ-Alkalaev, and A. Yu. Leĭderman, *Double-Injection Currents in Semiconductors* (Sovetskoe Radio, Moscow, 1978), Sect. 3.2.

Translated by D. Mashovets

Semiconductors, Vol. 37, No. 9, 2003, pp. 1114–1118. Translated from Fizika i Tekhnika Poluprovodnikov, Vol. 37, No. 9, 2003, pp. 1138–1142.
Original Russian Text Copyright © 2003 by Boltovets, Ivanov, Konakova, P. Lytvyn, O. Lytvyn, Milenin, Prokopenko.

PHYSICS OF SEMICONDUCTOR DEVICES

Phase and Structural Changes Stimulated in Multilayer Contacts to *n*-GaAs by Rapid Thermal Annealing

N. S. Boltovets*, V. N. Ivanov*, R. V. Konakova, P. M. Lytvyn**, O. S. Lytvyn**, V. V. Milenin**, and I. V. Prokopenko****

**State Enterprise Research Institute "Orion," Kiev, Ukraine*

***Lashkarev Institute of Semiconductor Physics, National Academy of Sciences of Ukraine, Kiev, 03028 Ukraine*

e-mail: konakova@isp.kiev.ua

Submitted September 10, 2002; accepted for publication December 17, 2002

Abstract—Phase, structural, and electrical properties of Au–Mo–TiB_x–AuGe–GaAs multilayer contact systems, which are used in the process of formation of GaAs-based Gunn diodes, were investigated. The phase composition and level of residual stresses were investigated by X-ray diffraction, the morphological specific features of Au films were investigated by the AFM method, and current–voltage characteristics were investigated in the region of a weak electric field. The investigations were carried out prior to and after rapid thermal annealing in hydrogen at $T = 400$, 600, and 800°C for 60 s. It is shown that right up to the annealing temperature $T = 600$°C, the buffer properties of TiB_x are retained. The role of internal mechanical stresses in the degradation of nonrectifying Au–Mo–TiB_x–AuGe–GaAs contacts is established. © *2003 MAIK "Nauka/Interperiodica".*

1. INTRODUCTION

The formation of nonrectifying contacts is one of the most important tasks in the development of semiconductor devices. For the fabrication of GaAs-based Gunn diodes, the eutectic Au–Ge alloy metallized with an Ni layer is widely used [1–8]. The Au–Ge alloy provides for the formation of nonrectifying contacts to *n*-GaAs with a carrier density above 10^{13} cm^{-3}. To increase the durability of these nonrectifying contacts, various procedures are used. These are the formation of buffer metal layers, which prevent the diffusion of metal from the upper metallization layer; the formation of a single-crystal low-resistivity GaAs film between the active layer and metal contact; and chemically stable antidiffusion layers based on nitrides and borides of refractory metals. However, despite this, the problem of degradation of multilayer contacts to the Gunn diodes is as topical as before.

The main factors which cause the degradation of multilayer contacts are the phase formation and mutual atomic diffusion of contact components, as well as the formation of inhomogeneous fields of strains at the interface and in the thin near-contact layer. The phenomena mentioned for the metal–GaAs contacts in a certain temperature interval may be eliminated. This is achieved by introducing layers of "pure" metals or metallic compounds with high thermal stability and chemical inactivity into the metallization composition. Thus, it is possible to increase the thermal threshold of degradation of contacts. These properties are precisely those which are characteristic of Mo and TiB_x.

The purpose of this study is to investigate the phase and structural transformations under the effect of rapid thermal annealing (RTA) at the interface and in the metallization layer of nonrectifying Au–Mo–TiB_x–AuGe–GaAs contacts, and to investigate the effect of these transformations on the contact resistance of the Gunn diode.

2. EXPERIMENTAL

Nonrectifying contacts were fabricated by magnetron sputtering after photonic cleaning of the (100) surface of the SAG-1B epitaxial GaAs structure of the n–n^+–n^{++} type. The following films were sequentially deposited on this structure: Au (180 nm), Ge (20 nm), TiB_x (100 nm), Mo (20 nm), and Au (300 nm). The chosen Au/Ge weight ratios did not correspond to the AuGe eutectics. The epitaxial structures had an *n*-GaAs active layer 2–3 μm thick with a carrier density of (5–9) × 10^{15} cm^{-3}, a buffer n^+-GaAs layer 5–8 μm thick with a carrier density higher than 8×10^{17} cm^{-3}, and a n^{++}-GaAs substrate 300–350 μm thick with a carrier density higher than 2×10^{18} cm^{-3}. After deposition of metallization layer to form the nonrectifying contact, the samples were annealed in hydrogen at $T = 500$°C for 60 s. Such annealing activates the penetration of Ga atoms into the AuGe layer and Ge atoms into the surface GaAs region, thus forming n^+-GaAs [9]. To investigate the thermal stability of thus formed nonrectifying contacts, they were subjected to RTA in hydrogen for 60 s at temperatures $T_{ann} = 400$, 600, and 800°C.

Prior to and after the RTA, the internal stresses, the phase composition, and the surface profile were investigated for the test structures. Depending on the RTA modes, the mesa resistance R and the forward-to-

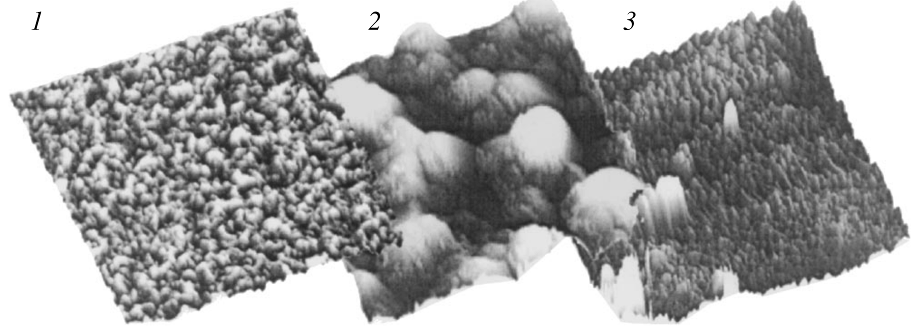

Fig. 1. Variation in the surface profile for the Au film on the Mo–TiB_x–AuGe–GaAs structure due to rapid thermal annealing: (*1*) initial sample; (*2*, *3*) after annealing at 600 and 800°C, respectively. The image size is $5 \times 5 \times 0.3$ μm^3.

reverse current ratio α, as well as the contact resistivity ρ_k, were measured for direct mesas of Gunn diodes with a diameter of 35 μm.

The phase composition and the level of residual stresses in the multilayer Au–Mo–TiB_x–AuGe–GaAs systems were investigated by the complex use of X-ray diffraction, optical microscopy, and atomic-force microscopy (AFM) of the surface.

The X-ray investigations of the phase composition of the system of films were carried out using CuK_α radiation. The average stress in the surface GaAs layers was estimated using the approximate formula

$$\sigma = \frac{Et}{2r(1-\nu)},$$

where E and ν are the Poisson and Young moduli for GaAs; t is the GaAs thickness; and r is the radius of curvature of the sample determined using a double-crystal diffractometer (CuK_α radiation).

To determine the variations in the surface profile of Au films, which gives indirect information on the structural-phase variations in the surface metallization layers, a commercial NanoScope IIIa atomic-force microscope was used. The measurements were carried out in the mode of periodic contact with Si probes (Nanosensors). The console length is 124 μm, the resonance frequency is 330 kHz, and the nominal tip radius is ~5 nm.

3. RESULTS AND DISCUSSION

AFM investigations of the contacts prior to and after annealing showed that the surface of the Au film prior to annealing consisted of close-packed irregular-shaped grains with the average dimensions of 140 nm and a height as large as 92.61 nm (Fig. 1). The analysis of X-ray diffraction patterns of the initial sample (Fig. 2, X-ray diffraction pattern *1*) showed the presence of Au in the polycrystalline phase with the prevailing orientation of crystallites being in the ⟨111⟩ direction. In addition, an insignificant amount of $AuGa_2$ was found. Wide, albeit low, intensity peaks in the low-angle region (15°–20°) point to the presence of quasi-amorphous TiB_x and Mo phases. Annealing at 400°C caused neither variation in the shape and size of surface grains nor phase transformations of the metallization layer.

After annealing at 600°C, a sharp change of the Au surface profile was observed. Most of the grains are ~200 nm in size; the size of some grains reaches 900 nm; the profile is substantially more nonuniform, specifically, the height variance is 291.84 nm. In our

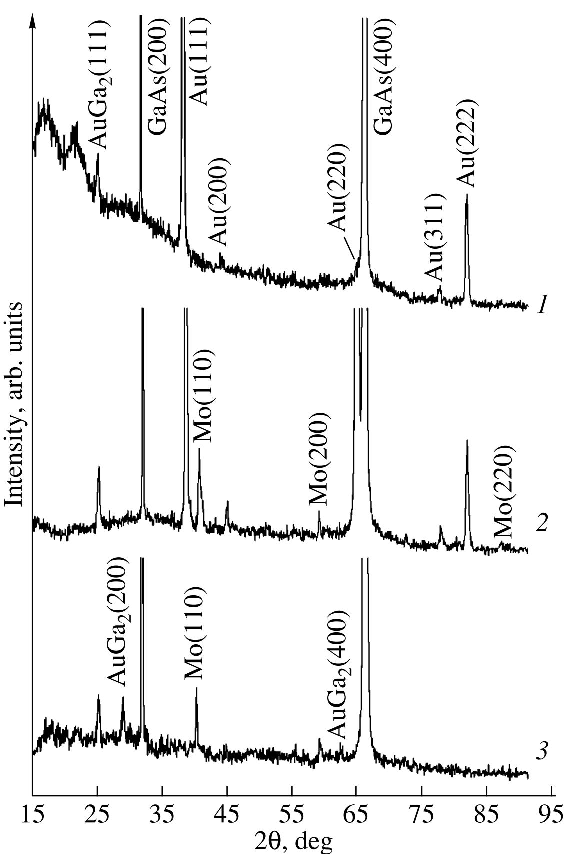

Fig. 2. X-ray diffraction patterns of the Au–Mo–TiB_x–AuGe–GaAs system (*1*) prior to and (*2*) after annealing at 600 and (*3*) 800°C.

Table 1. Average stresses in the near-contact GaAs region in relation to the RTA conditions

Annealing temperature, °C	Initial	400	600	800
Stress, MPa	–10.723–3.707	3.282	1.958	2.509

opinion, the Au film is recrystallized in this case. This is confirmed by the close fit of reflection peaks to those of polycrystalline Au in the X-ray diffraction pattern, which points to the distortions of the prevailing crystallite orientation (Fig. 2, X-ray diffraction pattern *2*). It should also be noted that, in this case, the layer of quasi-amorphous Mo was recrystallized to the polycrystalline phase, whereas a crystalline TiB_x phase was not detected.

The surface of the Au film after annealing at 800°C consists of smooth close-packed ellipsoid-shaped grains of about 200 nm in size which are oriented in one direction. In the background, inclusions of about ~1000 nm in size are observed. The crystalline structure of the film is destroyed (Fig. 2, X-ray diffraction pattern *3*), and the fraction of the $AuGa_2$ phase considerably increases, which points to the destruction of the Au film and diffusion of Au atoms as far as to GaAs, i.e., to the loss of antidiffusion properties by the TiB_x and Mo layers. This fact is consistent with the data of study [9], where similar results are obtained using X-ray photoelectron spectroscopy.

The phase transformations under consideration are caused by the RTA. They are accompanied by varying stresses in contact systems, which emerge during the film deposition. The stresses before and after annealing are listed in Table 1. It can be seen that the deformations in the starting system are not only the largest, they also change their sign within the sample. Annealing at 400 and 600°C causes a decrease in stresses, whereas a further increase in the annealing temperature to 800°C leads to an insignificant increase in these stresses. The latter effect may be explained by making allowance for the diffusion of the atoms of the upper Au layer into GaAs and by the formation of a considerable amount of new phases in the region of the heterointerface; these phases comprise the concentrator of stresses. We note also that similarly to study [9], after the RTA at T_{ann} = 600 and 800°C, cracking of some samples was observed.

It is known that the determination of the curvature of the structure from the X-ray diffraction data yields only an integral estimate of stresses (the depth of the informative layer ~10 μm). Application of the X-ray diffraction procedures, which should show the strain profile of the structures investigated, is restricted by the small width of the transition layer and the degree of its ordering (ranging from the amorphized to the ordered states). However, the inhomogeneity of residual internal stresses in the metal–GaAs system is mainly concentrated at the interface, as a consequence of interphase interactions, which manifest themselves to a lesser degree during the fabrication of the samples and to a greater degree during the RTA. Making allowance for this, we made an attempt to estimate the distribution of strain fields in a contact structure based on investigations of fresh cleaved surfaces, which were obtained as a result of brittle fracture of the structures normal to the interface, i.e., along the GaAs (110) plane.

The analysis of the optical microscopy data (Fig. 3) showed a different character of the plastic relaxation on the cleaved surfaces of the initial structures and structures which were subjected to the RTA. As can be seen from Fig. 3a, the cleaved surface of the initial sample is smooth, whereas, for all annealed samples, the terraces with different densities are observed on the cleaved surfaces (Figs. 3b–3d). The smallest density of terraces is characteristic of the structures subjected to the RTA at 400°C. With the annealing temperature increasing to 600°C, the density of terraces in the structure section increases, which corresponds to the lowest level of stresses (see Table 1). On the heterointerface side, the direction of terraces is parallel to the $\langle 110 \rangle$ direction, whereas at the depth of about 150 μm, they change their direction to $\langle 111 \rangle$. After the RTA at 800°C, damage to the heterointerface is observed.

The emergence of terraces on the cleaved surfaces of the annealed structures can be attributed to the relaxation with the generation of dislocations in the heterointerface region and their motion into the GaAs bulk. The dislocation density increases with an increase in temperature. We analyzed the latter circumstance in study [10]. For a considerable dislocation density, their propagation along the slip planes (111) is more energetically favorable.

On the nanometer scale, the cleaved surface was investigated using AFM. Since the surface GaAs layers in the initial structures were compressed compared with the sample bulk, the cleavage caused plastic relaxation. This manifested itself in the formation of a ridge over the entire cleaved surface with the largest height of 600 nm and the width of about 570 nm (Fig. 4a). The characteristic specific feature of the ridge is the formation of a clear boundary from the substrate side. As can be seen from Table 1, after annealing at 600°C, the average stresses are lowest. Correspondingly, the cleavage of the sample did not lead to a noticeable plastic deformation of the cleavage (Fig. 4b). In contrast, since annealing at 800°C leads to an increase in stresses, the plastic relaxation during brittle cleavage causes the emergence of an inhomogeneous surface with protru-

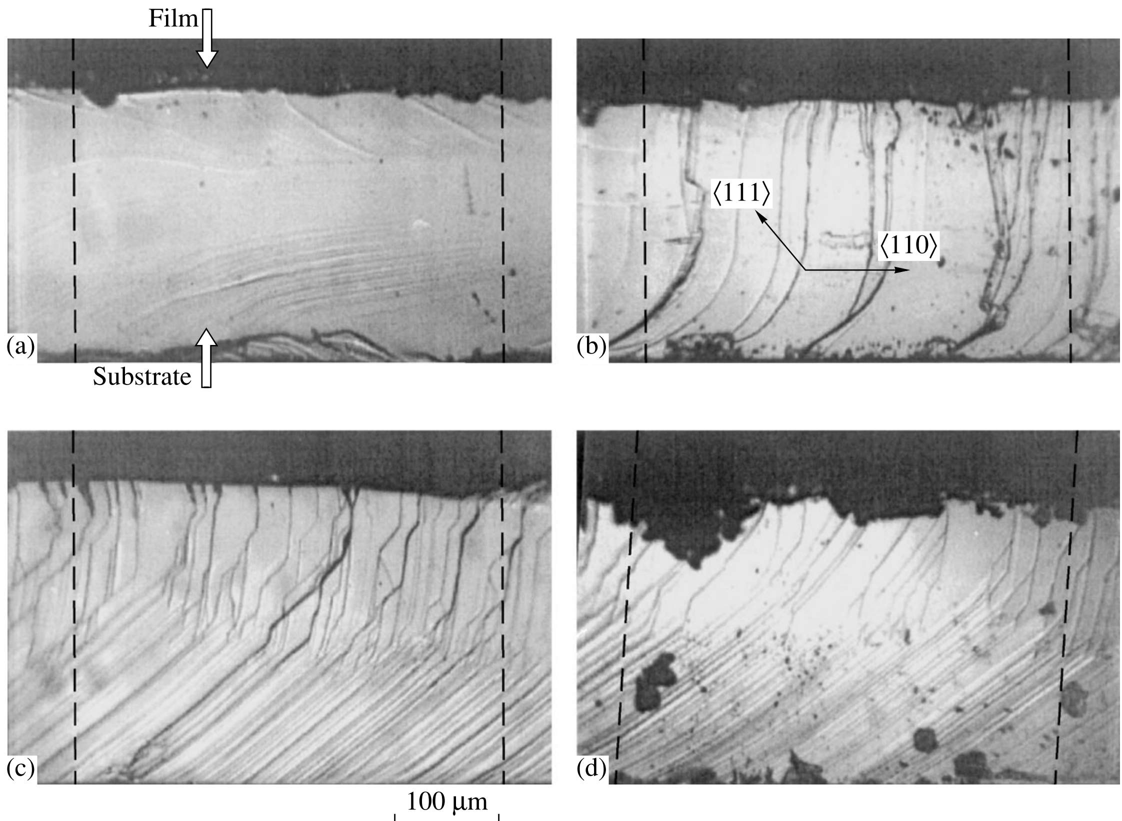

Fig. 3. Image of cleaved surfaces over the (100) plane of the Au–Mo–TiB_x–AuGe–GaAs contact structures (the image was obtained using an optical microscope): (a) initial sample; (b, c, and d) after annealing at 400, 600, and 800°C, respectively.

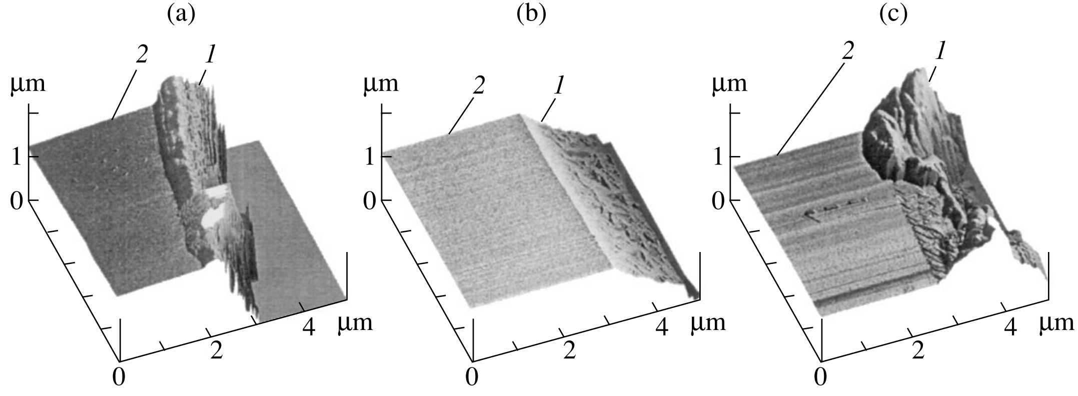

Fig. 4. AFM image of the cleaved surfaces in the (110) plane of the Au–Mo–TiB_x–AuGe–GaAs contact structures: (a) initial; (b) and (c) annealed at 600 and 800°C, respectively. (*1*) The surface region of the substrate; (*2*) the deformation-free region of the substrate.

sions and depressions in the heterointerface region (Fig. 4c). On average, the width of such a cleavage inhomogeneity is ~2000 nm. The latter fact points to the formation of fields of elastic strains in the region of the metal–GaAs interface, whose propagation depth into the substrate is nonuniform and considerably larger than for initial samples.

The experimental data obtained on the structural and phase composition of the heterointerface correlate with the measurements of ohmic resistance and contact resistivity (ρ_k) of breadboard models of Gunn diodes, which were fabricated in the form of direct mesas. The results of measurements are given in Table 2.

It can be seen from Table 2 that the optimum temperature for the formation of the ohmic contact corresponds to the RTA at 500°C. In this case, the current–voltage (*I–V*) characteristics of the contacts in the initial portion (the voltage range of 0–0.3 V) are linear and

Table 2. Effect of the RTA temperature on the resistance of the diode structure (R) and the forward-to-reverse current ratio (α) for the voltage $U = 0.3$ V

T_{ann}, °C	R, Ω	ρ_k, Ω cm^2	α
400	5.45	5.2×10^{-5}	2.09
500	2.05	1.9×10^{-5}	1.05
600	2.6	2.5×10^{-5}	1.08
800	38	3.6×10^{-4}	5.2

symmetric with a coefficient $\alpha \approx 1.03$–1.05. The tendency of the I–V characteristic to deviate from linearity is observed after the RTA at $T_{ann} = 600$°C. The destruction of the contact, which is accompanied by an increase in the ohmic resistance and resistivity by more than an order of magnitude, follows after the RTA at $T_{ann} = 800$°C. However, the RTA at 400°C is evidently insufficient to form a contact with the lowest resistance and the linear I–V characteristic. The reason is that the process is limited by the degree of completeness of reactions between Au, Ge, and GaAs when the weight ratios between Au and Ge do not correspond to the eutectic composition.

4. CONCLUSION

It is shown that, after the RTA at temperatures up to 600°C, the antidiffusion TiB_x layer retains its buffer properties and a quasi-amorphous structure, which ensures the linearity of the current–voltage characteristic and nonrectifying properties of the contact. The optimum temperature of formation of the nonrectifying contact in the Au–Mo–TiB_x–AuGe–GaAs system corresponds to the RTA at 500°C.

The RTA at 800°C leads to destruction of the layered structure of the contact and to an increase in the inhomogeneity of the interface. This is indicated by an increase in the content of the $AuGa_2$ phase, the magnitude of internal stresses in the region of the heterointerface, and considerable deviation of the current–voltage characteristic from linearity, as well as by an increase in the contact resistivity by more than an order of magnitude.

REFERENCES

1. G. Y. Robinson, Solid-State Electron. **18**, 331 (1975).
2. A. K. Rai, R. S. Bhattacharya, and Y. S. Park, Thin Solid Films **114**, 379 (1984).
3. B. A. Lapshinov, A. B. Kamnev, L. N. Kravchenko, *et al.*, Zarubezh. Élektron. Tekh., No. 5, 58 (1987).
4. A. A. Raskin and S. V. Shalimov, Zarubezh. Élektron. Tekh., No. 12, 32 (1990).
5. Yu. A. Gol'dberg, Fiz. Tekh. Poluprovodn. (St. Petersburg) **28**, 1681 (1994) [Semiconductors **28**, 935 (1994)].
6. A. G. Baca, F. Ren, J. C. Zolper, *et al.*, Thin Solid Films **308–309**, 599 (1997).
7. M. E. Levinshteĭn, Yu. K. Pozhela, and M. S. Shur, *The Gunn Effect* (Sovetskoe Radio, Moscow, 1975).
8. V. N. Ivanov, L. E. Kovalenko, T. S. Sumskaya, *et al.*, Élektron. Tekh., Ser. 2: Poluprovodn. Prib., No. 4 (195), 49 (1988).
9. V. V. Milenin, R. V. Konakova, V. N. Ivanov, *et al.*, Zh. Tekh. Fiz. **70** (11), 80 (2000) [Tech. Phys. **45**, 1452 (2000)].
10. N. L. Dmitruk, I. B. Ermolovich, R. V. Konakova, *et al.*, Appl. Surf. Sci. **166**, 520 (2000).

Translated by N. Korovin

Semiconductors, Vol. 37, No. 9, 2003, pp. 1119–1122. Translated from Fizika i Tekhnika Poluprovodnikov, Vol. 37, No. 9, 2003, pp. 1143–1147.
Original Russian Text Copyright © 2003 by Zhukov, Kovsh, Mikhrin, Semenova, Maleev, Vasil'ev, Nikitina, Kryzhanovskaya, Gladyshev, Shernyakov, Musikhin, Maksimov, Ledentsov, Ustinov, Alferov.

PHYSICS OF SEMICONDUCTOR DEVICES

Metamorphic Lasers for 1.3-μm Spectral Range Grown on GaAs Substrates by MBE

A. E. Zhukov, A. R. Kovsh, S. S. Mikhrin, E. S. Semenova, N. A. Maleev, A. P. Vasil'ev, E. V. Nikitina, N. V. Kryzhanovskaya, A. G. Gladyshev, Yu. M. Shernyakov, Yu. G. Musikhin, M. V. Maksimov, N. N. Ledentsov, V. M. Ustinov, and Zh. I. Alferov

Ioffe Physicotechnical Institute, Russian Academy of Sciences, St. Petersburg, 194021 Russia

Submitted February 27, 2003; accepted for publication March 4, 2003

Abstract—A new method for the epitaxial formation of 1.3-μm injection lasers on GaAs substrates is reported. A metamorphic heterostructure with an In content of about 20% is deposited onto an intermediate buffer layer intended for mismatch strain relaxation. The laser active region is formed by quantum wells with a higher In content (about 40%). Lasers with 100-μm-wide stripes demonstrate room-temperature lasing at 1.29 μm with a minimum threshold current density of 3.3 kA cm^2 (0.4 kA cm^2 at T = 85 K). *© 2003 MAIK "Nauka/Interperiodica".*

1. INTRODUCTION

In recent years, considerable attention has been drawn to the design of heterostructures on GaAs substrates emitting in the 1.3-μm spectral range for replacing InP injection lasers in mediumrange fiber-optic communication links. Passing to GaAs substrates could enable the fabrication of uncooled stripe lasers with distributed feedback and vertical cavity surface emitting lasers (VCSELs) with standard GaAs–AlAs Bragg reflectors for the 1.3- to 1.6-μm spectral range employed in fiber-optic communication lines. Stripe lasers for this spectral range, with self-arranged In(Ga)As quantum dots (QDs) [1–3] or strained InGaAsN QDs [4, 5] as the active region, were demonstrated earlier. At the same time, to the authors' knowledge, the possibility of fabricating long-wavelength QW lasers based on metamorphic heterostructures on GaAs substrates has not been discussed in the literature, even though this approach is widely used in the formation of transistor structures [6–8].

The present communication demonstrates that, when special modes are used in the deposition of an intermediate buffer layer, strain relaxation occurs predominantly via the formation of mismatch dislocations localized near the interface. This allows the subsequent growth of dislocation-free InGa(Al)As layers with an In content of about 20% which form the laser structure. When 8-nm-thick $In_{0.4}Ga_{0.6}As$ QWs are inserted into this metamorphic structure, they have sharp interfaces and are elastically strained. As a result of the higher In content in the QW and in the surrounding matrix, compared with that in similar InGaAs/GaAs structures, 1.3-μm emission can be obtained from nitrogen-free QWs. This makes it possible, on the one hand, to avoid the use of untypically low temperatures during deposition of the active region and, on the other hand, to use high optical gains characteristic of QWs.

2. EXPERIMENTAL

The laser structure under study was MBE-grown on a (100) n^+-GaAs substrate in a Riber 32P setup with a solid-state As source. An intermediate Si-doped InGaAs buffer layer with an In content of about 20% was deposited directly onto the GaAs surface. For the buffer layer, the deposition temperature was 400°C; subsequent layers were deposited at 500°C. Shallow-mesa lasers with a stripe width of 100 μm were fabricated on the grown structures. No coating was deposited onto the cavity faces obtained by cleavage. Contacts of n- and p-types were formed by the sputtering and alloying (at 450°C) of AuGe/Ni/Au and AuZn/Ni/Au metallic layers, respectively. The laser characteristics were studied in the temperature range 85–290 K with driving current pulses of 0.2-μs duration. The signal was detected with a Ge photodiode.

The structure was studied by transmission electron microscopy (TEM) in the cross-sectional mode on a Philips EM 420 microscope with 100-kV acceleration voltage. Cross-sectional samples were prepared by standard technology, with a finishing treatment with Ar^+ ions in a Gatan DouMill600 installation.

3. RESULTS AND DISCUSSION

Generally, the relaxation of mismatch strains during the deposition of an InGaAs intermediate buffer layer on the GaAs surface is followed by the formation of interfacial mismatch dislocations propagating along the heterointerface between the buffer layer and the substrate and threading dislocations aligned with the direc-

1063-7826/03/3709-1119$24.00 © 2003 MAIK "Nauka/Interperiodica"

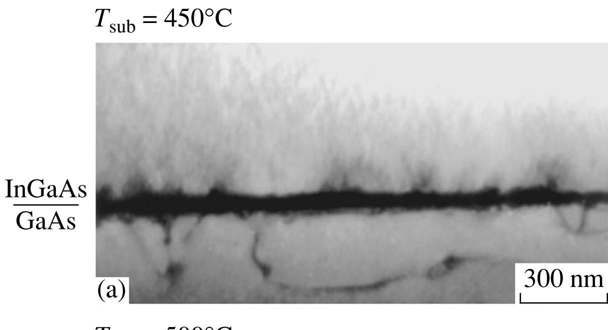

Fig. 1. Cross-sectional TEM micrographs of $In_{0.2}Ga_{0.8}As$ test layers deposited onto GaAs at temperatures of (a) 450 and (b) 500°C. Bright-field images obtained with (220) reflection excited are shown.

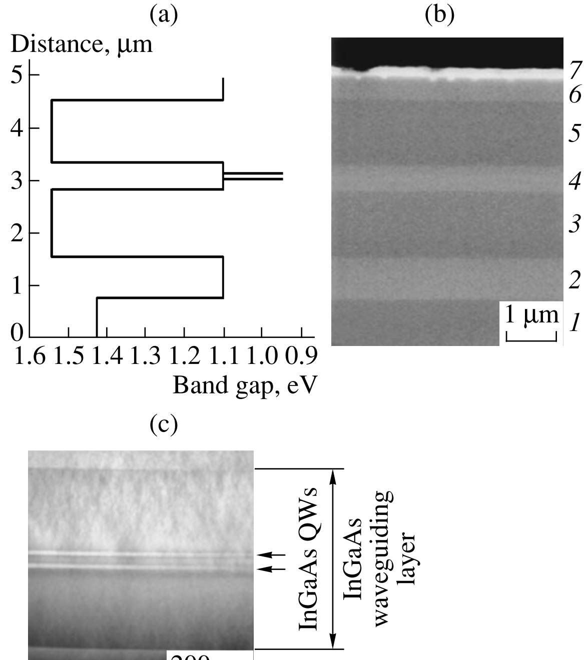

Fig. 2. (a) Band gap variation in the layers of a laser structure along the growth direction; (b) overall cross-sectional SEM image of the laser structure. Digits denote: (*1*) the n^+-GaAs substrate, (*2*) the n^+-InGaAs buffer layer, (*3*) the *n*-InAlGaAs underlying emitter, (*4*) the *n*-InGaAs waveguide layer, (*5*) the *p*-InAlGaAs top emitter, (*6*) the *n*-InGaAs contact layer, and (*7*) the ohmic contact. (c) Dark-field TEM micrograph of the active region obtained with (200) reflection excited.

tion of epitaxial growth. For the concept of metamorphic growth to be applicable to light-emitting devices, it is essential to minimize the density of dislocations that can thread into the upper layers of the structure in which the injected carriers recombine.

Figure 1 demonstrates the effect of the temperature at which the buffer layer is deposited on the character of the strain relaxation. It shows cross-sectional TEM micrographs of test samples at the InGaAs/GaAs interface. When the buffer layer is deposited at temperatures of 450°C (Fig. 1 a) or lower, mostly mismatch dislocations localized in the interfacial region are formed. In this case, the density of threading dislocations does not exceed 10^6 cm^{-2}. By contrast, at higher temperatures of buffer-layer deposition the density of threading dislocations sharply increases, reaching 10^9 cm^{-2} for 500°C (Fig. 1 b). Thus, deposition of the buffer layer at low enough temperatures suppresses the threading of dislocations to subsequent layers of a metamorphic laser structure.

Figure 2a shows the band diagram of the laser structure under study. As the laser waveguide, we used an undoped $In_{0.2}Ga_{0.8}As$ layer of about 0.4 µm thickness confined on both sides with 1.2-µm-thick $In_{0.2}Al_{0.3}Ga_{0.5}As$ *n*- and *p*-type emitter layers doped with 10^{18} cm^{-3} of Si or Be, respectively. Two $In_{0.4}Ga_{0.6}As$ QWs of 8-nm thickness were introduced in the middle of the waveguide layer. The structure was completed with a ~0.4-µm-thick $In_{0.2}Ga_{0.8}As$ contact layer Be-doped to a concentration of 10^{19} cm^{-3}. Thus, the design of the metamorphic laser structure is similar to the typical design of a QW laser on GaAs substrate. However, the use of an intermediate buffer makes it possible to raise the In content by about 20% in all layers of the laser structure.

During epitaxial growth of metamorphic structures, a frequently observed effect is the formation of microscopic roughness and corrugation of the growing surface [9]. The deposition of a metamorphic structure (with the exception of a buffer layer) at 500°C suppresses this undesirable effect. As a result, a high planarity of all the heterointerfaces is achieved, as seen in a cross-sectional micrograph obtained by means of scanning electron microscopy (SEM) of the laser structure (Fig. 2b).

The abrupt change in the In content at the interface between the waveguide and QW is chosen so that emission at a wavelength of about 1.3 µm is obtained at room temperature and the QW width does not exceed the critical thickness of the pseudomorphic layer. Figure 2c shows the TEM image of the laser active region (the waveguide and QWs). As is seen, 8 nm-thick $In_{0.4}Ga_{0.6}As$ layers embedded in the $In_{0.2}Ga_{0.8}As$ matrix have sharp interfaces (no transition to island growth occurs), and the formation of dislocations is not observed. Thus, the active region of the metamorphic laser under study is constituted by elastically strained

QWs. It is necessary to note that no dislocations threading from the buffer layer are observed either.

Also noteworthy are the good electrical characteristics of $In_{0.2}Al_{0.3}Ga_{0.5}As$ layers used as emitters in the laser structure. $In_{0.2}Al_{0.3}Ga_{0.5}As$ is a direct-gap semiconductor, unlike, e.g., $Al_xGa_{1-x}As$ (x > 40%); this makes it possible to avoid a downward shift of the donor level and the related decreasing of the free carrier density. In particular, $In_{0.2}Al_{0.3}Ga_{0.5}As$ test layers doped with Si at the level of 2.5×10^{18} atoms/cm^3 demonstrated a free electron density of $(2.4–2.5) \times 10^{18}$ cm^{-3} at room temperature. The mobility was 600–700 cm^2/(V s), which exceeds by nearly an order of magnitude the typical mobility values in n-$Al_{0.8}Ga_{0.2}As$ layers used as emitters in 1.3-μm QD laser structures on GaAs substrates. The cutoff voltage of the current–voltage characteristics of laser diodes was 0.9 V, which is in good agreement with the expected energy of the optical transition involving the ground state. This fact is indicative of the absence of additional barriers to the injection of carriers within the metamorphic structure, e.g., on the heterointerfaces between the buffer and underlying emitter, or between the top emitter and contact layer.

Figure 3 shows room-temperature spectra of photoluminescence (PL) spectra from the surface of a part of the laser structure etched in $H_2SO_4 : H_2O_2 : H_2O$ solution. With the etching time rising, it is possible to observe successively the luminescence from the $In_{0.2}Ga_{0.8}As$:Be contact layer (a line peak energy of 1.10 eV), the $In_{0.2}Al_{0.3}Ga_{0.5}As$:Be emitter layer (1.54 eV), the $In_{0.4}Ga_{0.6}As$ QWs, and the $In_{0.2}Ga_{0.8}As$ waveguide (0.96 and 1.12 eV, respectively).

In stripe lasers 1.5 and 0.75 mm in length, room-temperature lasing is obtained at a threshold current density of 3.3 and 6 kA cm^2, respectively, at wavelengths of 1294 and 1279 nm. The spectral position of the line indicates that the generation is related to an optical transition involving the ground state of a QW at the $In_{0.4}Ga_{0.6}As/In_{0.2}Ga_{0.8}As$ heterointerface for the entire range of studied cavity lengths.

Figure 4 shows the temperature dependences of the threshold current density and lasing wavelength recorded from a laser of 1 mm length. The lasing spectrum recorded at 290 K is shown in the inset. At 290 K, the threshold current density and the lasing wavelength were 5.2 kA cm^2 and 1286 nm, and, at 85 K, 420 A cm^2 and 1209 nm, respectively. The long-wavelength temperature shift of the generation line is 0.4 nm/K, which is close to the value (0.45 nm/K) commonly observed in QD lasers for the 1.3-μm spectral range. The temperature dependence of the threshold current density is described by characteristic temperatures T_0 = 110 K in the range 85–200 K and T_0 = 65 K at 200–290 K. Further study is necessary to account for the observed bend of the temperature dependence at about 200 K. A plausible cause for this may be the thermal population of the matrix, which manifests itself in room-temperature PL spectra in the form of an extra peak at an energy of about 1.12 eV (see Fig. 3).

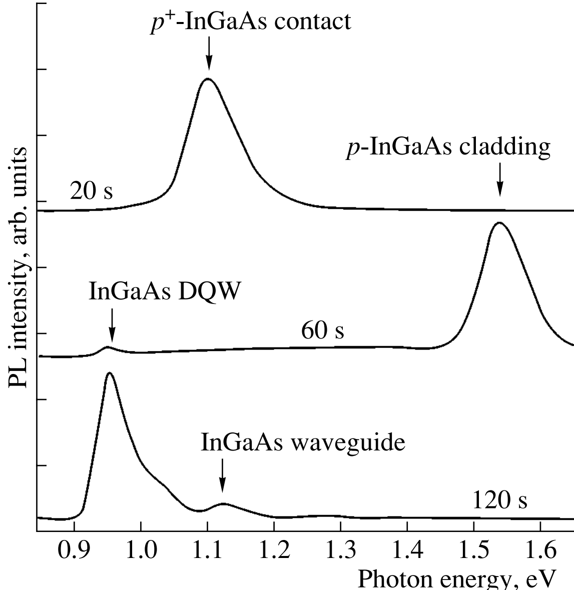

Fig. 3. Room-temperature PL spectra recorded from the part of the laser structure that is etched in $H_2SO_4 : H_2O_2 : H_2O$ solution for periods of time indicated in the figure.

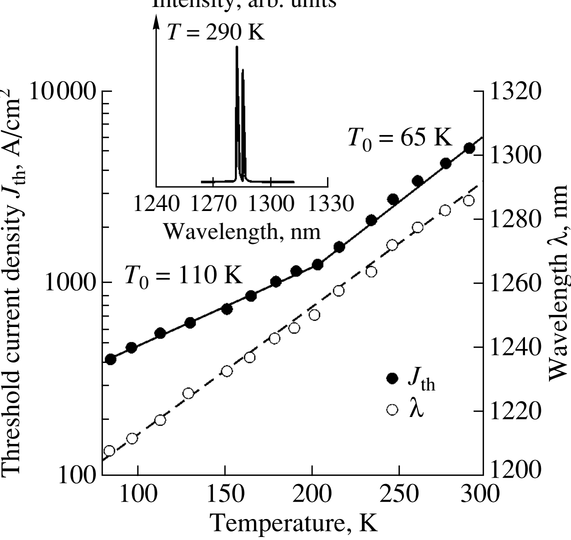

Fig. 4. Temperature dependences of the threshold current density J_{th} and lasing wavelength λ in a stripe laser of 1 mm length. Inset: the lasing spectrum at 290 K.

At room temperature, $In_{0.2}Ga_{0.8}As$ and $In_{0.2}Al_{0.3}Ga_{0.5}As$ layers used as the waveguide and emitters in the laser structure under study have the band gaps of about 1.1 and 1.55 eV, respectively. Their combination makes it possible to obtain a band gap offset at the waveguide–emitter interface that is large enough to prevent the leakage of injected carriers to emitter lay-

ers. In this system of materials, the abrupt change in the refractive index is close to that obtained in $GaAs/Al_{0.3}Ga_{0.7}As$ structures. Our study of 0.94- to 0.98-μm lasers [10] has shown that reasonable optical confinement can also be achieved at a smaller contrast between the waveguide and emitters (e.g., $Al_{0.15}Ga_{0.85}As/Al_{0.3}Ga_{0.7}As$). Thus, quaternary compounds with a wider band gap, like $In_{0.2}Al_{0.15}Ga_{0.65}As$ for instance, max be used in the waveguide of metamorphic lasers in the future. This will make it possible to raise the localization energy of the ground state in QWs relative to the waveguide to improve the temperature stability of the threshold current density. The reduction of the threshold current density at room temperature due to further improvement of the structural perfection of metamorphic heterostructures is also expected.

4. CONCLUSION

The concept of metamorphic growth opens the way for obtaining lasing in the 1.3-μm spectral range at room temperature in structures deposited onto GaAs substrates, without using arrays of self-organized QDs or nitrogen-containing QWs. The suggested approach can, in principle, be used to extend the spectral range to longer wavelengths. In particular, to obtain a 1.55-μm wavelength, it is necessary to raise the In content by approximately 15% both in QWs and in the matrix. In this case, it is probably necessary to use a multistep design of the intermediate buffer layer similar to the one used in metamorphic GaAs transistor structures.

ACKNOWLEDGMENTS

The authors are grateful to V.M. Busov for the SEM studies and M.M. Kulagina for the fabrication of the stripe lasers.

This study was supported by the Joint Project of the Ioffe Physicotechnical Institute, Russian Academy of Sciences, and Nanosemiconductors, Germany.

REFERENCES

1. G. Park, O. B. Shchekin, D. L. Huffaker, and D. G. Deppe, IEEE Photonics Technol. Lett. **13**, 230 (2000).
2. G. T. Liu, A. Stinz, H. Li, *et al.*, IEEE J. Quantum Electron. **36**, 1272 (2000).
3. A. R. Kovsh, N. A. Maleev, A. E. Zhukov, *et al.*, Electron. Lett. **38**, 1104 (2002).
4. A. Yu. Egorov, D. Bernklay, B. Borchert, *et al.*, J. Cryst. Growth **227–228**, 545 (2001).
5. N. Tansu, N. J. Kirsh, and L. J. Mawst, Appl. Phys. Lett. **81**, 2523 (2002).
6. M. Beher, K. van der Zanden, G. Gorghs, and A. Behres, Appl. Phys. Lett. **73**, 2760 (1998).
7. M. Zaknoune, Y. Cordier, S. Bollaert, *et al.*, Solid-State Electron. **44**, 1685 (2000).
8. Y. Zeng, X. Cao, L. Cui, *et al.*, J. Cryst. Growth **227–228**, 210 (2001).
9. Y. Cordier and D. Ferre, J. Cryst. Growth **201–202**, 263 (1999).
10. S. S. Mikhrin, A. R. Kovsh, A. E. Zhukov, *et al.*, in *Proceedings of 26th International Conference on Physics of Semiconductors, Edinburgh, UK* (2002), Paper L2.3.

Translated by D. Mashovets

Semiconductors, Vol. 37, No. 9, 2003, pp. 1123–1126. Translated from Fizika i Tekhnika Poluprovodnikov, Vol. 37, No. 9, 2003, pp. 1148–000.
Original Russian Text Copyright © 2003 by Grekhov, Kyuregyan, Mnatsakanov, Yurkov.

PHYSICS OF SEMICONDUCTOR DEVICES

On the Fast Recovery of the Blocking Property of Silicon Carbide Diodes

I. V. Grekhov*, A. S. Kyuregyan, T. T. Mnatsakanov**, and S. N. Yurkov**

**Ioffe Physicotechnical Institute, Russian Academy of Sciences, Politekhnicheskaya ul. 26, St. Petersburg, 194021 Russia*

***Lenin Electrotechnical Institute, Moscow, Russia*

***e-mail: kyureg@vei.ru*

Submitted February 10, 2003; accepted for publication February 17, 2003

Abstract—The influence of various factors controlling the recovery dynamics of the blocking property of silicon carbide diodes is comparatively analyzed. It is shown that the mechanism related to the large ratio of electron and hole mobilities in SiC is dominant. This mechanism results in the effect of ultrafast (subnanosecond) current break independently of the emitter efficiency asymmetry, which causes initial plasma inhomogeneity in the high-resistivity base. This effect can be observed during the recovery of silicon carbide diodes with a *p*-type base, while "soft" recovery is inherent only to diodes with an *n*-type base. © *2003 MAIK "Nauka/Interperiodica".*

Silicon carbide is one of the most promising materials for developing the components of high-power electronics. In recent decades, SiC-based rectifier diodes with *p–n* junctions [1] and Schottky barriers [2], bipolar [3] and MOS (metal–oxide–semiconductor) transistors [4], as well as thyristors [5], have been fabricated. These devices, in many respects, are superior to silicon analogues. Recently [6], a radically new field of SiC diode applications was experimentally demonstrated, i.e., fast current breakers, which can be employed in oscillators of high-voltage nanosecond and subnanosecond pulses with an inductive energy storage device [7]. The effect of ultrafast recovery of the blocking property (referred to as "hard" recovery), required for such an application, was observed only in diodes with a *p*-type high-resistivity base, while diodes with an *n*-type base were recovered "softly." The authors of [6] assumed that the major cause of these features of SiC diode recovery is the abrupt (dozens of times) shortening of the lifetime of nonequilibrium charge carriers in the thin (on the order of 0.1 μm) layer at the interface between the high-resistivity base and the p^+ emitter.[1] According to [6], such a recombination layer gives rise to initial asymmetry in the bipolar plasma distribution in the diode base, which can also be caused by a significant decrease in the p^+ emitter injection ratio. Therefore, it was assumed that the mechanism of "hard" recovery of SiC diodes with a *p*-type base is the same as in the case of inversely recovering silicon diodes (IRD) with an *n*-type base and a low-efficiency n^+ emitter [7]. However, in addition to this mechanism, the SiC diode recovery dynamics can be affected by at least three other factors.

[1] This assumption was based on the results of lifetime measurements in SiC diodes using various methods. These results were made consistent and explained assuming only the existence of such a recombination layer [8].

One of these is the high (0.24 eV) ionization energy of Al acceptor levels in SiC [9]. Therefore, the room-temperature concentration of charged acceptors (N_a^-) and holes (p) in the p^+ emitter is tens and hundreds of times lower than the total Al concentration N_{Al}. For example, at $N_{Al} = 10^{19}$ cm^{-3}, we have $N_a^- = 2.3 \times 10^{17}$ cm^{-3}. At high current densities (1 kA/cm^2 in the experiments of [6]), such light doping also causes a decrease in the p^+ emitter injection ratio and "hard" recovery, in the same way as in IRDs. Another factor is the large ratio b of the electron μ_n and hole μ_p mobilities (in 4*H*-SiC, $b = 7.5$ [9]), which was indicated as a cause of "hard" recovery of silicon diodes with a *p*-type base as early as in [10], it was also mentioned in [6]. Finally, an important role can be played by the ratio between the maximum reverse voltage U_m and the "punch-through voltage" $U_d = qNd^2/2\varepsilon$, at which the space-charge region (SCR) fills the entire high-resistivity base of thickness d (here, q is the elementary charge, N is the concentration of charged impurities in the base, and ε is the semiconductor permittivity). This means that, if $U_m > U_d$, the entire nonequilibrium plasma will be removed from the base at the diode voltage $U \le U_d < U_m$, after which an abrupt current break inevitably takes place [10, 11].

It is obvious that the efficient design of various-purpose silicon carbide diodes calls for a clear understanding of the relative role of all four mechanisms controlling the dynamics of blocking property recovery, which is currently lacking. This study is devoted to the solution of this problem.

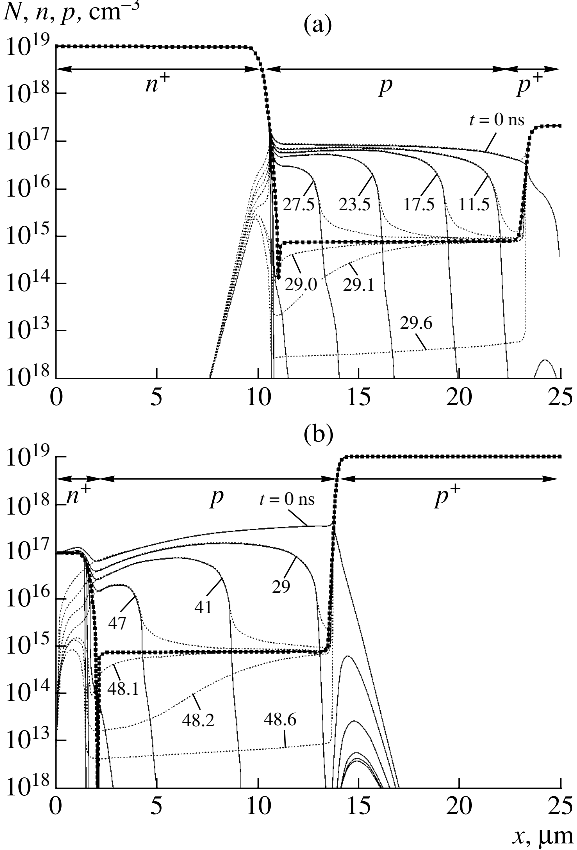

Fig. 1. Distributions of ionized impurities (dotted curve), electrons (solid curves), and holes (dashed curves) in the (a) *p*-1- and (b) *p*-5-type diodes. The numbers at curves indicate the time points (in nanoseconds) after reversals of the diode current sign.

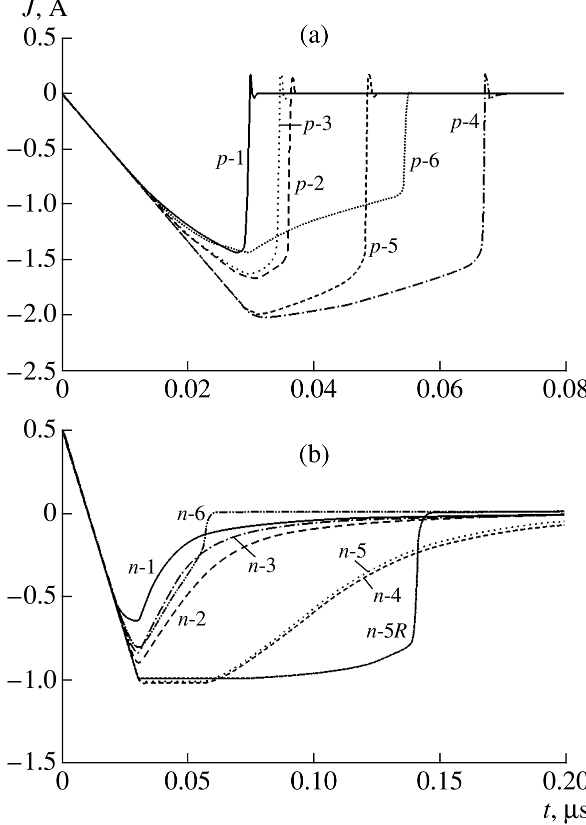

Fig. 2. Characteristics of the recovery kinetics of silicon carbide diodes with (a) *p*- and (b) *n*-type bases, whose parameters are listed in the table.

We analyzed the recovery processes by numerical simulation of the dynamics of nonequilibrium electron–hole plasma in the diode structures with *n*- and *p*-type bases, similar to those described in [6]. To compare the roles of various factors, we considered six types of structures of either conduction type, differing in the ionized donor N_d^+ or acceptor N_a^+ concentrations in the emitters, the presence or absence of recombination layers at the emitter–base interfaces, and base thicknesses. The recombination layer parameters (the thickness is 0.1 μm and the lifetime is 0.3 ns) were the same as those in [8]. The doping profiles are shown in Fig. 1; the basic electrical parameters are listed in the table. The modes set by the external circuit were very close to those in the experiments of [6]: the amplitude and duration of a rectangular pulse of the forward current were equal to 2 A and 500 ns, respectively. With a structure area $S = 2 \times 10^{-3}$ cm^2, these conditions ensured a current density amplitude of 1 kA/cm^2. The reverse current at the stage of high reverse conductivity was controlled by the power supply voltage $U^- = (50–300)$ V, as well as by series and load resistors. The time of forward-to-reverse current switching (60 ns), the lifetime in the base (100 ns), and the spurious series inductance (20 nH) were selected to provide the best fit between the calculated and experimental data for the *n*-1 and *p*-2 structures (see table), for which the influence of all the above-mentioned factors on the recovery dynamics was taken into account. The calculations were carried out using the Issledovanie code [12] adapted for simulating 4*H*-SiC-based devices [13].

Figures 1 and 2 show the calculated results, the analysis of which allows the following conclusions.

(i) The recovery kinetic characteristics calculated for the *p*-1- and *n*-1-type diodes conform well to the experimental results of [6].

(ii) Under the conditions corresponding to the experiments of [6], all the diode types with a *p*-type base are recovered “hard,” and diodes with an *n*-type base (except for the *n*-6-type diode, see below) are recovered “softly.” This was also valid for the *p*-4- and *n*-4-type diodes, which did not contain a recombination layer, and the hole concentration in the p^+ emitter was set equal to 10^{19} cm^{-3}.

(iii) Introduction of a recombination layer near the p^+ emitter (the *p*-2- and *n*-2-type diodes) and a decrease in its hole concentration to 2×10^{17} cm^{-3} (the *p*-3- and

Table

Structure designation	d, μm	$N_{a,d}$, cm^{-3}	N_d^+, cm^{-3}	N_a^+, cm^{-3}	Recombination layer	
					near the p^+ layer	near the n^+ layer
p-1	12	8×10^{14}	10^{19}	2×10^{17}	Yes	No
p-2	12	8×10^{14}	10^{19}	10^{19}	Yes	No
p-3	12	8×10^{14}	10^{19}	2×10^{17}	No	No
p-4	12	8×10^{14}	10^{19}	10^{19}	No	No
p-5	12	8×10^{14}	10^{17}	10^{19}	No	Yes
p-6	37.0	8×10^{14}	10^{19}	2×10^{17}	Yes	No
n-1	37	5×10^{14}	10^{19}	2×10^{17}	Yes	No
n-2	37	5×10^{14}	10^{19}	10^{19}	Yes	No
n-3	37.0	5×10^{14}	10^{19}	2×10^{17}	No	No
n-4	37	5×10^{14}	10^{19}	10^{19}	No	No
n-5	37	5×10^{14}	10^{17}		No	Yes
n-6	12.0	5×10^{14}	10^{19}	2×10^{17}	Yes	No

n-3-type diodes) reduce the extracted charge by approximately three times. However, both methods for decreasing the p^+ emitter efficiency leave the recovery dynamics the same as in the case of the high-efficiency p^+ emitter (the p-4- and n-4-type diodes).

(iv) Even the hard-to-realize "inversion" of efficiency asymmetry of injection from the emitter junctions (p-5- and n-5-type diodes) leaves the recovery dynamics unchanged; although the density of nonequilibrium plasma at the interface with the p^+ emitter is five to ten times higher than near the n^+ emitter (see Fig. 1) in these cases.

(v) An increase in the p-type base thickness to 37 μm (the p-6-type diode, for which the punch-through voltage U_d was several times higher than the highest reverse voltage U_m) does not change the recovery dynamics. However, this causes a decrease in the current at which the "hard" recovery stage sets in. A change in the ratio of U_m and U_d in diodes with an n-type base leads to a much different result: a decrease in d to 12 μm (the n-6 diode) and an increase in U_m to values at which $U_d < U_m$ (curve n-5R in Fig. 2b; in this calculation version, U_m and the series resistance R were simultaneously increased by a factor of 30 to keep the previous current unchanged) give rise to the recovery stage.

(vi) The "break time" estimated for all types of diodes with a p-type base was found to be 0.5 ± 0.05 ns, which conforms to the experiment of [6]. In the diodes with a p-type base, the break time was about 3 ns because of either the low current density at the break stage (the n-6-type diode) or the large time constant for the barrier-capacitance recharging of the diode (curve n-5R in Fig. 2b).

The major factor controlling the recovery dynamics is the large ratio b of electron μ_n and hole μ_p mobilities. This circumstance is caused by the fact that the rate of plasma "extraction" by the reverse current is significantly (by factors of b^3 and b, respectively, before and after recovery of the emitter junctions) higher from the near-anode region than from the near-cathode one [10]. This phenomenon has also long been known in silicon diodes with $b = 3$ [10]. However, in silicon carbide, where $b = 7.5$, it is much more pronounced and dominates in all diode types independently of asymmetry in the emitter efficiency and the initially nonuniform distribution of plasma over the high-resistivity base. Therefore, the qualitative pattern of plasma evolution was identical in all cases under consideration. This is evident in Fig. 1, which shows the distributions of the electron and hole densities in the p-1- (a) and p-5-type (b) diodes at various instants of time after current sign reversal. We can see that the plasma-free base region arises at the anode in both cases and, expanding with time, reaches the cathode well before the cathode emitter junction has time to be recovered. In this respect, the silicon carbide diodes considered in this study and in [6] differ drastically from high-voltage silicon diodes [7, 10].

Finally, two important conclusions, which are important for practical applications, follow from the results obtained. The rectifier diodes, which should exhibit as "soft" as possible recovery to prevent critical overvoltages in circuits with inductances, should be SiC-based with high-resistivity n-type bases. On the contrary, diodes with high-resistivity p-type bases are applicable to fast current breakers. In this case, there is no need to form special doping profiles, preset different recombination rates, or employ short forward pumping. The dynamics of nonequilibrium plasma evolution required for the efficient operation of current breakers [7] takes place in the p-base almost always as a result of high b.

This study was supported by the Russian Foundation for Basic Research, project no. 02-02-16496.

REFERENCES

1. Y. Sugawara, K. Asano, R. Singh, *et al.*, Mater. Sci. Forum **338–342**, 1371 (2000).
2. P. Alexandrov, J. H. Zhao, W. Wring, *et al.*, Electron. Lett. **37**, 1139 (2001).
3. P. A. Ivanov, M. E. Levinshtein, A. K. Agarwal, *et al.*, Semicond. Sci. Technol. **16**, 521 (2001).
4. S.-J. Run, A. K. Agarwal, J. Richmond, *et al.*, in *Proceedings of ICSCRM, Japan* (2001), p. 1265.
5. A. K. Agarwal, P. A. Ivanov, M. E. Levinshtein, *et al.*, Sci. Technol. **16**, 260 (2001).
6. I. V. Grekhov, P. A. Ivanov, A. O. Konstantinov, and T. P. Samsonova, Pis'ma Zh. Tekh. Fiz. **28** (13), 24 (2002) [Tech. Phys. Lett. **28**, 544 (2002)].
7. I. V. Grekhov, Izv. Ross. Akad. Nauk, Énerg., No. 1, 53 (2000).
8. M. E. Levinstein, T. T. Mnatsakanov, P. A. Ivanov, *et al.*, IEEE Trans. Electron Devices **48**, 1703 (2001).
9. *Properties of Advanced Semiconductor Materials GaN, AlN, InN, BN, SiC, SiGe*, Ed. by M. E. Levinstein, S. L. Rumyantsev, and M. S. Shur (Wiley, New York, 2001).
10. H. Benda and E. Shpenke, Proc. IEEE **55**, 1331 (1967).
11. M. T. Rahimo and A. Shammas, Microelectron. J. **30**, 499 (1999).
12. T. T. Mnatsakanov, I. L. Rostovtsev, and N. I. Philatov, Solid-State Electron. **30**, 579 (1987).
13. M. E. Levinstein, T. T. Mnatsakanov, P. A. Ivanov, *et al.*, Electron. Lett. **36**, 1241 (2000).

Translated by A. Kazantsev

Semiconductors, Vol. 37, No. 9, 2003, pp. 999–1030. Translated from Fizika i Tekhnika Poluprovodnikov, Vol. 37, No. 9, 2003, pp. 1025–1055.
Original Russian Text Copyright © 2003 by Blank, Gol'dberg.

REVIEW

Semiconductor Photoelectric Converters for the Ultraviolet Region of the Spectrum

T. V. Blank* and Yu. A. Gol'dberg

Ioffe Physicotechnical Institute, Russian Academy of Sciences, Politekhnicheskaya ul. 26, St. Petersburg, 194021 Russia

**e-mail: tblank@delfa.net*

Submitted November 14, 2002; accepted for publication November 14, 2002

Abstract–Recently, ultraviolet photoelectronics emerged in response to the needs of medicine, biology, military equipment, and the problem of the hole in the ozone layer. A specific feature of this field of photoelectronics is the need to detect weak (albeit appreciably affecting vital human functions) signals against a background of intense radiation in the visible and infrared regions of the spectrum. Ultraviolet electronics relies on Si-based *p–n* structures and GaP-based Schottky barriers, *p–n* structures and Schottky barriers based on GaN and AlGaN ("solar-blind," i.e., solar-radiation-insensitive devices), SiC structures with potential barriers (high-temperature devices), and ZnO- and ZnS-based photoresistors and Schottky diodes. In this review, the parameters of starting wide-gap semiconductors are given, physical foundations for photoelectric conversion and the principles of formation of ohmic contacts are described, characteristics of corresponding devices are given, and the envisaged lines of further studies are outlined. © *2003 MAIK "Nauka/Interperiodica".*

1. INTRODUCTION

At present, semiconductor-based photoelectric converters are being actively developed worldwide for the ultraviolet (UV) region of the spectrum; these converters are urgently required in the following fields of science and technology:

(i) interference-tolerant UV location;

(ii) ecology (for example, for monitoring the size of the hole in the ozone layer in the stratosphere);

(iii) biotechnology (synthesis of vitamins D_2 and D_3); and

(iv) medicine (physiotherapy, autotransfusion of blood, preventive treatment of catarrhal illness, and protection from carcinogenic radiation);

Semiconductor-based photoelectric converters, especially structures with a potential barrier, feature high efficiency, low mass, and a small size; they are not affected by a magnetic field, but provide higher reliability compared to photoelectric tubes and can store charge and integrate a detected signal.

The first problem encountered by producers of semiconductor-based photoelectric converters was related to the material science of wide-gap semiconductors. UV photoelectronics originated in the 1960s and was first based on silicon devices, since silicon was already being produced on commercial level and showed good performance as a material for solar cells. At the same time, the high sensitivity of silicon photodetectors to visible (and, especially, infrared (IR)) radiation necessitated the use of semiconductors with a wider band gap. As a result, in the 1980s–1990s, GaP became the most widely used material in this field; at that time, GaP was used as a material for light-emitting diodes. However, the need for solar-blind photodetectors (mainly, for detection of the rockets' exhaust) gave rise to a "nitride boom" over the last five to ten years; i.e., wide-gap semiconductors, such as GaN, AlN, and ternary compounds based on them, have been actively studied and produced commercially. Scientific journals and conferences devoted to nitrides and related semiconductors are often encountered. At present, an urgent problem is the development of the technology for growing high-quality nitrides with parameters that are close to the theoretical limit, since this would increase the detectivity of devices.

The second important problem to be solved was related to the development of photoelectric-converter structures and to studying the mechanism of photoelectric conversion in these structures. Photoresistors feature a high photosensitivity and can operate in the multiplication mode; however, photoresistors cannot operate in the photoelectric generator mode and feature a nonlinear dependence of photocurrent on the flux density of radiation. Therefore, the development of photodetectors included mainly the production of structures with potential barriers. These structures had a high impedance, which allowed these structures to be used in the focal plane of readout devices; in addition, they can operate at high frequencies and are compatible with integrated-circuit technology. Schottky diodes are especially attractive for use in the UV region of the spectrum, since short-wavelength radiation is absorbed in the region with a high electric-field strength, which substantially increases the response speed and quantum efficiency. In this respect, an urgent task is the development of a photoconversion theory that would make it

1063-7826/03/3709-0999$24.00 © 2003 MAIK "Nauka/Interperiodica"

Table 1. Classification of UV radiation [1, 2]

Spectral region	λ, μm	λ, eV	The region of the most profound effect λ, μm
Ultraviolet radiation	0.01–0.38	3.2–124	
Near-UV radiation	0.20–0.38	3.2–6.2	
Long-wavelength (UV–A)	0.315–0.38	3.2–3.9	
Medium-wavelength (UV–B)	0.28–0.315	3.9–4.4	
Short-wavelength (UV–C)	0.20–0.28	4.4–6.2	
Far (vacuum) UV radiation	0.01–0.20	6.2–124	
Near UV	0.3–0.4	3.1–4.1	
Middle UV	0.2–0.3	4.1–6.2	
Far UV	0.1–0.2	6.2–12.4	
Extreme UV	0.01–0.1	12.4–124	
Pigmentation-forming	0.3–0.66	1.9–4.1	0.36–0.44
Erythematous	0.28–0.31	4.0–4.4	0.2967
	0.20–0.28	4.4–6.2	0.25
Vitamin-forming	0.249–0.315	3.93–4.98	0.29
Bactericidal	0.21–0.31	4.0–5.9	0.254
Carcinogenic	0.20–0.30	4.1–6.2	
Burn-inducing	<0.25	>5	

possible to choose the optimal structure and technology of the devices under consideration.

The third problem is related to the development of selective and band-restricted solar-blind devices, and devices for separate portions of the UV region of the spectrum (erythematous, bactericidal, vitamin-forming, and carcinogenic). The problem of solar-blind devices is solved to a great extent on the basis of GaN–AlN solid solutions, whereas the problem of selective devices is only beginning to be considered.

The fourth problem concerns ohmic contacts to wide-gap semiconductors. A number of metals and combinations of these have been tested; as a result, low-impedance contacts to heavily doped semiconductors have been devised. However, a general theory of contacts is still lacking, and the formation of a contact to a lightly doped semiconductor remains an unresolved issue. In addition, it is not clear which processes bring about the irreversible transformation of a Schottky barrier into an ohmic contact.

Finally, the fifth problem is related to the use of UV detectors for monitoring the environment, in particular, for studying the hole in the ozone layer; this field includes drawing up maps for the UV climate in various areas of the Earth, simulation of the processes occurring in the course of ozone-layer destruction, and development of methods for the restoration of the ozone layer.

2. ULTRAVIOLET RADIATION

2.1. Classification

UV radiation occupies the spectral region in the wavelength range $\lambda = 0.01$–0.38 μm (corresponding to the photon-energy range $h\nu = 3.2$–124 eV) [1] and is conventionally classified in the near and far (vacuum UV) regions (Table 1) [1, 2].

2.2. Applications

During the 200 years that have elapsed since the discovery of UV radiation, the following fields of UV applications and UV detectors have emerged [2–11]:

(I) medicine (physiotherapy, autotransfusion of blood, and irradiation of patients with solar light;

(II) agriculture (hotbed and hothouse technologies);

(III) biotechnology (synthesis of vitamins D_2 and D_3);

(IV) disinfection of water, air, cloths, instruments, and food in the cases of long-term storage or epidemics;

(V) astronavigation and UV location (in addition to infrared location);

(VI) astronomy (obtaining information about physical processes in space objects that can emit UV radiation);

(VII) materials science (determination of substance composition and electronic structure of elements);

(VIII) ecology (the problem of the ozone hole and detection of contaminants in the environment);

(IX) nuclear physics and power engineering (detection of nuclear particles using scintillators); and

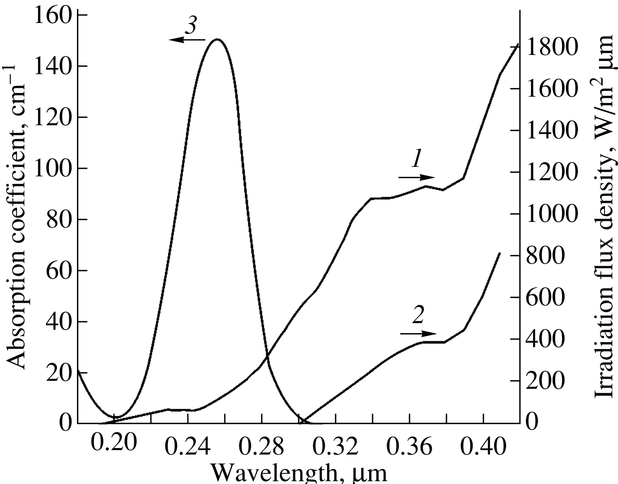

Fig. 1. Approximate solar-radiation spectrum in the UV region (*1*) beyond the Earth's atmosphere [9] and (*2*) at the Earth's surface at ocean level, at a Sun altitude of 45°, and in clear cloudless weather [10]; curve (*3*) represents the optical-absorption spectrum of ozone [7].

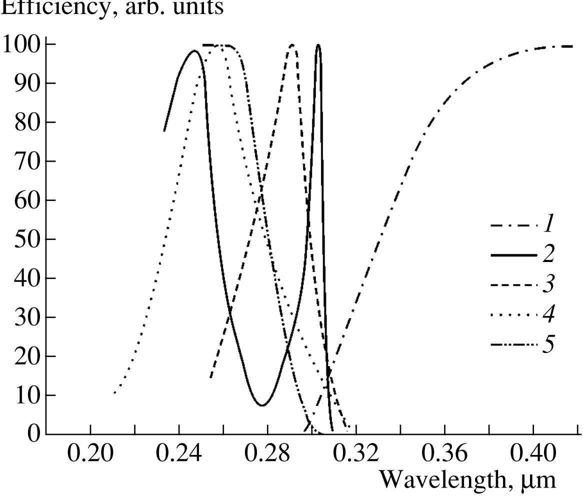

Fig. 2. The spectrum of the relative effect of various types of UV radiation [2–6, 11]: (*1*) pigmentation-forming, (*2*) erythematous, (*3*) vitamin-forming, (*4*) bactericidal, and (*5*) DNA-destroying.

(X) defectoscopy, crime detection, and art history (luminescent analysis based on the ability of substances to luminesce when exposed to UV radiation).

Recently, much attention has been given to the effect of UV radiation on humans, largely due to the problem of the ozone hole and to the increasing number of cancer cases. The effect of UV radiation on a human is different for various UV wavelengths and can be classified into the following several manifestations according to specific overlapping wavelength regions (see Figs. 1, 2; Table 1):

(i) pigmentation-inducing radiation gives rise to melanin in the skin (tan);

(ii) erythematous (biologically active) radiation is the most beneficial UV radiation for a human since it fortifies the circulatory and immune systems;

(iii) vitamin-forming radiation is necessary for synthesis of group-*D* vitamins by an organism;

(iv) bactericidal radiation can kill various bacteria and viruses; and

(v) carcinogenic radiation leads to destruction of DNA in human cells and gives rise to carcinoma.

2.3. The Problem of the Ozone Hole

Ozone (O_3) is an allotropic modification of oxygen. Ozone has a density of 1.62 relative to air, a melting point of –192.7°C, and a boiling point of –112°C. Ozone is formed from oxygen under exposure to UV radiation with photon energies $h\nu > 5.12$ eV ($\lambda <$ 0.242 µm):

$$3O_2 + 68\ \text{kcal} \longrightarrow 2O_3.$$

The absorptance of light by gaseous ozone (Fig. 1) in the visible region of the spectrum is very low (<0.06 cm^{-1}). However, in the UV spectral region at λ = 0.2–0.3 µm (the Hartmann band), the absorption coefficient can be as large as 150 cm^{-1}; the highest absorption [7] is at a wavelength of 0.2553 µm.

In the Earth's atmosphere, the largest amount of ozone (the ozone layer) is at altitudes of 10–50 km (the stratosphere) with a peak at 20–25 km. The density of air at these altitudes is very low; if we recalculate this density for normal conditions (760 Torr, 0°C), we find that the average thickness of the ozone layer is 2.5–3 mm (this density ranges from ~2 mm at the equator to ~4 mm near the poles) [7]. The total content of ozone in the stratosphere or in its separate portions is conventionally expressed in so-called Dobson units (DU): 100 DU correspond to 1-mm thickness of pure ozone layer if recalculated for normal conditions; thus, the total amount of ozone in the stratosphere amounts to 250–300 DU on average.

The total ozone content in the stratosphere is governed by a balance between ozone formation, transport, and destruction. Ozone destruction occurs according to the Chapman cycle; i.e.,

$$O_3 + O \longrightarrow 2O_2,$$

However, the following catalytic cycle is more important:

$$X + O_3 \longrightarrow XO + O_2,$$

$$\frac{XO + O \longrightarrow X + O_2}{O_3 + O \xrightarrow{X} 2O_2},$$

Table 2. Temporal variations in the total ozone content and in the ozone-hole area over Antarctic (the area of the region where the total ozone content <220 DU)

Year	Total ozone content, DU	The ozone-hole area, 10^6 km^2
1978	220	
1979	210	0.02
1980	195	0.47
1981	206	0.24
1982	182	3
1983	170	6.8
1984	154	9.33
1985	143	13.3
1986	159	9.90
1987	121	19.2
1988	179	8.19
1989	124	18.9
1990	126	17.7
1991	110	18.8
1992	121	21.2
1993	85	21.9
1994	90	24

Note: The measurements [20] were performed in different years in the interval from September 15 to October 15 using the TOMS/Meteor-3 satellites.

Here, the catalysts X can be represented, for example, by the OH, H, NO, Cl, and Br radicals; the chlorine and bromine radicals are most important [8, 12–14].

Natural loss of ozone occurs owing to the appearance of Cl and Br atoms (from the CH_3Cl and CH_3Br compounds) in the atmosphere as a result of biological processes in oceans, decomposition of biomass, and formation of sulfates in the course of volcanic eruptions [15]. Artificial loss of ozone as a result of the appearance of chlorides in the atmosphere due to anthropogenic factors is also important. The first source of ClO_x (beginning in the 1920s) was CCl_4, which was widely used as an industrial solvent [16]; since the 1930, chlorofluorocarbons (Freons) have become the main ozone-destructing agents). At present, the sources of chlorofluorocarbons are [17] air conditioners (19%), the production of foam plastics and isolators (28%), refrigerators (9%), solvents (12%), aerosols (5%), sterilizers (4%), and other sources (22%).

As a result of natural and artificial processes, the amount of ozone in the stratosphere has appreciably decreased; it is noteworthy that the amount of ozone [18–20]:

(I) decreases to a greater extent at high latitudes than near equator;

(II) varies with seasons; for example, the smallest amount of ozone in the South Pole region is observed from September to October; and

(III) decreases from year to year in all regions, especially at high latitudes; in ten years (from 1988 to 1998), the total content of ozone in the stratosphere decreased by 5–8%.

A local decrease in ozone content in the stratosphere is usually referred to as the ozone hole; this decrease manifests itself, first, in a steady lowering in the total content of ozone in autumn (for example, the total content of ozone in the region of the South Pole was lower in 1987 than in 1979 by a factor of 2) and, second, in a later onset of the maximal value for this same year. An unprecedentedly low ozone content in the stratosphere above Antarctic was detected in 1993 (85 DU instead of the typical value of 220 DU in October, 1978) (Table 2) [20].

The annual decrease in the total ozone content in the stratosphere above the Arctic amounts to 1.2–2%; as a result, the ozone content in the stratosphere above the Arctic in 1985–1986 became lower than that in 1979–1980 by 8–12% [8]. The total content of ozone at middle latitudes decreases to a lesser extent but steadily. For example [21], the amount of ozone above Sapporo (Japan, 43° N.L.) during the winter–spring season of 1992 decreased by 10–15% compared to that in 1985; it is noteworthy that this decrease occurred mainly at an altitude of ~24 km.

Recent satellite-based measurements revealed a steady decrease in the total ozone content at middle latitudes of the northern and southern hemispheres (by ~2–4% in a decade) and an absence of appreciable variations in the stratospheric ozone content in the tropics. In the northern hemisphere, the largest losses of ozone occurred at an altitude of 40 km (by 7.4 ± 2% over a decade), an altitude of 20 km (by 5.1 ± 1.8% over a decade), and at an altitude of 15 km (by 7.3 ± 4.6% over a decade) [22].

The ozone layer prevents harmful UV solar radiation with $\lambda = 0.2–0.3$ μm from reaching the Earth's surface; this radiation leads to the destruction of DNA and to carcinomas. As a result of the decrease in the ozone layer thickness, the flux density of UV radiation reaching the Earth's ground level has increased; this is especially true for the spectral UV region hazardous to human health. For example, as the total ozone content decreased from 280 to 240 DU at a rate of 0.12 DU per diem, the flux density of biologically harmful UV radiation ($\lambda = 0.305–0.34$ μm) increased at a rate of 0.13 mW/m^2 per diem in Tibet at the sun altitude of 30° [23]. Similar dependences were also observed in Europe [24]. Measurements in Reykjavik, Brussels, Garmisch-Partenkirchen, and Salonika at a zenith angle of 63° showed that a decrease in the total ozone content from ~360 to ~300 DU in 1990–1997 was the main cause of a long-term increase in the flux density of radiation at a wavelength of 0.305 μm by a factor of 1.7.

Epidemiological studies in the USA have shown that the rate of cancer deaths increases nonlinearly and appreciably as the ozone layer thickness decreases and as the intensity of biologically hazardous UV radiation increases. For example, as the total ozone content decreased by ~5%, the number of cancer cases increased by 11–13% [25]. If we do not make any efforts to reduce the production of chlorofluorocarbons, half of the ozone layer will be destroyed by 2075; as a result, the number of cancer cases may increase to 154 million per year (compared with 9.5 million per year at present), and the number of terminal cases may increase to three million (instead of 0.1 million at present) [17]. In this context, almost all countries signed the Montreal Protocol in 1988, which required a 50% decrease in the production of chlorofluorocarbons relative to the level in 1986 starting in July, 1988. The London Protocol was signed by a majority of countries in June, 1988; this protocol required a reduction in the production of ozone-destroying compounds to 50% by 1995 and complete cessation by 2000 (by 2010 for developing countries). It was assumed that either chlorofluorocarbons would be replaced by fluorocarbons or additions in the form of hydrogen molecules would be introduced in these compounds in order to destroy the latter in the low layers of the atmosphere. Such replacement would increase the production cost by a factor of 2–3; however, this replacement would make it possible to preserve the ozone layer. The above requirements were reinforced at the international meetings in Copenhagen in 1992 and in Vienna in 1995 [26, 27], where it was suggested to take steps to restore the ozone layer by the middle of the twenty-first century.

3. SEMICONDUCTIVE MATERIALS FOR ULTRAVIOLET PHOTOELECTRIC CONVERSION

Semiconductive photoelectric converters are typically characterized by a number of parameters, the most important of which are [28–30]

(i) the spectral range of photosensitivity $\Delta\lambda$;

(ii) the quantum efficiency $\gamma = (1 - R)\eta(1 - \sigma)$ or the current responsivity $S_I = \gamma/h\nu$;

(iii) the photosensitive surface area S_{eff};

(iv) the operating voltage V_{op};

(v) the dark current I_d and differential resistance at zero voltage $R_0 = nkT/qI_0$;

(vi) the specific detectivity $D^* = (2G/hct)^{1/2}$;

(vii) the photosensitivity threshold (the noise-equivalent power) $NEP = \Phi V_n/V_p(\Delta f)^{1/2}$;

(viii) the response speed τ (or the operating cutoff frequency f_d);

(ix) the parameters' temperature coefficients α_T;

(x) the capacitance C;

(xi) the highest dissipated power $P_{\max}$; and

(xii) the operation parameters (stability, ionizing-radiation resistance, the highest admissible operating voltage $V_{\max}$, the mass m, and the size).

Here, λ is the wavelength of incident radiation, R is the coefficient of reflection of light from the structure surface, η is the internal quantum yield, σ is the loss factor, $h\nu$ is the photon energy, n is the ideality factor, k is the Boltzmann constant, T is the temperature (expressed in K), q is the elementary charge, I_0 is the saturation current, G is the generation rate of charge carriers, h is Planck's constant, c is the speed of light, t is the detector thickness, Φ is the incident-radiation flux, V_p is the photoresponse voltage, V_n is the noise voltage, f is frequency, and Δf is the bandwidth.

We will consider the properties of starting semiconductors taking into account the aforementioned parameters.

The long-wavelength limit of an ideal photoelectric converter should correspond to the boundary between the visible and UV regions of the spectrum ($\lambda = 0.38$ μm); i.e., the absorption coefficient of light in the starting semiconductor should be as small as possible at $\lambda > 0.38$ μm and as large as possible at $\lambda < 0.38$ μm.

As a rule, the required spectral range can be attained by one of the following three methods:

(i) the use of semiconductors with a band gap E_g, which is close to 3.2 eV (these semiconductcors include GaN, AlGaN, 6*H*-SiC, and 4*H*-SiC compounds);

(ii) the use of indirect-band semiconductors with a value of E_g which is much less than 3.2 eV but with a threshold energy of direct transitions E_0 which is close to 3.2 eV (for example, GaP, for which $E_g = 2.26$ eV and $E_0 = 2.8$ eV); it is assumed that the absorption coefficient of light at $h\nu < E_0$ is fairly small, whereas it should be quite large at $h\nu > E_0$; and

(iii) the use of high-quality commercial semiconductors (such as Si) and the employment of correcting UV filters.

The energy-band parameters and absorption coefficients for the main semiconductive materials are listed in Table 3 [31–42].

The operating voltage of photodetectors in the photodiode mode is limited by the breakdown voltage. The breakdown voltage V_{BR} in the case of avalanche multiplication for abrupt *p–n* junctions and Schottky barriers [43] is approximately given by

$$V_{\text{BR}}[V] = 60\left(\frac{E_g}{1.1}\right)^{3/2}\left(\frac{N}{10^{16}}\right)^{-3/4};$$

for *p–n* junctions with a gradual (linear) distribution of impurities in the space-charge region, the breakdown voltage is expressed as

$$V_{\text{BR}}[V] = 60\left(\frac{E_g}{1.1}\right)^{3/2}\left(\frac{a}{3 \times 10^{20}}\right)^{-2/5},$$

Table 3. Energy-band parameters and absorption coefficients of the most important semiconducting materials at 300 K [31–42]

Semiconductor	Si	GaAs	$Al_xGa_{1-x}As$, $x = 0.491$	$Al_xGa_{1-x}As$, $x = 0.804$	GaP	GaN
E_g, eV	1.12	1.425	2.04	2.09	2.26	3.39
E_0, eV	3.4		2.08	2.6	2.78	
Photon energy, eV	Absorption coefficient, cm^{-1}					
2.4	1.465×10^4	9.0×10^4	4.997×10^4	8.7×10^4	8.6×10^4	3×10^2
2.6	2.381×10^4	1.42×10^5	7.7×10^4	2.742×10^4	2.94×10^4	
2.8	4.65×10^4	2.81×10^5	1.22×10^5	5.812×10^4	3.342×10^4	
3.0	8.173×10^4	5.92×10^5	2.08×10^5	1.07×10^5	6.826×10^4	2×10^3
3.2	2.043×10^5	7.42×10^5	4.34×10^5	1.75×10^5	1.093×10^5	6×10^3
3.4	9.32×10^5	7.15×10^5	6.62×10^5	3.07×10^5	1.96×10^5	
3.6	1.09×10^6	7.17×10^5	7.36×10^5	5.70×10^5	4.99×10^5	1×10^5
3.8	1.225×10^6	7.35×10^5	7.48×10^5	7.75×10^5	9.86×10^5	1.25×10^5
4.0	1.454×10^6	7.78×10^5	7.88×10^5	8.59×10^5	8.80×10^5	1.25×10^5
4.2	1.974×10^6	8.81×10^5	8.71×10^5	9.30×10^5	8.78×10^5	1.4×10^5
4.4	2.383×10^6	1.143×10^6	1.048×10^6	1.065×10^6	9.32×10^5	1.6×10^5
4.6	2.181×10^6	1.478×10^6	1.467×10^6	1.458×10^6	1.106×10^6	1.7×10^5
4.8	1.936×10^6	1.834×10^6	1.897×10^6	1.831×10^6	1.506×10^6	1.8×10^5
5.0	1.806×10^6	2.070×10^6	1.919×10^6	1.907×10^6	1.840×10^6	2×10^5
5.2	1.767×10^6	1.836×10^6	1.780×10^6	1.831×10^6	2.198×10^6	
5.4	1.842×10^6	1.685×10^6	1.666×10^6	1.699×10^6	2.129×10^6	
5.6	1.82×10^6	1.598×10^6	1.57×10^5	1.584×10^6	1.871×10^6	
5.8	1.79×10^6	1.543×10^6	1.512×10^6	1.505×10^6	1.724×10^6	
6.0	1.769×10^6	1.503×10^6	1.771×10^6	1.465×10^6	1.635×10^6	
Source	[31]	[31]	[33]	[33]	[31]	[38, 42]
Semiconductor	AlN	BN	4*H*-SiC	6*H*-SiC	ZnSe	ZnO
E_g, eV	6.2	4.5–5.5	3.23	3.0	2.7	3.46
E_0, eV		8.5	5–6	5–6		3.46
Photon energy, eV	Absorption coefficient, cm^{-1}					
2.4					2	
2.6					20	
2.8					2×10^2 (2.65 eV)	
3.0				15		
3.2			16	3×10^2		4×10^2
3.4			1×10^2	1.1×10^3		3.8×10^4
3.6			5×10^2	1.5×10^3		2×10^4
3.8			1.4×10^3	2×10^3		
4.0	5×10^2			4×10^3		
4.2	2×10^3			6×10^3		
4.4	4×10^3	1×10^4		10^4		
4.6	5×10^3					
4.8	6×10^3			3×10^4		
5.0	7×10^3	6×10^4		5×10^4		
5.2	8×10^3	7×10^4				
5.4	1×10^4	8×10^4				
5.6	2×10^4	1×10^5				
5.8	4×10^4	1.5×10^5				
6.0	5×10^4	5×10^5				
6.2	1.5×10^5					
Source	[36]	[35]	[34]	[32, 37]	[39]	[40]

Table 4. Main parameters of semiconductive materials [44–48]

Semiconductor	Si	GaAs	AlAs	GaP	GaN	AlN
Band gap, eV	1.12	1.425	2.17	2.26	3.39	6.1
Breakdown (critical) field, V/cm	3×10^5	4×10^5	6×10^5	1×10^6	5×10^6	$(1.2–1.5) \times 10^6$
Thermal velocity, cm/s:						
of electrons	2.4×10^7	4.4×10^7	2.3×10^7	2×10^7	2.6×10^7	1.85×10^7
of holes	1.65×10^7	1.8×10^7	1.3×10^7	1.3×10^7	9.4×10^6	0.41×10^7
Thermal conductivity, W/(cm K)	1.3	0.55	0.91	1.1	1.3	2.85
Melting point, °C	1412	1240	1740	1457	2500	2750
Dielectric constant:						
static	11.7	12.9	10.06	11.1	8.9	8.5
high-frequency		10.89	8.16	9.11	5.35	4.6
Density, g/cm^3	2.329	5.23	3.76	4.19	6.15	3.23
Semiconductor	BN(*b*)	4*H*-SiC	6*H*-SiC	C (diamond)	ZnO	ZnSe
Band gap, eV	4.5–5.5	3.23	3.0	5.5	3.46	2.7
Breakdown (critical) field, V/cm	$(1–6) \times 10^6$	$(3–5) \times 10^6$	$(3–5) \times 10^6$	10^6–10^7		
Thermal velocity, cm/s:						
of electrons		1.9×10^7	1.5×10^7	2.7×10^7		
of holes		1.2×10^7	1.2×10^7			
Thermal conductivity, W/(cm K)	7.4	3.7	4.9	6–20		
Melting point, °C	~4000	2800	2800	4370	2300	1793
Dielectric constant:						
static	5.1–6.8	9.66	9.66	5.7	8.7	9.1
high-frequency	4.2–4.5	6.52	6.52		3.7	6.3
Density, g/cm^3	3.48	3.21	3.21	3.52	5.67	5.28

where E_g is the band gap in eV, N is the concentration of uncompensated charge carriers in cm^{-3}, and a is the gradient of the charge-carrier concentration in the space-charge layer in cm^{-4}.

In Table 4, we list the main parameters of semiconductive materials [44–48]; the dependences of the breakdown voltage for abrupt junctions on the charge-carrier concentration in the starting material are shown in Fig. 3 [43, 47, 49, 50].

The concentration of majority charge carriers in a semiconductor should be, on the one hand, sufficiently high (to ensure a thin layer of the space charge) for ensuring a high photosensitivity and a low series resistance and, on the other hand, fairly low (a thick layer of the space-charge region) in order to ensure a small dark current, a small capacitance, and a high breakdown voltage.

The structural quality of a semiconductor can be determined to a high degree of accuracy from the values of the charge-carrier mobility and the diffusion length and lifetime of nonequilibrium charge carriers (Table 5 [44, 45, 51]) and from comparing these values with theoretical limits.

The temperature dependences of the main parameters of a photoelectric converter are related closely to the dependence $E_g = f(T)$ (for a starting semiconductor), which is commonly determined by the Varshni formula [52]

$$E_g = E_g(0) - \alpha_T \frac{T^2}{T + T_0},$$

where E_g and $E_g(0)$ are the band gaps (in eV) at temperatures T and 0 K. The values of the band gap at 0 K $E_g(0)$ and the parameters α_T, T_0, and dE_g/dT for various semiconductors are listed in Table 6 [44–46, 52, 53].

4. THE MECHANISM OF PHOTOELECTRIC CONVERSION IN STRUCTURES BASED ON WIDE-GAP SEMICONDUCTORS

The total density of current J through a structure with a potential barrier depends on the voltage V and luminous flux Φ as

$$J(V, \Phi) = J_d(V) - J_{ph}(\Phi),$$

$$J_{ph}(\Phi) = \eta q S \Phi,$$

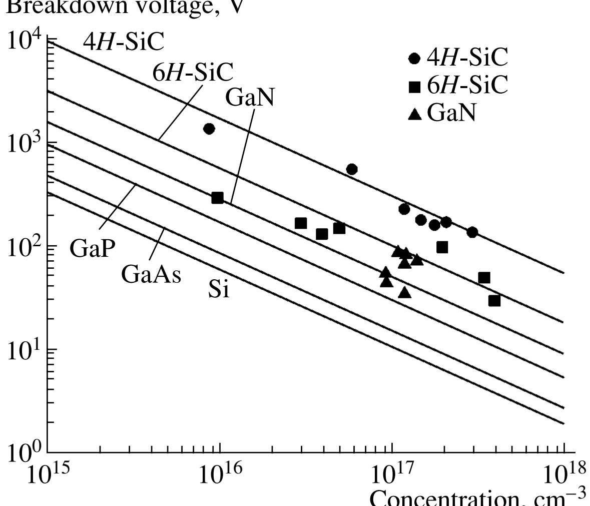

Fig. 3. Dependences of breakdown voltage for abrupt junctions on the concentration of majority charge carriers in several semiconductors at 300 K. Squares, circles, and triangles correspond to experimental data for 6*H*-SiC [48], 4*H*-SiC [49], and GaN [47]; the straight lines represent the results of theoretical calculations [43, 50]. Experimental data for Si, GaAs, and GaP virtually coincide with theory.

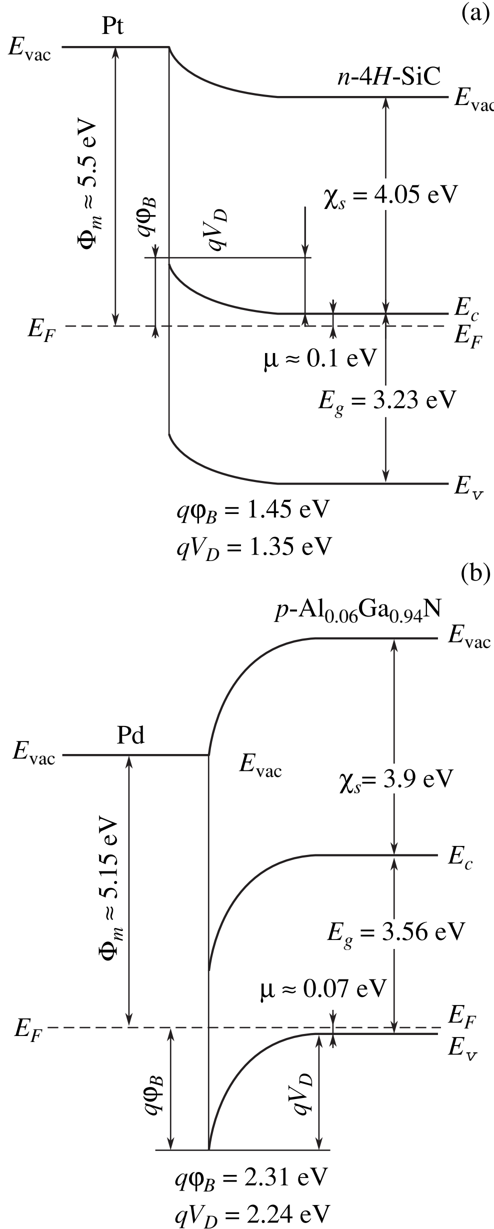

Fig. 4. Energy diagrams of Schottky barriers for the *n*- and *p*-type semiconductors by the example of (a) Pt–*n*-4*H*-SiC and (b) Pd–*p*-$Al_{0.06}Ga_{0.94}N$. E_{vac} is the vacuum level, E_F is the Fermi level, and E_c and E_v are the conduction- and valence-band edges.

where J_d is the dark-current density, J_{ph} is the photocurrent density, η is the quantum efficiency, and S is the active surface area.

4.1. Schottky Barriers

4.1.1. The energy-band diagram

Schottky diodes (surface-barrier diodes) with a metal–semiconductor (*m–s*) structure are widely used as UV photoelectric converters; the reason is that short-wavelength radiation is absorbed near the semiconductor surface (in the space-charge layer) where there is a strong electric field; as a result, surface recombination does not affect profoundly the photoelectric conversion.

The height of an ideal (not having an intermediate layer) Schottky barrier φ_B based on semiconductors with a low density of surface states is controlled by the work function for electrons leaving the metal Φ_m and by the electron affinity of the semiconductor χ_s (Fig. 4); i.e.,

$$q\varphi_B = \Phi_m - \chi_s \ (n\text{-type}),$$
$$q\varphi_B = E_g - \Phi_m + \chi_s \ (p\text{-type}).$$

If a semiconductor has a high density of surface states D_s concentrated at a level φ_0 within the band gap (as in GaAs) or in the conduction band (as in InAs) with only half of these states occupied, it is then stated that the Fermi level is pinned at the neutrality state φ_0 at the semiconductor surface. If the semiconductor has *n*-type conductivity, the height of the Schottky barrier containing an intermediate insulating layer with a thickness δ is given by

$$q\varphi_B \approx \gamma(\Phi_m - \chi_s) + (1-\gamma)(E_g - \varphi_0),$$

where

$$\gamma = \frac{\varepsilon_s}{\varepsilon_s + q\delta D_s}.$$

Here, ε_s is the permittivity of the semiconductor.

Table 5. Largest attained experimental values of charge-carrier mobility and the diffusion length and lifetime of nonequilibrium charge carriers in semiconductors at T = 300 K [44, 45, 51]

Semiconductor	GaAs	GaP	C (diamond)	$Al_xGa_{1-x}As$	GaN
Mobility, $cm^2 V^{-1} s^{-1}$:					
electrons	8500	250	2200	$-255 + 1160x - 720x^2$ ($x > 0.45$)	1245
holes	400	150	1800	$370 - 970x + 740x^2$	350
Lifetime of nonequilibrium charge carriers, s:					
electrons	5×10^{-9}	1×10^{-7}		3×10^{-8} ($x = 0.4$)	
holes	3×10^{-6}	1×10^{-6}		10^{-9} ($x = 0.3$)	
Diffusion length, μm:					
electrons	10	7			
holes	30–50	20			3.5
Semiconductor	AlN	BN	ZnO	4*H*-SiC	6*H*-SiC
Mobility, $cm^2 V^{-1} s^{-1}$:					
electrons	300	200	2 (at 10^{18} cm^{-3})	900	400
holes	14	500		120	90
Lifetime of nonequilibrium charge carriers, s:					
electrons				10^{-9}	10^{-9}
holes				6×10^{-7}	4.5×10^{-7}
Diffusion length, μm:					
electrons				1.5	1.0
holes				12	10

Table 6. Values of the band gap at 0 K $E_g(0)$ and the parameters α_T, T_0, and dE_g/dT for various semiconductors [44–46, 52, 53]

Semiconductor	Si	GaAs	AlAs	GaP	GaN	AlN
$E_g(0)$, eV	1.17	1.519	2.249	2.34	3.47	6.14
α_T, eV/K	1.73×10^{-4}	5.41×10^{-4}	4.6×10^{-4}	6.2×10^{-4}	7.7×10^{-4}	1.8×10^{-3}
T_0, K	636	204	204	460	600	1462
Semiconductor	4*H*-SiC	6*H*-SiC	CdS	ZnO	ZnS	ZnSe
$E_g(0)$, eV	3.26	3.02	2.557			
α_T, eV/K	6.5×10^{-4}	6.5×10^{-4}	8.21×10^{-4}			
T_0, K	1300	1200	450			
dE_g/dT, eV/K				-2.9×10^{-4}	-5.1×10^{-4}	-4.5×10^{-4}

The values of Φ_m [43, 54], χ_s [44, 45], D_s [43, 55, 56], and tentative values of the height for a Schottky potential barrier $q\varphi_B$ [43, 57–70] are listed in Table 7.

4.1.2. The dark current

There are three main types of mechanisms for the flow of dark current I_d through Schottky barriers based on wide-gap semiconductors with a high mobility of majority charge carriers [71] (Table 8).

(I) If the charge-carrier concentration is low (the potential barrier is thick), the current flows owing to thermal excitation of electrons and their transfer from the semiconductor to the metal or vice versa (thermionic emission). In this situation, the voltage dependence of current is exponential and the slope of this dependence on the semilog scale is equal to q/nkT, where the ideality factor n should be equal to 1.01–1.05 if the effect of image forces on the potential-barrier height is taken into account. The dependence I_0/AT^2 =

Table 7. The electron work function for metals Φ_m [43, 54], electron affinity for semiconductors χ_s [44, 45], the surface-state density for semiconductors D_s [43, 55, 56], and approximate heights of Schottky barriers $q\varphi_B$

Semiconductor		Si		GaAs		GaP		CdS
E_g, eV		1.12		1.425		2.26		2.43
χ_s, eV		4.05		4.07		3.8		4.77
D_s, cm^{-2} eV^{-1}		2.7×10^{13}		12.5×10^{13}		2.7×10^{13}		1.6×10^{13}
Metal	Φ_m, eV	$q\varphi_B$, eV						
		n	*p*	*n*	*p*	*n*	*p*	*n*
Mg	3.61					1.04		
In	3.97							
Ti	3.83–4.33	0.61				1.12		0.84
Al	4.18	0.72	0.58	0.80		1.07		0
Ag	4.42	0.78	0.54	0.88	0.63	1.20		0.56
W	4.55	0.45		0.80				
Cr	4.4–4.6	0.61	0.50			1.06		
Cu	4.59	0.58	0.46	0.82		1.20		0.50
Au	5.1–5.2	0.80	0.34	0.90	0.42	1.30 1.19 [57]	0.72	0.78
Ni	5.15–5.2	0.67	0.51	0.9		1.19 [57] 1.27		0.45
Pt	5.43–5.65			0.84		1.45		1.10

Semiconductor		4*H*-SiC	6*H*-SiC	GaN (wurtzite)		ZnSe	ZnO	ZnS
E_g, eV		3.23	3.0	3.39		2.7	3.46	3.60
χ_s, eV		4.05	4.07	4.1		4.09		
D_s, cm^{-2} eV^{-1}		$\sim 10^{13}$	$\sim 10^{13}$	$(1–2) \times 10^{11}$ (for SiO_2–GaN) [56]				
Metal	Φ_m, eV	$q\varphi_B$, eV						
		n	*n*	*n*	*p*	*n*	*n*	*n*
Mg	3.61		0.3 [58]					
In	3.97						0.30	1.50
Ti	3.83–4.33			0.59 [54]	0.65 [59]			
Al	4.18		0.3 (Si) 0.9–1.0 (C) [58]			0.76	0.68	0.80
Ag	4.42		0.8–1 (Si) 1.1–1.5 (C) [58]			1.21	0.9 [60]	1.65
Cr	4.4–4.6	1.5 [61]		0.53–0.58 [62]				
Cu	4.59	1.15 [63]		1.35–1.41 [64]		1.10	0.45	1.75
Au	5.1–5.2		1.2–1.3 (C) 1.4–1.5 (Si) [58]	1.03 [59] 0.87–0.94 [59]	0.57 [59] 2.48 [65]	1.36	0.65	2.00
Pd	5.12–5.17		1.6 (C) 1.1–1.3 (Si) [58]	0.91 [54]			0.68	1.87
Ni	5.15–5.2		1.29 [66]	0.9–1 [67]	0.50 [59] 2.4 [68]			
Pt	5.43–5.65	1.4–2.1 [69]	1–1.4 [69]	1.03 [54]	0.50 [59] 0.47 [70]	1.40	0.75	1.84

Note: In the case when the source is not specified, the data for $q\varphi_B$ are taken from [43]; in other cases, the data from [57–70] are used; designations *p* and *n* refer to the conductivity type.

Table 8. Main mechanisms of current flow in Schottky barriers based on wide-gap semiconductors with high mobility of majority charge carriers

Mechanism	Condition for realization	The form of I–V characteristic	Special features of the I–V characteristic
Thermionic emission	$kT > E_{00}$	$I_f = A^*ST^2\exp\left(\frac{-q\varphi_B}{kT}\right)\exp\left(\frac{qV}{nkT}-1\right) = I_0\exp\left(\frac{qV}{nkT}-1\right)$, $I_r = A^*ST^2\exp\left(\frac{-q\varphi_B}{kT}\right)$	$I_f \propto \exp V$; $\frac{I_0}{AT^2} \propto \exp\left(\frac{1}{T}\right)$
Field-enhanced thermal emission	$kT \approx E_{00}$	$I_f = I_0\exp\left(\frac{qV}{E_0}\right)$, $E_0 = E_{00}\coth\left(\frac{E_{00}}{kT}\right)$, $E_{00} = \left(\frac{q\hbar}{2}\right)\sqrt{\frac{N}{\varepsilon_0\varepsilon_s m^*}} = 18.5\times10^{15}\sqrt{\frac{N}{\varepsilon_s m^*}}$	
Tunneling (field emission)	$kT < E_{00}$	$I_f = I_0\exp\left(\frac{qV}{E_0}\right)$	$I_f \propto \exp\frac{B}{\sqrt{N}}$

Note: I_0 is the saturation current, V is voltage, I_f is the forward current, I_r is the reverse current, A^* is the effective Richardson constant, S is the device area, φ_B is the potential-barrier height, N and m^* are the concentration and effective mass of uncompensated charge carriers, and ε_0 and ε_s are the permittivities of the free space and semiconductor.

$f(1/T)$ (the Richardson plot) should be linear on the semilog scale, and the slope of this dependence should be equal to $q\varphi_B/k$.

(II) If the charge-carrier concentration in the semiconductor is very high (the potential barrier is fairly thin), the current flows owing to tunneling through the barrier over its entire height (field emission).

(III) If the charge-carrier concentration in the semiconductor is not sufficiently high for the charge carriers to tunnel through the barrier over its entire height, the current is caused by thermal excitation of charge carriers and their tunneling through the barrier top (thermionic-field emission).

Generally, under normal conditions and for typical charge-carrier concentrations in GaAs, GaP, and GaN, experimental data are consistent with the theory of thermionic emission [57, 62, 72, 73].

4.1.3. Photocurrent

The photosensitivity of *m–s* structures is governed by the following two processes (Table 9):

(i) generation of electrons in the metal and their transfer to the semiconductor at photon energies $h\nu > q\varphi_B$ (the Fouler law) [74, 75]; and

(ii) generation of electron–hole pairs in the semiconductor and their separation by the space-charge field at photon energies $h\nu > E_g$ (the Gartner formula) [76].

The second process is much more efficient than the first one; as a result, the long-wavelength cutoff of the short-circuit photocurrent spectrum is typically close to the band gap E_g in direct-gap semiconductors and to the threshold energy of direct optical transitions E_0 in indirect-gap semiconductors.

At $h\nu \gg E_g$, a decrease in the quantum efficiency of photoelectric conversion is always observed as $h\nu$ increases. Several theories have been developed in order to explain this falloff [77–85]. It was assumed by Li *et al.* [77] that the falloff in the case of the Au–Si structure was related to the motion of thermalized electrons opposite to the electric field, their capture at the semiconductor surface, and recombination with holes. This falloff was attributed [78, 79] to the diffusion of thermalized electrons from the semiconductor into the

Table 9. Main mechanisms of photocurrent flow in Schottky barriers

Mechanism	Condition for realization	$I_{ph} = f(V)$
Emission from metal	$q\varphi_B < h\nu < E_g$	$I_{ph} \propto (h\nu - q\varphi_B)^2$
Fundamental absorption and charge-carrier separation	$h\nu > E_g(E_0)$	$I_{ph} = -q\eta D\Phi \frac{1-\exp(\alpha W)}{1+\alpha L_p}$

Note: η is the internal quantum yield, D is the transmission coefficient, Φ is the flux density of incident photons, α is the optical-absorption coefficient, W is the thickness of the space-charge layer, and L_p is the diffusion length of minority charge carriers (holes).

metal. However, thermalized electrons can efficiently surmount a potential barrier with a height no larger than kT/q; the effective length at which the potential at the surface varies by kT/q amounts to kT/qE_m (E_m is the strongest electric field in the space-charge layer). Therefore, only the photoelectrons that were generated near the surface within a layer with a thickness of kT/qE_m can be pulled into the metal. This layer's thickness is typically much less than the light-absorption depth (for example, this thickness is <10 nm for *m–s* structures based on *n*-GaAs and *n*-GaP at $N \approx 10^{17}$ cm^{-3}); as a result, diffusion of thermalized electrons should not bring about an appreciable decrease in photonductivity. It has been assumed [80, 81] that the thermionic emission of electrons and holes into a metal governs the short-wavelength falloff of the quantum efficiency. The diffusion–drift approximation in the theory of thermionic emission was used [82] to take into account the recombination processes at the surface and derive the dependence of the quantum efficiency of photoelectric conversion γ on the absorption coefficient α, the thickness of the space-charge layer W, and the diffusion length of minority charge carriers (holes) L_p; i.e.,

$$\gamma = A\left(1 + \frac{\alpha L_p}{W}\right)^{-1} + B,$$

where A and B are coefficients.

It was assumed in [83, 84] that a decrease in photosensitivity was caused by the transport of hot photoelectrons into the metal and by their cooling there, since the thermalization-region thickness in the structures based on III–V smiconductors was fairly large (~100 nm) and was comparable to the light-absorption depth. It was assumed by Konstantinov *et al*. [85] that the short-wavelength falloff could be related to the formation of electron–hole pairs, in which one of the charge carriers had a negative effective mass and, thus, moved in the direction opposite to the electric field and was excluded from the process of photoelectric conversion. However, experimental data are consistent with current theories of photocarrier losses at $h\nu \approx E_g$ and $h\nu \gtrsim E_g$ and only in very narrow ranges at $h\nu \gg E_g$; it is noteworthy that the latter region of photon energies is most important for UV photometry.

It was assumed by Blank *et al.* [86] that the decrease in the quantum efficiency at $h\nu \gg E_g$ was caused by the formation of hot excitons in the space-charge layer. The possibility of forming such excitons was theoretically predicted as far back as in 1961 [87]; in the derived theory [87], the reciprocal effective mass m^* is given by

$$\frac{1}{m^*} = 2\frac{d^2}{d(\hbar k)^2}[E_c(k)E_v(k)]|_{k = k_m},$$

where k_m is the point corresponding to the narrowest energy gap between the conduction and valence bands. In the **k** space of the Brillouin zone in a number of semiconductors (GaAs, GaP, and 4*H*-SiC), there are regions where the *E*–**k** profiles of the conduction-band bottom and the valence-band top are similar; it is noteworthy that these regions are the most important for the absorption of UV radiation. For example, such regions for GaP are represented by the neighborhood of the *L* point in the Brillouin zone with an energy gap of ~3.9 eV and the neighborhood of the *X* point with an energy gap of ~4.8 eV; for 4*H*-SiC, such a region is located between the γ and *M* points of the Brillouin zone and corresponds to an energy gap of ~5 eV. A photoelectron and a photohole generated in these regions

move in one direction with almost the same magnitudes of velocities and, as a result of Coulomb interaction, can form a hot exciton with a large effective mass and a high binding energy (due to a small dispersion-relation curvature). Such an exciton tightly binds an electron and hole (preventing the contact field from separating these particles in the space-charge layer), can reach the metal or the quasi-neutral region, and eliminates the photocarriers from further photoconversion.

Goldberg *et al.* [88, 89] studied the temperature dependence of the quantum efficiency for Schottky photodiodes; it was found that the quantum efficiency increases with increasing temperature, which was attributed to the capture of photocarriers by fluctuation-related traps. It is assumed in the theory that imperfections, which inevitably exist in the surface region of a semiconductor, can give rise to fluctuations in the profiles of the conduction-band bottom and the valence-band top. In the absence of an electric field, such fluctuations bring about localization of only a single type of charge carrier (Figs. 5a, 5b). However, an electric field of the space-charge layer transforms these fluctuations into traps for both electrons and holes (Figs. 5c, 5d). An electron and a hole captured by such a trap are found to be localized in space and recombine with time as a result of tunneling. A variation in temperature leads to a change in the concentration of free thermalized photocarriers due to the capture of a fraction of these carriers by fluctuation-related traps. As temperature increases, the concentration of free thermalized photocarriers increases as a result of thermal dissociation of electron–hole pairs captured by traps. Consequently, the higher the temperature, the higher the quantum efficiency of photoelectric conversion. This tendency holds as long as the traps are not completely empty. The quantum efficiency γ is equal to the product of probabilities of a number of consecutive events: the entry of photons into the semiconductor $(1 - R)$; the generation of an electron–hole pair η by a photon; the thermalization of this pair in the space-charge layer $(1 - \delta_{hot})$; and the dissociation of an electron–hole pair in an electric field $(1 - \delta_{therm})$ (R is the reflection coefficient, η is the internal quantum yield, and δ_{hot} and δ_{therm} are the loss coefficients for the hot and thermalized photocarriers). Thus,

$$\gamma = (1-R)\eta(1-\delta_{hot})(1-\delta_{therm}).$$

The quantity δ_{therm} depends only on the ratio between the concentrations of the photocarriers captured by the traps n_{loc} and the concentration of free photocarriers n_f; i.e.,

$$\delta_{therm} = \frac{n_{loc}}{n_f + n_{loc}}.$$

Assuming that $\eta = 1$ and that the release of charge carriers from the traps with an activation energy of ΔE occurs according to the Boltzmann statistics

$$1 - \delta_{therm} = \exp(-\Delta E/kT),$$

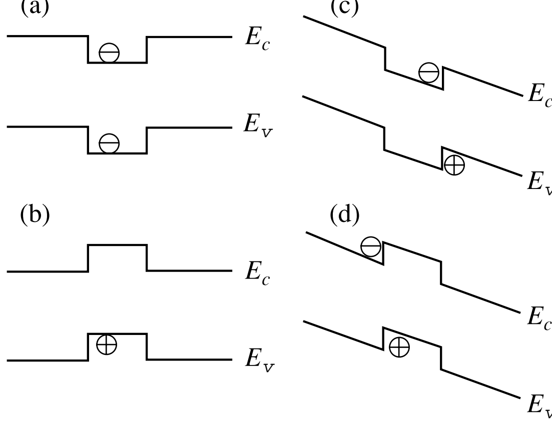

Fig. 5. Fluctuations of a semiconductor's energy bands at the surface in the (a, b) absence and (c, d) presence of an electric field. E_c is the conduction-band bottom and E_v is the valence-band top.

we obtain

$$\gamma = (1-R)(1-\delta_{hot})\exp(-\Delta E/kT).$$

The approximation of experimental data using the suggested theoretical dependence showed that the theory of fluctuation-related traps for temperature dependences of quantum efficiency is in good agreement with experiment for photodetectors based on GaAs [89], GaP [89], and 4*H*-SiC [90].

4.2. The p–n Structures

In contrast to the Schottky barriers, the potential-barrier height in *p–n* junctions is larger and is close to the semiconductor band gap E_g (Fig. 6).

The dependence of the dark current I_d on the voltage V for an ideal *p–n* junction [43], in which case the current is controlled by the diffusion and recombination of charge carriers in the quasi-neutral bulk (the Shockley theory), is given by

$$I_d \equiv I_{dif} = I_0\left[\exp\left(\frac{qV}{nkT}\right) - 1\right]$$
$$= S\left(\frac{qD_p p_{n0}}{L_p} + \frac{qD_n n_{p0}}{L_n}\right)\left[\exp\left(\frac{qV}{nkT}\right) - 1\right],$$

where I_0 is the saturation current; n is the ideality factor; S is the surface area; D_p and L_p and D_n and L are the diffusion coefficients and diffusion lengths of holes in the n-type region and electrons in the p-type region, respectively; and p_{n0} and n_{p0} are the equilibrium concentrations of holes in the n-type region and electrons in the p-type region, respectively. In this situation, the *I–V* dependence is linear on the semilog scale with a slope of q/kT (i.e., $n = 1$). However, if the current flows owing to recombination in the space-charge layer, the dependence of the dark current on the voltage V for a sym-

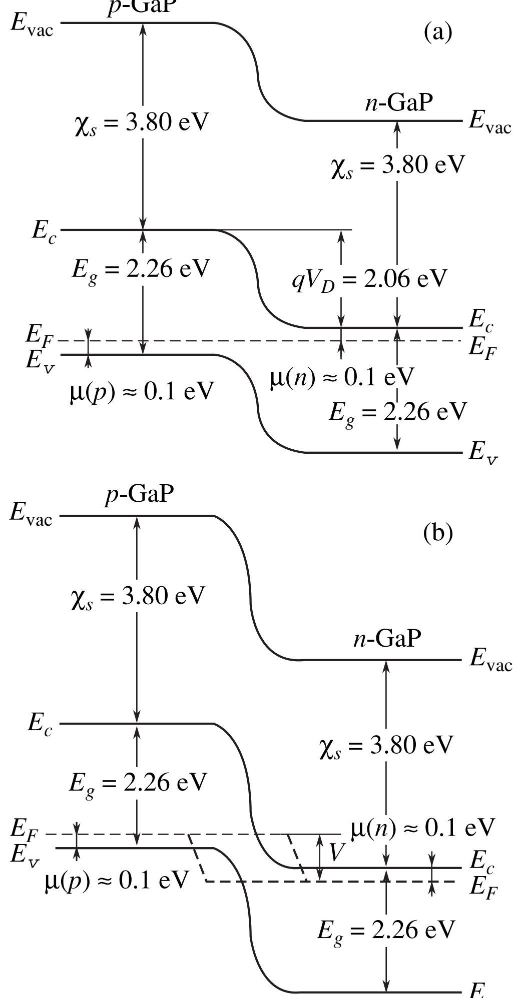

Fig. 6. Energy diagrams of p–n junctions (a) without bias and (b) under a reverse bias using the example of GaP. E_{vac} is the vacuum level, E_F is the Fermi level, and E_c and E_v are the edges of the conduction and valence bands.

metric junction (according to the Sah–Noyce–Shockley theory) is given by

$$I_d \equiv I_{rec} = I_0\left[\exp\left(\frac{qV}{2kT}\right) - 1\right]$$

$$\approx \frac{n_i WkT}{2(V_d - V)\tau_{n0}}\left[\exp\left(\frac{qV}{2kT}\right) - 1\right],$$

where n_i is the intrinsic concentration of charge carriers in a semiconductor, W is the thickness of the space-charge layer, V_d is the built-in potential, and τ_{n0} is the ultimate lifetime of electrons. In this situation, the slope of the I–V characteristic plotted on the semilog scale is equal to $q/2kT$ (i.e., $n = 2$). In actual devices based on wide-gap semiconductors, recombination in the space-charge layer is observed at low voltages, whereas the diffusion and recombination in the semiconductor bulk are observed at high voltages [43, 91]. Between the portions of I–V characteristics corresponding to $n = 1$ and $n = 2$, the portions with fractional values of n were also observed, which was attributed to recombination in the space-charge layer via multicharged deep-level centers [92, 93].

The contribution of each region of the p–n structure (quasi-neutral n- and p-type regions and the space-charge layer) is important in the photoelectric conversion; i.e., we have

$$\eta = \eta_n + \eta_p + \eta_W.$$

General expressions for the terms in this formula are fairly complex; for example, they were reported in [94]. These expressions are appreciably simplified for an asymmetric junction in which the light is absorbed exclusively in the p-type region. If the ohmic contact is located at a distance of several diffusion lengths from the p–n junction, we obtain

$$\eta(\lambda) = (1-R)\frac{\alpha(\lambda)L_p}{1+\alpha(\lambda)L_p},$$

where R is the reflection coefficient, α is the absorption coefficient, λ is the radiation wavelength, and L_p is the diffusion length of holes in the n-type region. If the distance d between the p–n junction and the ohmic contact is smaller than L_p, we have

$$\eta(\lambda) = (1-R)\{1-\exp[-\alpha(\lambda)d]\}.$$

4.3. Noise

The noise properties of structures with a potential barrier are governed by

(1) thermal (Johnson) noise arising as a result of chaotic thermal motion of electrons (the corresponding noise current is denoted by I_J);

(2) shot noise related to chaotic fluctuations of current through the barrier (the corresponding noise current is denoted by I_s); and

(3) flicker ($1/f$) noise caused by chaotic variations in the structure resistance (chaotic variations in the concentration and mobility of charge carriers); the corresponding noise current is denoted by I_f.

The total noise current is expressed as

$$I_N^2 = I_J^2 + I_s^2 + I_f^2, \quad I_J^2 = 4kT\Delta f R_0,$$

$$I_s^2 = 2qI\Delta f, \quad I_f^2 = kI\Delta f/f,$$

where Δf is the system bandwidth, R_0 is the shunting resistance, I is the dark current, and k in the formula for flicker noise is a coefficient that depends on a specific material and on the geometrical parameters of the diode.

The Johnson current is dominant in the structures with small leakage currents, in particular, in the structures operating as photoelectric generators at high load resistances.

The shot noise is prevalent in large-area structures which operate as photodiodes with large leakage currents; this noise is especially important when signals with very small amplitudes are detected.

The flicker noise is dominant at very low frequencies (lower than 1 kHz).

The photosensitivity threshold (the noise-equivalent power, NEP) Φ_{max} is the incident-light power equivalent to the noise level of a device. The photosensitivity threshold in the unit bandwidth

$$\mathrm{NEP}[\mathrm{W \cdot Hz^{-1/2}}] = \Phi_{max} V_n / V_p f^{1/2}$$

and the specific photosensitivity threshold

$$\mathrm{NEP^*}[\mathrm{W \cdot Hz^{-1/2} \cdot cm^{-1}}] = \Phi_{max} V_n / V_p f^{1/2} S^{1/2}$$

define the detectivity of a photodetector

$$D[\mathrm{W^{-1}\ Hz^{1/2}}] = 1/\mathrm{NEP}$$

and the specific detectivity of a photodetector

$$D^*[\mathrm{W^{-1}\ Hz^{1/2}\ cm}] = 1/\mathrm{NEP^*};$$

it is noteworthy that

$$D^* = G^{1/2}(2hct)^{-1/2},$$

where G is the generation rate and t is the detector thickness.

The upper theoretical limit for D^* at room temperature [95] for the UV region of the spectrum is $\sim 10^{17}$ W^{-1} Hz$^{1/2}$ cm, whereas the experimental values of D^* for the UV photoconverters are 10^{12}–10^{15} W^{-1} Hz$^{1/2}$ cm. The value of D^* increases as the radiation wavelength and the photodetector's quantum efficiency increase and as the dark current decreases.

4.4. The Response Speed

The time constant of photodiodes with a *p–n* structure is controlled by the rms value of the time of charge transport through the depletion region τ_c, the time of diffusion of charge carriers from the location of their generation to the space-charge layer τ_d, and the time constant of the resistance–capacitance (*RC*) circuit τ_{RC}; i.e.,

$$\tau^2 = \tau_c^2 + \tau_d^2 + \tau_{RC}^2.$$

For conventional *p–n* junctions, we have

$$\tau_c = W/v_s < 1 \text{ ns},$$

$$\tau_{RC} = \frac{SR_T}{2}\sqrt{\frac{\varepsilon_s \varepsilon_0 q N}{V_{op}}} < \tau_d \quad \text{and} \quad \tau \approx \tau_d;$$

only for very shallow *p–n* junctions at high reverse-bias voltages and with very large optical-absorption coefficients are the relations $\tau_{RC} > \tau_d$ and $\tau \approx \tau_{RC}$ valid (W is the space-charge layer thickness; v_s is the so-called saturation drift velocity for a specific semiconductor; ε_0 and ε_s are permittivities of the free space and semiconductor, respectively; S is the surface area; N is the concentration of uncompensated charge carriers; and V_{op} is the operating voltage).

For Schottky diodes, we invariably have $\tau \approx \tau_{RC}$, since the value of τ_c is very small and the diffusion is insignificant; it is important that the resistance R_T depend on the series resistance R_s of the structure, differential resistance R_d, and the load resistance R_L as

$$R_T = \frac{R_d(R_s + R_L)}{R_d + R_s + R_L},$$

$$R_d = kT(I + I_0)/q,$$

where I is the direct current through the structure and I_0 is the preexponential factor in the expression for the *I–V* characteristic. With optimal geometric parameters, the response time of Schottky diodes can be as short as the energy-relaxation time for charge carriers ($\sim 10^{-9}$ s), whereas the response time is close to the charge-carrier lifetime ($\sim 10^{-7}$ s) for conventional *p–n* junctions.

4.5. Photoresistors

A photoresistor is a semiconductor device whose electrical resistance decreases under exposure to light. When a luminous flux is incident on a photoresistor, the differential photosensitivity is defined as

$$S_I = \frac{dI_{ph}}{d\Phi} = \frac{wtV_{op}}{q}\frac{d\Delta\sigma}{d\Phi}.$$

The quantum efficiency γ and the voltage photosensitivity S_V are given by [94]

$$\gamma = \frac{\eta(1-R)[1-\exp(\alpha t)]}{1 - R\exp(\alpha t)},$$

$$S_V = \frac{V_s}{P_\lambda} = \frac{V_{op}\gamma\lambda\tau}{lwthcn_0}.$$

Here, V_{op} is the operating voltage; γ is the internal quantum yield; R is the coefficient of reflection from the illuminated surface; α is the optical absorption coefficient; V_s is the open-circuit voltage; $P_\lambda = \Phi S h\nu$ is the absorbed power of monochromatic light; n_0 is the average concentration of charge carriers under thermal equilibrium; τ is the lifetime of nonequilibrium charge carriers; t, w, and l are the thickness, width, and length of the photoresistor; and $\Delta\sigma$ is the change in the photoresistor conductivity as a result of exposure to light.

Photoresistors feature a very high photosensitivity and can operate in the amplification mode; however, the I_{ph}–Φ characteristic of photoresistors is nonlinear and they cannot operate without a bias voltage.

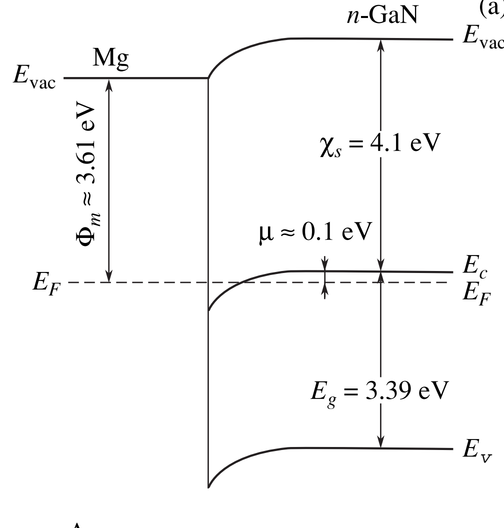

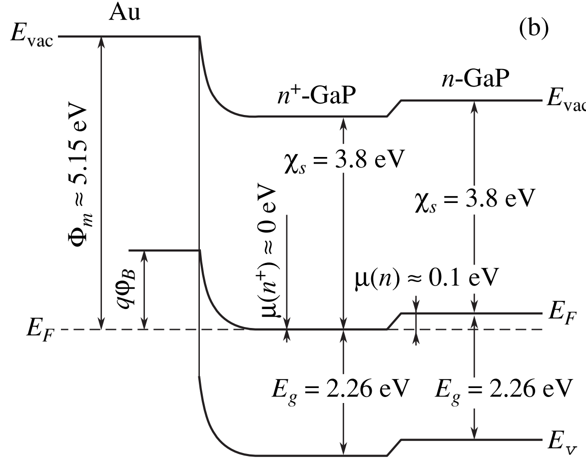

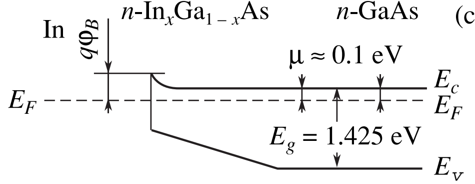

Fig. 7. Energy diagrams of three types of ohmic contacts to the *n*-type semiconductors: (a) there are no surface states in the semiconductor's band gap and $\Phi_m < \chi_s$ (using the example of Mg–*n*-GaN); (b) the surface region of the semiconductor is heavily doped (using the example of Au–*n*-GaP); and (c) a narrow-gap layer is grown on the starting material (using the example of In–*n*-GaAs). E_{vac} is the vacuum level, E_F is the Fermi level, and E_c and E_v are the conduction- and valence-band edges.

5. OHMIC METAL–SEMICONDUCTOR CONTACTS

5.1. Formation of an Ohmic Contact

As is well known, a metal–semiconductor contact can be either rectifying (of the barrier type) if the potential barrier between the metal and semiconductor is impermeable for tunneling or ohmic if the potential barrier is absent or is permeable for the tunneling of electrons.

Typically, an ohmic contact is formed if (Fig. 7)

(I) there is no potential barrier between a metal and semiconductor; i.e., a metal with an electron work function which is smaller than the electron affinity of the semiconductor is chosen as the contact to an *n*-type semiconductor with a low density of surface states in the band gap (a contact of the first type);

(II) there is a potential barrier but it is thin (permeable for tunneling), which is attained by heavy doping of the semiconductor's surface region (a contact of the second type); and

(III) there is a potential barrier but it is low and can be easily overcome owing to thermionic emission, which is most often attained by varying the semiconductor's chemical composition in the vicinity of the contact, for example, by the formation of a narrow-gap near-contact layer (a contact of the third type).

5.2. Contact Resistance

The main characteristic of an ohmic contact is its resistance relative to the unit area. This resistance consists of the following series components:

(i) the resistance of the near-contact region; and

(ii) the resistance related to penetration of electrons through the barrier.

The resistance of the near-contact region consists of the resistance of the heavily doped region and the resistance of the n–n^+ or p–p^+ junctions. The resistance of the heavily doped region is typically very low. For example, the resistance of an n^+-GaAs layer with an electron concentration $n^+ = 10^{19}$ cm^{-3}, a mobility of ~10^3 cm^2/V s, and a thickness of ~1 μm is ~$6 \times 10^{-8}\ \Omega$ cm^2. The resistance of an n–n^+ junction is inversely proportional to the electron concentration [96, 97]; i.e.,

$$R_{n-n^+} \approx \frac{L_D N_c}{q\mu_n^* k_B N N^+},$$

where L_D is the Debye length for the *n*-type region, N_c is the effective density of states in the conduction band, μ_n^* is the electron mobility in the *n*-type region, N and N^+ are the electron concentrations in the *n*- and n^+-type regions, and k_B is the coefficient accounting for the ratio between the electron concentration at the Fermi level in the n^+-type region and concentration N^+. The resistance under consideration makes a major contribution to the resistance of the ohmic contact to GaAs for $N < 5 \times 10^{17}$ cm^{-3}.

According to Kupka and Anderson [98], an n–n^+ junction can be treated as a Schottky diode without a poten-

Table 10. Mechanisms of current flow through an ohmic contact

Mechanism	Reduced resistance	$R_c = f(T)$	$R_c = f(N)$
Thermionic emission	$R_c = \left(\frac{k}{qA^*T}\right)\exp\left(\frac{q\varphi_B}{kT}\right)$	$R_cT \propto \exp\left(\frac{1}{T}\right)$	
Tunneling	$R_cT \propto$ $\exp\left[\left(\frac{2\sqrt{\varepsilon_s\varepsilon_0 m^*}}{\hbar}\right)\left(\frac{\varphi_B}{N^{1/2}}\right)\right]$	Temperature-independent	$R_c \propto \exp\frac{1}{\sqrt{N}}$

Note: k is the Boltzmann constant, T is temperature, A^* is the effective Richardson constant, φ_B is the potential-barrier height, $\hbar$ is Planck's constant, N and m^* are the concentration and effective mass of uncompensated charge carriers, and ε_0 and ε_s are the permittivities of the free space and semiconductor.

tial barrier and with the thermionic mechanism of current flow; the resistance of such a junction is given by

$$R_{n-n^+} = \left(\frac{k}{qA^*T}\right)\frac{1}{\ln[1+\exp(\mu/kT)]},$$

where A^* is the effective Richardson constant, $A^* = Am^*/m_0$ ($A = 120$ A/cm^2 K^2); m^*/m_0 is the relative effective mass of the majority charge carriers; and μ is the energy of the Fermi level located in the n-type region and reckoned from the conduction-band bottom. If $\mu \gg kT/q$ in a lightly doped semiconductor, we have

$$R_{n-n^+} = \left(\frac{kN_c}{qA^*TN}\right).$$

As a result, the resistance under consideration amounts to $\sim 10^{-7}\ \Omega$ cm^2 for GaAs at $N = 10^{17}$–10^{19} cm^{-3}.

We now consider the resistance related to overcoming the potential barrier. There are two main mechanisms of current flow through an ohmic contact; these are thermionic emission and tunneling.

According to the theory of thermionic emission [71], the specific contact resistance, which is equal to $R_c = dV/dJ$ at $V \longrightarrow 0$, depends exponentially on the reciprocal temperature (Table 10).

According to the theory of tunneling [71], the contact resistance per unit area is given by

$$\frac{1}{R_c} = \frac{m^*q^2}{2\pi\hbar^3}\int_0^\infty\left(\frac{T(E)}{\{\exp[(E-\mu)/kT]\}-1}\right)dE,$$

where $T(E)$ is the probability for a charge carrier with energy E to penetrate through the barrier with a height which is lower than $q\varphi_B$ by ΔE. The contact resistance R_c depends exponentially on $N^{-1/2}$ and is virtually independent of temperature [99]. The theoretical dependence of the lowest attainable contact resistance on the doping level of a semiconductor was reported in [98] for the case of thermionic emission and in [100] for the case of tunneling.

The theoretical value of the resistance of a tunneling contact to p-GaN was shown [101] to depend on the crystallographic orientation of GaN when tunneling of light and heavy holes was taken into account (see Fig. 8).

It is worth mentioning the ohmic contact to a heterostructure with a two-dimensional electron gas [102], for example, to GaN/$Al_xGa_{1-x}N$. In this case, the current flowing from the semiconductor to the metal consists of thermionic and tuneling currents through the structure and the tunneling current caused by quantum wells; the latter current is predominant. The probability of tunneling for electrons in the ith subband with an energy E_i is given by

$$T(E_i) = \exp\left(-\frac{q\varphi_B - qV - (E_i - E_F)}{E_{00}}\right)$$

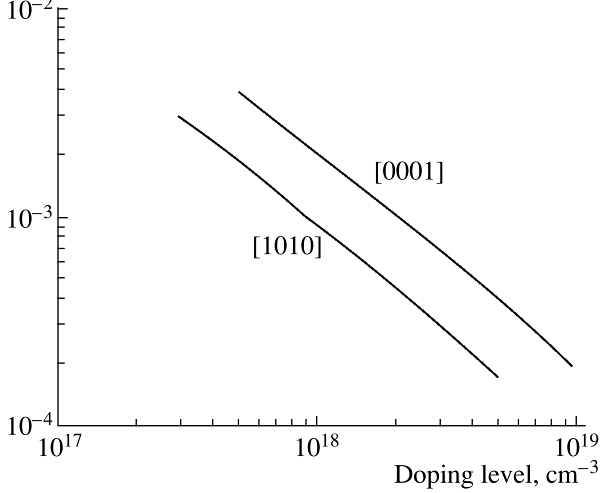

Fig. 8. Theoretical resistance of an ohmic contact to p-GaN with allowance made for tunneling of light and heavy holes in relation to the concentration of uncompensated acceptors for two crystallographic orientations of the GaN surface [101].

(E_F is the Fermi level energy), and the contact resistance is equal to

$$R_c = \left\{ \sum_{E_i < E_F} \frac{2qm^*kT}{\pi^2 h^3 (i+1)} E_i \left(\frac{q}{E_{00}} \ln 2 + \frac{q}{2kT} \right) \right.$$

$$\times \exp\left(-\frac{q\varphi_B - (E_i - E_F)}{E_{00}}\right) + \sum_{E_i > E_F} \frac{2qm^*kT}{\pi^2 h^3 (i+1)} E_i \frac{q}{E_{00}}$$

$$\left. \times \ln\left(-\frac{E_i + E_F}{kT}\right) \exp\left(-\frac{q\varphi_B - (E_i - E_F)}{E_{00}}\right) \right\}^{-1}.$$

In particular, the contact resistance of Al/Ti/Ta–n-GaN/$Al_xGa_{1-x}N$ structures with a two-dimensional electron gas decreases with temperature almost by an exponential law, from ~10^{-4} A at 77 K to ~10^{-6} A at 300 K.

We now consider the relevant experimental data.

The contacts of the first type (without a potential barrier) are formed, for example, on ZnSe, where the density of surface states is low. In particular, In or the Ti/Pt/Au alloy ($\Phi_m = 4.3$ eV) provide an ohmic contact to n-ZnSe; in forming this contact, it is only necessary to remove a possible intermediate layer, which is attained by heat treatment at $T > 200°C$ [103]. The resistance of the In–n-ZnSe contact was lower than 10^{-3} Ω cm^2 [104].

At the same time, in the case of p-ZnSe, there is no metal with a work function larger than the sum of the electron affinity and the band gap ($\Phi_m > \chi_s + E_g$); in addition, it is impossible to form a tunneling-permeable contact to the heavily doped surface region since the highest attainable hole concentration in ZnSe does not exceed ~5×10^{17} cm^{-3}. Therefore, one has to form contacts of a third type (with intermediate layer) by growing a graded-gap p-$ZnSe_xTe_{1-x}$ layer on the p-ZnSe surface and using HgSe ($\Phi_m = 6.1$ eV) as a metallic film. As a result, the HgSe–p-ZnSe barrier height of 0.55 eV [105] reduces to 0.4 eV after overgrowth of the $ZnSe_{0.8}Te_{0.2}$ layer.

A similar situation is also observed in the case of an ohmic contact to n-GaN. The Fermi level is hardly pinned at all at the GaN surface [106, 107]; however, conventional chemically stable metals have a work function which exceeds the electron affinity for GaN ($\chi_s = 4.1$ eV). Therefore, the multicomponent contacts based on Ti ($\Phi_m = 3.8$–4.3 eV) and Ti_xN ($\Phi_m = 3.74$ eV) are most frequently used. There are also no metals with $\Phi_m > \chi_s + E_g = 7.5$ eV in the case of p-GaN; therefore, either the compounds with a large work function are used or a narrow-gap surface layer is formed [108]. For example, several binary intermetallic phases which reduce the potential barrier are formed when Au/Ni is fused to GaN at 600°C [109]; at the same time, fusion of Au/C/Ni makes it possible to additionally dope the surface layer [110], since C acts as an acceptor. The Ru/Ni contact annealed in the O_2 atmosphere can also be used for p-GaN. The RuO_2 compound lowers the effective barrier height, whereas NiO acts as a barrier to the diffusion of the released Ga and N atoms. Such a contact features a high optical transmissivity (84.6%) and a low resistance (4.5×10^{-5} Ω cm^2) [111]. It was noted [112] that the dependence of the Pd–p-GaN contact resistance on the hole concentration is anomalous: $R_c = 8.9 \times 10^{-2}$ Ω cm^2 at $n = 2.2 \times 10^{17}$ cm^{-3} (which corresponds to the Mg concentration $N_{Mg} = 4.5 \times 10^{19}$ cm^{-3}), whereas $R_c = 5.5 \times 10^{-4}$ Ω cm^2 at $n = 2 \times 10^{16}$ cm^{-3} ($N_{Mg} = 1 \times 10^{20}$ cm^{-3}). The Ti/Al/Ni/Au or V/Al/Ni/Au systems are conventionally used as contacts to $Al_xGa_{1-x}N$ solid solutions [113]. The values of resistances of some of the most widely used ohmic contacts to GaN are listed in Table 11 [114–128].

The Group IV and III–V semiconductors (except for nitrides and n-InAs) typically have a high concentration of surface states that lie deep in the band gap, which gives rise to a rigid pinning of the Fermi level at the surface. Therefore, in order to form an ohmic contact to the aforementioned semiconductors, one has to either reduce the density of surface states or use the second or third types of contacts.

When GaAs is treated in Na_2S or $(NH_4)_2S$ solutions, the impurity O atoms near the surface are replaced with S atoms which are retained owing to physical adsorption. The resulting released energy (<40 kJ/mol) is lower than the energy released in the course of chemical adsorption (>100 kJ/mol); thus, the physical-adsorption energy is not sufficient for the formation of intrinsic defects which bring about pinning of the Fermi level [129–132]. For example, the density of surface states D_s in GaAs is typically higher than 10^{14} cm^{-2} eV^{-1}; this density of states is reduced to 2×10^{13} cm^{-2} eV^{-1} after treatment in $(NH_4)_2S$ and to 1×10^{13} cm^{-2} eV^{-1} after treatment in $(NH_4)_2S_x$. An even lower density of surface states in GaAs (7.6×10^{12} cm^{-2} eV^{-1}) can be obtained by growing a very thin (3.5 nm) n-GaAs:Be layer (with an electron concentration $n = 5 \times 10^{16}$ cm^{-3}) on the surface [133]; in this situation, the Fermi level is virtually not pinned at the GaAs surface.

Treatement of the GaN surface in $(NH_4)_2S_x$ resulted in the decrease of D_s from 1×10^{12} to 8.3×10^{10} cm^{-2} eV^{-1}; at the same time, the height of the Ni/Cu–n-GaN Schottky barrier amounted to 1.099 eV, which is close to the limiting height of a Schottky barrier (1.10 eV) [134]. Passivation of ohmic Ti/Al–n-GaN:Si ($n = 3 \times 10^{18}$ cm^{-3}) structures resulted in a decrease in the contact resistance by about two orders of magnitude owing to the oxide removal from the GaN surface and to the shift of the Fermi level to the conduction-band bottom [135].

Passivation of 4H-SiC in NO and NH_3 brought about [136] a decrease in D_s from ~10^{13} to ~2×10^{12} cm^{-2} eV^{-1}.

Table 11. Specific resistance of ohmic contacts to *n*- and *p*-GaN (114–128]

Metals	Conductivity type	Charge-carrier concentration in GaN, cm^{-3}	Contact resistance, Ω cm^2	Source
Ti/Al	*n*	10^{17}	8×10^{-6}	[114]
	n	10^{17}	8×10^{-6}	[115]
	n	3.67×10^{18}	8.63×10^{-6}	[116]
Ti/Al/Ni/Au	*n*	2×10^{17}	1.19×10^{-7}	[117]
	n	4×10^{17}	8.9×10^{-8}	
Ni/Si	*n*	2×10^{17}	1.6×10^{-3}	[118]
Pd/Au	*p*	3×10^{17}	1×10^{-4}	[119]
	p	10^{18}	1.5×10^{-6}	
Ti/Al	*p*	6×10^{17}	$(2–6) \times 10^{-3}$	[120]
Pt/Ru	*p*	$(2–3) \times 10^{17}$	2.2×10^{-6}	[121]
Ni/In	*p*	2×10^{17}	$(8–9) \times 10^{-3}$	[122]
Ni/Pt/Au	*p*	9.4×10^{16}	2.1×10^{-2}	[123]
Ni/Au	*p*	2×10^{17}	4×10^{-6}	[124]
Pt/Ni	*p*	1.7×10^{17}	8×10^{-3}	[125]
Ta/Ti	*p*	7×10^{17}	3×10^{-5}	[126]
Ni/Cr/Au	*p*	5×10^{17}	1.6×10^{-2}	[127]
Ni/Pd/Au	*p*		4.5×10^{-6}	[128]

An Al–*n*-GaAs ohmic contact with $R_c = (1–3) \times 10^{-4}$ Ω cm^2 was formed owing to a reduction in the density of surface states in GaAs ($n = 1 \times 10^{18}$ cm^{-3}) [137] as a result of treating the surface in H_2S solutions; however, this method has not yet been widely recognized.

In the case of GaAs, contacts of the second type with a heavily doped (to the level of 10^{20}–10^{21} cm^{-3}) surface layer are typically used; this layer is formed owing to interface chemical reactions, which include dissociation of GaAs and the growth of a new layer composed of heavily doped GaAs [109]. For example, in the case of fusion of the widely used Al/Ge/Ni contact, Ni initially reacts with GaAs at $T < 250°C$ and forms Ni_xGaAs; at $T > 250°C$, this phase decomposes with the formation of $NiGa_y$ and $NiAs_z$. In addition, Ni also reacts with Ge (so that NiGe is formed) and with Al (so that Ni_xAl_y is formed); in the course of cooling, an n^+-GaAs:Ge layer grows, with the electron concentration in this layer being as high as 10^{19}–10^{20} cm^{-3}.

In the case of the Ni/[Au + Ge(27%)]/Ni/Au–*n*-GaAs contact, Ge first diffuses from the Au + Ge alloy to the upper layer during heating, whereas Ni reacts with GaAs and forms Ni_xGaAs. At temperatures of 375–400°C, Au reacts with Ga and forms the β-AuGa phase, whereas Ge penetrates into Ni_xGaAs and replaces Ga. The contact acquires the β-AuGa/NiAs:Ge/GaAs structure; as a result of cooling, a new layer of heavily doped GaAs is formed [138]. The resistance of these contacts to *n*-GaAs can be as low as 3.6×10^{-6} Ω cm^2 at $n = 1 \times 10^{16}$ cm^{-3} (according to [139]), 1×10^{-6} Ω cm^2 at $n = 2 \times 10^{16}$ cm^{-3} (according to [140]), 5×10^{-7} Ω cm^2 at $n = 1.5 \times 10^{17}$ cm^{-3} [141], and 4×10^{-7} Ω cm^2 at $n = 2.2 \times 10^{18}$ cm^{-3} [141]. As the technology improved, with each passing decade the resistance of ohmic contacts to GaAs was reduced by approximately an order of magnitude [142]; notably, the specific resistance was inversely proportional to the charge-carrier concentration [143].

The contacts of the third type with a graded-gap layer and a low barrier have often been formed on GaAs and GaP. For example, when the (W/Ni + In/Ni)–*n*-GaAs contact is heated to ≈300°C, Ni interacts with GaAs and forms Ni_2GaAs, whereas In penetrates into W and Ni_2GaAs. An $In_{0.6}Ga_{0.4}As$ layer is formed at a temperature of ~700°C; this layer covers almost the entire GaAs surface at ~900°C. Notably, the layer under consideration has a much narrower band gap than GaAs; in addition, the Fermi level in InAs is found to be pinned within the conduction band. This circumstance brings about an appreciable decrease in φ_B and R_c [144]. An $In_xGa_{1-x}P$ solid-solution layer is formed between Pd and GaP after heating a Pd/In–*n*-GaP contact to $T = 600°C$ for 1 min. This layer reduces the potential-barrier height [145]; as a result, R_c was found to be lower than 10^{-4} Ω cm^2 after cooling.

When the Ni–4*H*-SiC structure is heated to 900°C, the Ni_2Si compound is formed. This compound has a work function for electrons which is larger than the work function in Ni by 0.36 eV. In the course of heating, excess C atoms diffuse to the structure surface; notably, V_C vacancies act as donors [146].

Table 12. Mechanisms of current flow in ohmic contacts

Contact	Charge-carrier concentration, cm^{-3}	The current-flow mechanism	Potential-barrier height, eV	References
Ti/Pt/Au–p-GaAs	4×10^{20}	Tunneling	0.5	[147]
Pt/Ti–p-GaAs	5×10^{18}–1×10^{19}	Thermionic emission	0.068	[148]
Au/Zn/Ni–p-InP		Thermionic emission	0–0.2	[149]
Pt/Ti–p-$In_{0.53}Ga_{0.47}As$	5×10^{18}	Thermionic emission	0.13	[150]
Ti/Al/Ni/Au–n-GaN	10^{17}–10^{18}	Tunneling		[117]
Ti/Ag–n-GaN	1.5×10^{17}–1.7×10^{19}	Tunneling	0.067	[151]
Pt–p-GaN	1.8×10^{17}	Thermionic emission	0.53	[70]
	1.0×10^{18}	Tunneling	0.42	
Pd/p-$Al_{0.06}Ga_{0.94}N$	3×10^{18}	Thermionic emission	0.05	[152]
	1.0×10^{19}	Tunneling (T = 90–190 K)	0.05	
		Thermionic emission (T > 300 K)		
$NiSi_2$–n-6H-SiC			0.44	[153]
$NiSi_2$–n-4H-SiC			0.3	
Al/Ti/Ta–AlGaN	Surface concentration 1.7×10^{13} cm^{-2}	Tunneling	0.42	[102]

5.3. Mechanism of Current Flow in an Ohmic Contact

Experimental dependences $R_c = f(T)$ and $R_c = f(N)$ for ohmic contacts and comparison of these dependences with theory make it possible to determine the mechanism of current flow through the contacts under consideration: thermionic emission and tunneling (Table 12) [70, 102, 117, 147–153].

6. PHOTOELECTRIC CONVERTERS FOR THE ULTRAVIOLET REGION OF THE SPECTRUM

6.1. Photodetectors Based on Si

So far, silicon p–n photodetectors represent the most widely used type of UV photoelectric converters [154–158]. This circumstance is related first of all to the fact that silicon is inexpensive and is produced commercially by the industry; in addition, photodetectors based on Si have advantages as solar cells.

Taking into account that the surface-recombination rate in Si is high ($v_r \approx 10^4$ cm/s) and that this rate appreciably affects the photoelectric-conversion quantum efficiency of p–n structures, Si–SiO_2 structures ($v_r \approx$ 1 cm/s) are used [159] or structures with a pulling field (for example, as a result of nonuniform doping) are fabricated in order to reduce v_r.

Three main types of Si detectors were developed: (I) with an inversion layer, (II) with a p^+–n structure, and (III) with an n–p structure. In the structures of type I [160], a thin n-Si inversion layer is formed between the p-Si substrate and oxide layer; corresponding devices feature a narrow interval of linearity of the I_{ph}–Φ characteristic as a result of a high resistivity of the inversion layer. In the structures of type II (p^+–n) [161] two junctions are formed in order to widen the spectral range; one of these junctions is shallow (~0.1 μm) and the other is deeper (~5 μm): an n-Si layer is grown epitaxially on the p-Si substrate and double diffusion of boron into this layer is then performed. The corresponding devices were found to be insufficiently stable as a result of uncontrolled boron diffusion from the Si surface into the oxide layer. The n–p photodetectors [162–164] feature the highest stability. These photodetectors were produced by diffusion of As [162] or P [164] into p-Si (with a resistivity of ρ = 100 Ω cm), the formation of p^+- and n^+-type guard rings, and the deposition of an antireflection coating with a thickness of ~60 nm. The corresponding photodiodes featured a current photosensitivity S_I = 0.25 A/W at λ = 0.41 μm.

Diodes with an Si–SiO_2 structure have the highest efficiency in the UV spectral region [154, 165]; the p–n structure fabricated using local epitaxy featured a quantum efficiency γ = 0.86 and a dark-current density $J_d = 8 \times 10^{-12}$–7×10^{-10} A/cm^2.

Commercial Si photodiodes have a spectral photosensitivity range of 0.2–1.1 μm (Fig. 9); the peak of photosensitivity lies in the IR spectral region (0.8–1.0 μm). The responsivity of these photodiodes can be as high as 0.5 A/W at 0.8–1.0 μm and amounts to 0.1 A/W at 0.2–0.25 μm, the detectivity is $D \approx 10^{15}$ W^{-1} $Hz^{1/2}$ at the spectrum peak, the dark current is $I_d \approx$ 100 nA, and the optimal operating voltage V_{op} = 5–10 V.

At the same time, the p–n photodetectors based on Si have two serious drawbacks. First, the photosensitivity of these photodetectors in the IR and visible regions of the spectrum appreciably exceeds that in the UV

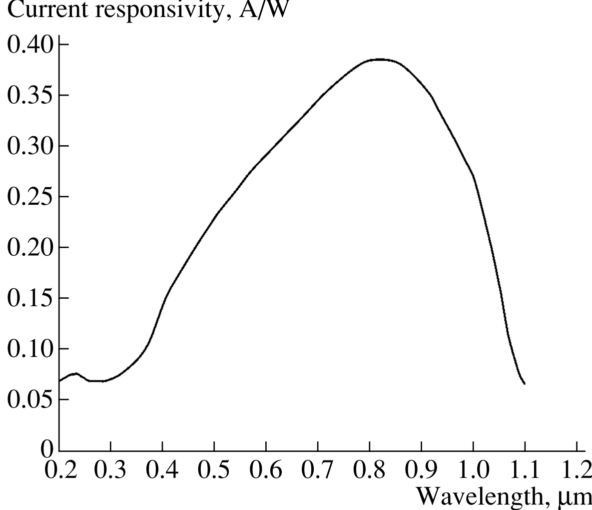

Fig. 9. The photosensitivity spectrum of a commercial Si-based photoelectric converter with a *p–n* junction [155–158]. $T = 300$ K.

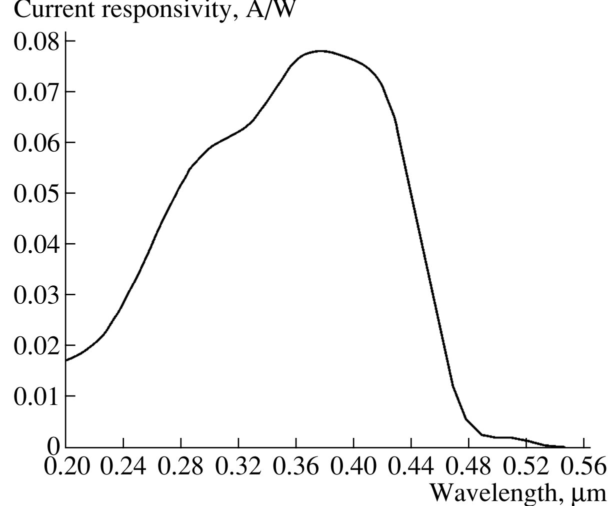

Fig. 10. The photosensitivity spectrum of an Au–*n*-GaP photoelectric converter with a Schottky barrier [183]. $T = 300$ K.

spectral region, which gives rise to large measurement errors, since a typically small UV signal is measured against the background of high-intensity visible or IR radiation; in addition, glass-based UV optical filters feature high transmission in the IR spectral region but block the visible region of the spectrum. Second, degradation is observed in Si-based *p–n* structures; this degradation consists in a decrease in the quantum efficiency by a factor of 2–3 as a result of continuous exposure to UV radiation for ~0.5 h [166–169].

Degradation of PtSi–*n*-Si and Pt–Si Schottky barriers was not observed [170, 171]; however, the photosensitivity peak was in the IR spectral region (~0.7 μm), as in the case of *p–n* structures.

Fabrication of MOS structures with a thin insulator layer was reported [172–177]; these structures featured $\gamma = 0.2$–0.4 [173, 174] and were used in charge-coupled devices as UV detectors. 1024 × 1024 arrays of UV detectors were fabricated [177]; these detectors featured $\gamma = 0.177$ in the spectral range of 0.124–0.52 μm.

Further investigations in the field of UV photoelectric converters were aimed at using semiconductors with a wider band gap, such as GaAs [178, 179] and InP [180]. Photoresistors based on InP ($E_g = 1.344$ eV) featured a broad quantum-efficiency spectrum (0.2–1 μm) with a peak ($\gamma \approx 0.65$) in the IR region of the spectrum (~0.9 μm) [180].

6.2. Photodetectors Based on GaP and Its Solid Solutions

Wilson and Lyall [181, 182] substantiated the advantages of photoelectric converters based on $GaAs_{0.63}P_{0.37}$ ($E_g = 1.848$ eV at 300 K) in comparison with those based on Si. These advantages consist in a much lower sensitivity to IR radiation (the photosensitivity range of 0.2–0.68 μm); a high differential resistance at zero bias (~10^4 ΓΩ), which ensures a low noise level; high stability; and good matching to optical filters. The current responsivity of the structures under consideration is $S_I \approx 0.2$ A/W at the peak and $S_I = 0.02$–0.03 A/W at $\lambda = 0.254$ μm, with the temperature coefficient of S_I being equal to 5.8×10^{-4} K^{-1}; the specific detectivity is $D^* = 10^{14}$–10^{15} W^{-1} Hz$^{1/2}$ cm.

The use of GaP in photoelectric converters operating in the UV region of the spectrum is based on the fact that, although GaP has $E_g = 2.27$ eV (which is much smaller than the energy of UV photons), GaP is an indirect-gap semiconductor whose threshold energy for direct optical transitions with high absorbance of light is equal to $E_0 = 2.8$ eV; this energy is quite close to the low-energy edge of the UV spectral region. The operating spectral region of the Au–GaP Schottky photodiodes [157, 183–185] ranged from 0.2 to 0.55 μm (Fig. 10), with a photosensitivity peak at ~0.4 μm. The value of S_I was as large as 0.12 A/W at the spectrum peak and was equal to 0.03 A/W at $\lambda = 0.254$ μm. The value of D^* in these structures [184] was as large as 10^{13}–10^{14} W^{-1} Hz$^{1/2}$ cm, and the noise-equivalent power was equal to NEP = 10^{-15}–10^{-14} W Hz$^{-1/2}$; when combined with a measuring device, it was found that NEP = (1–2) × 10^{-14} W Hz$^{-1/2}$. The use of ITO (indium–tin oxide) instead of Au [186] made it possible to enhance the photosensitivity to 0.3–0.4 A/W.

In order to suppress the sensitivity to visible light, GaP-based photodiodes are equipped with UV optical filters; the use of a UFS-6 filter makes the radiation spectrum close to that of solar UV radiation [187]. In order to reduce the sensitivity to visible light, one can use Au–$Al_xGa_{1-x}P$–GaP structures [188, 189]; how-

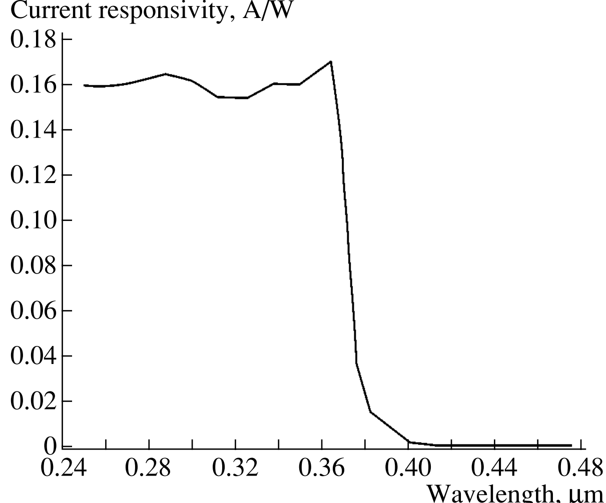

Fig. 11. The photosensitivity spectrum of a Pd–n-GaN photoelectric converter with a Schottky barrier [191]. $T = 300$ K.

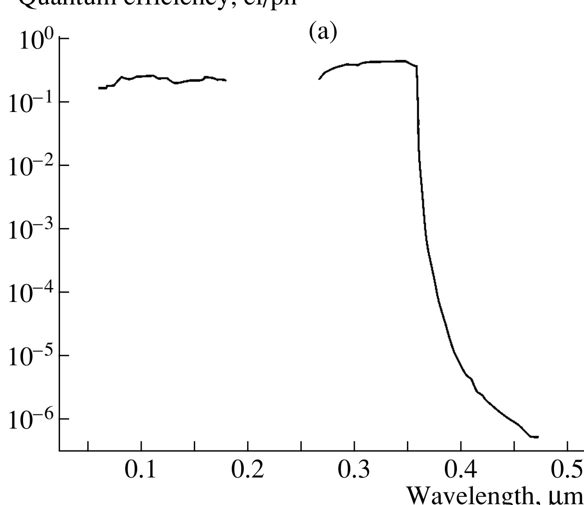

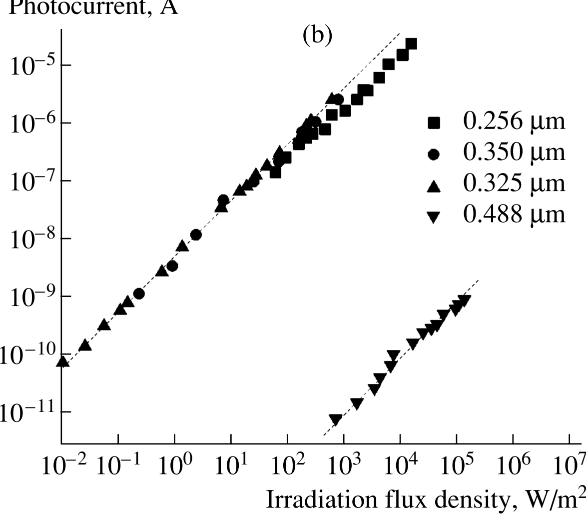

Fig. 12. (a) The photosensitivity spectrum of a GaN-based photoelectric converter with an MSM structure at a bias voltage of 5 V and (b) the dependence of photocurrent on the radiation flux density for several wavelengths [194]. $T =$ 300 K.

ever, the low stability of $Al_xGa_{1-x}P$ in atmospheric air limits application of these structures. We note in addition that photodiodes with heterojunctions and avalanche photodiodes in an AlGaAs–GaAs system have been used to detect UV radiation in nuclear-particle counters [190].

6.3. Photodetectors Based on Nitrides

Photodetectors based on nitride semiconductors are promising for the UV region of the spectrum since these are direct-gap materials with a band gap which is close to the boundary between the visible and UV regions of the spectrum; in addition, an AlN–GaN system forms a continuous series of direct-gap solid solutions, which make it possible to fabricate photodetectors with a sharp long-wavelength photosensitivity falloff, which can be located at practically any position in the near-UV region of the spectrum.

The Schottky diodes based on Pd–n-GaN–n^+-GaN structures ($n = 3 \times 10^{16}$–10^{17} cm^{-3}, $n^+ = 3 \times 10^{18}$ cm^{-3}) featured a photosensitivity spectral range of 0.25–0.37 μm; the value of $S_I = 0.18$ A/W ($\gamma \approx 0.6$) varied only slightly in the entire spectral range (Fig. 11). The major noise in the structures was that with the $1/f$ dependence [191].

Fabrication of another type (metal–semiconductor–metal, MSM)) of the structures was reported in [192–194] (Fig. 12). The devices here featured the same operating spectral region and $S_I = 0.17$ A/W. The Ag–GaN:H–Au sandwich-type Schottky diodes [195], in which GaN:H was doped heavily with magnesium, featured a sharp cutoff of the photocurrent spectrum at $\lambda =$ 0.36 μm ($\gamma = 0.4$, $S_I = 0.11$ A/W at $\lambda = 0.32$ μm, and $I_d =$ 10^{-11} A at $V = -1$ V). As the reverse bias increases to –5 V, the value of S_I first increases appreciably and then levels off [196]. Vertical and lateral GaN-based photodetectors with Schottky barrier were fabricated [193, 194]; it was shown that photodetectors with a vertical structure had a higher efficiency due to improved characteristics of the rear ohmic contact and a higher detectivity as a result of a lower level of $1/f$ noise; the latter circumstance was due to a less significant influence of dislocations on the charge-carrier transport.

The characteristics of photoelectric converters (in particular, MSM structures) depend heavily on the structural properties of the starting material and, consequently, on the value of mismatch $\Delta a/a$ between the lattice parameters of the substrate and the layer. Typically, GaN layers are grown on sapphire ($\Delta a/a = 16\%$) or SiC ($\Delta a/a = 3.2\%$); in addition, the $LiGaO_2$ substrate shows promise ($\Delta a/a = 0.19\%$) [197]. It was noted recently [198] that irradiation of finished Au–GaN structures

with neutrons (at a dose of 1×10^{13} cm^{-2}) reduces the number of vacancies and improves the characteristics of devices.

For a transparent metal in GaN-based Schottky diodes, ITO can be used instead of Au, which, as in the case of GaP, brings about an increase in the quantum efficiency from 27 to ~40% [199].

The Schottky photodiodes based on *n*-GaN ($n = 3 \times 10^{16}$ cm^{-3}) and passivated with an SiO_2 layer had a time constant of 15 ns, determined by the *RC* circuit, and a noise spectral density of 5×10^{-23} A^2/Hz at a frequency of 10 Hz; notably, internal current amplification was observed under a forward bias [200]. This amplification is caused by the fact that the surface states at the metal–semiconductor interface can capture holes and thus reduce the potential-barrier height $q\varphi_B$ (for example, the value of $q\varphi_B$ in Ti/Pt–GaN structures decreased from 1.08 to 0.75 eV as a result of illumination) [201].

The dark-current densities of the Schottky mesa diodes based on Pd–*n*-GaN ($n = 5 \times 10^{17}$ cm^{-3}) are very low ($I_d = 2.1 \times 10^{-8}$ A/cm^2 at –2 V); the noise spectral density at 1 Hz is 9×10^{-29} A^2/Hz, with the noise power varying with frequency *f* as 1/*f* [202].

GaN-based *p*–*n* structures were formed on n^+-GaN substrates ($n^+ = 10^{18}$ cm^{-3}) by growing an n^--type layer ($n^- = 10^{16}$ cm^{-3}) and a *p* layer ($p = 10^{18}$ cm^{-3}) [203]; these structures featured $S_I = 0.11$ A/W at the photosensitivity peak ($\lambda = 0.36$ μm) and $\tau = 8.2$ μs. The *p*–π–*n* structures, in which compensated *p*-GaN was located between the heavily doped *p*- and *n*-type layers, featured $S_I = 0.1$ A/W at $\lambda = 0.363$ μm, $I_d = 2.7$ μA at $V = -3$ V, and NEP = 6.6×10^{-15} W Hz$^{-1/2}$; the time constant was controlled by the *RC* circuit [204].

The GaN-based avalanche p^+–*i*–n^+ photodiodes with a multiplication factor larger than 25 and an efficiency of 13% were fabricated [205, 206]. The leakage currents of these avalanche diodes did not exceed 20 nA at $V = 0.9V_{BR}$; the temperature coefficient of the breakdown voltage V_{BR} amounted to +0.2 V/K.

The GaN-based photoresistors feature an abrupt long-wavelength falloff of photosensitivity and a very high current responsivity. A responsivity as high as $S_I = 2000$ A/W (according to [207]) or even $S_I = 3200$ A/W (according to [208]) at 5–15 V was attained; at $\lambda = 0.254$ μm, $S_I = 125$ A/W at $V = 25$ V (according to [209]) and $S_I = 30$ A/W at $V = 14$ V (according to [210]). Large values of S_I are caused by modulation of the bulk GaN resistivity as a result of the photoeffect in the space-charge layer at the GaN surface and due to variations in the thickness of this layer in the course of charge-carrier generation [211, 212].

The GaN–AlN solid solutions are used in the fabrication of solar-blind photodetectors, i.e., detectors which are insensitive to all solar radiation reaching the Earth's surface ($\lambda < 0.3$ μm), and also detectors which are insensitive to visible and IR radiation ($\lambda < 0.38$ μm)

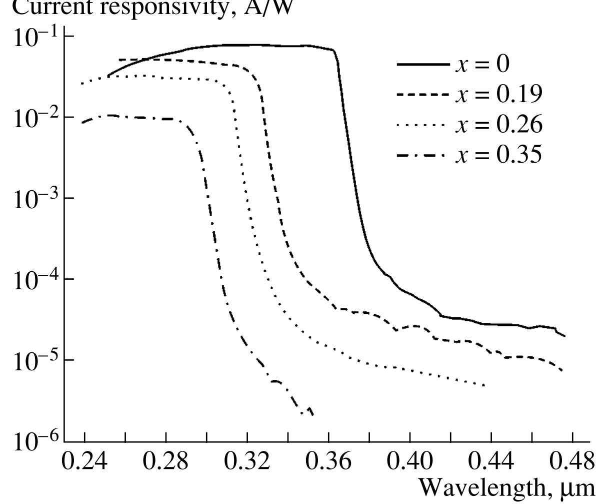

Fig. 13. Photosensitivity spectra of $Al_xGa_{1-x}N$ photoelectric converters with a Schottky barrier for various values of *x* (AlN content) in the solid solution [220]. $T = 300$ K.

[213]; the latter are used to detect UV solar radiation in space and at the Earth's surface.

As the content of AlN in an $Al_xGa_{1-x}N$ solid solution increases, the long-wavelength photosensitivity edge shifts to shorter wavelengths [214–220] (Fig. 13). This edge corresponds to $\lambda = 0.365$ μm (at $x = 0$), $\lambda = 0.32$ μm (at $x = 0.35$), $\lambda = 0.23$ μm (at $x = 0.75$), and $\lambda = 0.2$ μm (at $x = 1$) [208, 214]. Typically, the photosensitivity edge is very steep: as the wavelength λ increases from 0.3 to 0.36 μm (at $x = 0.36$) [208] or from 0.285 to 0.35 μm (at $x = 0.35$) [215], the current responsivity S_I decreases by four orders of magnitude. In the UV spectral region, the value of S_I remains virtually constant [216] and is equal to 0.025–0.3 A/W (at $x = 0.22$) [217], 0.05 A/W at $V = 0$ V and 0.11 A/W at $V = -5$ V (at $\lambda = 0.232$ μm) [216], 0.05 A/W (at $\lambda = 0.257$ μm) [214], and 0.033 A/W (at $\lambda = 0.275$ μm) [218].

Theoretical analysis [219, 220] shows that the value of S_I in the $Al_xGa_{1-x}N$–GaN structures increases as the thickness of the solid-solution layer decreases from 4 to 1 μm (as a result of a decrease in the series resistance), as the electron concentration in this layer increases from 1×10^{15} to 1×10^{16} cm^{-3}, and with decreasing AlN content (*x*).

The specific detectivity *D** of AlGaN-based Schottky barrier detectors is typically in the range of 1.2×10^9–2.3×10^{10} Hz$^{1/2}$ W^{-1} cm; the time constant is limited by the *RC* circuit (14 ns at $x = 0.22$). The main noise components in the forward-biased $Al_{0.4}Ga_{0.6}N$ Schottky diodes are the 1/*f* noise and the generation–recombination noise. The noise spectral density [221] increased with current *I* as $I^{1.5}$ at low currents and as $I^{2-2.5}$ at high currents.

Photodetectors based on the *p*–*i*–*n* structures [222] had parameters which were close to those mentioned above: the current responsivity was $S_I = 0.12$ A/W at $\lambda =$

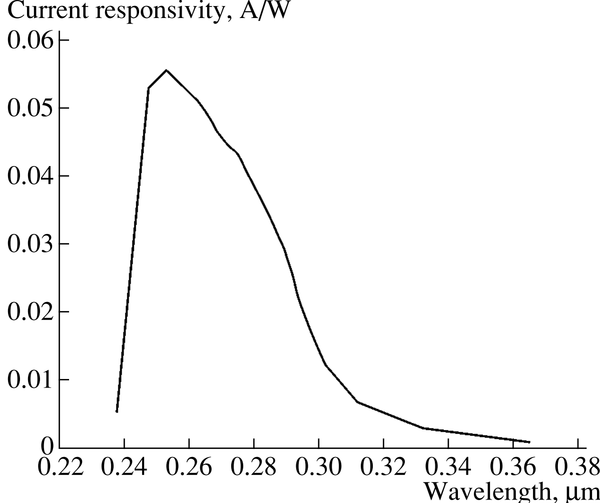

Fig. 14. The photosensitivity spectrum of a Cr–4*H*-SiC photoelectric converter with a Schottky barrier [90]. $T = 300$ K.

0.364 μm and decreased by three orders of magnitude at $\lambda > 0.39$ μm. Tarsa *et al.* [215] reported the fabrication of *p–i–n* photodiodes which could be illuminated from both the upper-layer side ($S_I = 0.08$ A/W at $\lambda = 0.285$ μm) and the substrate side ($S_I = 0.033$ A/W at $\lambda = 0.275$ μm). For photodetectors based on *p–i–n* structures, $D^* = 4.85 \times 10^{13}$ Hz$^{1/2}$ W^{-1} cm (according to [223]) and $\gamma = 0.35$ at $\lambda = 0.28$ μm (according to [224]). For a *p–i–n* structure with an $Al_{0.6}Ga_{0.4}N$ window, $\gamma = 0.46$ and $D^* = 2 \times 10^{14}$ Hz$^{1/2}$ W^{-1} cm [225]. Very low reverse currents (1×10^{-10} A at –5 V) and large values of D^* (2.4×10^{14} Hz$^{1/2}$ W^{-1} cm) were observed in *p*-$Al_{0.13}Ga_{0.87}N$–*n*-GaN heterostructures; the main noise at $f < 1$ kHz and $V < 10$ V was the $1/f$ noise and at $f > 1$ kHz, it was the thermal and shot noise [226]. More detailed data on solar-blind photodetectors based on GaN and AlGaN *p–n* structures can be found in [227].

6.4. Photodetectors Based on SiC

Silicon carbide has a great number of polytypes; the most important for UV photometry are the 6*H*-SiC and 4*H*-SiC polytypes with $E_g = 3.0$ and 3.23 eV, respectively. The important advantages of SiC are the high saturation velocity of electrons, absence of degradation under high-power continuous UV irradiation, and insensitivity of SiC photodiodes to visible and IR radiation. The SiC-based devices can operate at high temperatures (the high-temperature electronics) and at high voltages and currents [228].

The photodetectors with a Cr–*n*-SiC Schottky barrier [229], as well as commercial JECO-type photodetectors [230], feature a spectral photosensitivity range of 0.2–0.4 μm with a peak at 0.275 μm, $S_I = 0.15$ A/W, $I_d < 10^{-12}$ A/cm^2, and NEP = 10^{-13}–10^{-14} W Hz$^{-1/2}$ at $\lambda = 0.25$ μm. These devices can operate at high voltages and temperatures. For example, the Au–*n*-6*H*-SiC photodiodes ($n = 5 \times 10^{16}$–10^{17} cm^{-3}) can operate at temperatures as high as 573 K; the breakdown voltage $V_{BR} = 100$–170 V at 300 K (the reverse current at $V < V_{BR}$ was no higher than 10^{-10} A), and $S_I = 0.15$ A/W ($\gamma = 0.8$) [231] at $\lambda = 0.215$ μm. Comparison of Schottky photodiodes based on *n*-6*H*-SiC with those based on *p*-6*H*-SiC [232] showed that a higher photosensitivity can be attained in the latter photodiodes as a result of a larger contact-potential difference and the fact that the diffusion length for electrons is larger than that for holes.

The photosensitivity limit of photodiodes corresponded to 0.435 and 0.410 μm for the Schottky barriers and *p–n* structures based 6*H*-SiC and 4*H*-SiC, respectively. These structures were used for the detection of ozone [233], as detectors of nuclear particles [234, 235], and as detectors of flames from gas turbines and rockets [236].

The special features of the energy-band structure of 4*H*-SiC provide a unique opportunity to develop a band-limited photodetector with a photosensitivity range which virtually coincides with the spectrum of bactericidal radiation: the spectral region of 0.24–0.3 μm with a peak at 0.252 μm ($\gamma = 0.3$) [90] (Fig. 14).

The SiC-based photodetectors with *p–n* junctions have parameters which are close to those of Schottky diodes. For example, *p–n* structures [229] obtained by diffusion of Al or B into *n*-SiC ($n = 10^{18}$ cm^{-3}) feature a spectral photosensitivity range of 0.2–0.4 μm with $S_I = 0.15$ A/W. Mesa structures including *p*-6*H*-SiC substrate and the *p*-SiC ($p = (5$–$8) \times 10^{17}$ cm^{-3}) and n^+-SiC ($n^+ = 5 \times 10^{18}$–1×10^{19} cm^{-3}) layers featured $\gamma = 0.7$–0.85 ($S_I = 0.15$–0.175 A/W at $\lambda = 0.27$ μm) [237]. The dark-current density in the *p–n* structures based on 6*H*-SiC was 10^{-11} A/cm^2 (at –1 V and 473 K); these diodes operated successfully as UV photodetectors [238, 239] at temperatures as high as 623 K.

Photodetectors based on *n*-4*H*-SiC with $n = (3$–$5) \times 10^{15}$ cm^{-3} and a shallow (0.6 μm) p^+–*n* junction formed by ion-implantation doping [240] combine the advantages both of *p–n* junctions and of Schottky diodes: at photon energies of 3.5–4.25 eV, the efficiency of collecting the minority charge carriers was close to 100%, and the reverse currents at $T = 500$°C and $V = -10$ V were no larger than 10^{-7} A.

6.5. Photodetectors Based on II–VI Semiconductors

The first II–VI semiconductor used for the fabrication of photodetectors was CdS ($E_g = 2.43$ eV); the spectral range of CdS-based photoresistors was close to the photosensitivity region of the human eye [241]. The Schottky diodes based on $Cu_{0.18}S$–CdS were used in the UV region of the spectrum [242], although they are also sensitive to visible light. As advances into the UV region were made, II–VI compounds with wider band gaps were used, in particular, ZnSe ($E_g = 2.7$ eV), ZnS ($E_g = 3.6$ eV), and solid solutions based on ZnSe and

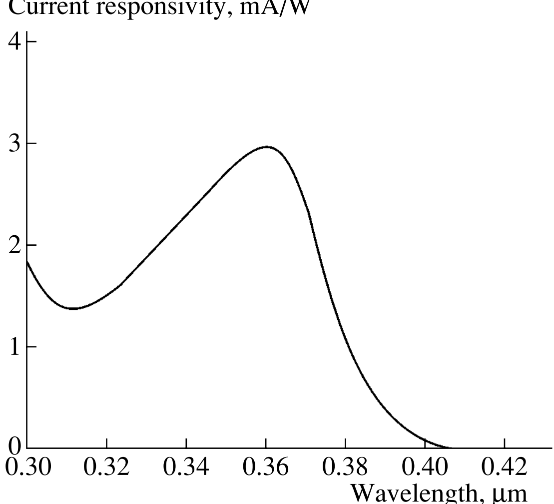

Fig. 15. The photosensitivity spectrum of an Au–ZnO photoelectric converter with a Schottky barrier [256]. $T = 300$ K.

ZnS [243–247]. A ZnSe layer is easily grown on the GaAs substrate and is used in the blue and UV regions of the spectrum, mainly for the detection of laser radiation. Photodetectors based on ZnS Schottky barriers [247] featured a very steep falloff of photosensitivity, $S_I = 0.1$ A/W (at $V = -3.5$ V), and $D^* = 1.4 \times 10^{12}$ Hz$^{1/2}$ W^{-1} cm.

The ZnMgBeSe-based photodetectors with Schottky barriers featured $S_I = 0.17$ A/W (at $\lambda = 0.375$ μm), $D^* = 2 \times 10^{12}$ Hz$^{1/2}$ W^{-1} cm, and $\gamma = 0.5$ at $\lambda = 0.315$–0.38 μm; the time constant (1.5 μs) was controlled by the *RC* circuit of the structure [248]. For *p–i–n* structures [249], the value of S_I was equal to 0.22 A/W at $\lambda = 0.42$ μm, was largest at $\lambda = 0.45$ μm, decreased by three orders of magnitude at $\lambda = 0.515$ μm, and decreased by four orders of magnitude at $\lambda = 0.65$ μm [250].

The ZnSe-based avalanche p^+–n photodiodes feature a spectral photosensitivity range of 0.35–0.47 μm [251]; as the voltage increases from 0 to 15 V, the value of γ increases from 0.3 to 0.6, while the gain is as high as 60.

The ZnSSe [252] and ZnSTe [253] solid solutions were used to shift the long-wavelength photosensitivity limit in the Schottky barriers. This limit corresponded to $\lambda = 0.37$ μm ($S_I = 0.12$ A/W) for $ZnS_{0.8}Se_{0.2}$ structures, $\lambda = 0.34$ μm ($S_I = 0.10$ A/W) for $ZnS_{0.95}Te_{0.05}$ structures, and $\lambda = 0.338$ μm ($S_I = 0.15$ A/W) for ZnS structures; notably, the photosensitivity edge was more abrupt in ZnSSe structures than in ZnSTe structures. The value of S_I increased with increasing temperature [254].

Zinc oxide (ZnO) is a promising material for the UV region of the spectrum ($E_g = 3.46$ eV). Zinc oxide is radiation-resistant and is used in the fabrication of low-threshold blue and UV lasers, which, owing to a high exciton-binding energy (60 meV), can be coupled to

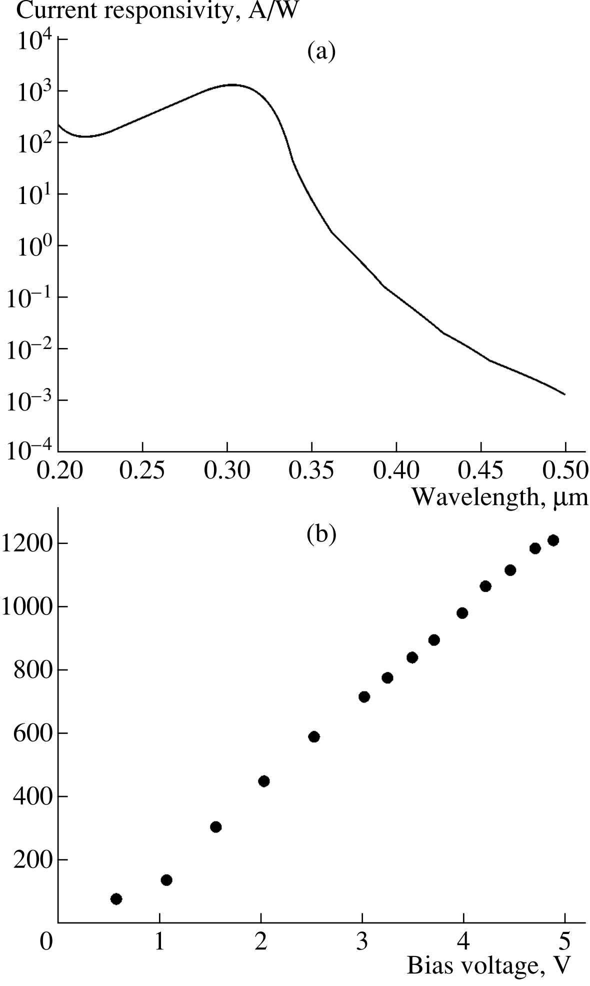

Fig. 16. (a) The photosensitivity spectrum of a $Mg_{0.34}Zn_{0.66}O$ photoresistor at a bias voltage of 5 V and (b) the dependence of current photosensitivity on the bias voltage at $\lambda = 0.308$ μm [258]. $T = 300$ K.

ZnO-based photodetectors; ZnO is easily grown on GaN substrates [255]. The Schottky barriers [256] (Fig. 15) of MSM photodiodes [257] based on ZnO were fabricated; $Mg_{0.34}Zn_{0.66}O$ ($E_g = 4.05$ eV) was used to fabricate solar-blind photoresistors (Fig. 16) [258]. These photoresistors had a current responsivity S_I of 1200 A/W at $\lambda = 0.308$ μm and $V = 5$ V. The value of S_I was smaller at $\lambda = 0.4$ μm than at $\lambda = 0.308$ μm by four orders of magnitude; the increase in voltage from 0.5 to 5 V increased S_I by a factor of 6 (Fig. 16b). The build-up and decay times for ZnO-based MSM structures were as short as 8 ns.

Photoresistors based on layers of porous ZnO obtained using magnetron sputtering featured a high sensitivity in the UV region of the spectrum (0.365 μm); the build-up and decay times were equal to ~800 ms. Degradation of photoresistors was virtually absent [259]. The aforementioned layers can also be used as photoanodes in photochemical solar cells [260]. Photodetec-

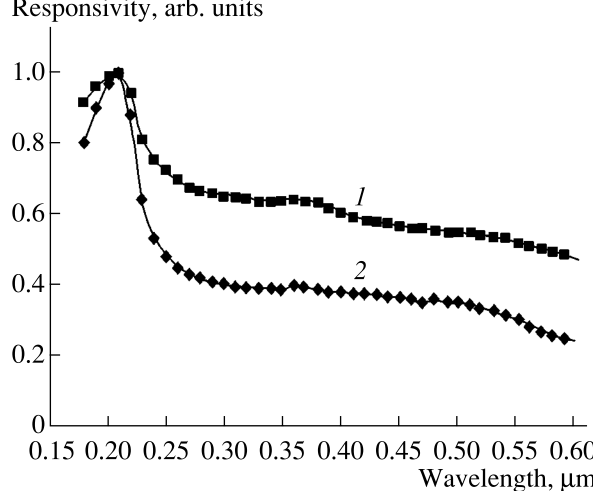

Fig. 17. Photosensitivity spectra (normalized) of photoelectric converters based on diamond films: (*1*) a photoresistor and (*2*) a Schottky photodiode [268]. $T = 300$ K.

tors with a ZnO(ITO)/*a*-Si:H(*n*)/*c*-Si(*p*)/Al structure can be used as photodetectors of linearly polarized light, with the ZnO (ITO) layers acting as antireflection films [261].

6.6. Photodetectors Based on Diamond and Other Semiconductors

Diamond ($E_g \approx 5.5$ eV, $E_0 \approx 7.3$ eV) is a semiconductor with the widest band gap among all known semiconducting materials; however, diamond is only starting to come into use. Diamond-based Schottky diodes [262] feature a long-wavelength photosensitivity limit at about 0.22 μm, which virtually corresponds to the band gap of diamond. These devices were solar-blind and were used to detect vacuum UV radiation [263]. Diamond-based photodetectors with a *p–n* structure [264, 265] had a photosensitivity range of 0.12–0.6 μm. Diamond was also used to fabricate photoresistors [266, 267]; the photosensitivity of these photoresistors in the UV spectral region (0.2 μm) was higher than in the visible region of the spectrum by six orders of magnitude; the dark current was lower than 0.1 nA. The diamond-based Schottky diodes had a dark current of 10 pA and a time constant of 20 μs [268]. The photosensitivity spectra of a photoresistor and a Schottky photodiode based on diamond film [268] are shown in Fig. 17. A diamond film is typically formed by chemical vapor deposition [269]. In order to suppress degradation processes, the films are grown in a nitrogen-contaning atmosphere with a nitrogen content of 10–15% [270].

Interest has recently been growing in amorphous and polycrystalline semiconducting materials in relation to the development of thin-film field-effect transistors and solar cells. At the same time, these materials are coming into use in the UV region of the spectrum. The devices based on *a*-Si:H feature a low production cost and a large active area and are fabricated at relatively low temperatures. The *a*-Si/*a*-SiC structures were used as wide-gap windows to Si-based photodetectors [271]. It was noted [272] that these structures could be used as photodetectors of near and far UV radiation; the *p–i–n* structures 5×5 cm^2 in area featured a current responsivity $S_I = 0.28$ A/W at 0.365 μm. The Pd/*i*-*a*-Si:H/n^+-*a*-Si:H/Mo(Ni, Cr)/A_2O_3 structures were used as photodetectors in the range from 0.2 to 0.5 μm [273]. The *p–i–n* structures based on *a*-Si:H with a semitransparent Ag layer featured $S_I \approx 0.08$ A/W in the range from 0.3 to 0.4 μm; the photosensitivity was lower at 0.45 μm by a factor of 2 [274]. Devices based on *a*-Si [275] and on fluorite [276] were used as detectors in the vacuum-UV spectral region. The use of UV-radiation photodetectors based on amorphous *n*-GaN for monitoring the ozone holes over Antartica was reported [277].

In conclusion, we note that organic semiconductors [278], semiconductive opal ($E_g \approx 5.5$ eV) [279], LaCuOS ($E_g \approx 3.1$ eV) [280], and polymeric films [281] show promise and are already coming into use as materials for photoelectric converters. In particular, film-based photodetectors have a spectral photosensitivity range from 0.3 to 0.7 μm with $S_I = 0.16$–0.17 A/W at 0.44–0.48 μm.

7. SUMMARY AND THE LINES OF FURTHER RESEARCH

Ultraviolet photoelectronics originated over the last two decades in response to the needs of medicine, biology, defence, and in relation to the problem of the ozone hole. The special feature of UV photoelectronics is its ability to detect weak (albeit profoundly affecting vital human functions) UV signals against the background of high-intensity radiation in the visible and IR regions of the spectrum.

At present, photoelectric converters are based on the following structures:

(i) silicon *p–n* structures; these are widely used as they are inexpensive and are produced commercially by industry; however, photodetectors based on Si *p–n* structures require complex systems of optical filters in order to eliminate IR photosensitivity;

(ii) Schottky barriers based on GaP, which is an indirect-gap semiconductor; as a result, the corresponding photodetectors are sensitive only to blue and violet radiation (in addition to UV radiation) and can be used in combination with simple glass-based optical filters to monitor UV solar radiation;

(iii) Schottky barriers and *p–n* structures based on GaN and AlGaN; as a result of the wide band gap of these direct-gap semiconductors, they are the principal materials for modern photoelectronics of solar-blind devices because, by varying the chemical composition of AlGaN solid solution, one can easily shift the long-

wavelength photosensitivity limit over almost the entire near UV region of the spectrum; and

(iv) Schottky barriers and *p–n* structures based on SiC; the corresponding devices are promising for high-temperature photoelectronics and for the detection of bactericidal radiation of the sun and UV lamps.

In addition, we are presently witnessing rapid progress in the field of potentially promising *p–n* structures, photoresistors, and Schottky barriers based on II–VI semiconductors (ZnO, ZnS, ZnSe, and so on) and on polymeric films, which, in the future, may bring about a revolution in device technology.

The largest values of the current responsivity presently attainable correspond to a quantum efficiency of 0.7–0.9, which virtually coincides with the theoretical limit. The time constants of photodetectors (especially those with Schottky barriers) are also close to the limit governed by the *RC* circuit. At the same time, the specific detectivity of the best devices is at the level of 10^{13}–10^{15} $Hz^{1/2}$ W^{-1} cm, which is appreciably lower than the theoretical limit (~10^{17} $Hz^{1/2}$ W^{-1} cm); in order to increase the detectivity, it is necessary to reduce the dark current, which will eventually call for the improvement of the quality of starting materials.

We now consider important lines of further research in the field of UV photoelectric converters:

(I) the development of a general theory of photoelectric conversion in structures that contain potential barriers and are based on wide-gap semiconductors;

(II) optimization of the technology for wide-gap semiconductors (GaN, AlN, SiC, ZnO) with the aim of developing dislocation-free materials and materials with a charge-carrier mobility and lifetime that are close to theoretical limits (as has been already done for Si, GaAs, and GaP); such progress will make it possible to increase the detectivity of photodetectors;

(III) the development of selective and narrow-band photodetectors for separate important portions of the UV spectral region; i.e., solar-blind photodetectors operating at elevated temperatures, photodetectors of erythematous radiation, photodetectors of carcinogenic radiation, and photodetectors of vitamin-forming radiation; and

(IV) the development of small-sized measurement devices (dosemeters, intensitometers) based on the aforementioned photoelectric converters and the use of these devices for UV monitoring throughout Russia with the aim of determining the effect of UV radiation on vital human functions.

ACKNOWLEDGMENTS

We thank O.V. Konstantinov for his helpful participation in discussions.

This study was supported by the Russian Foundation for Basic Research, project no. 02-02-07014.

REFERENCES

1. *GOST* (State Standard) *26148-84: Photometry. Terms and Definitions* (1992), Suppl. 1.
2. L. R. Koller, *Ultraviolet Radiation* (Wiley, New York, 1965).
3. E. E. Anderson, *Fundamentals of Solar Energy Conversion* (Addison-Wesley, Reading, MA, 1983).
4. I. E. Gamelina and K. A. Samoĭlova, *Mechanism of the Impact of Blood Exposed by Ultraviolet Radiation on Human and Animal Organisms* (Nauka, Leningrad, 1986).
5. V. G. Boksha, *Handbook on Climatotherapy* (Zdorov'e, Kiev, 1989).
6. *WHO Environmental Hygienic Criterions. Ultraviolet Radiation* (International Radiation Protection Association and WHO, Geneva, 1994), p. 160.
7. A. Vassy, *Atmospheric Ozone* (New York, 1965; Mir, Moscow, 1968), Advances in Geophysics, Vol. 1.
8. D. J. Karoly, Cancer Forum **30**, 1 (1996).
9. M. P. Thekaekara, Appl. Opt. **13**, 518 (1974).
10. D. V. Lazarev and L. N. Lyapunova, in *Problems of Practical Photobiology* (Nauchn. Tsentr Biol. Issled. Akad. Nauk SSSR, Pushchino, 1977), p. 11.
11. É. L. Aleksandrov, Yu. A. Izraél', I. L. Karol', and A. Kh. Khrgian, *Ozone Shield of the Earth and Its Variation* (Gidrometeoizdat, St. Petersburg, 1992).
12. P. Fraser, in *Proceedings of 2nd Menzies Foundation Conference on Health Consequences of Ozone Depletion* (Hobart, Australia, 1996).
13. R. Stalarski and R. Cicerone, Can. J. Chem. **52**, 1610 (1974).
14. M. J. Molina and F. S. Rowlard, Nature **249**, 810 (1974).
15. D. J. Hofmann, S. J. Oltmans, B. J. Johnson, *et al.*, Geophys. Res. Lett. **22**, 2493 (1995).
16. I. E. Galbally, Science **193**, 573 (1976).
17. S. L. Roan, *Ozone Crisis: the 15-Year Evolution of a Sudden Global Emergency* (Wiley, New York, 1989; Mir, Moscow, 1993).
18. J. Austin, D. J. Hofmann, N. Butchart, and S. J. Oltmans, Geophys. Res. Lett. **22**, 2489 (1995).
19. D. J. Hofmann, Nature **383**, 129 (1996).
20. J. R. Herman, P. A. Newman, and O. D. Lark, Geophys. Res. Lett. **22**, 3227 (1995).
21. Y. Kondo, Y. Zhao, O. Uchino, *et al.*, Geophys. Res. Lett. **22**, 3223 (1995).
22. S. Staehelin, N. R. P. Harris, C. Appenzeller, and J. Eberhard, Rev. Geophys. **39**, 231 (2001).
23. P. B. C. Ren, F. Sigernes, and Y. Gjessing, Geophys. Res. Lett. **24**, 1359 (1997).
24. C. S. Zerefos, D. S. Balis, A. F. Bais, *et al.*, Geophys. Res. Lett. **24**, 1363 (1997).
25. *Impact of Climatic Change on the Biosphere*, Part 1: *UV Radiation Effects* (CIAP, Washington, D.C., 1975), Monography 5, DOT-TST-75-55.
26. *World Meteorological Organization (WMO). Scientific Assessment of Ozone Depletion* (WMO Global Ozone Research and Monitoring Project, Geneva, 1994), Report 37.

27. *World Meteorological Organization (WMO) and United National Environment Program (UNEP). Climate Change 1995—The Science of Climate Change, Summery of Policymakers, Working Group 1* (IPCC, Geneva, 1995), p. 56.
28. Yu. A. Goldberg, Semicond. Sci. Technol. **14** (37), R41 (1999).
29. *GOST* (State Standard) *17772-1988: Semiconductor Photoelectrical Detectors and Photodetectors* (1988).
30. *GOST* (State Standard) *21934-1983: Semiconductor Photoelectrical Detectors and Photodetectors. Terms and Definitions* (1983).
31. D. E. Aspnes and A. A. Studna, Phys. Rev. B **27**, 985 (1983).
32. H. R. Philipp and E. A. Taft, *Silicon Carbide—A High Temperature Semiconductor* (Pergamon Press, Oxford, 1960).
33. D. E. Aspnes, S. M. Kenso, R. A. Logan, and R. Bhat, J. Appl. Phys. **60**, 754 (1986).
34. S. G. Sridhara, R. P. Devaty, and W. J. Choyke, J. Appl. Phys. **84**, 2963 (1998).
35. Noriyuki Miyata, Rfzunori Moriki, Osumu Mishima, *et al.*, Phys. Rev. B **40**, 12028 (1989).
36. C. R. Aita, C. J. G. Kubiak, and F. Y. H. Shih, J. Appl. Phys. **66**, 4360 (1989).
37. R. Groth and E. Kauer, Phys. Status Solidi **1**, 445 (1961).
38. J. F. Muth, J. H. Lee, I. K. Shmagin, *et al.*, Appl. Phys. Lett. **71**, 2572 (1997).
39. J. Baillou, J. Daunay, P. Bugnet, *et al.*, J. Phys. Chem. Solids **41**, 295 (1980).
40. J. W. Tomm, B. Ullrich, X. G. Qiu, *et al.*, J. Appl. Phys. **87**, 1844 (2000).
41. A. Zunger, A. Katzir, and A. Halperin, Phys. Rev. B **13**, 5560 (1976).
42. O. Ambacher, W. Rieger, P. Ansmann, *et al.*, Solid State Commun. **97**, 365 (1997).
43. S. Sze, *Physics of Semiconductor Devices*, 2nd ed. (Wiley, New York, 1981; Mir, Moscow, 1984).
44. *Handbook Series on Semiconductor Parameters*, Ed. by M. Levinshtein, S. Rumyantsev, and M. Shur (World Sci., Singapore, 1996 and 1999), Vols. 1 and 2.
45. *Properties of Advanced Semiconductor Materials*, Ed. by M. Levinshtein, S. Rumyantsev, and M. Shur (Wiley, New York, 2001).
46. H. Morkoç, S. Strite, G. B. Gao, *et al.*, J. Appl. Phys. **76**, 1363 (1994).
47. Lei Wang, M. I. Nathan, T.-H. Lim, *et al.*, Appl. Phys. Lett. **68**, 1267 (1996).
48. M. Rebien, W. Henrion, M. Bar, and C.-H. Fisher, Appl. Phys. Lett. **80**, 3518 (2002).
49. R. Trew, J. B. Yan, and P. M. Mock, Proc. IEEE **79**, 598 (1991).
50. A. O. Konstantinov, Q. Wahab, N. Nordell, and U. Lindefelt, Appl. Phys. Lett. **71**, 90 (1997).
51. Technical Report, III–V Review **15** (2), 17 (2002).
52. Y. P. Varshni, Physica (Amsterdam) **34**, 149 (1967).
53. D. Matsuura, T. Kanemitsu, T. Kushida, *et al.*, Appl. Phys. Lett. **77**, 2289 (2000).
54. J. D. Guo, M. S. Feng, R. J. Guo, *et al.*, Appl. Phys. Lett. **67**, 2657 (1995).
55. A. N. Andreev, A. A. Lebedev, M. G. Rastegaeva, *et al.*, Fiz. Tekh. Poluprovodn. (St. Petersburg) **29**, 1833 (1995) [Semiconductors **29**, 957 (1995)].
56. M. Sawada, T. Sawada, Y. Yanagata, *et al.*, in *Proceedings of Second International Conference on Nitride Semiconductors* (Tokushino, Japan, 1997), p. 706.
57. B. V. Tsarenkov, Yu. A. Gol'dberg, and E. A. Posse, Fiz. Tekh. Poluprovodn. (Leningrad) **7**, 2326 (1973) [Sov. Phys. Semicond. **7**, 1546 (1973)].
58. J. R. Waldrop, R. W. Grant, Y. C. Wang, and R. F. Davis, J. Appl. Phys. **72**, 4757 (1992).
59. T. Mori, T. Kozawa, T. Ohwaki, *et al.*, Appl. Phys. Lett. **69**, 3537 (1996).
60. H. Sheng, S. Muthukumar, N. W. Emanetoglu, and Y. Lu, Appl. Phys. Lett. **80**, 2132 (2002).
61. R. G. Verenchikova, V. I. Sankin, and E. I. Radovanova, Fiz. Tekh. Poluprovodn. (Leningrad) **17**, 1757 (1983) [Sov. Phys. Semicond. **17**, 1123 (1983)].
62. E. V. Kalinina, N. I. Kuznetsov, A. I. Babanin, *et al.*, Diamond Relat. Mater. **6**, 1528 (1997).
63. S. Yu. Davydov, A. A. Lebedev, O. V. Posrednik, and Yu. M. Tairov, Fiz. Tekh. Poluprovodn. (St. Petersburg) **35**, 1437 (2001) [Semiconductors **35**, 1375 (2001)].
64. Wei-Chin Lai, in *Abstracts of International Conference on SiC, III-Nitrides Related Materials* (Stockholm, 1997), p. 12.
65. N. I. Kuznetsov, E. V. Kalinina, V. A. Soloviev, and V. A. Dmitriev, Mater. Res. Soc. Symp. Proc. **395**, 837 (1999).
66. F. Lavia, F. Roccaforte, V. Raineri, *et al.*, in *Technical Digest of International Conference on SiC and Related Materials* (Tsukuba, Japan, 2001), Th-P-41, p. 641.
67. Q. Z. Liu, L. S. Yu, F. Deng, *et al.*, J. Appl. Phys. **84**, 881 (1998).
68. L. S. Yu, D. Qiao, L. Jia, *et al.*, Appl. Phys. Lett. **79**, 4536 (2001).
69. O. Shigiltchoff, T. Kimoto, D. Hoodgood, *et al.*, in *Technical Digest of International Conference on SiC and Related Materials* (Tsukuba, Japan, 2001), We-B-23, p. 291.
70. Ja-Soon Jang and Tae-Yeon Seong, Appl. Phys. Lett. **76**, 2743 (2000).
71. E. H. Rhoderick, *Metal–Semiconductor Contacts* (Clarendon Press, Oxford, 1978; Radio i Svyaz', Moscow, 1982).
72. Yu. A. Gol'dberg, E. A. Posse, B. V. Tsarenkov, and M. I. Shul'ga, Fiz. Tekh. Poluprovodn. (Leningrad) **25**, 439 (1991) [Sov. Phys. Semicond. **25**, 266 (1991)].
73. Yu. A. Gol'dberg, E. A. Posse, and B. V. Tsarenkov, Fiz. Tekh. Poluprovodn. (Leningrad) **9**, 513 (1975) [Sov. Phys. Semicond. **9**, 337 (1975)].
74. R. H. Fowler, Phys. Rev. **38**, 45 (1931).
75. C. L. Anderson, C. R. Crowell, and T. W. Kao, Solid-State Electron. **18**, 705 (1975).
76. W. W. Gartner, Phys. Rev. **116**, 84 (1959).
77. S. S. Li, F. A. Lindholm, and C. T. Wang, J. Appl. Phys. **43**, 4123 (1972).

78. A. A. Gutkin and V. E. Sedov, Fiz. Tekh. Poluprovodn. (Leningrad) **9**, 1761 (1975) [Sov. Phys. Semicond. **9**, 1155 (1975)].
79. J. M. Caywood and C. A. Mead, Appl. Phys. Lett. **15**, 14 (1969).
80. M. Lavange, J. P. Pique, and Y. Marfing, Solid-State Electron. **20**, 235 (1969).
81. A. M. Cowley and S. M. Sze, J. Appl. Phys. **36**, 3212 (1965).
82. B. I. Reznikov and G. V. Tsarenkov, Fiz. Tekh. Poluprovodn. (Leningrad) **25**, 1922 (1991) [Sov. Phys. Semicond. **25**, 1158 (1991)].
83. O. A. Mezrin and S. I. Troshkov, Fiz. Tekh. Poluprovodn. (Leningrad) **22**, 176 (1988) [Sov. Phys. Semicond. **22**, 110 (1988)].
84. Yu. A. Gol'dberg, T. V. L'vova, O. A. Mezrin, and S. I. Troshkov, Fiz. Tekh. Poluprovodn. (Leningrad) **24**, 1835 (1990) [Sov. Phys. Semicond. **24**, 1143 (1990)].
85. O. V. Konstantinov, O. A. Mezrin, and G. V. Tsarenkov, Fiz. Tekh. Poluprovodn. (Leningrad) **22**, 129 (1988) [Sov. Phys. Semicond. **22**, 78 (1988)].
86. T. V. Blank, Yu. A. Goldberg, and O. V. Konstantinov, in *Abstracts of 13th International Conference on Solid State Dosimetry* (Athens, Greece, 2001).
87. R. F. Kazarinov and O. V. Konstantinov, Zh. Éksp. Teor. Fiz. **40**, 936 (1961) [Sov. Phys. JETP **13**, 654 (1961)].
88. Yu. A. Gol'dberg, O. V. Konstantinov, E. A. Posse, and B. V. Tsarenkov, Fiz. Tekh. Poluprovodn. (St. Petersburg) **29**, 421 (1995) [Semiconductors **29**, 215 (1995)].
89. Yu. A. Goldberg, O. V. Konstantinov, O. I. Obolensky, *et al.*, J. Phys.: Condens. Matter **11**, 455 (1999).
90. T. V. Blank, Yu. A. Gol'dberg, E. V. Kalinina, *et al.*, Pis'ma Zh. Tekh. Fiz. **27** (18), 43 (2001) [Tech. Phys. Lett. **27**, 776 (2001)].
91. A. L. Fahrenbruch and R. H. Bube, *Fundamentals of Solar Cells. Photovoltaic Solar Energy Conversion* (Academic, New York, 1983; Énergoizdat, Moscow, 1987).
92. M. M. Anikin, V. V. Evstropov, N. V. Popov, *et al.*, Fiz. Tekh. Poluprovodn. (Leningrad) **23**, 647 (1989) [Sov. Phys. Semicond. **23**, 405 (1989)].
93. M. M. Anikin, V. V. Evstropov, N. V. Popov, *et al.*, Fiz. Tekh. Poluprovodn. (Leningrad) **23**, 1813 (1989) [Sov. Phys. Semicond. **23**, 1122 (1989)].
94. M. Razeghi and A. Rogalski, J. Appl. Phys. **79**, 7433 (1996).
95. P. W. Kruse, *Optical Infrared Detectors* (Berlin, 1977).
96. W. Dingfen and K. Heime, Electron. Lett. **18**, 940 (1982).
97. W. Dingfen, W. Dening, and K. Heime, Solid-State Electron. **29**, 489 (1987).
98. R. K. Kupka and W. A. Anderson, J. Appl. Phys. **69**, 3623 (1991).
99. A. Y. C. Yu, Solid-State Electron. **13**, 239 (1970).
100. S. M. Cho, J. D. Lee, and H. H. Lee, J. Appl. Phys. **70**, 282 (1991).
101. Noriaki Mochida, Tohru Honda, Tomoe Shirasawa, *et al.*, J. Cryst. Growth **189–190**, 716 (1998).
102. D. Qiao, L. S. Yu, L. Jia, *et al.*, Appl. Phys. Lett. **80**, 992 (2002).
103. Lu-Min Liu, G. Lindauer, W. B. Alexander, and P. H. Holloway, J. Vac. Sci. Technol. B **13**, 2238 (1995).
104. Y. X. Wang and P. H. Holloway, Vacuum **43**, 1149 (1992).
105. J. J. Fijol, J. T. Trexler, L. Calhoun, *et al.*, J. Vac. Sci. Technol. B **14**, 159 (1996).
106. S. Miller and P. H. Holloway, J. Electron. Mater. **25**, 1709 (1996).
107. A. Durbha, S. J. Pearton, C. R. Abernathy, *et al.*, J. Vac. Sci. Technol. B **14**, 2582 (1996).
108. T. Gessmann, Y. L. Li, E. L. Waldron, *et al.*, Appl. Phys. Lett. **80**, 986 (2002).
109. P. H. Holloway, T. J. Kim, J. T. Trexler, *et al.*, Appl. Surf. Sci. **117–118**, 362 (1997).
110. C. R. Abernathy, J. D. MacKenzie, S. J. Pearton, and W. S. Hobson, Appl. Phys. Lett. **66**, 1969 (1995).
111. Ho Won Jang, W. Urbanek, M. C. Yoo, and Jong-Lam Lee, Appl. Phys. Lett. **80**, 2937 (2002).
112. Joon Seop Kwak, Ok-Hyun Nam, and Yongjo Park, Appl. Phys. Lett. **80**, 3554 (2002).
113. K. O. Schweitz, P. K. Wang, S. E. Mohney, and D. Gotthold, Appl. Phys. Lett. **80**, 1954 (2002).
114. H. Morkoç, S. Strike, G. B. Gao, *et al.*, J. Appl. Phys. **76**, 1363 (1994).
115. M. E. Lin, Z. Ma, F. Y. Huang, *et al.*, Appl. Phys. Lett. **64**, 1003 (1994).
116. S. Prakashs, L. S. Tan, K. M. Ng, *et al.*, in *Abstracts of International Conference on SiC and Related Materials* (Sheraton, 1999), p. 48.
117. Zhifang Fan, S. Noor Mohammad, Wook Kim, *et al.*, Appl. Phys. Lett. **68**, 1672 (1996).
118. E. Kaminska, A. Piotrowska, A. Barcz, *et al.*, Mater. Res. Soc. Symp. Proc. **482**, 1077 (1998).
119. A. Lunev, V. Chaturvedi, A. Chitmis, *et al.*, in *Abstracts of International Conference on SiC and Related Materials* (Sheraton, 1999), p. 159.
120. J. B. Fedison, T. P. Chow, H. Lu, and T. B. Bhat, in *Abstracts of International Conference on SiC and Related Materials* (Sheraton, 1999), p. 463.
121. Ja-Soon Jang, Seong-Ju Park, and Tae-Yeon Seong, Appl. Phys. Lett. **76**, 2898 (2000).
122. D. B. Ingerly, Y. A. Chang, and Y. Chen, MRS Internet J. Nitride Semicond. Res. **4S1**, G6.49 (1999).
123. J. S. Jang, H. G. Kim, K. H. Park, *et al.*, Mater. Res. Soc. Symp. Proc. **482**, 1653 (1998).
124. Jin-Kuo Ho, Charng-Shyang Jong, Chien C. Chiu, *et al.*, Appl. Phys. Lett. **74**, 1275 (1999).
125. D. B. Ingerly, Y. A. Chang, and Y. Chen, Appl. Phys. Lett. **74**, 2480 (1999).
126. Masaaki Suzuki, T. Arai, T. Kawakami, *et al.*, J. Appl. Phys. **86**, 5079 (1999).
127. R. W. Chuang, A. Q. Zou, and H. P. Lee, MRS Internet J. Nitride Semicond. Res. **4S1**, G6.42 (1999).
128. Chen-Fu Chu, C. C. Yu, Y. K. Wang, *et al.*, Appl. Phys. Lett. **77**, 3423 (2000).
129. M. S. Carpenter, M. R. Melloch, M. S. Lundstrom, and S. P. Tobin, Appl. Phys. Lett. **52**, 2157 (1988).
130. M. S. Carpenter, M. R. Melloch, and T. E. Dungan, Appl. Phys. Lett. **53**, 66 (1988).

131. Yasuo Nannichi, Jia-Fa Fan, Haruhiro Oigawa, and Atsushi Koma, Jpn. J. Appl. Phys. **27**, L2367 (1988).
132. Jia-Fa Fan, Haruhiro Oigawa, and Yasuo Nannichi, Jpn. J. Appl. Phys. **27**, L2125 (1988).
133. S. Logha, D. B. Janes, and N. P. Chen, Appl. Phys. Lett. **80**, 4452 (2002).
134. Ching-Ting Lee, Yow-Jon Lin, and Day-Shan Liu, Appl. Phys. Lett. **79**, 2573 (2001).
135. J. O. Song, Seong-Ju Park, and Tae-Yeon Seong, Appl. Phys. Lett. **80**, 3129 (2002).
136. G. Y. Chung, C. C. Tin, J. R. Williams, *et al.*, in *Abstracts of E-MRS Spring Meeting, Symposium F: Amorphous and Crystalline Silicon Carbide, Material and Applications* (2001), F7.
137. J. Massies, J. Chaplart, M. Lavirou, and N. T. Linh, Appl. Phys. Lett. **38**, 693 (1981).
138. Yih-Cheng Shin, Masanori Murakami, E. L. Wilkie, and A. C. Callegari, J. Appl. Phys. **62**, 582 (1987).
139. M. Otsubo, H. Kumabe, and H. Miki, Solid-State Electron. **20**, 617 (1977).
140. A. Christou, Solid-State Electron. **22**, 141 (1979).
141. C. L. Chen, L. J. Mahoney, M. C. Finn, *et al.*, Appl. Phys. Lett. **48**, 535 (1986).
142. Yu. A. Gol'dberg, Fiz. Tekh. Poluprovodn. (St. Petersburg) **28**, 1681 (1994) [Semiconductors **28**, 935 (1994)].
143. Yu. A. Gol'dberg and B. V. Tsarenkov, Fiz. Tekh. Poluprovodn. (Leningrad) **3**, 1718 (1969) [Sov. Phys. Semicond. **3**, 1447 (1969)].
144. Yih-Cheng Shih, Masanori Murakami, and W. H. Price, J. Appl. Phys. **65**, 3539 (1989).
145. C.-F. Lin, D. B. Ingerly, and Y. A. Chang, Appl. Phys. Lett. **69**, 3543 (1996).
146. Sang Youn Han, Ki Honh Kim, Jong Kyu Kim, *et al.*, Appl. Phys. Lett. **79**, 1816 (2001).
147. Hidenori Shimawaki, Naoki Furuhata, and Kasuhiko Honjo, J. Appl. Phys. **69**, 7939 (1991).
148. A. Katz, S. Nakahara, W. Savin, and B. E. Weir, J. Appl. Phys. **68**, 4133 (1990).
149. T. Clausen and O. Leistiko, Appl. Phys. Lett. **62**, 1108 (1993).
150. S. N. G. Chu, A. Katz, T. Boone, *et al.*, J. Appl. Phys. **67**, 3754 (1990).
151. J. D. Guo, C. I. Lin, M. S. Feng, *et al.*, Appl. Phys. Lett. **68**, 235 (1996).
152. T. V. Blank, Yu. A. Gol'dberg, E. V. Kalinina, *et al.*, Fiz. Tekh. Poluprovodn. (St. Petersburg) **35**, 550 (2001) [Semiconductors **35**, 529 (2001)].
153. T. Nacamura and M. Satoh, in *Abstracts of International Conference on SiC and Related Materials* (Tsukuba, Japan, 2001), Technical Digest Th-P-41, p. 631.
154. E. I. Ivanov, L. B. Lopatina, V. L. Sukhanov, *et al.*, Fiz. Tekh. Poluprovodn. (Leningrad) **15**, 1343 (1981) [Sov. Phys. Semicond. **15**, 775 (1981)].
155. *High Performance Silicon Photodiodes*, Centronic Lim. Catalog (1995).
156. *Optoelectronics Data Book*, EG and G Vactec Catalog (1991).
157. *Photodiodes*, Hamamatsu Photonics Catalog (1995).
158. *Optoelectronics Data Book*, Advanced Photonics Catalog (1995).
159. R. W. Williams, J. Opt. Soc. Am. **52**, 1237 (1962).
160. T. E. Hansen, Phys. Scr. **18**, 471 (1978).
161. W. Munch, Jpn. J. Appl. Phys., Suppl. **16**, 271 (1977).
162. R. Korde and J. Geist, Appl. Opt. **26**, 5248 (1987).
163. R. Korde and J. Geist, Solid-State Electron. **30**, 89 (1987).
164. L. R. Canfield, J. Kerner, R. Korde, and J. Geist, Appl. Opt. **28**, 3940 (1989).
165. Yu. A. Gol'dberg, V. V. Zabrodskiĭ, O. I. Obolenskiĭ, *et al.*, Fiz. Tekh. Poluprovodn. (St. Petersburg) **33**, 344 (1999) [Semiconductors **33**, 343 (1999)].
166. Technology Report, Laser Focus **21**, 256 (1985).
167. E. Tegeler and N. Krumrey, Nucl. Instrum. Methods Phys. Res. A **282**, 701 (1989).
168. N. Krumrey and E. Tegeler, Nucl. Instrum. Methods Phys. Res. A **288**, 714 (1990).
169. N. Krumrey, E. Tegeler, J. Barth, *et al.*, Appl. Opt. **27**, 4336 (1988).
170. M. V. Schneider, Bell Syst. Tech. J. **45**, 1611 (1966).
171. C. K. Chen, B. Nechay, and B. Y. Tsaur, IEEE Trans. Electron Devices **38**, 1094 (1991).
172. M. M. Blouke, M. W. Cowens, J. E. Hall, *et al.*, Appl. Opt. **19**, 3318 (1980).
173. G. Leveque, J. Peisner, and Y. Sangare, Appl. Opt. **33**, 1857 (1994).
174. J. R. Janesick, K. P. Klaasen, and T. Elliott, Opt. Eng. (Bellingham) **26**, 972 (1987).
175. G. Naletto, E. Pace, G. Tondello, and A. Boscolo, Meas. Sci. Technol. **5**, 1491 (1994).
176. A. D. Conder, J. Dunn, and B. K. F. Young, Rev. Sci. Instrum. **66**, 709 (1995).
177. P. F. Morrissey, S. R. McCandliss, P. D. Feldman, and S. D. Friedman, Appl. Opt. **33**, 2535 (1994).
178. Yu. A. Gol'dberg, T. V. L'vova, and B. V. Tsarenkov, Prib. Tekh. Éksp. **19** (4), 212 (1976).
179. M. Caria, L. Barberini, S. Cadeddu, *et al.*, Appl. Phys. Lett. **81**, 1506 (2002).
180. T. F. Deutsch, F. J. Leonberger, A. G. Foyt, and D. Mills, Appl. Phys. Lett. **41**, 403 (1982).
181. A. D. Wilson and H. Lyall, Appl. Opt. **25**, 4530 (1986).
182. A. D. Wilson and H. Lyall, Appl. Opt. **25**, 4540 (1986).
183. B. V. Tsarenkov, Yu. A. Gol'dberg, G. V. Gusev, and V. I. Ogurtsov, Fiz. Tekh. Poluprovodn. (Leningrad) **8**, 410 (1974) [Sov. Phys. Semicond. **8**, 264 (1974)].
184. V. I. Stafeev and I. D. Anisimova, Fiz. Tekh. Poluprovodn. (St. Petersburg) **28**, 461 (1994) [Semiconductors **28**, 281 (1994)].
185. R. C. Hughes, T. E. Zipperian, L. R. Dawson, *et al.*, J. Appl. Phys. **69**, 6500 (1991).
186. A. I. Malik and T. G. Grushka, Fiz. Tekh. Poluprovodn. (Leningrad) **25**, 1691 (1991) [Sov. Phys. Semicond. **25**, 1017 (1991)].
187. Yu. A. Gol'dberg and B. V. Tsarenkov, Zh. Tekh. Fiz. **66** (8), 195 (1996) [Tech. Phys. **41**, 850 (1996)].
188. A. R. Annaeva, A. Berkeliev, V. N. Bessolov, *et al.*, Fiz. Tekh. Poluprovodn. (Leningrad) **15**, 1122 (1981) [Sov. Phys. Semicond. **15**, 646 (1981)].

189. A. R. Annaeva, A. Berkeliev, V. N. Bessolov, *et al.*, Fiz. Tekh. Poluprovodn. (Leningrad) **15**, 109 (1981) [Sov. Phys. Semicond. **15**, 64 (1981)].
190. V. M. Andreev, V. S. Kalinovskiĭ, V. R. Larionov, *et al.*, Pis'ma Zh. Tekh. Fiz. **16** (19), 56 (1990) [Sov. Tech. Phys. Lett. **16**, 748 (1990)].
191. Q. Chen, J. W. Yang, A. Osinsky, *et al.*, Appl. Phys. Lett. **70**, 2277 (1997).
192. C. Carrano, P. A. Grudowski, C. J. Eiting, *et al.*, Appl. Phys. Lett. **70**, 1992 (1997).
193. O. Katz, V. Garber, B. Meyler, *et al.*, Appl. Phys. Lett. **80**, 347 (2002).
194. E. Monroy, T. Palacios, O. Hainaut, *et al.*, Appl. Phys. Lett. **80**, 3198 (2002).
195. Shigeru Yagi, Appl. Phys. Lett. **76**, 345 (2000).
196. Z. M. Zhao, R. L. Jiang, P. Chen, *et al.*, Appl. Phys. Lett. **77**, 444 (2000).
197. S. W. Seo, K. K. Lee, Sangbeom Kang, *et al.*, Appl. Phys. Lett. **79**, 1372 (2001).
198. Ching-Wu Wang, Appl. Phys. Lett. **80**, 1568 (2002).
199. Necmi Biyikli, Tolga Kartaloglu, Orhau Aytur, *et al.*, Appl. Phys. Lett. **79**, 2838 (2001).
200. V. Adivarahan, G. Simin, J. W. Yang, *et al.*, Appl. Phys. Lett. **77**, 863 (2000).
201. O. Katz, V. Garber, B. Meyler, *et al.*, Appl. Phys. Lett. **79**, 1417 (2001).
202. P. W. Deelman, R. N. Bicknell-Tassius, S. Nikishin, *et al.*, Appl. Phys. Lett. **78**, 2172 (2001).
203. J. M. Van Hove, R. Hickman, J. J. Klaassen, *et al.*, Appl. Phys. Lett. **70**, 2282 (1997).
204. A. Osinsky, S. Gangopadhyay, R. Gaska, *et al.*, Appl. Phys. Lett. **71**, 2334 (1997).
205. J. C. Carrano, D. J. H. Lambert, C. J. Eiting, *et al.*, Appl. Phys. Lett. **76**, 924 (2000).
206. K. A. McIntosh, R. J. Molnar, L. J. Mahoney, *et al.*, Appl. Phys. Lett. **76**, 3938 (2000).
207. M. Asif Khan, J. N. Kuznia, D. T. Olson, *et al.*, Appl. Phys. Lett. **60**, 2917 (1992).
208. D. Walker, X. Zhang, P. Kung, *et al.*, Appl. Phys. Lett. **68**, 2100 (1996).
209. A. Misra, T. D. Moustakas, R. P. Vaudo, *et al.*, Proc. SPIE **2519**, 78 (1995).
210. K. S. Stevens, M. Kinniburgh, A. F. Schwartzman, *et al.*, Appl. Phys. Lett. **66**, 3179 (1995).
211. J. P. Basrur, F. S. Choa, P.-L. Liu, *et al.*, Appl. Phys. Lett. **71**, 1385 (1997).
212. J. A. Garrido, E. Monroy, I. Izpura, and E. Muñoz, Semicond. Sci. Technol. **13**, 563 (1998).
213. J.-F. Hochedez, J. Alvarez, F. D. Auret, *et al.*, Diamond Relat. Mater. **11**, 427 (2002).
214. J. L. Pau, E. Monroy, F. B. Naranjo, *et al.*, Appl. Phys. Lett. **76**, 2785 (2000).
215. E. J. Tarsa, P. Kozodoy, J. Ibbetson, *et al.*, Appl. Phys. Lett. **77**, 316 (2000).
216. D. Walker, V. Kumar, K. Mi, *et al.*, Appl. Phys. Lett. **76**, 403 (2000).
217. E. Monroy, F. Calle, E. Muñoz, *et al.*, Appl. Phys. Lett. **73**, 2146 (1998).
218. V. Adivarahan, G. Simin, G. Tamulaitis, *et al.*, Appl. Phys. Lett. **79**, 1903 (2001).
219. A. Bouhdada, M. Hanzaz, P. Gibart, *et al.*, J. Appl. Phys. **87**, 8286 (2000).
220. E. Monroy, F. Calle, J. L. Pau, *et al.*, J. Appl. Phys. **88**, 2081 (2000).
221. S. L. Rumyantsev, N. Pala, M. S. Shur, *et al.*, Appl. Phys. Lett. **79**, 866 (2001).
222. G. Y. Xu, A. Salvador, W. Kim, *et al.*, Appl. Phys. Lett. **71**, 2154 (1997).
223. C. J. Collins, T. Li, D. J. H. Lambert, *et al.*, Appl. Phys. Lett. **77**, 2810 (2000).
224. D. J. H. Lambert, M. M. Wong, U. Chowdhury, *et al.*, Appl. Phys. Lett. **77**, 1900 (2000).
225. C. J. Collins, U. Chowdhury, M. M. Wong, *et al.*, Appl. Phys. Lett. **80**, 3754 (2002).
226. V. V. Kuryatkov, H. Temkin, J. C. Campbell, and R. D. Dupuis, Appl. Phys. Lett. **78**, 3340 (2001).
227. H. Morkoc, A. Di Carlo, and R. Cingolani, Solid-State Electron. **46**, 157 (2002).
228. Technical Report, III–V Review **15** (7), 14 (2002).
229. R. G. Verenchikova, Yu. A. Vodakov, D. P. Litvin, *et al.*, Fiz. Tekh. Poluprovodn. (St. Petersburg) **26**, 1008 (1992) [Sov. Phys. Semicond. **26**, 565 (1992)].
230. *SiC UV Detectors, Laser Components Catalog* (Electronics Corp., Boston, 1996).
231. M. M. Anikin, A. N. Andreev, S. N. Pyatko, *et al.*, Sens. Actuators A **33**, 91 (1992).
232. C. Frojdn, G. Thungstrom, H. E. Nilsson, and C. S. Petersson, Phys. Scr. **54**, 169 (1994).
233. V. I. Sankin and V. P. Chelibanov, Phys. Status Solidi **185**, 153 (2001).
234. A. A. Lebedev, N. S. Savkina, A. M. Ivanov, *et al.*, Fiz. Tekh. Poluprovodn. (St. Petersburg) **34**, 245 (2000) [Semiconductors **34**, 243 (2000)].
235. G. Violina, A. Andreev, and E. Violin, in *Proceedings of Second European Conference on High Temperature Electronics, HITEC* (1996), p. 195.
236. D. M. Brown, E. Downey, J. Kretchmer, *et al.*, in *Proceedings of Second European Conference on High Temperature Electronics, HITEC* (1996), p. 23.
237. D. M. Brown, E. T. Downey, M. Chezzo, *et al.*, IEEE Trans. Electron Devices **40**, 325 (1993).
238. J. Edmond, H. Kong, A. Suvorov, *et al.*, Phys. Status Solidi A **162**, 481 (1997).
239. J. A. Edmond, H. S. Kong, and C. H. Carter, Jr., Physica B (Amsterdam) **185**, 453 (1993).
240. G. N. Violina, E. V. Kalinina, G. F. Kholujanov, *et al.*, Fiz. Tekh. Poluprovodn. (St. Petersburg) **36**, 750 (2002) [Semiconductors **36**, 710 (2002)].
241. D. M. Aksenenko and M. L. Baranochnikov, *Handbook on Optical Detectors of Radiation* (Radio i Svyaz', Moscow, 1987).
242. S. Yu. Pavelets, Yu. N. Bobrenko, A. V. Komashchenko, and T. E. Shengeliya, Fiz. Tekh. Poluprovodn. (St. Petersburg) **35**, 626 (2001) [Semiconductors **35**, 605 (2001)].
243. A. Gerhard, J. Nurnberg, K. Schull, *et al.*, J. Cryst. Growth **184–185**, 1319 (1998).
244. H. Hong and W. A. Anderson, IEEE Trans. Electron Devices **46**, 1127 (1999).

245. F. Vigué, E. Tournié, and J.-P. Faurie, Electron. Lett. **36**, 352 (2000).
246. F. Vigué, P. de Mierry, J.-P. Faurie, *et al.*, Electron. Lett. **36**, 826 (2000).
247. E. Monroy, F. Vigué, F. Calle, *et al.*, Appl. Phys. Lett. **77**, 2761 (2000).
248. F. Vigué, E. Tournié, J.-P. Faurie, *et al.*, Appl. Phys. Lett. **78**, 4190 (2001).
249. A. Siess, G. Reuscher, P. Grabs, *et al.*, J. Cryst. Growth **201–202**, 965 (1999).
250. F. Vigué, E. Tournié, and J.-P. Faurie, Appl. Phys. Lett. **76**, 242 (2000).
251. Hitoshi Ishikura, Tomoki Abe, Nariyuki Fukuda, *et al.*, Appl. Phys. Lett. **76**, 1069 (2000).
252. Z. H. Ma, I. K. Sou, K. S. Wong, *et al.*, Appl. Phys. Lett. **73**, 2251 (1998).
253. I. K. Sou, Z. H. Ma, and G. K. L. Wong, Appl. Phys. Lett. **75**, 3707 (1999).
254. I. K. Sou, Z. H. Ma, Z. Q. Zhang, and G. K. L. Wong, Appl. Phys. Lett. **76**, 1098 (2000).
255. A. Zeuner, H. Alves, D. M. Hofmann, *et al.*, Appl. Phys. Lett. **80**, 2078 (2002).
256. H. Fabricius, T. Skettrup, and P. Bisgaard, Appl. Opt. **25**, 2764 (1986).
257. Y. Liu, C. R. Gorla, S. Liang, *et al.*, J. Electron. Mater. **29**, 69 (2000).
258. W. Yang, R. D. Vispute, S. Choopun, *et al.*, Appl. Phys. Lett. **78**, 2787 (2001).
259. P. Sharma, A. Mansingh, and K. Sreenivas, Appl. Phys. Lett. **80**, 553 (2002).
260. K. Keis, E. Magnusson, H. Lindstom, *et al.*, Sol. Energy Mater. Sol. Cells **73** (1), 51 (2002).
261. Yu. A. Nikolaev, V. Yu. Rud', Yu. V. Rud', *et al.*, Fiz. Tekh. Poluprovodn. (St. Petersburg) **36**, 1128 (2002) [Semiconductors **36**, 1048 (2002)].
262. M. D. Whitfield, S. S. M. Chan, and R. B. Jackman, Appl. Phys. Lett. **68**, 290 (1996).
263. F. Foulon, P. Bergonzo, C. Borel, *et al.*, J. Appl. Phys. **84**, 5331 (1998).
264. G. Popovici, A. Melnikov, V. V. Varichenko, *et al.*, J. Appl. Phys. **81**, 2429 (1997).
265. Satoshi Koizumi, Kenji Watanabe, Masataka Hasegawa, and Hisao Kanda, Diamond Relat. Mater. **11**, 307 (2002).
266. R. D. McKeag, S. S. M. Chan, and R. B. Jackman, Appl. Phys. Lett. **67**, 2117 (1995).
267. S. Salvatori, A. Della Scala, M. C. Rossi, and G. Conte, Diamond Relat. Mater. **11**, 458 (2002).
268. L. Thaiyotin, E. Ratanaudompisut, T. Phetchakul, *et al.*, Diamond Relat. Mater. **11**, 442 (2002).
269. S. P. Lansley, O. Gaudin, Haitao Ye, *et al.*, Diamond Relat. Mater. **11**, 433 (2002).
270. T. V. Semikina and A. N. Shmyryeva, Diamond Relat. Mater. **11**, 1329 (2002).
271. S. Noguchi, H. Kuriyama, T. Matsuyama, and H. Tarui, Sanyo Tech. Rev. **23**, 70 (1991).
272. P. Mandracci, M. L. Rastello, P. Rava, *et al.*, Thin Solid Films **337**, 232 (1999).
273. Zh. Ataev, V. A. Vasil'ev, A. S. Volkov, *et al.*, Fiz. Tekh. Poluprovodn. (Leningrad) **25**, 1350 (1991) [Sov. Phys. Semicond. **25**, 815 (1991)].
274. M. Topič, H. Stiebig, M. Krause, and H. Wagner, Appl. Phys. Lett. **78**, 2387 (2001).
275. G. de Cesare, F. Irrera, F. Palma, *et al.*, Appl. Phys. Lett. **67**, 335 (1995).
276. V. V. Sobolev and A. I. Kolugin, Fiz. Tekh. Poluprovodn. (St. Petersburg) **36**, 155 (2002) [Semiconductors **36**, 148 (2002)].
277. A. Mills, III–V Review **15** (2), 36 (2002).
278. B. Chu, D. Fan, W. L. Li, *et al.*, Appl. Phys. Lett. **81**, 10 (2002).
279. Peigen Ni, Bingying Cheng, and Daozhong Zhang, Appl. Phys. Lett. **80**, 1879 (2002).
280. Hidenori Hiramatsu, Kazushige Ueda, Hiromichi Ohta, *et al.*, Appl. Phys. Lett. **81**, 598 (2002).
281. S. A. Jenekhe and Shujian Yi, Appl. Phys. Lett. **77**, 2635 (2000).

Translated by A. Spitsyn